RAPID SOLIDIFICATION OF HIGH-CONDUCTIVITY COPPER ALLOYS

by

THEODORE ATLAS BLOOM

Submitted in partial fulfillment of the
requirements for the degree of
Doctor of Philosophy in Metallurgical and Materials Engineering
in the School of Advanced Studies of
Illinois Institute of Technology

Approved _____
Adviser

Chicago, Illinois
August, 1989

ACKNOWLEDGMENT

The author wishes to acknowledge the financial support of the NASA Lewis Research Center. Special thanks are extended to my adviser, Dr. P. Nash, for his encouragement, guidance and assistance throughout the course of this study. In addition, the author is grateful for the encouragement and guidance provided by Mr. T. K. Glasgow who acted as co-adviser at the NASA Lewis Research Center. The skillful assistance of Mr. N. Orth and Mr. J. King in producing all of the melt spun alloys is greatly appreciated. The author extends thanks to all of the people at NASA who assisted the progress of this work in one way or another. An incomplete list of these people includes Dr. H. Gray, Dr. R. Dreshfield, Dr. I. Locci, Mr. B. Buzek, Mr. D. Hull, Mr. W. McCort, Mr. H. Gerringer and Mr. S. White. Special thanks are extended to all of the IIT METM faculty and graduate students for their support and encouragement. Finally, the author is grateful to his parents for their encouragement and patience during the course of this program.

T.A.B.

TABLE OF CONTENTS

LIST OF TABLES

LIST OF FIGURES

ABSTRACT

The purpose of the present work was to develop improved copper alloys of high strength and high thermal and electrical conductivity. Chill block melt spinning was used to produce binary alloys of Cu-Cr and Cu-Zr, and ternary alloys of Cu-Cr-Ag. By quenching from the liquid state, up to five atomic percent of Cr and Zr were retained in metastable extended solid solution during the rapid solidification process. Eutectic solidification was avoided and the full strengthening benefits of the large volume fraction of precipitates were realized by subsequent aging treatments. The very low solid solubility of Cr and Zr in Cu result in a high conductivity Cu matrix strengthened by second phase precipitates. Tensile properties on as-cast and aged ribbons were measured at room and elevated temperatures. Precipitate coarsening of Cr in Cu was studied by changes in electrical resistance during aging. X-ray diffraction was used to measure the lattice parameter and the degree of supersaturation of the matrix. The microstructures were characterized by optical and electron microscopy.

CHAPTER I

INTRODUCTION

High strength, high conductivity copper (Cu) alloys have many important applications in the electronic and electrical industries. Circuit elements, electrical connectors, and current conducting cables all benefit from lower resistance losses and higher strength which can reduce both the initial and operating costs of these devices. Resistance welding electrodes utilize the high current density capacity and resistance to softening at elevated temperatures that is made possible by selective alloying of Cu. While these applications all rely on the high electrical conductivity of Cu alloys, there are many uses for these alloys in environments where high thermal conductivity is the critical property for a material's selection. Some examples are mold and die liners used in metal casting, heat exchangers used in refrigeration and heating systems, advanced turbine engine components for aerospace applications, and regeneratively cooled rocket combustion chambers. It is this last application that is the purpose for the present work.

Advanced liquid hydrogen fueled rocket engines operate under extremely severe conditions. Combustion chamber pressures of 3000 psi and thermal fluxes of 100 $BTU/in^2 \cdot s$ have been measured during operation on test stands. It is also desirable that these engines be durable enough to allow for multiple firing and the resultant thermal cycling in the Orbital Transfer Vehicle. Current designs utilize regeneratively cooled Cu alloy thrust chambers. Cryogenic liquid hydrogen is pumped through channels in the wall of the thrust chamber prior to injection in the combustion chamber, Figure 1.1. Cu alloys provide the thermal conductivity necessary for efficient heat transfer. This results in reduced operating temperatures for the thrust chamber for increased engine life, and improves

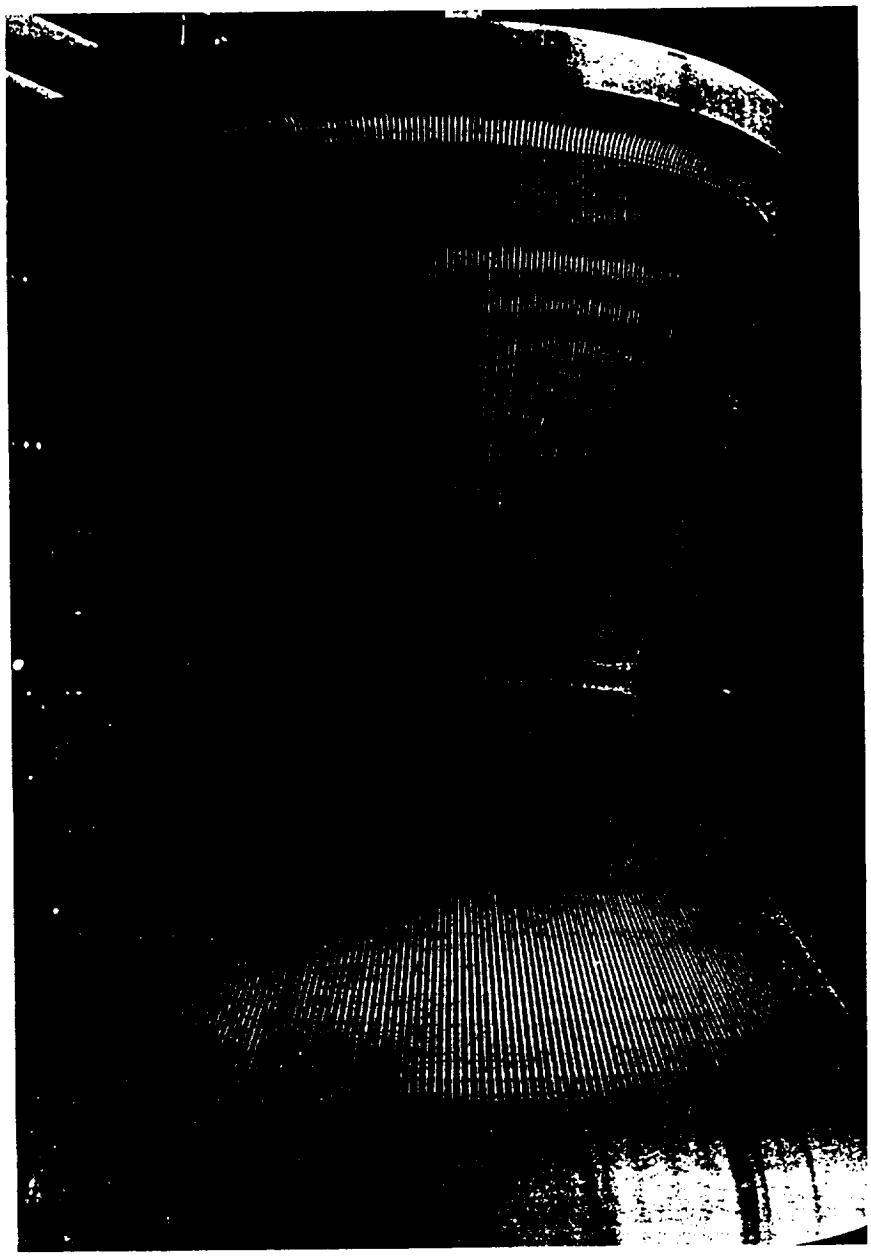

Figure 1.1. Rocket Thrust Chamber Showing Vertical Channels for Regenerative Cooling prior to Nickel Electroplate Closeout

engine efficiency by returning heat to the fuel prior to combustion. The combustion chamber liner is essentially a high flux, high efficiency heat exchanger that must be compatible with a hydrogen environment over an extreme range of temperature.

Thrust chambers constructed from NARloy-Z (Cu-3 wt.% Ag-.5 wt.% Zr), an alloy developed by Rocketdyne specifically for this application, have proved more durable than those constructed from high purity Oxygen Free High Conductivity (OFHC) Cu or Zirconium Copper (Cu-0.15 wt.% Zr) [1,2,3] †. The principal mode of failure for thrust chambers results from the formation and growth of radial cracks in the cooling channel wall which then cause a decrease in engine efficiency from internal cryogenic fuel leaks. It was found that these cracks usually initiate at nonmetallic inclusions in the Cu alloys [1,2]. Improvements in service life should be possible with inclusion shape control or the casting of cleaner alloys. In Figure 1.2 it can be seen that the cooling channels have deformed after firing and have assumed a "doghouse" shape. This is indicative of the large plastic strains that occur during thermal cycling. Failed chambers typically have radial cracks from the nose of the "doghouse" to the inner free surface of the combustion chamber cavity. These failures have been attributed to high temperature low cycle fatigue (LCF) and thermal-mechanical fatigue (TMF).

The purpose of the present work was to develop improved Cu alloys for thrust chambers. It is felt that the LCF-TMF properties and more importantly the thrust chamber lifespan can be enhanced by increasing the elevated temperature strength and the thermal conductivity of the thrust chamber. The approach that was taken was to use rapid solidification processing (RSP) of carefully selected Cu alloys to produce a high volume fraction of fine precipitates in an

† Numbers in [ ] refer to reference numbers in the bibliography.

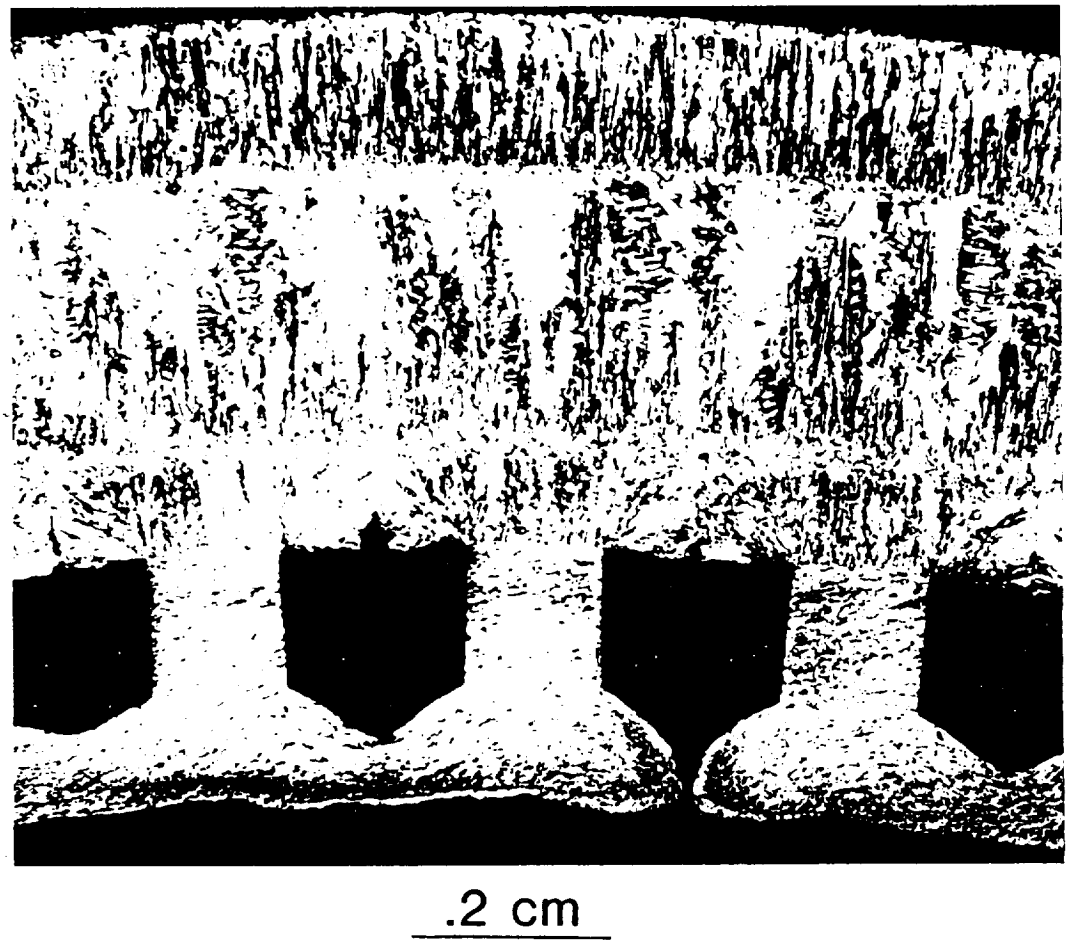

Figure 1.2. Cross Section of Failed Thrust Chamber Showing Deformed "Doghouse" Shape and Radial Crack

inclusion free, high conductivity Cu matrix. It is also desirable that these precipitates are stable at elevated temperature so that the mechanical properties of the alloy do not degrade during service.

In conventional ingot cast Cu alloys, high conductivity is in general incompatible with high strength. Alloying elements which improve strength by solid solution hardening (Zn, Ni, Sn, Si) also produce large lattice distortions in the Cu matrix. While these lattice distortions are necessary for effective solution hardening, they also cause scattering of conduction electrons. This results in greatly reduced thermal and electrical conductivity.

Alloying elements which form second phase precipitates in Cu are not nearly as deleterious to conductivity as alloys in solution. However, all conventional ingot cast, precipitation hardening Cu alloys suffer from one of two problems; either they retain too much solute in solution after aging for good conductivity, or solid solubility is too restricted at elevated temperature to supersaturate and produce a large volume fraction of precipitates necessary for high strength. Beryllium-Copper alloys are the best examples of the former where tensile strengths can approach 220 ksi, but the conductivity is only 20 % IACS due to the solubility of Be in Cu at ambient temperature. IACS refers to the International Annealed Copper Standard where conductivity is reported as a percentage of the value for pure Cu (100 % IACS=$1.7241\times10^{-6}\Omega$-cm). Alloys of Cu with Cr or Zr fall into the latter category where the solid solubility is less than 0.1 at. % at room temperature, but the maximum solid solubility is less than 1 at. % which results in a low volume fraction of precipitates and a corresponding low strength ($\approx$50 ksi).

In the present work, alloying elements with extremely limited solid solubility in Cu were selected in order to retain the excellent conductivity of the matrix. Binary alloys of Cu-Cr and Cu-Zr, and ternary alloys of Cu-Cr-Ag were produced

by chill block melt spinning (CBMS). These alloys are completely soluble in the liquid melt and insoluble in the solid. By quenching from the liquid state, up to 5 at.% Cr and Zr were retained in metastable extended solid solution during the rapid solidification process. Eutectic solidification was avoided and the full strengthening benefits of the large volume fraction of precipitates were realized by subsequent aging treatments. In order to utilize these novel alloys, it is necessary to fully understand their physical and mechanical properties and their response to thermal treatment. Tensile properties on as-cast and aged ribbons were measured at room and elevated temperatures. Precipitate coarsening was studied by changes in electrical resistance during aging. X-ray diffraction was used to measure the lattice parameter and the degree of supersaturation of the matrix, and to detect the presence of other phases. The microstructures were fully characterized by optical microscopy, transmission electron microscopy (TEM), scanning electron microscopy (SEM), and energy dispersive X-ray spectrometry (EDS). SEM fractography was used to characterize the mode of fracture in uniaxial tension tests. Thus the suitability of these alloys to applications in combustion chamber liners and the upper temperature/time limits for consolidation and retention of the mechanical and physical properties introduced during RSP were determined.

CHAPTER II

LITERATURE REVIEW

2.1 Introduction

Copper is one of the oldest known metals and also one of the most technologically important. The development of high-strength, high-conductivity Cu alloys in this study was dependent upon the great body of knowledge that has been published on Cu and its alloys. This literature survey is not intended to be a complete review of Cu alloys but instead contains only the necessary information for the reader to follow the development of the specific alloys in this study.

The first section of this review will describe the production of commercial grades of Cu and the refining and melting practices necessary to produce the higher purity Oxygen Free High-Conductivity (OFHC) Cu. The next sections are devoted to thermal and electrical conductivity and the effects of alloying elements and impurity defects. From this information, the selection of 3 alloy systems, Cu-Cr, Cu-Zr, and Cu-Ag, will be discussed, and a detailed review of each of these systems will be made. The mechanical properties, elevated temperature aging behavior, thermal and electrical conductivity, and precipitation studies will be discussed in greater detail for the Cu-Cr system and in lesser detail for the Cu-Zr and Cu-Ag systems. Finally, a section on Rapid Solidification Processing (RSP) including CBMS and the rationale for its application to these alloy systems will be presented.

2.2 Copper Production

Copper and Cu alloys have been used for many centuries because of their electrical and thermal conductivity, strength with good formability, resistance to corrossion, relatively low cost, and ability to be easily recycled. Alloying additions

in Cu are made in an effort to improve the strength and/or castability, or to lower the cost of the material. These additions however, always cause a degradation of the thermal and electrical conductivity of the Cu. Since the conductivity is so dependent on the purity of the Cu, the following discussion of the production of high-purity OFHC Cu is included.

Copper is produced using any of three sources of raw materials. These include scrap Cu, oxidized Cu minerals, and sulfide Cu minerals. The production of Cu from sulfide Cu minerals is used to illustrate the process of pyrometallurgical and electrolytic refining. Some of the processes used in production from sulfide minerals are also applicable to oxidized and scrap Cu sources.

Sulfide Cu ores typically contain between 0.75 wt.% and 3 wt.% Cu [4]. Smelting of these dilute ores is not economical without the concentration process of beneficiation. The dilute ores are crushed in rod and ball mills, in preparation for the flotation concentration of beneficiation. The flotation process involves the selective attachment of copper minerals to rising air bubbles in an aqueous solution. The Cu rich froth is then collected and dried to be sent on for smelting. The flotation concentrates typically contain about 25% Cu. In pyrometallurgical coppermaking, the process has been divided into two steps; sequential smelting and converting. The purpose of both steps is the removal of iron and sulfur by high-temperature oxidation with air, and the removal of iron oxides and rock with silica fluxes. The process is performed at high temperature so that the products have good fluidity during transport. Smelting is accomplished by the reaction of oxygen-enriched air with the dried beneficiated ore in an electric or reverberatory furnace. The reaction is autogenous in the presence of sufficient oxygen. Smelting results in the production of liquid Cu-Fe-S matte, which contains about 70% Cu. The matte is then further reacted in a Pierce-Smith converting furnace by forced air injection to produce liquid blister Cu. The product contains about

99.5 wt.% Cu, 0.5 wt.% O, and 0.05 wt.% S along with traces of arsenic (As), bismuth (Bi), iron (Fe), nickel (Ni), lead (Pb), tellurium (Te), selenium (Se), antimony (Sb), cobalt (Co), silver (Ag), gold (Au), and platinum (Pt). Blister copper may also be produced by melting recycled Cu scrap in a Pierce-Smith converting furnace. In most cases the Cu is then further refined by an electrolytic process. Electrorefining begins with the melting and casting of anodes. Before the metal is poured, sulfur and oxygen are removed by sequential reaction with oxygen and hydrocarbons. In the past, green tree limbs or poles were used as the source of hydrocarbons because of the gassing and stirring action. The reaction had to carefully controlled to avoid contamination with excess hydrogen and subsequent embrittlement of the overpoled Cu. In modern coppermaking, tree limbs have been replaced by hydrocarbon gases with reaction rates that can be more easily monitored. The cast anodes are placed in an electrolytic cell along with high-purity Cu cathodes. The electrolyte consists of a solution of copper sulfate, sulfuric acid, and water. Organic smoothing agents in the bath promote the formation of dense, smooth plating on the cathode when a low-voltage, direct current is passed between the electrodes. The purity of this electrolytically refined Cu is quite high, however in commercial practice the metal picks up oxygen during subsequent melting to form electrolytic tough pitch (ETP) copper.

ETP copper is made from washed Cu cathodes which are melted in a gas fired vertical shaft furnace. The cathodes are loaded in the top of the furnace, and the melted Cu flows continuously from the bottom of the furnace into a holding furnace prior to casting. Both the electrical conductivity and the formability are adversely affected by the impurities present in the ETP Cu, so chemical analysis is a routine procedure for process control. ETP Cu contains from about 0.03 wt.% to 0.06 wt.% oxygen [5]. This amount of oxygen is equivalent to a range of 7.7% to 15.4% Cu-Cu_2O eutectic. ETP Cu is entirely satisfactory for most ordinary

purposes, and is by far the most widely marketed of the unalloyed coppers. The presence of oxides in ETP Cu however, makes it unsuitable for the hydrogen environment of a rocket chamber nozzle. At elevated temperatures, hydrogen can diffuse into the Cu and react with the Cu_2O to form high-pressure water vapor. Voids are opened up along grain boundaries, and this results in severe cracking at low stresses. The embrittlement occurs at temperatures as low as 400°C, and the severity of the effect increases with temperature. Deoxidants such as phosphorous (P), calcium (Ca), or magnesium (Mg) are often added to ETP Cu prior to casting to avoid hydrogen embrittlement.

Rather than using deoxidants, low oxygen levels can be obtained in OFHC Cu by the melting, casting, and solidification of electrolytically refined cathode Cu under a reducing cover gas. This results in a residual oxygen content of less than 0.001 wt.% and an electrical conductivity of ≈101.5% IACS [5]. The deoxidized coppers are much inferior to OFHC Cu in high-conductivity applications. For example, phosphorous deoxidized copper containing only 0.02 wt.% P has an electrical conductivity of 85% IACS. A more complete discussion of the effects of alloying additions in Cu on the thermal and electrical conductivity will be included in the following sections.

2.3 Thermal and Electrical Conductivity Relationships

Pure copper has the highest thermal and electrical conductivities of any element other than silver. As in most metals, the thermal and electrical conductivities of Cu and its alloys are closely related. This relationship is fortunate because thermal conductivity is a difficult property to measure. However, quite accurate estimates of thermal conductivity can be made from more easily measured electrical conductivity. Klemens and Williams [6] reviewed the current theory of thermal conductivity of metals and alloys and showed that this mode of

conduction is a complex process. Fortunately, in Cu the bulk of the thermal conduction is by electrons, and this results in the close relationship between thermal and electrical conductivities.

The overall thermal conductivity (λ) of metals and alloys is composed of two components: a lattice quantum energy or phonon component (λ_g) and a mobile electron component (λ_e).

$$\lambda = \lambda_g + \lambda_e \tag{2.1}$$

In high-conductivity materials, the phonon component will be insignificant when the room temperature electrical conductivity is greater than $\approx$ 86% IACS [6]. The electron component of thermal conductivity roughly follows the Wiedemann–Franz–Lorenz relation

$$\lambda_e = \frac{L_o T}{\rho} \tag{2.2}$$

at room temperatures and above where L_o is the Sommerfeld prediction of the electronic Lorenz function, T is the absolute temperature, and ρ is the electrical resistivity. The value of L_o is not strictly a constant, but can change with temperature due to electron–electron scattering, vertical movement on the Fermi surface [6], and Fermi smearing [7,8]. Despite these limitations, the Wiedemann–Franz–Lorenz relation is reasonably accurate for elemental Ag, Cu, Li, Au, Al, and Mg [9].

In alloys, the electrons are scattered by solute atoms and this greatly reduces λ_e. In addition, electrons may also be scattered by phonons, other mobile electrons, localized magnetic moments, and lattice defects. The phonon contribution λ_g thus becomes more important in the overall thermal conductivity.

Smith and Palmer [10] developed an empirical formula that accurately relates the thermal and electrical conductivities of Cu alloys over a temperature

range of 20°C to 200°C:

$$\lambda = \frac{AL_oT}{\rho} + B \tag{2.3}$$

In this expression, $\frac{AL_oT}{\rho}$ represents the electronic or metallic contribution to the thermal conductivity as in the Lorenz function. The constant B represents the nonmetallic contribution to the thermal conductivity. When numerical values are substituted for the constants, the Smith–Palmer equation becomes:

$$\lambda = (2.39 \times 10^{-8})\frac{T}{\rho} + 0.075\,\mathrm{Wm^{-1}K^{-1}} \tag{2.4}$$

The Smith–Palmer equation, while developed for a relatively small range of temperatures, has been found to be accurate for pure Cu [10,11] at temperatures up to 625°C, and for dilute binary and ternary alloys of Cu with Cr, Zr, Te, Mg, and Ag at temperatures up to 650°C [12]. While the ratio between thermal and electrical conductivities of Cu alloys varies greatly with temperature, the thermal conductivity is almost a linear function of the product of the electrical conductivity ($\sigma = \frac{1}{\rho}$) and the absolute temperature, Figure 2.1.

It is not surprising that the electrical conductivity is also a function of the absolute temperature and is nearly proportional to T^{-1} for temperatures greater than the Debye temperature, which in this case has been reported as 37°C for pure Cu [6,13]. When this substitution is made for ρ in equation 2.4, it can be seen that the thermal conductivity will be temperature independent above the Debye temperature. In fact, the thermal conductivity of pure Cu decreases slightly with an increase in temperature. Alloying additions in Cu result in an increase in thermal conductivity with temperature. At low temperatures, solutes have a large effect on the thermal conductivity due to electron scattering. Electron scattering due to phonon interaction is small at low temperatures but becomes significant as the temperature is increased. Since solute–electron scattering is largely temperature independent, at high temperatures the overall thermal conductivity is controlled

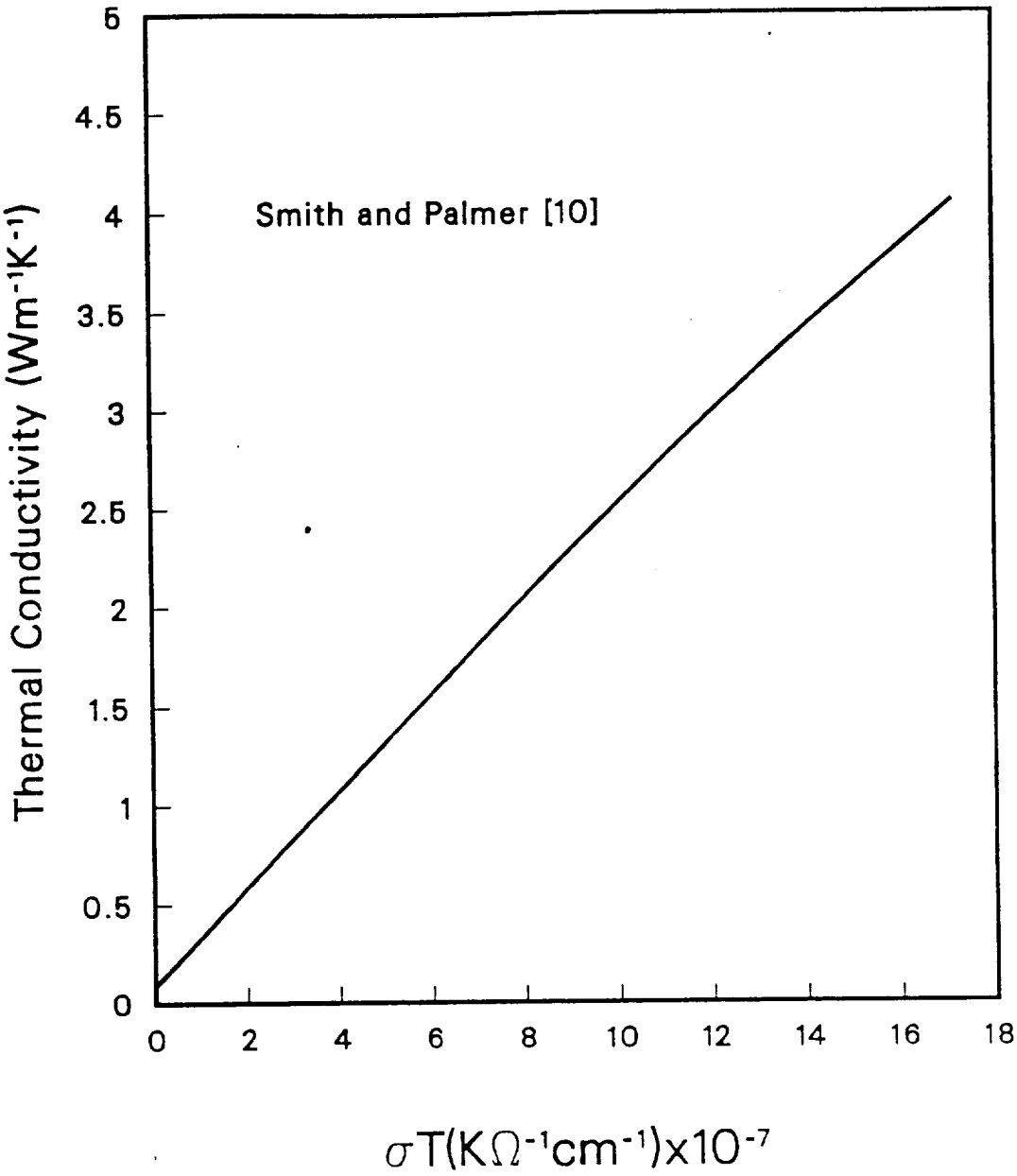

Figure 2.1. Relationship of Thermal Conductivity to the Product of Electrical Conductivity and Temperature for Copper Alloys [10]

by the electron–phonon scattering. A general rule is that Cu alloys with less than 95% IACS electrical conductivity show an increase in thermal conductivity with increasing temprature. As a result of these effects, the thermal conductivities of these alloys will approach but never surpass those of pure Cu at elevated temperatures, Figure 2.2 [12]. This is a very beneficial effect for the development of high-strength, high-conductivity alloys to be used at elevated temperatures. Alloying additions, which are necessary for mechanical strength, are not nearly as deleterious to the high-temperature thermal conductivity as they are to the low-temperature electrical and thermal conductivities. This holds true for both solution hardened and precipitation hardened Cu alloys [14].

2.4 Electrical Conductivity

It was shown in the Smith–Palmer equation that the thermal conductivity is nearly proportional to the electrical conductivity. For this reason, the relevant features of the theory of electrical conductivity will be presented. The modern theory is based upon Sommerfeld's application of quantum mechanics to the older Drude-Lorentz theory. The electrical conductivity

$$\sigma = \frac{Ne^2 l}{2mv} \tag{2.5}$$

where N is the number of electrons per unit volume free to move under the action of an electric field, e and m are the charge and mass of the electron, v is the velocity of the electrons of highest energy, and l is the mean free path of the electrons and is of the order of a hundred times the atomic diameter [15].

In a crystal lattice, the electrons move in a periodically varying potential field. A perfect lattice offers no resistance to electron flow except when the wave vector $\mathbf{k}$ of the electron is characterized by certain critical values which meet the Bragg condition for diffraction. Real crystals have electrical resistance because

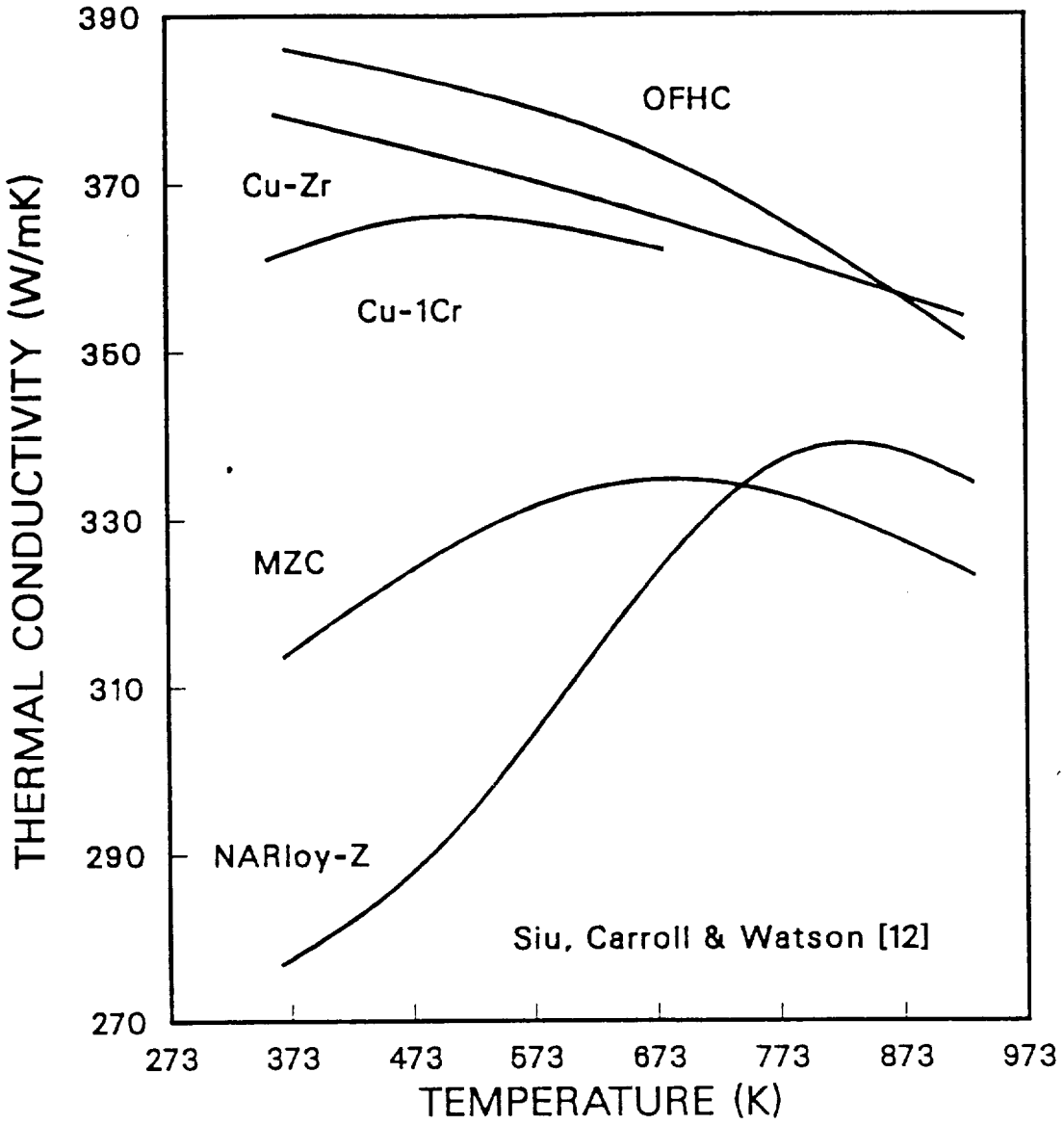

Figure 2.2. Thermal Conductivity as a Function of Temperature for OFHC Cu and Four Alloys of Cu [12]. Note the Increase in Conductivity with Temperature for the Alloys with Poorest Conductivity at Low Temperature

the lattice and the periodic potential field are imperfect, and electron scattering occurs when the wave vector **k** has values other than the critical Bragg values.

For a pure annealed metal, it is found that as the temperature is lowered, the resistivity steadily decreases and approaches zero as the absolute zero of temperature is approached. The resistance is due to the electron scattering from lattice disturbances caused by the thermal motion of the atoms. The resistivity may be expressed as

$$\rho = \frac{CT}{M\theta^2} \tag{2.6}$$

where C is a constant, characteristic of the electron energy band structure of the particular element, M is the atomic mass, and T is the absolute temperature which must be larger than the characteristic Debye temperature θ [15]. At ordinary and elevated temperatures the resistivity is roughly proportional to the absolute temperature. At very low temperatures the resistivity is proportional to T^5 [16].

In the case of a dilute solid solution alloy at the absolute zero of temperature, there remains a limiting residual resistivity. This is the result of electron scattering from the disturbances in the periodicity of the lattice due to the solutes. In his classical work on the resistivity of alloys, Matthiessen [17] showed that the total resistivity ρ was the sum of the temperature-dependent resistivity ρ_T of the pure metal and the temperature-independent residual resistivity ρ_R due to electron–solute scattering.

$$\rho = \rho_T + \rho_R \tag{2.7}$$

This expression has been found to hold true for dilute alloys in general, although there are exceptions. Mathiessen's rule implies that the variation of resistivity with temperature is independent of alloy composition,

$$\frac{\mathrm{d}\rho}{\mathrm{d}T} = \frac{\mathrm{d}\rho_T}{\mathrm{d}T} \tag{2.8}$$

and the resistivity–temperature curves for different compositions should all be parallel. It will also follow that the temperature coefficient of resistivity

$$\alpha = \frac{1}{\rho}\frac{\mathrm{d}\rho}{\mathrm{d}T} = \frac{1}{\rho}\frac{\mathrm{d}\rho_T}{\mathrm{d}T} \tag{2.9}$$

which by rearrangement yields

$$\alpha\rho = \frac{\mathrm{d}\rho_T}{\mathrm{d}T} \tag{2.10}$$

is a constant for each solvent metal. Equation 2.10 is a particularly useful form of Mathiessen's rule for resistivity measurements of specimens. Resistivity is not a direct measurement, but is typically calculated using the measured resistance R and the measured geometry of the specimen. Significant errors may be introduced by variations in the specimen dimensions and also by the presence of internal cracks or voids. The temperature coeffficient of resistance however, is independent of specimen geometry,

$$\alpha = \frac{1}{\rho}\frac{\mathrm{d}\rho}{\mathrm{d}T} = \frac{1}{R}\frac{\mathrm{d}R}{\mathrm{d}T} \tag{2.11}$$

so that measurement of the temperature coefficient of resistance can be used to accurately determine the resistivity.

The residual resistivity ρ_R due to 1 at.% solute atoms is about as large as the temperature-dependent resistivity ρ_T for most alloys at room temperature. The ratio of the room temperature resistivity to the resistivity at 4 K is often used as a measure of the purity of a metal. In a very pure, defect free metal this ratio will approach a value of 10^5, and for alloys will be less than 10. Norbury [18] found that the effect of a 1 at.% solute addition on the resistivity of a solvent metal is dependent upon the difference in valence between the two. Linde [19] showed the increase in resistivity to be proportional to the square of the difference in valencies. Mott [20] explained Linde's results by showing that a solute atom distorts the lattice by the displacement of neighboring atoms, and also by changing the magnitude of the local electric field. The extra resistance from the solute atom

is mainly a result of the difference in the electric field between the solvent and solute atom. If the difference in valency is Z, then the charge difference on the ion core of the solute atom is Ze. The scattering of electrons, according to the Rutherford Scattering Law, is proportional to the square of the scattering charge or in this case $(Ze)^2$. Linde's emprical relationship for Cu, Ag, and Au solid solution alloys may be expressed as

$$\Delta\rho = \{K_2 + K_1(Z_\beta - Z_\alpha)^2\}A \tag{2.12}$$

where K_1 and K_2 are coefficients, A is the atomic fraction of solute, and Z_α and Z_β are the valencies of the solvent and solute respectively. The values of the coefficients K_1 and K_2 are constant for a given chemical period, but vary for the different periods. Hibbard [21] showed that these coefficients are dependent upon the lattice parameter, the ionic charge, and compressibility of the solute atom in the parent metal.

Higher concentration alloys have their resistivity modified not only by the lattice distortion effects, but also by changes in the electronic factors controlling conduction. The number of free electrons will change and this will affect the probability of electron scattering. In the case of a phase change, the electron band structure will be modified and abrupt changes in resistivity will occur.

The electrical conductivities of binary alloys are related to their phase diagrams by the LeChatelier-Guertler rules, as illustrated in Figure 2.3. In alloy systems consisting of a heterogenous mixture of two phases, the electrical conductivity and the temperature coefficient of resistance ($\alpha = \Delta R/\Delta T R_0$) vary linearly with the volume fractions of the phases. As a result of this rule, two-phase alloys with high conductivity can be produced if the 2nd phase is insoluble in the parent metal. In solid solutions, the electrical conductivity and the temperature coefficient of resistance are lower than those of the solvent metal. There

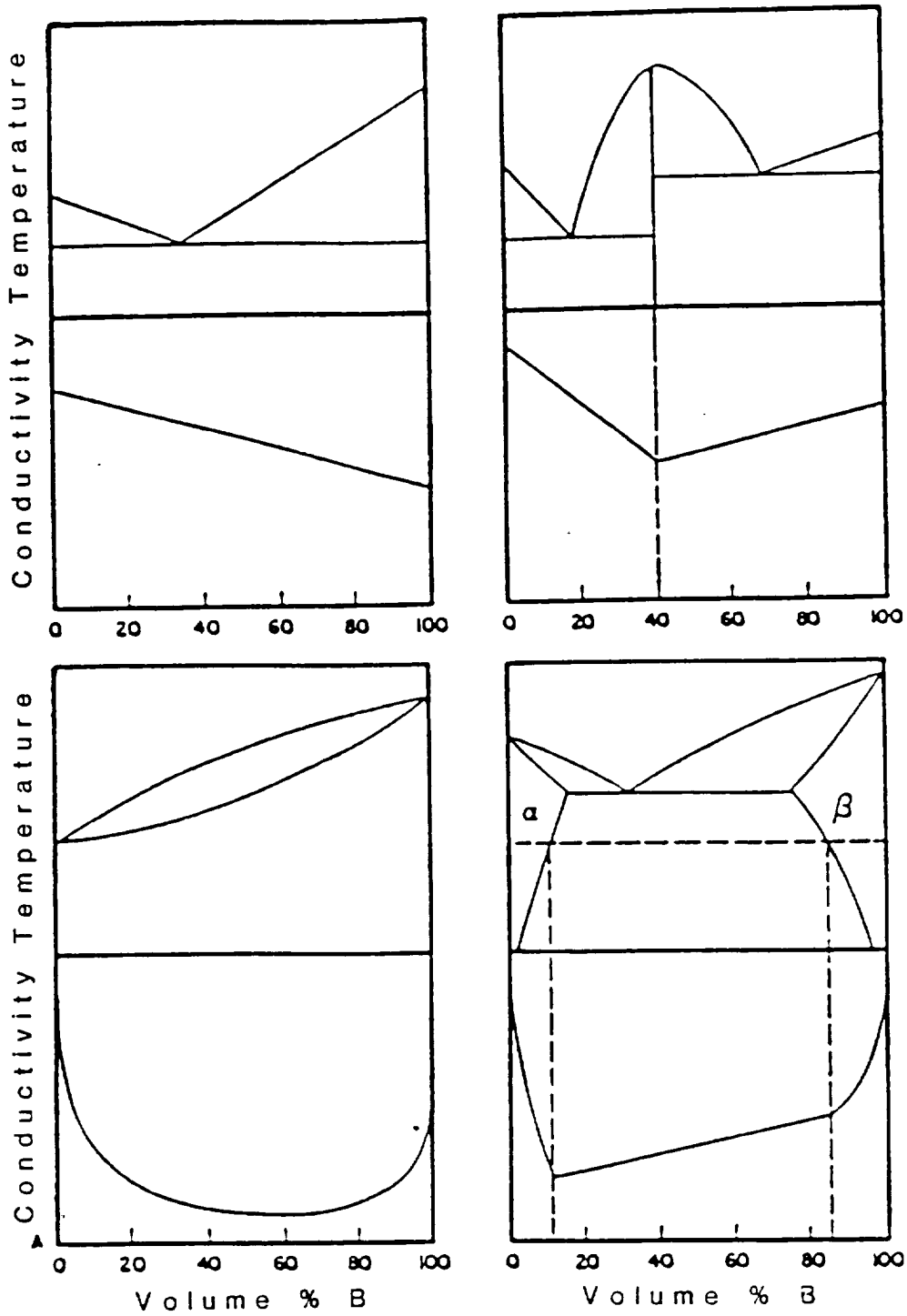

Figure 2.3. Electrical Conductivity of Binary Alloys as a Function of Composition for Different Classes of Phase Diagrams

is usually a large decrease with the first small addition of the solute. If the components form a continuous series of solid solutions, then the conductivity and temperature coefficient curves form a U-shape. The shape of this curve for a completely disordered alloy was modeled by Nordheim [22], who showed that the temperature-independent residual resistivity

$$\rho_R \propto x(1-x) \tag{2.13}$$

where x is the solute concentration. This relationship is found to be in good agreement with experiment for Ag-Au, Figure 2.4 [22,23].

When one of the components of the alloy is a transition metal the resistivity composition curve is assymetric. In the case of Ag-Pd it can be seen that the resistivity maximum is skewed towards the the palladium side of the curve, Figure 2.4. This behavior was explained by Mott [24] who proposed that an extra resistance occurs in the high-Pd concentration alloys due to transitions of the electrons into unfilled 'd' energy bands. There are no theories that can accurately predict the effects of solute additions of transition metals on electrical conductivity because the ionic charge of the transition elements is not well understood. The transition elements in general do not follow the simple relationships of Norbury, Linde, Mott, and Hibbard, and may be as much as five times more effective in increasing the resistivity than would be predicted [21]. The transition elements which are of technological importance in the development of high-conductivity, high-strength Cu alloys are Zr, Cr, W, and Nb.

In alloys that form continuous solid solutions with perfectly ordered superlattices, the lattice periodicity is restored and the residual resistivity ρ_R becomes very small. Resistivity measurements can thus be used to detect the presence of order-disorder transformations. The theory however is not advanced enough to calculate the exact degree of ordering based on the measured resistivity [15].

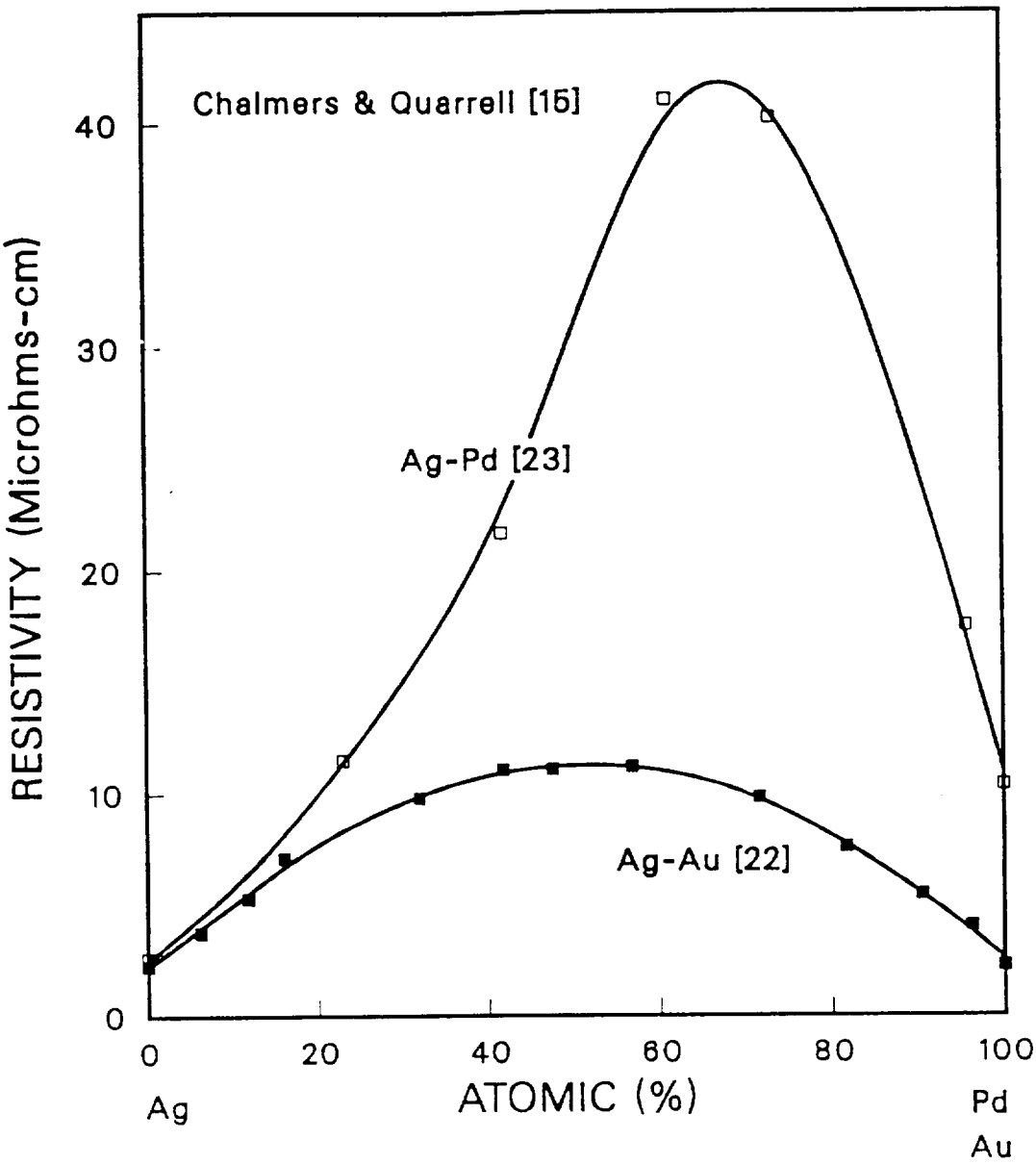

Figure 2.4. Resistivity of Two Alloys of Silver as a Function of Composition. Data for Ag–Pd [23] and Ag–Au [22] Alloys Determined at 273 K. After Chalmers and Quarrell [15]

Despite the unavailability of a suitable theoretical treatment, the effects of most of the important alloying additions on the electrical conductivity of Cu are well documented. Pawlek and Reichel [25] showed that solid solution alloying additions up to 0.10 wt.% and/or 0.10 at.% in Cu could be represented by a series of linear resistivity/composition curves with a characteristic slope for each element, Figure 2.5. It should be noted that for some of these elements, the equilibrium solid solubility in Cu has been exceeded by quenching from high temperatures, and thus the resistivity is higher than would be expected for the equilibrium two-phase mixtures. Similarly for any alloying addition in Cu, the resistivity will be a function of the thermal history of the alloy when the equilibrium solid solubility at the temperature of resistivity measurement has been exceeded.

The ideal alloying addition for high conductivity according to the first rule of LeChatelier–Guertler would be totally insoluble in Cu at the service temperature. This ideal is not very practical for production of the alloy by conventional ingot metallurgy. Alloying elements which have low solubility at ambient temperatures also tend to have a limited maximum solid solubility at elevated temperatures, or may even be insoluble in the melt. In the first case, conventional solidification of a concentrated alloy results in a very coarse microstructure with no strengthening benefits from the alloy addition. In the second case, the insoluble element cannot be alloyed in the melt and this results in extreme segregation. While conventional casting techniques are not practical for the insoluble addition, these alloys can be prepared by mechanical alloying of elemental powders.

In addition, it is desirable for the alloying element to cause as small a resistivity increase as possible for the amount of equilibrium solute concentration at the service temperature. That is the slope of the resistivity/concentration curve in Figure 2.5 should be as shallow as possible. The curve for Ag illustrates that the resistivity of Cu alloys is hardly affected by small additions of this solute.

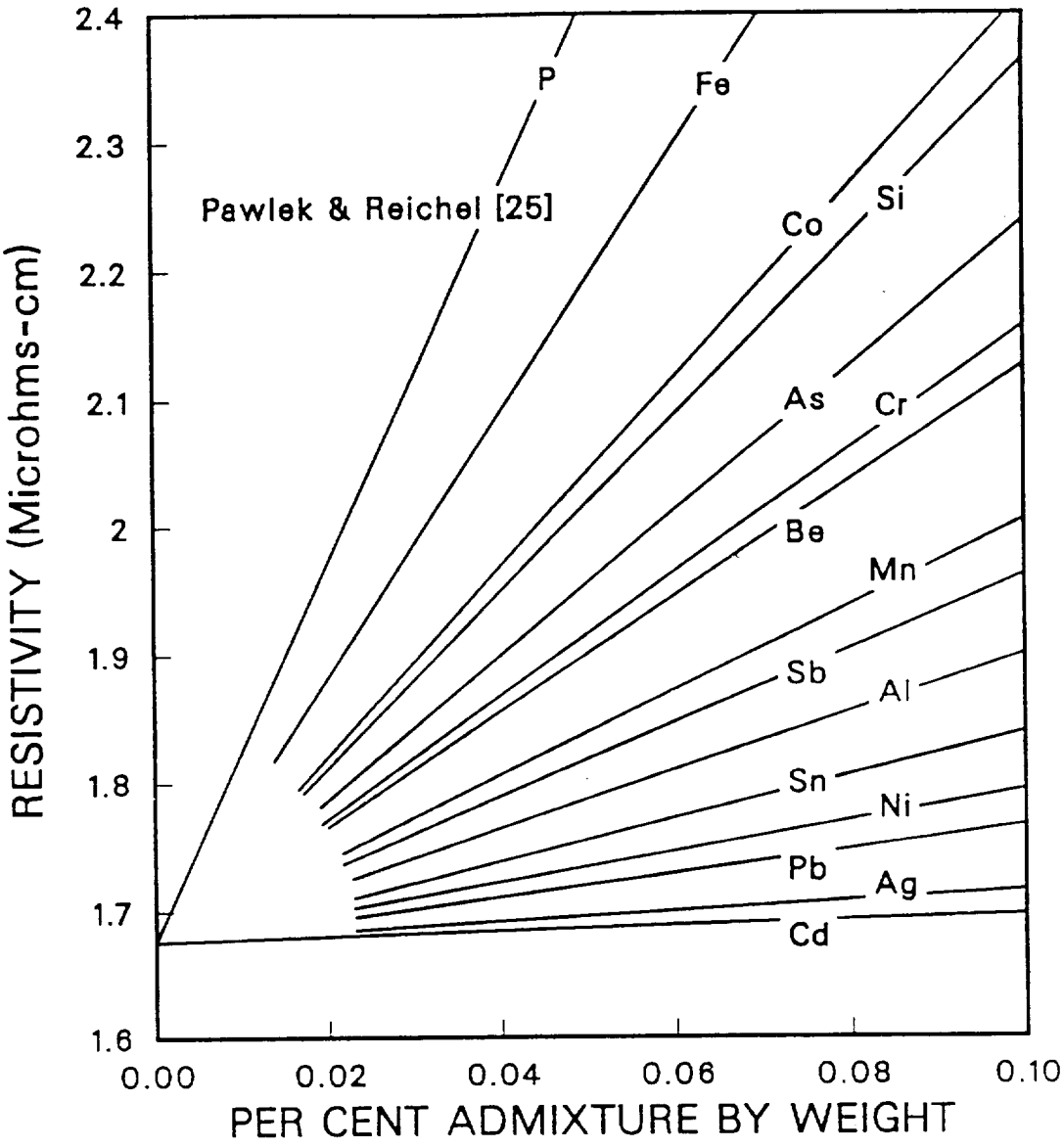

Figure 2.5. Increase of Electrical Resistivity of Copper by Solid Solution Alloying with Various Elements. Data from Pawlek and Reichel [25]

It can also be seen in this figure that P has the most deleterious effect on the conductivity of Cu alloys based upon wt.% of addition. Although the effect of Cr additions is intermediate between these two elements, the conductivity of Cu-Cr alloys is still very high due to the low room-temperature solubility of Cr in Cu. The specific effects of Cr, Zr, and Ag additions on the conductivity of Cu alloys will be presented in later sections of this review.

Besides the irregularities in the periodicity of the lattice due to thermal vibration and solute atoms, there are several other sources of electron scattering. Plastic deformation of metals results in an increase in resistivity. This effect has been attributed to the creation of defects such as dislocations, vacancies, and interstitials during cold work. Decreases in resistivity have been measured during annealing of alloys prior to recrystallization. Another source of resistivity is due to lattice strain from coherent precipitates. Resistivity measurements have been used to monitor the formation of G.P. zones in Al alloys. The resistivity rises initially as the coherent particles are formed, and later decreases as the particles overage and lose coherency. The resistivity due to defects, ρ_D, and coherent precipitate strains, ρ_S, follows Matthiessen's rules and is additive with the thermal and solute contributions of resistivity.

$$\rho = \rho_D + \rho_S + \rho_T + \rho_R \tag{2.14}$$

In the case of concentrated alloys there may be significant deviations from the simple additive behavior of equation 2.14.

2.5 The Chromium-Copper Phase Diagram

The Cu-Cr system is the first of three systems to be presented in this review. Chakrabarti and Laughlin [26] recently published a comprehensive review of this system and those interested in this subject would do well to read their paper. The equilibrium Cu-Cr phase diagram presented in Figure 2.6 [26] is the accepted version from their work and is of the eutectic type with complete liquid miscibility. Earlier diagrams included a miscibility gap in the liquid that is not supported by recent experimental evidence [27] or thermodynamic calculations [28,26]. The region of liquid immiscibility reported in the older work [29,30] has been attributed to the presence of impurities in their materials.

The most important feature of this phase diagram for selection as a candidate for high-conductivity alloy production is the limited width of the solid-solution Cu field. The solid solubility of Cr in Cu has been the subject of many studies [31,32,33,34,35,36]. There is a variation in the experimental results, as shown in Figure 2.7 [26]. The equilibrium solid solubility of Cr in Cu can be approximated by the following thermodynamic equation [37]:

$$\ln X_{\mathrm{Cr}}^{(\mathrm{Cu})} = \frac{{}^{\mathrm{E}}\Delta\overline{S}_{\mathrm{Cr}}^{(\mathrm{Cu})}}{R} - \frac{\Delta\overline{H}_{\mathrm{Cr}}^{(\mathrm{Cu})}}{RT} \tag{2.15}$$

where $\Delta\overline{H}_{\mathrm{Cr}}^{(\mathrm{Cu})}$ is the change in enthalpy of the fcc (Cu) by the dissolution of 1 mole of bcc Cr, ${}^{\mathrm{E}}\Delta\overline{S}_{\mathrm{Cr}}^{(\mathrm{Cu})}$ is the relative partial molar excess entropy of Cr between the bcc and fcc phases, and $X_{\mathrm{Cr}}^{(\mathrm{Cu})}$ is the equilibrium solubility of Cr in Cu. This equation has been used to check the relative accuracy of the experimental solubility data for this system [26]. The logarithm of solubility should yield a linear curve when plotted against T^{-1}. Figure 2.8 [26] shows the results of such a plot using the available solubility data [31-36]. It can be seen that the data do not fit into a single straight line. This lack of agreement in the data has been

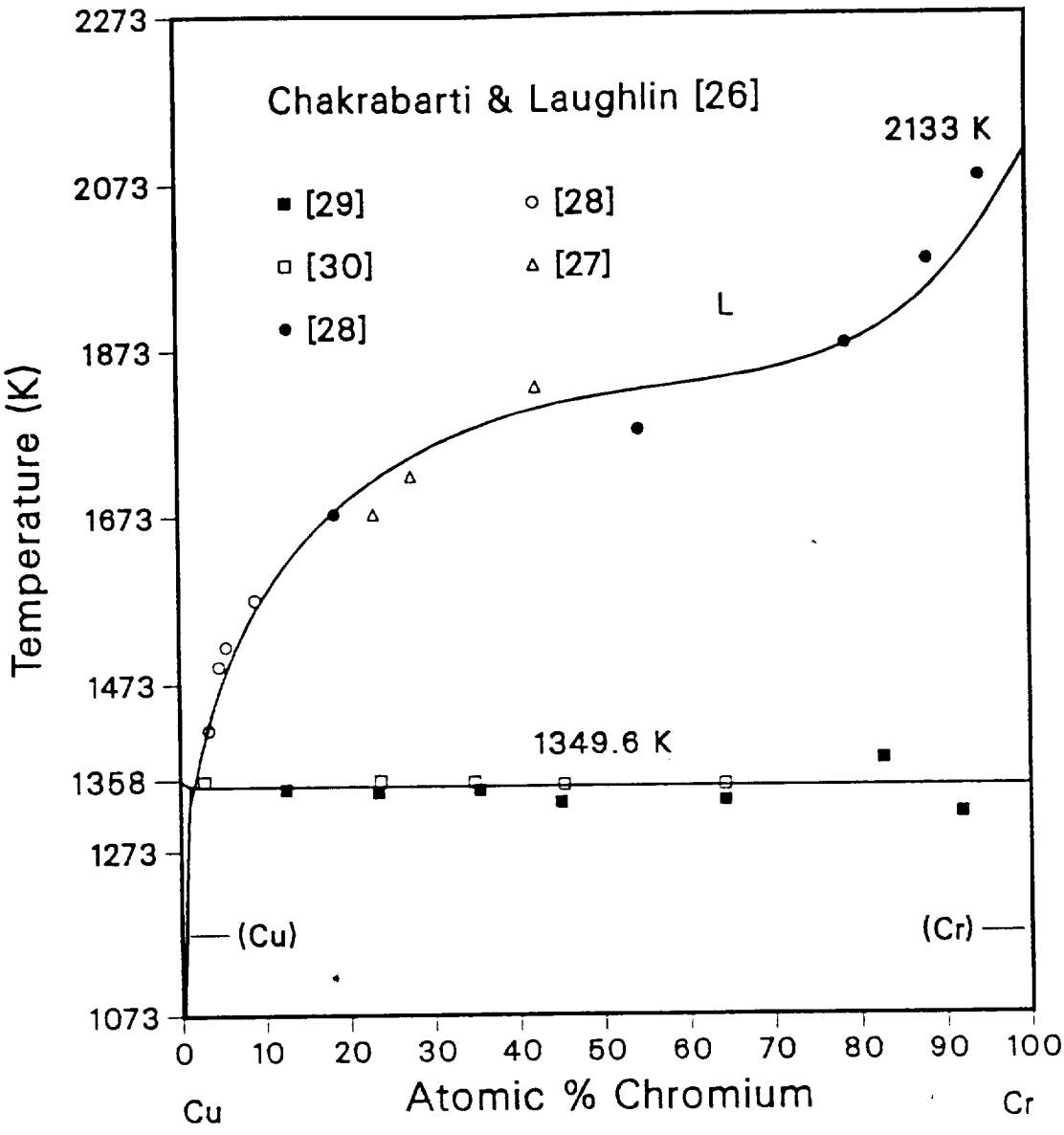

Figure 2.6. Copper-Chromium Equilibrium Phase Diagram from the Review of Chakrabarti and Laughlin [26] with Data from Published Work [27–30]

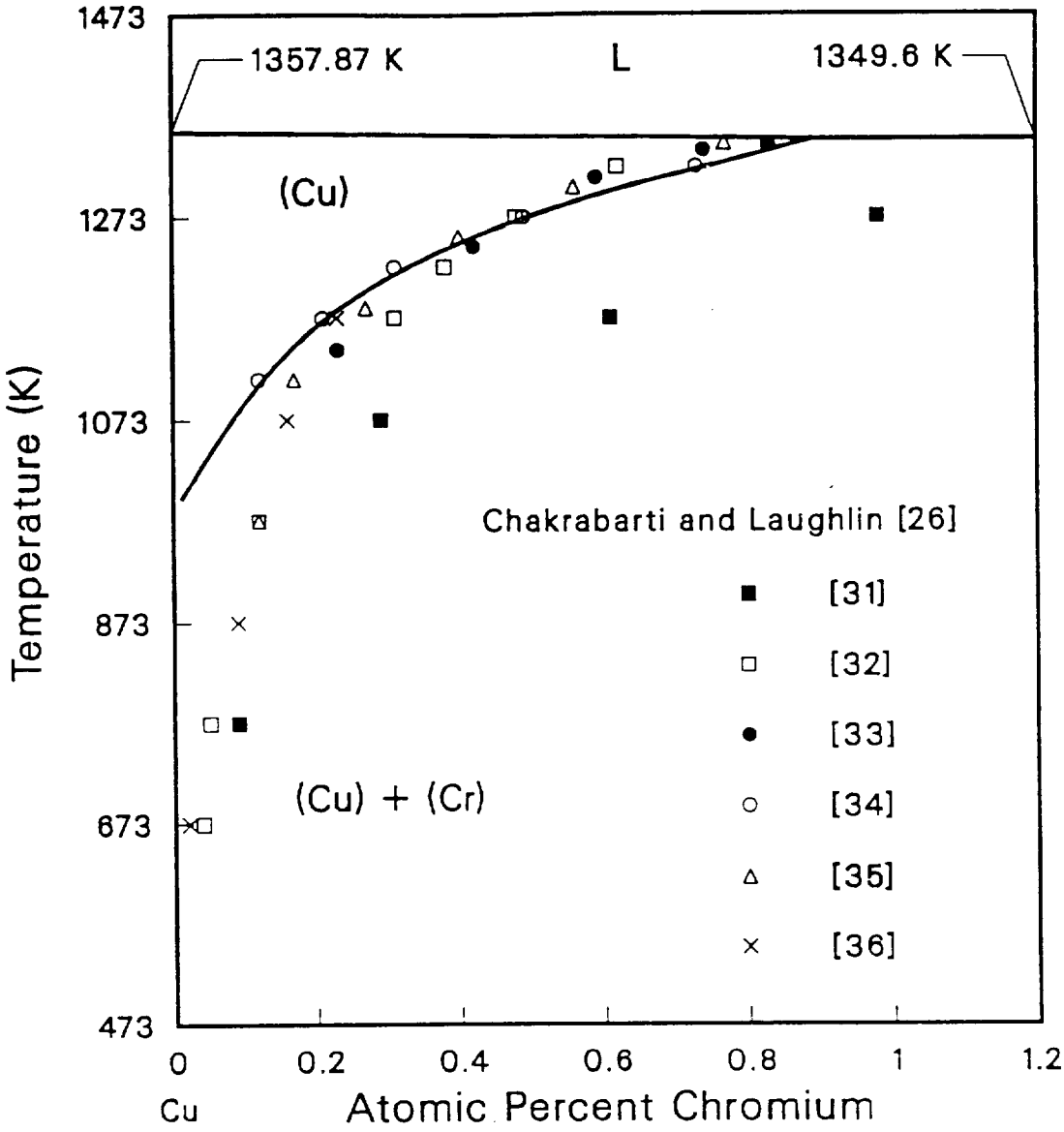

Figure 2.7. Copper-Rich Side of the Cu-Cr Equilibrium Phase Diagram Showing the (Cu) Solvus. From the Review of Chakrabarti and Laughlin [26] with Selected Published Data [31–36]

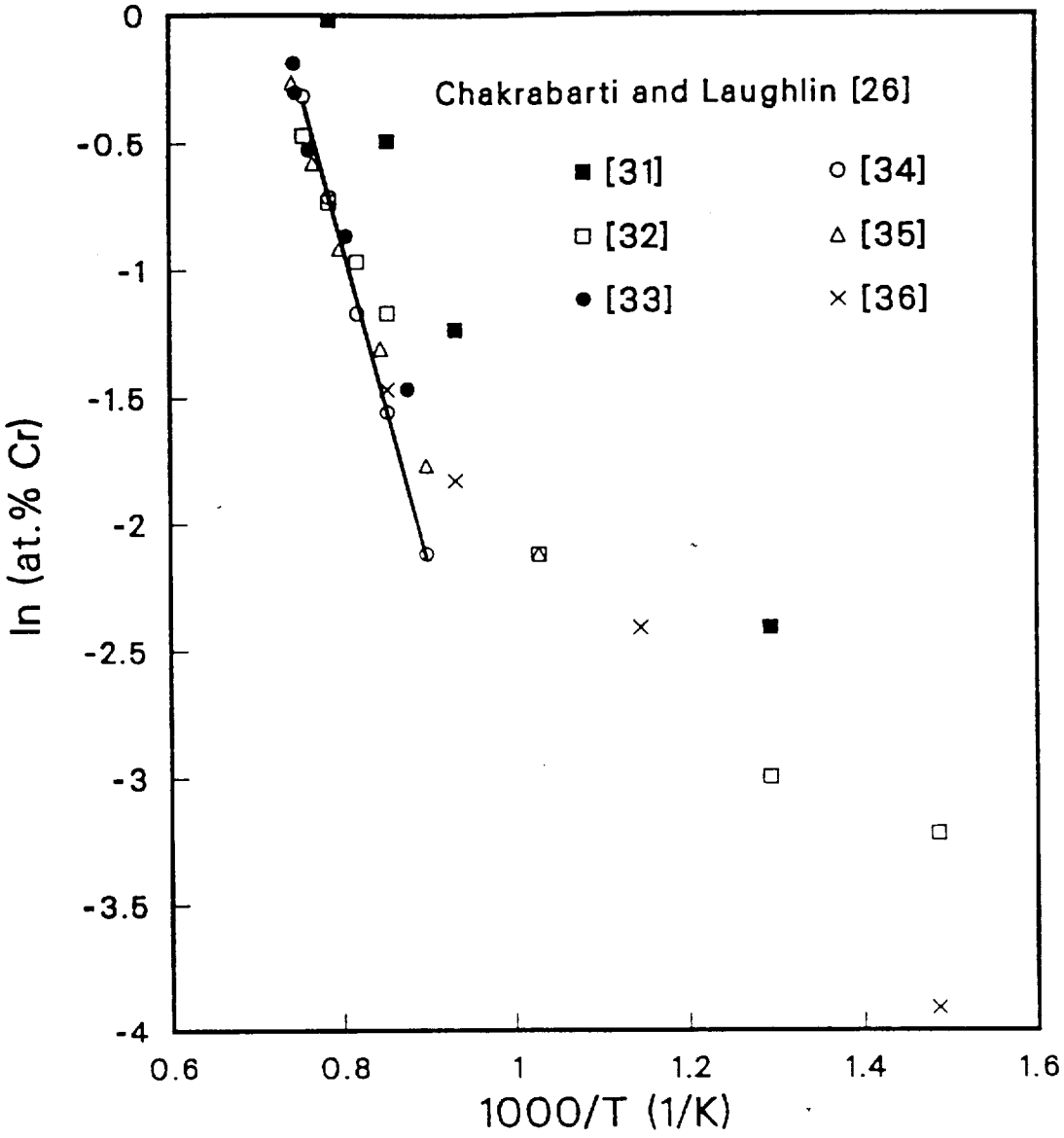

Figure 2.8. Equilibrium Solubility of Chromium in Copper as a Function of Temperature. From the Review of Chakrabarti and Laughlin [26] with Selected Published Data [31–36]

attributed to the difficulty in achieving equilibrium at the lower temperatures. The data of Doi [34] show a good linear fit and this is indicative of near equilibrium conditions in his study. The electrical resistivity method used by Doi [34] has been shown to be more accurate than methods that utilize X-ray, chemical analysis, or microscopy [38]. Although the data of Doi [34] do not extend to temperatures lower than 840°C, the solubility at lower temperatures can be calculated using the extrapolated line from Figure 2.8. The equation of this line [26] is:

$$X_{\mathrm{Cr}}^{(\mathrm{Cu})} = 24,840 \exp(\frac{-114,880}{RT})(\mathrm{at.\%}) \qquad (2.16)$$

where R has units of $\mathrm{J/mol \cdot K}$. These results indicate that the solid solubility of Cr in Cu at low temperatures is much less than has been indicated previously. The calculated solubility at 773 K is only 0.00043 at.%, and this value is much too low to be reasonable. The room-temperature resistivity of commercial Cu-0.8 at.% Cr alloy aged at 773 K for two hours has been reported as $1.914 \times 10^{-6}\Omega$-cm [39] and this value corresponds to a solid solubility of approximately 0.045 at.% Cr using the data presented in Figure 2.5 [25]. If it is assumed that equilibrium has been achieved in two hours at 773 K, then the low temperature extrapolation using equation 2.16 [26,34] is not valid. In any event, the solubility of Cr in Cu is less than 0.06 at.% at 773 K, a practical temperature for ageing, and this results in the high conductivity of these alloys.

The maximum solid solubility of Cr in Cu is 0.89 at.% at the eutectic temperature of 1349.6 K [34,26]. This relatively low solubility limits the effectiveness of precipitation-hardening in these alloys because of the resulting low volume of precipitates that form during ageing. Conventional Cu-Cr alloys produced by ingot metallurgy may contain up to 1.2 at.% Cr, but the Cr in excess of the maximum solid solubility is ineffective for precipitation strengthening. The excess Cr however, may cause grain refinement in these alloys by pinning the grain boundaries at solutionizing temperatures.

The accepted eutectic composition is approximately 1.56 at.% Cr [26], although the composition has been reported to range from 0.61 at.% Cr to 2.43 at.% Cr [29-35]. On the Cr-rich side of the phase diagram, the solubility of Cu in the bcc Cr phase is considered to be negligible [26] although there is no available experimental data on the composition of the solvus. The results of Kuznetsov et al [28], from lattice parameter measurements as determined by X-ray diffraction, indicate a retrograde solidus with a solubility of 0.085 at.% Cu at 1423 K.

2.6 The Zirconium-Copper Phase Diagram

The phase diagram of the Cu-Zr system has been the subject of numerous investigations over many years. The accepted diagram from the work of Lou and Grant [40] is complex and characterized by six intermediate phases, Figure 2.9. The identities of these phase compositions have been in dispute since many contradictory results exist in the literature. Much of the controversy centers around the Cu-rich side of the diagram which is most important in the development of high-conductivity alloys. It is only recently that these discrepancies have been resolved.

The solid solubility of Zr in Cu, like that of Cr in Cu, is very small. Pogodin, *etal.* [41] reported a maximum solubility of 1.0 wt.% Zr at the eutectic temperature. This very high value has not been supported by any other results in the literature. Allibone and Sykes [42] reported that an as-cast 0.2 wt.% Zr alloy is single phase at room temperature. Raub and Engel [43] indicated that the solubility of Zr in Cu is less than 0.13 wt.% at 940°C. Similar results were presented by Saarivirta [44] who showed the Zr solubility to be 0.15 wt.% at the eutectic temperature, 980°C. Zwicker [45] reported a slightly lower solubility

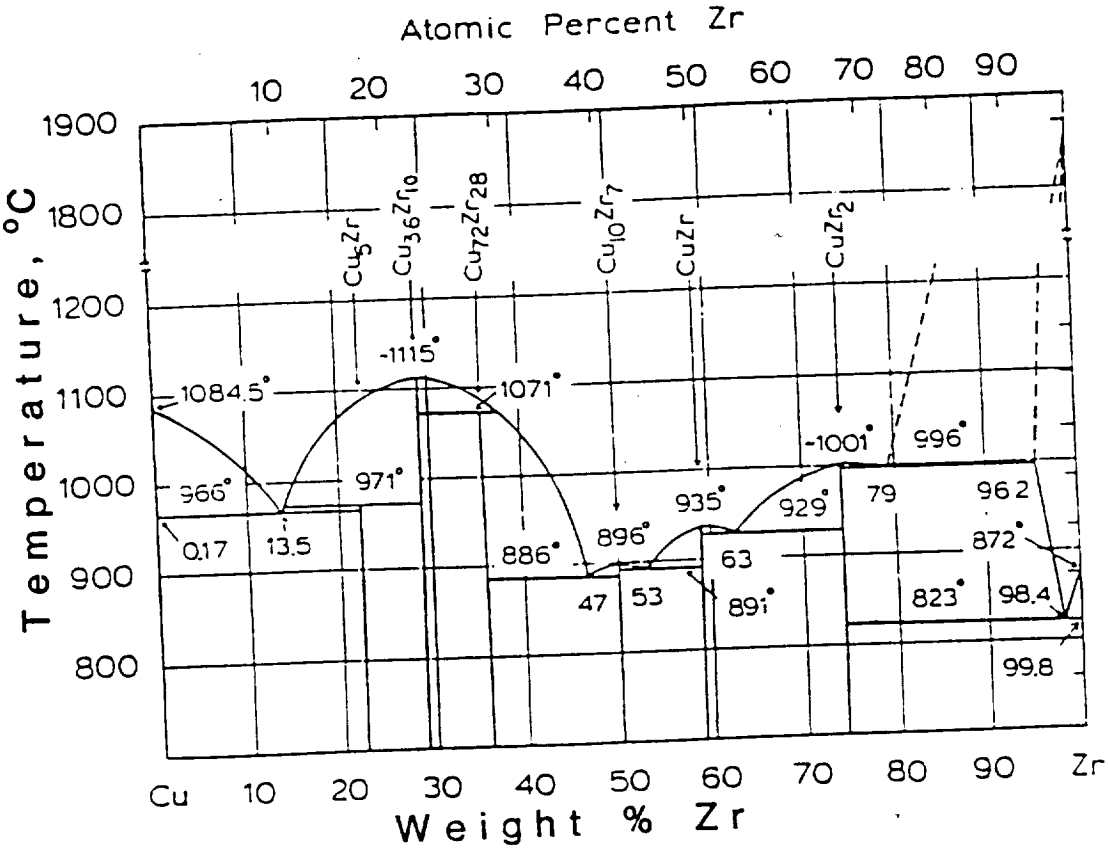

Figure 2.9. Copper–Zirconium Equilibrium Phase Diagram. From the Work of Lou and Grant [40]

of 0.11 wt.% Zr. All of these studies used the technique of metallographic examination to determine phase boundaries. Donachie [46], however, used X-ray microprobe analysis following solidification of a series of alloys containing less than 11.3 wt.% Zr. The maximum concentration in the terminal solid solution was found to be 0.17 wt.% Zr although a range of concentrations was found on probe analysis due to the variation in solidification rates. The Zr concentration measured by Donachie [46] does not preclude the possibility of greater solubility under conditions of slower solidification. Showak [47] determined the Zr solubility by a combination of metallographic, resistivity, and thermal analysis methods. In addition, the log of the Zr concentration when plotted against T^{-1} according to the thermodynamic analysis of Gordon [37], as in equation 2.15, yields a good linear fit. Based on this plot, Showak [47] expressed the solubility of Zr in Cu as:

$$\log X = 4.268 - \frac{6321}{T} \tag{2.17}$$

where X is the concentration of Zr in at.% and T is the absolute temperature in K. Showak determined that the maximum solubility was 0.24 wt.% Zr at the eutectic temperature of 980°C by extrapolation from this equation. While his method shows larger values of solubility than reported by others, the good fit of his data to the thermodynamic analysis [47] lends strong support to his results.

In any event, the equilibrium maximum solid solubility of Zr in Cu is very small, even less than that of Cr in Cu. At 773 K, a typical precipitation hardening temperature for the Cu-Zr alloys, the calculated solubility using equation 2.17 is only 0.00012 at.% Zr, which results in high conductivity after ageing. As in the case of Cu-Cr, the strength of the Cu-Zr alloys are limited by the low volume fraction of precipitates that result from the small maximum solid solubility.

The temperature of the eutectic has also been a subject of some dispute. Many researchers have reported a eutectic temperature of 980°C [41,44,47]. Raub

and Engel [43] reported a slightly lower temperature of 977°C. Others have reported even lower temperatures. Donachie [46] has given the temperature as 970°C which is in good agreement with Perry and Hugi [48], 971°C. Lou and Grant [40] have shown a eutectic temperature of 966°C in Figure 2.9 but have not given the source of this temperature.

On the Cu-rich side of the diagram, the composition of the first intermetallic phase has been a most important point of disagreement. This phase was identified by Lundin et al. [49] and in most of the earlier works [41-45] as Cu_3Zr. Other researchers, using electron microprobe analysis, have identified this phase as Cu_4Zr [46], Cu_9Zr_2 [50], or Cu_5Zr [51,52,48]. Lou and Grant [40] used electrolytic extractions to isolate the Cu-Zr precipitates in a Cu-0.18 wt.% Zr alloy. The residue was analyzed by the Debye–Scherrer X-ray diffraction method. The diffraction pattern was in agreement with the calculated and observed pattern for Cu_5Zr from the results of Forey [53]. The results of Bsenko [54], also based on X-ray diffraction analysis, indicate the presence of a Cu_5Zr phase isostructural with $GdAg_{3.6}$. The Cu_5Zr composition has become the accepted phase for the precipitate in the Cu-rich alloys.

The identification of the other five intermediate phases in the Cu-Zr diagram has been only slightly less controversial. The most recent results of Lou and Grant [40], given in Figure 2.9, indicate that the intermediate phases are $Cu_{36}Zr_{10}$, $Cu_{72}Zr_{28}$, $Cu_{10}Zr_7$, CuZr, and $CuZr_2$. These phases would not be expected to be present in commercial Cu-Zr alloys as the nominal compositions typically are about 0.15 wt.% Zr. The Zr content would have to be hyperperitectic ($\geq$ 13.5 wt.%) to form precipitates other than Cu_5Zr under equilibrium conditions. During rapid solidification processing, however, any of these phases might be present if the thermodynamics and kinetics are favorable.

2.7 The Silver-Copper Phase Diagram

The phase diagram of the Cu-Ag system is of the simple eutectic type, Figure 2.10 [55]. The composition of the eutectic has been reported in the range of 39.8 at.% Cu to 40.9 at.% Cu [56-59] with an accepted value of 39.9 at.% Cu [60]. The maximum equilibrium solid solubility of Ag in Cu is significantly greater than for Cr or Zr in Cu, but in all three systems the solubility decreases rapidly at lower temperatures. The solubility of Ag in Cu has been reported in the range of 4.25 at.% to 5.6 at.% [61-65] at the eutectic temperature of 779°C. The accepted value in the literature is 4.9 at.% Ag [55]. The Ag solubility in Cu at 773 K, a typical ageing temperature for these alloys, is 0.8 at.%. As was discussed previously, Ag in solution does not have a large effect on the conductivity of Cu alloys. Because of the large maximum solubility of Ag in Cu at the eutectic temperature, high-concentration precipitation-hardened Cu-Ag alloys can be produced by conventional ingot metallurgy. The precipitate formed is the Ag-rich fcc terminal solid solution with a maximum solubility of 14.1 at.% Cu at the eutectic temperature. It has also been shown that complete metastable solid solubility can be obtained in this system by splat quenching to room temperature [66].

2.8 Mechanical and Physical Properties of Chromium-Copper

The Cu-Cr alloys are some of the strongest high temperature high-conductivity alloys that are produced by conventional ingot metallurgy techniques. These alloys are strengthened by cold work and precipitation hardening. The decreasing solubility of Cr in Cu with decreasing temperature results in an essentially solute-free high-conductivity Cu matrix strengthened by Cr precipitates. The volume fraction of precipitates is limited by the maximum equilibrium solid solubility of Cr in Cu, as has been discussed previously. For these reasons, Cu-Cr

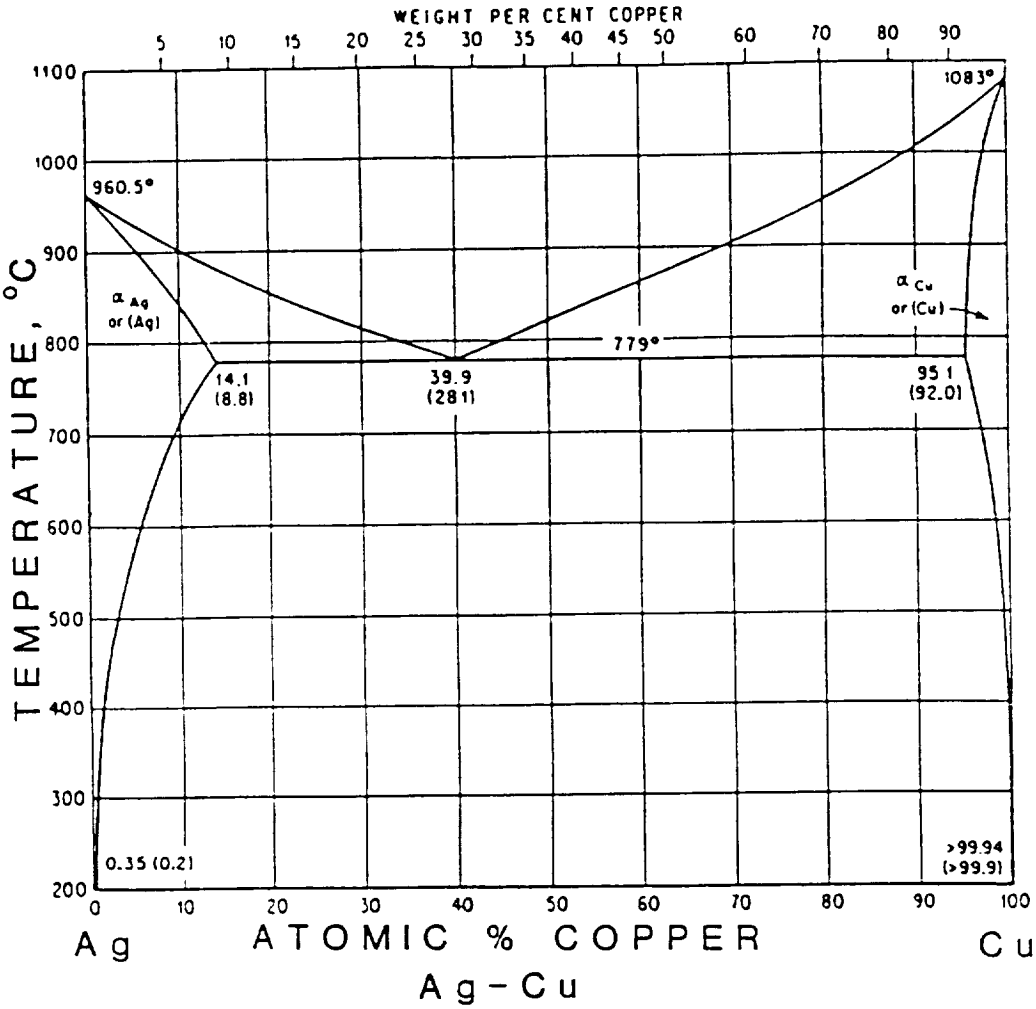

Figure 2.10. Copper–Silver Equilibrium Phase Diagram. From Hansen and Anderko [55]

alloys are ideal candidates for rapid solidification processing in order to extend the equilibrium solubility and increase the volume fraction of strengthening precipitates. In order to compare the benefits of RSP Cu-Cr to conventionally processed alloys, a review of the mechanical and physical properties of commercial Cu-Cr alloys is presented.

The mechanical properties of these alloys are largely controlled by their thermo-mechanical history. In order to obtain the highest strength, the alloys are always solution treated at a temperature near 1000°C prior to ageing. Doi [67] found that the optimum solution temperature is dependent upon the Cr content of the alloy. He showed that the ideal temperatures were 1050°C, 1000°C, 950°C, and 900°C for Cr concentrations of 0.81 wt.%, 0.53 wt.%, 0.29 wt.%, and 0.10 wt.% respectively. These temperatures/compositions correspond to a solution annealing band in the two-phase region of the phase diagram adjacent to the solvus. The higher temperatures, for the concentrated alloys, are necessary to achieve greater supersaturation by dissolution of the Cr. The solutionizing temperature is held just below the solvus in order to minimize grain growth by the presence of second phase particles. Doi's results [67] showed that these temperatures produced significant increases in strength and hardness for the more concentrated alloys, and it is doubtful whether there is any benefit to using an increased alloy content without also raising the solution temperature accordingly. Despite these results, commercial alloys are not solution treated at temperatures greater than about 1000°C even though they may contain up to 1.2 wt.% Cr. The maximum equilibrium solubility of Cr in Cu at this temperature is only 0.37 wt.%. In contrast to Doi's results [67], Priester *etal.* [39] found only marginal strengthening benefits from solutionizing temperatures greater than 975°C. In commercial practice, the lower temperatures are used to prevent excessive grain growth and to reduce the rate of oxidation when solutionizing is performed in air.

The recommended time for the solution treatment is one hour at temperature per inch of section thickness with a minimum of 1/2 hour at temperature [68]. The solution anneal is followed by a rapid water quench. The cooling rate during the quench should be as rapid as possible to retain most of the Cr in solution prior to ageing. It has been found that less severe quenches result in lower strength alloys following ageing [69].

Following the solution treatment, Cu-Cr alloys exhibit very low electrical conductivity, typically about 35 % to 60 % IACS [70], the exact value being dependent upon the Cr concentration, the solutionizing temperature, and the severity of the quench. Similarly, the mechanical properties of the solutionized alloy are poor, with room temperature tensile strengths of 34 ksi and 45 ksi being reported for commercial flat products and rods, respectively [71]. The yield strength of the alloys in this condition is in the range of 14 ksi to 19 ksi, also being dependent upon the product section thickness [71]. The larger section products exhibit higher strengths due to precipitation during the slower cooling rate quench. Tensile strengths as high as 68 ksi [70] have been reported for Cu-1.05 wt.% Cr alloys in the solutionized condition, but these values are atypical.

Elevated temperature ageing of these alloys results in an almost ideal balance of strength and electrical conductivity. Commercial alloys are aged in a temperature range of 450°C to 500°C with longer time at the lower temperature; at 500°C the time is usually 3 hr/in. of section [68]. In Figure 2.11, reproduced from the work of Doi [67], it can be seen that the maximum precipitation hardening effect for an ageing time of one hour occurs near 500°C, and that the size of the strengthening effect increases with an increase in solution temperature. Doi [67] also showed that the location of the ageing temperature peak is nearly concentration independent. The room temperature tensile strength of 80 ksi [67] for the Cu-1.02 wt.% Cr alloy, in Figure 2.11, is significantly larger than the typical

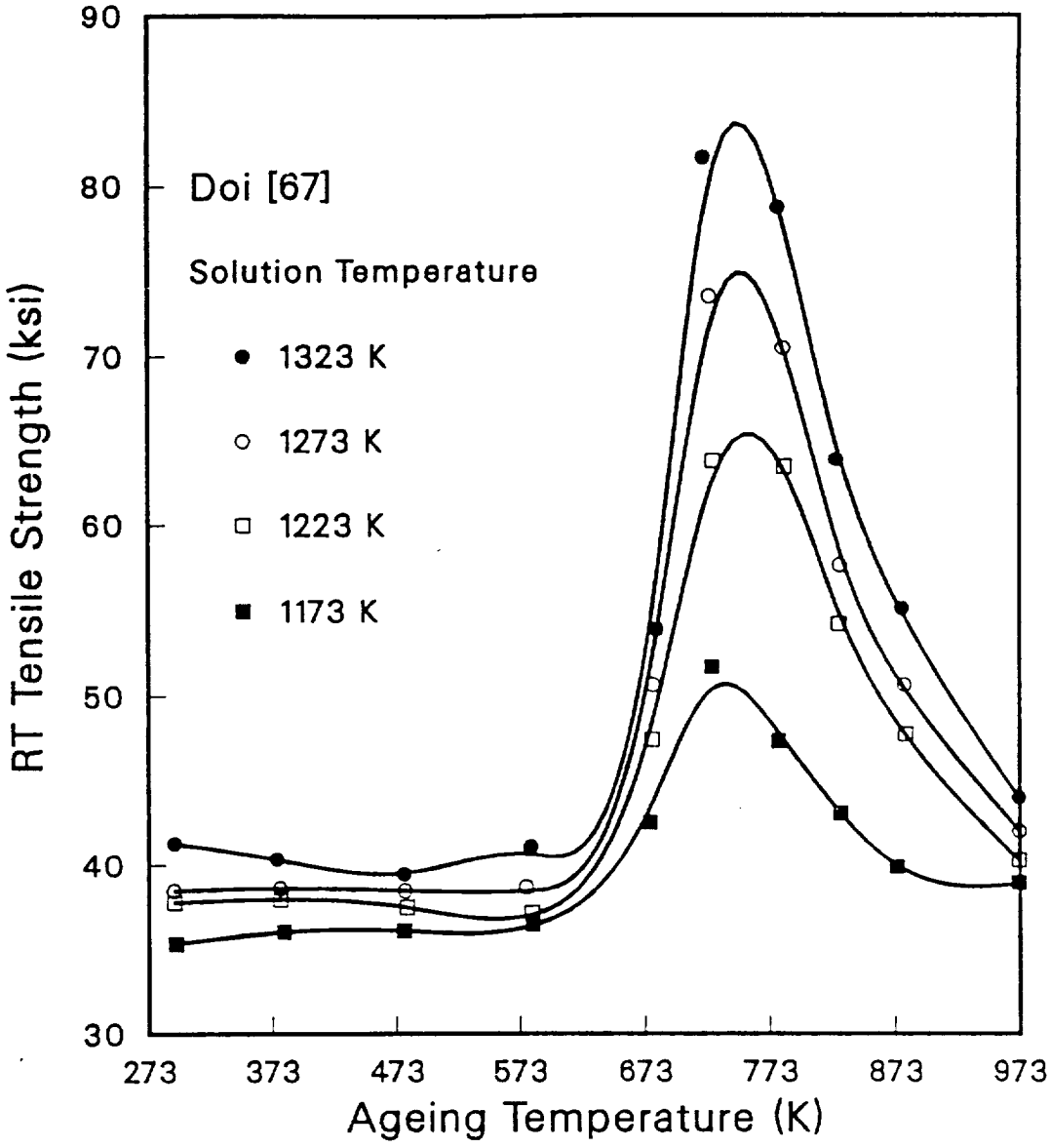

Figure 2.11. Effects of Solution and Ageing Temperatures on the Room Temperature Tensile Strength of a Cu-1.02 wt.% Cr Alloy [67]. Specimens Aged for One Hour

values for commercial alloys which range from 51 ksi to 72 ksi [71], depending upon section thickness. The optimum ageing time for these alloys is a function of the temperature; lower temperatures require longer times to reach peak hardness. In Figure 2.12 [72], Cu-0.5 wt.% Cr alloy specimens aged at 400°C, 450°C, and 500°C exhibit this behavior. For the 500°C ageing, the maximum hardness is achieved in one hour, followed by a loss in hardness over the next few hours due to overageing. Ageing at 450°C produces the same value of maximum hardness, but the peak occurs at 3 hours of ageing. The loss of hardness, due to overageing, is also delayed at the lower ageing temperature. At an ageing temperature of 400°C, the peak hardness has still not been achieved in 10 hours. Commercial alloys are usually aged at 450°C to 500°C in order to reach the highest strength in the minimum time, and to avoid the rapid deterioration in properties due to overageing at higher temperatures.

Artificial ageing, while producing good strength in these alloys, also produces a ductility minimum. In Figure 2.13 [67], it can be seen that the elongation decreases from 30 % for the solution treated alloy to about 10 % for the 1.02 wt.% Cr alloy aged to the peak strength. Commercial alloys exhibit the same behavior although the amount of the ductility loss is not as severe. A typical value for elongation in quenched and aged commercial alloys is about 22 % [71]. In contrast to this behavior, alloys which are cold-reduced after solution treatment show a ductility increase upon aeging [70]. In all cases, overageing results in a restoration of the ductility lost during ageing to peak strength.

Ageing of these alloys at elevated temperature also removes Cr from solution during precipitation to increase the electrical and thermal conductivities. This is evident from Figure 2.14 [71] as the room temperature electrical conductivity of commercial Cu-Cr increases from 40 % to 90 % IACS after ageing at 500°C for two hours. Similar behavior is exhibited by other Cu alloys with up

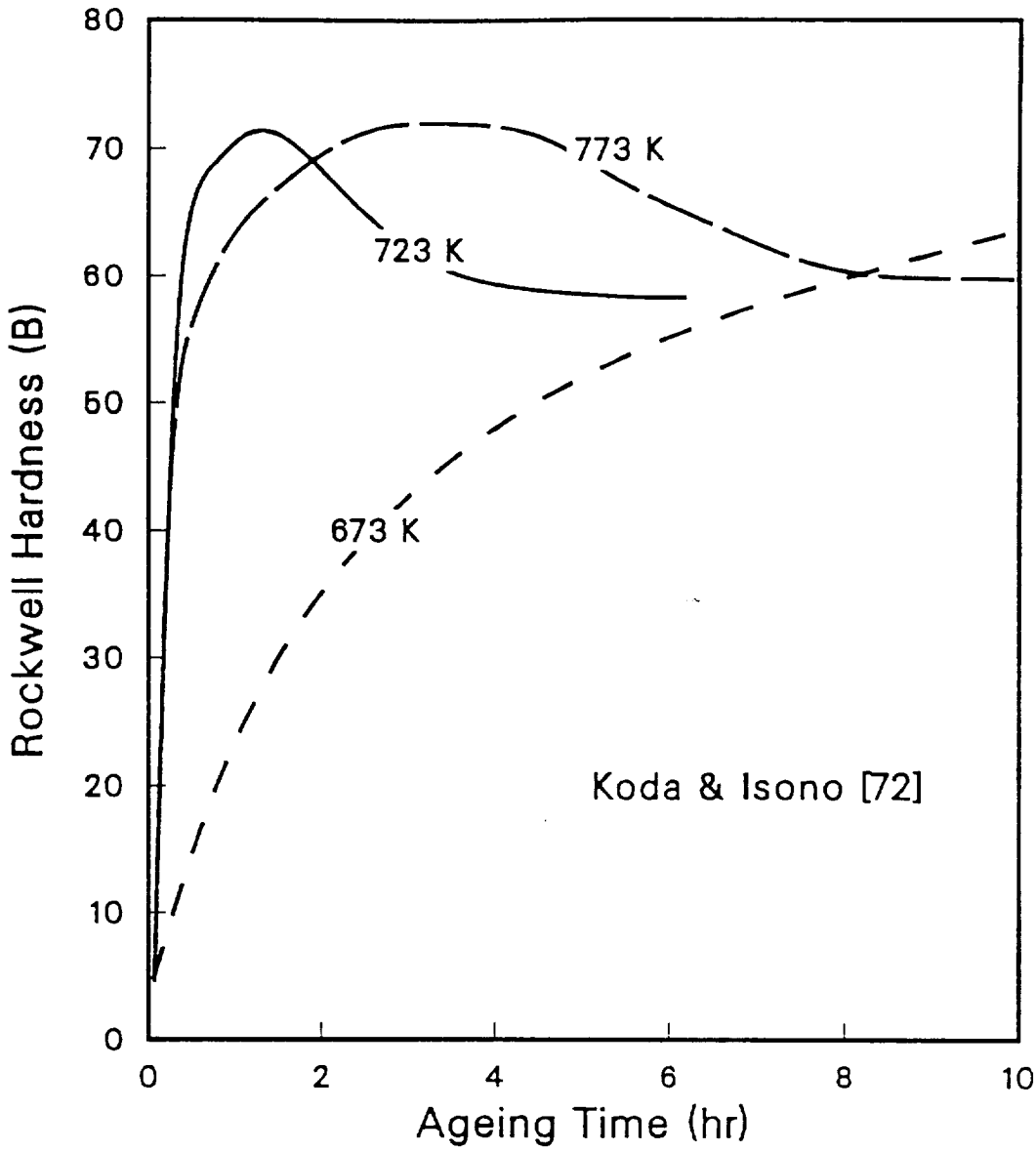

Figure 2.12. Hardness of a Cu-0.5 wt.% Cr Alloy as a Function of Ageing Time for Three Temperatures [72]

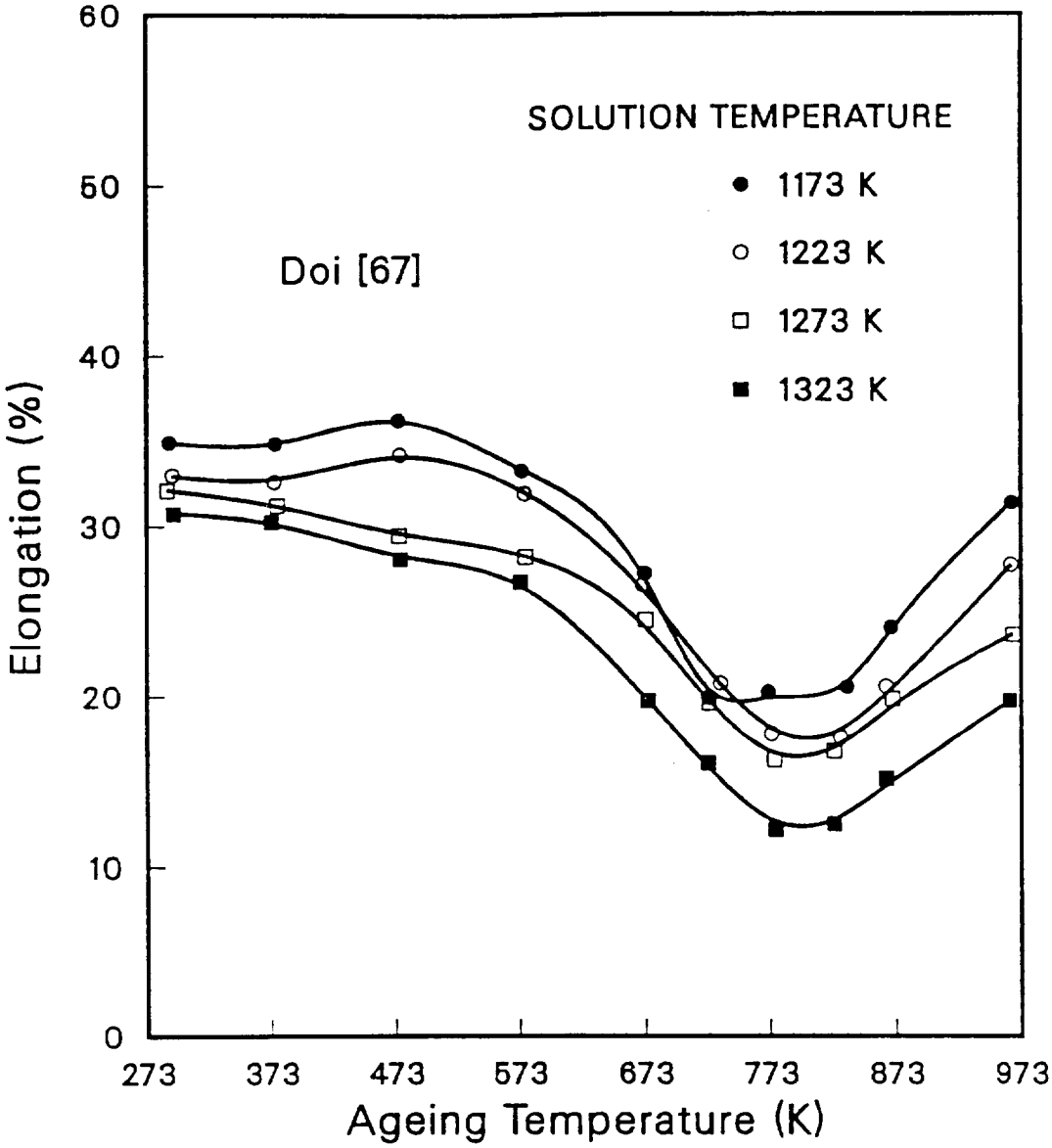

Figure 2.13. Effects of Solution and Ageing Temperatures on the Room Temperature Tensile Elongation of a Cu-1.02 wt.% Cr Alloy. From the Work of Doi [67]

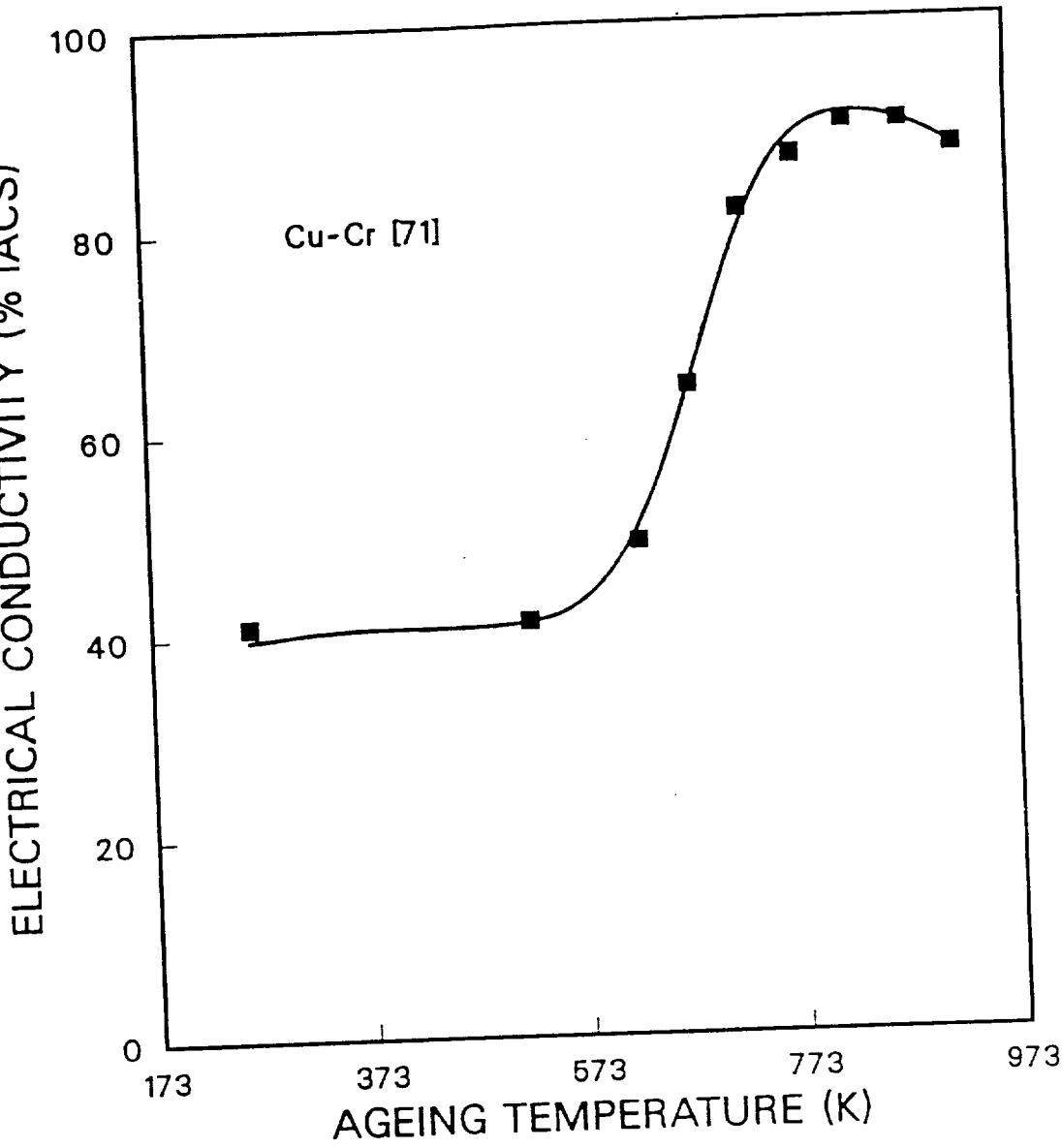

Figure 2.14. Effect of Ageing Temperature on the Room Temperature Electrical Conductivity of Commercial Cu-1.0 wt.% Cr Alloy, Solution Treated at 1273 K and Aged for Two Hours [71]

to 0.91 wt.% Cr [73]. Figure 2.15 shows the effect of ageing time at 500°C on the room temperature electricical resistivity for several alloy compositions. It can be seen that the minimum resistivity is reached in about 1/2 hour for all Cr concentrations studied. When Figure 2.15 and Figure 2.12 are compared, it is evident that the minimum electrical resistivity occurs prior to the strength peak during ageing at 500°C. Overageing produces no further change in conductivity, thus the alloys can be aged to optimize both strength and electrical conductivity. The same behavior has been shown for alloys aged at 450°C where the resistivity minimum occurs in about one hour [73]. From Figure 2.12, it can be seen that there is about a two hour difference between the conductivity and strength maximums.

Commercial Cu-Cr alloys are usually cold worked prior to ageing in order to strain harden the product. The increase in strength is accompanied by a loss in ductility. The electrical conductivity, however, is not significantly affected by cold reduction. The room temperature tensile strength increases linearly with cold work, Figure 2.16 [71,74]. This behavior is followed for alloys cold worked after solution treatment and for alloys which were subsequently aged. As would be expected, cold working causes an improvement in the room temperature yield strength of these alloys. In Figure 2.17 [71,74] it can be seen that the solutionized alloy exhibits a linear increase in yield strength above 20 % cold work. Alloys which are aged following cold work show further improvements in yield strength. Aeging treatments following cold work also result in significant improvements in tensile strength and ductility. The optimum ageing temperature for cold worked alloys is about 450°C; this lower temperature is used to prevent loss of strength from recovery and recrystallization. Cold work after ageing may be necessary

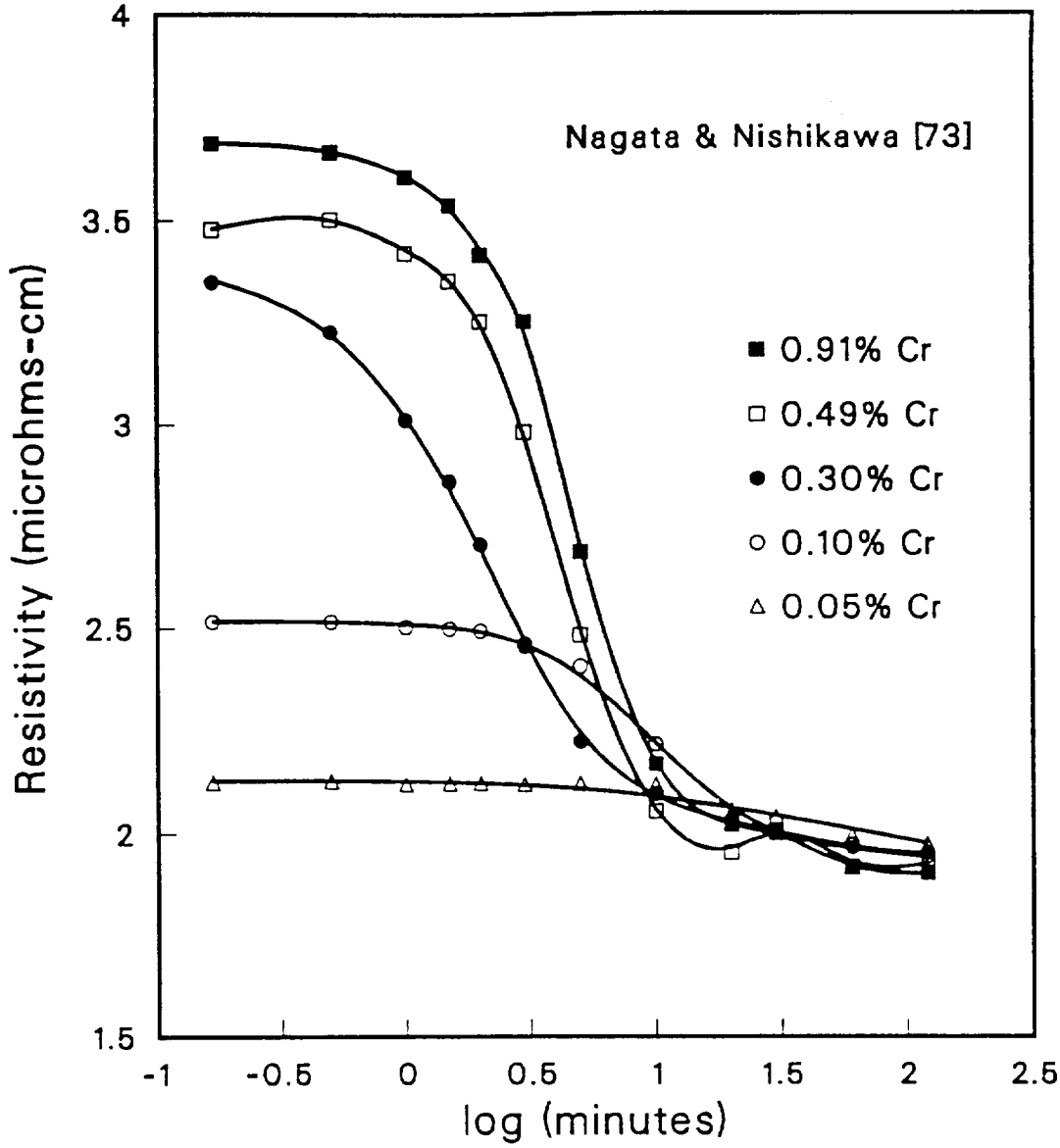

Figure 2.15. Effect of Ageing Time at 773 K on the Electrical Resistivity of Five Alloys of Cu-Cr [73]

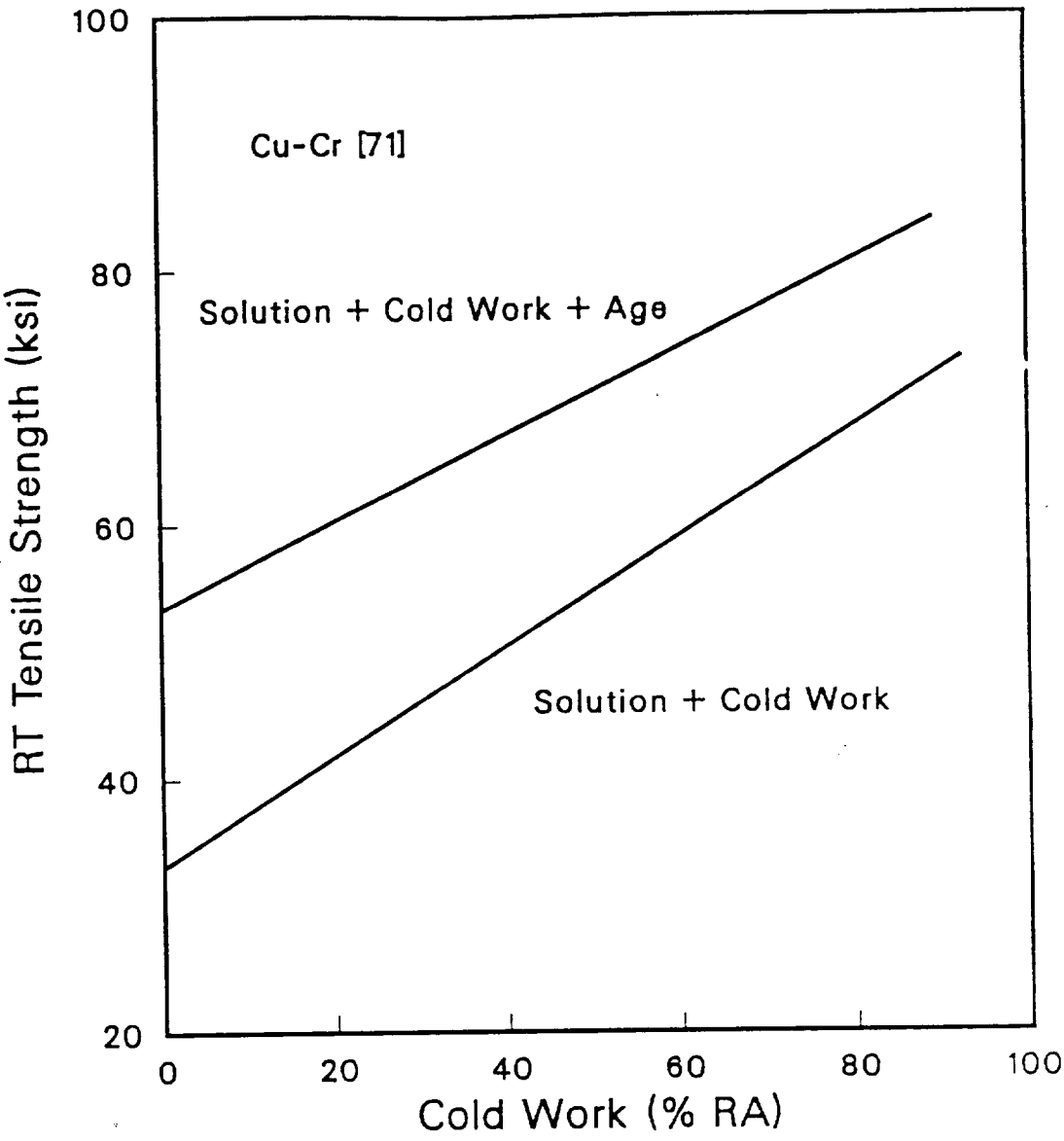

Figure 2.16. Effect of Cold Work on the Room Temperature Tensile Strength of Commercial Cu-1.0 wt.% Cr Alloy, Solution Treated at 1273 K and Aged at 723 K for Two Hours [71,74]

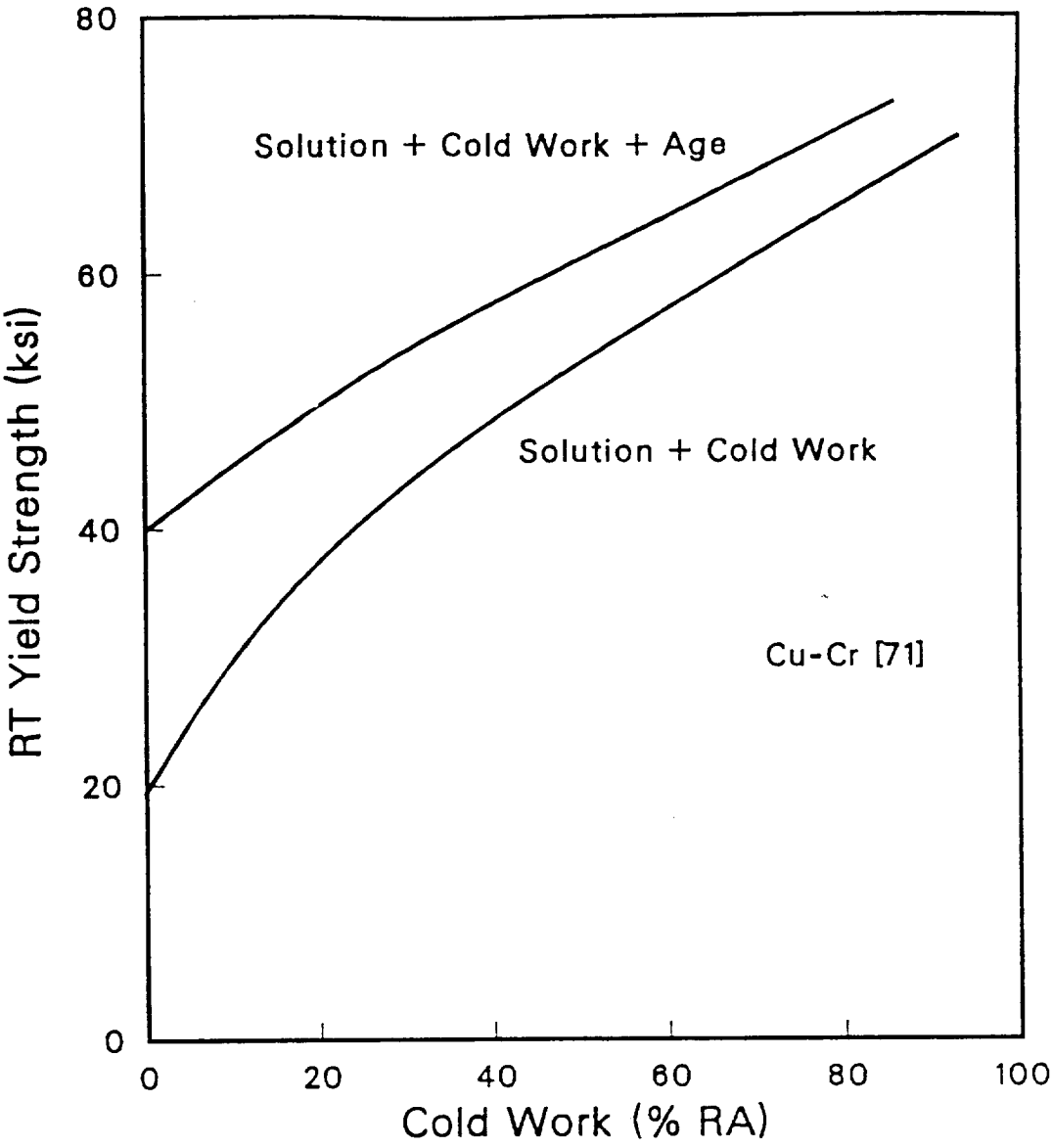

Figure 2.17. Effect of Cold Work on the Room Temperature Yield Strength of Commercial Cu-1.0 wt.% Cr Alloy, Solution Treated at 1273 K and Aged at 723 K for Two Hours [71,74]

for commercial products for a good surface finish or increased strength, but produces undesirable losses in ductility. The ductility may again be restored by low temperature re-ageing.

The room temperature properties of Cu-Cr alloys vary widely with the thermomechanical history. The tensile strengths can range from 34 ksi to 86 ksi and ductilities can range from 0 % to 40 % tensile elongation. In comparison with other high-conductivity Cu alloys, the nominal 1.0 wt.% Cr alloy has the highest room temperature tensile and yield strength of any available alloy. At elevated temperatures the mechanical properties of Cu-Cr deteriorate. Figure 2.18 [75] shows a linear decrease in tensile strength of Cu-0.7 wt.% Cr alloy with increasing test temperature up to about 500°C; beyond this temperature there is a rapid decrease in strength. The material in this study was solution treated at 1000°C, cold worked 84 %, and aged at 450°C to peak strength prior to tensile testing [75]. In Figure 2.19 [75], it can be seen that the ductility as measured by % RA also suffers at elevated temperature; a severe ductility trough occurs at 500°C for the same alloy. The loss of ductility of these alloys at elevated temperature may make them unsuitable for applications in rocket chambers as this may exacerbate the thermal cracking.

Since these alloys are frequently used as electrical conductors at elevated temperatures, it is important to understand the change in conductivity with temperature. The electrical resistivity of the Cu-Cr alloys exhibits a linear increase with absolute temperature. In Figures 2.20 and 2.21 [75], the electrical resistivity and conductivity of a Cu-0.70 wt.% Cr alloy are plotted as a function of temperature; data are included for OFHC Cu and Cu-0.15 wt.% Zr for comparison. The Cu-Cr alloy used in this study was cold drawn 84 % prior to ageing at 450°C to peak strength. The Cr addition has a purely additive effect on the electrical resistivity for all temperatures up to 500°C. It can also be observed that the

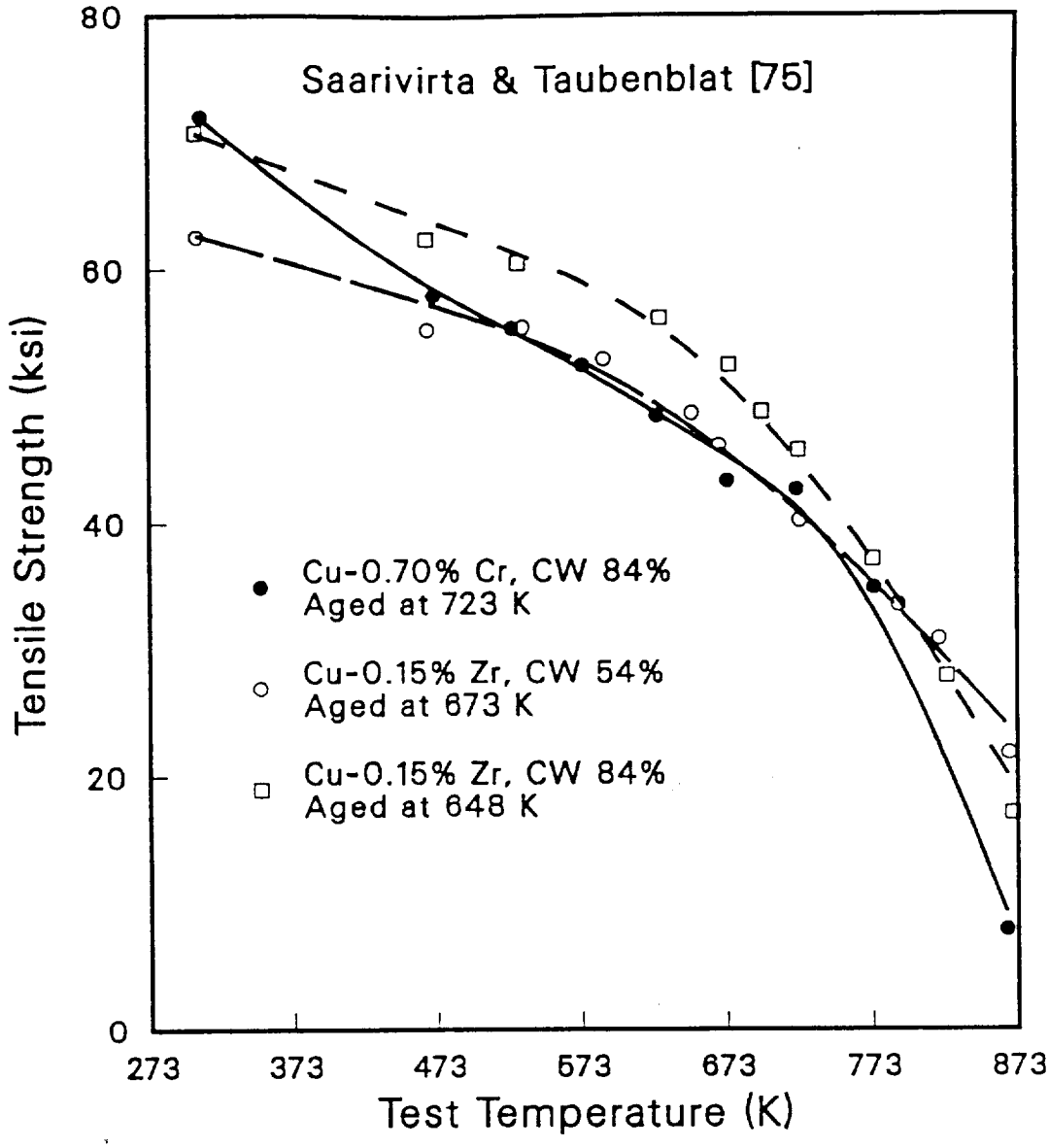

Figure 2.18. Elevated Temperature Tensile Strength of Cold Worked and Aged Cu-0.15 wt.% Zr and Cu-0.70 wt.% Cr Alloys [75]

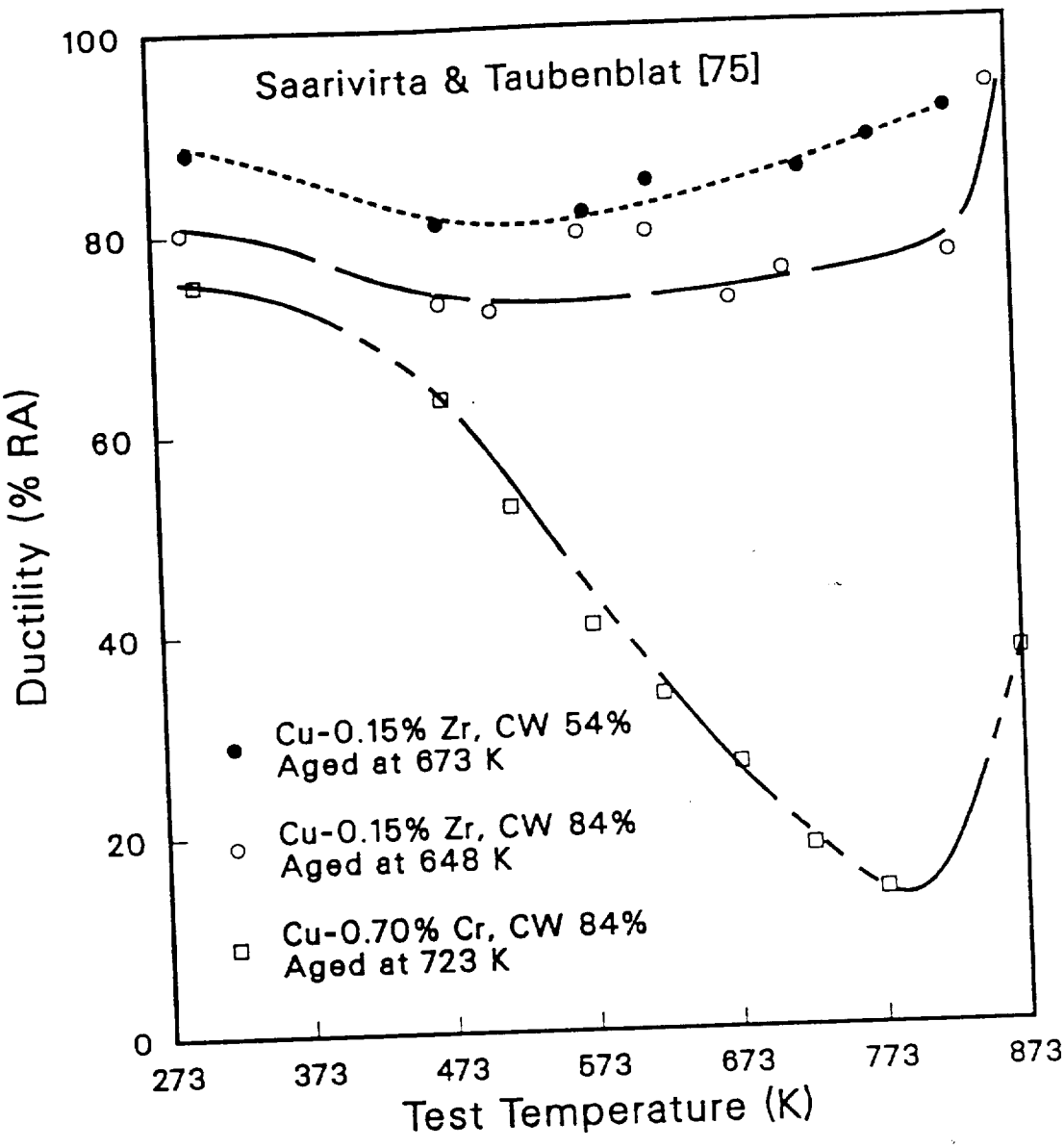

Figure 2.19. Elevated Temperature Tensile Ductility of Cold Worked and Aged Cu-0.15 wt.% Zr and Cu-0.70 wt.% Cr Alloys [75]

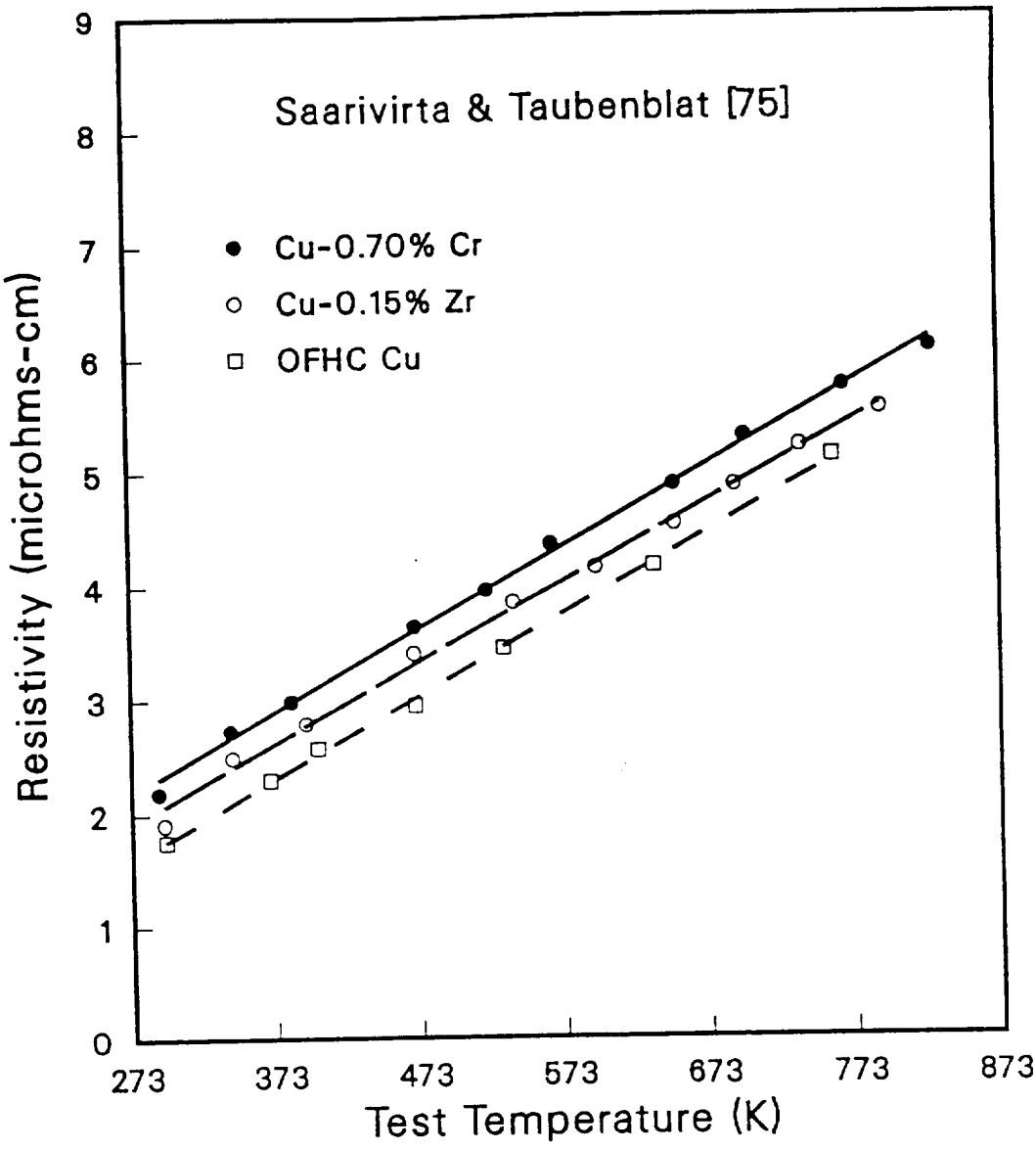

Figure 2.20. Electrical Resistivity as a Function of Temperature. Alloys Cold Worked 84 % and Aged Prior to Testing. OFHC Cu Tested in Annealed Condition [75]

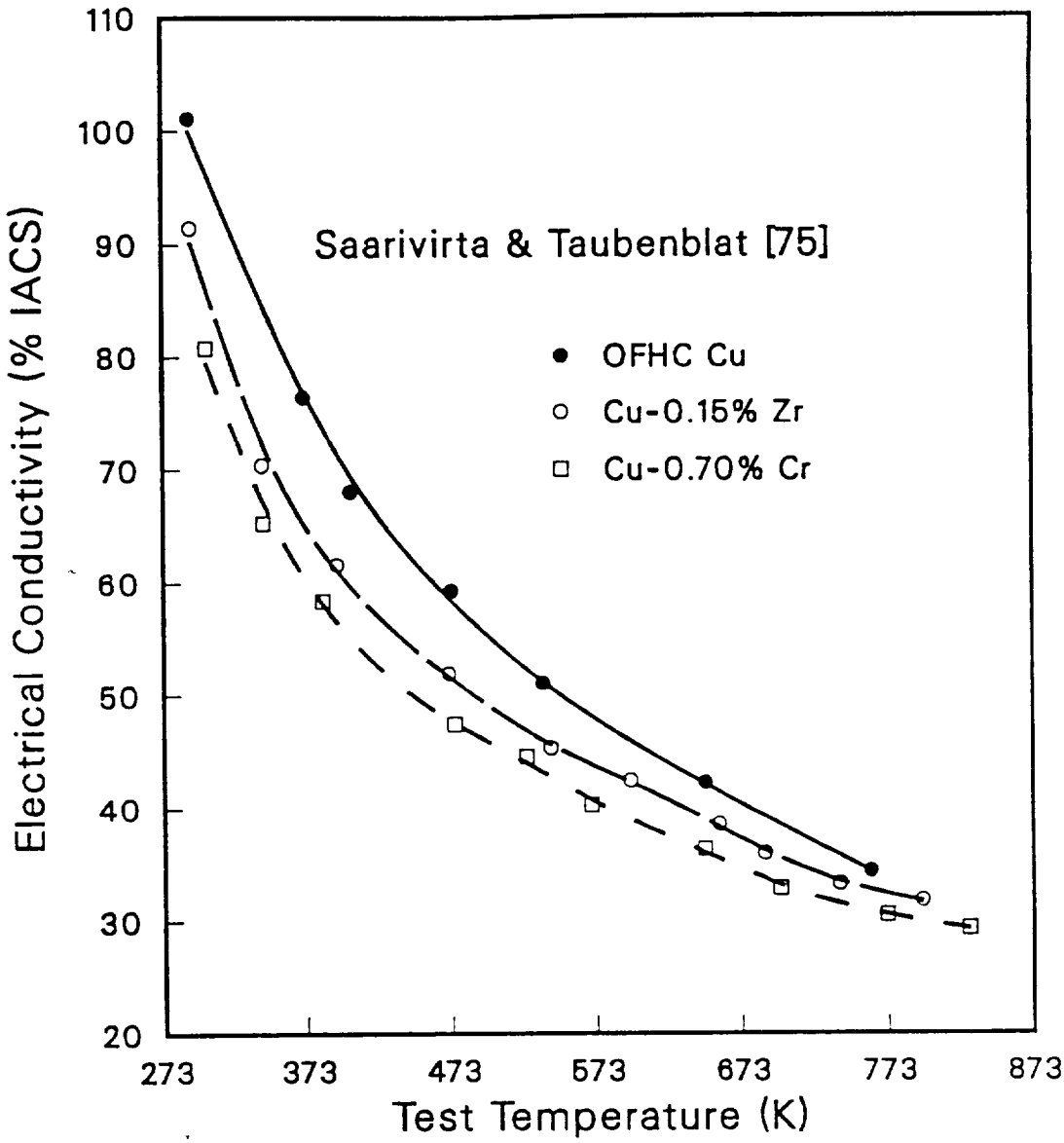

Figure 2.21. Electrical Conductivity as a Function of Temperature. Identical Treatment as Figure 2.21 [75]

contribution of solutes to the resistivity is relatively insignificant when compared with the thermal scattering contribution to the resistivity at 500°C; only about 12 % of the resistivity is from Cr in solution.

The thermal conductivity of the Cu-Cr alloys as a function of temperature was shown earlier in Figure 2.2 [12]. In contrast to the electrical conductivity, the thermal conductivity of dilute alloys actually exhibits a mild increase with temperature, as was explained in section **2.3**. Other published data [71] on these alloys does not show this increase in thermal conductivity with temperature and also shows lower values of thermal conductivity for all temperatures. The inconsistency in these results is probably due to the difficulty in making accurate measurements of thermal conductivity, and differences in the composition and thermomechanical processing of the alloys. The conductivity for these alloys is most likely in the range of 330 $Wm^{-1}K^{-1}$ to 360 $Wm^{-1}K^{-1}$ for temperatures between 20°C and 400°C, although further experimental work is needed for verification.

Although commercial Cu-Cr alloys contain Cr in the range 0.5 at.% to 1.4 at.%, there is little data available on the effects of Cr in excess of the solid solubility limit; 0.89 at.% at the eutectic temperature. When alloys are solution treated at the usual temperature of 1000°C, the equilibrium solubility is only 0.49 at.% Cr. Very little improvement in mechanical properties would be expected for the alloys with Cr in excess of the solid solubility for the corresponding solution temperature. The excess undissolved Cr particles coarsen at high temperature and do not effectively contribute to precipitation strengthening. Suzuki *etal.* [70] found that the room temperature tensile strength does not improve with increasing Cr concentration in the range of 0.69 wt.% to 1.43 wt.%. The alloys in his study were solution treated at 1000°C, cold reduced 83 %, and aged at 450°C for one hour. The room temperature electrical conductivity of the alloys was also

similarly unaffected by the excess Cr concentration; a conductivity of 82 % IACS was measured for three compositions in the given range. For commercial alloys, it seems that the only benefit of excess Cr is to prevent grain growth during the solution treatment.

Rapid solidification processing, however, can utilize Cr in excess of the solid solubility by quenching from the melt. A metastable extended solid solution of Cr in Cu may be produced if the cooling rates are very large during the quench. Elevated temperature ageing of the highly supersaturated alloy results in a strong precipitation hardening effect because of the large volume fraction of precipitates. In a recent study [76] on melt-spun Cu-2 at.% Cr and Cu-5 at.% Cr alloys, significant increases in yield and tensile strengths of both as-cast and heat-treated ribbons were reported as a result of the rapid solidification processing. The room temperature tensile strength of Cu-5 at.% Cr ribbon aged for one hour at 450°C was 110 ksi. For the lower Cr concentration alloy tested under the same conditions, the tensile strength was 87 ksi. The optimum ageing temperature for peak strength of the RSP alloys was 450°C for one hour, which is comparable to the heat-treatment schedule for conventional Cu-Cr alloys. These high values of strength were obtained even though the quench was not rapid enough to retain all the Cr in solution for the high concentration alloy. Primary Cr particles as large as 67 nm in diameter were formed near the free surface of the ribbon during melt-spinning of the Cu-5 at.% Cr alloy, and smaller particles were formed through the ribbon thickness. Even at the wheel surface of the ribbon where the cooling rates are the highest, Cr particles of 36 nm diameter were formed during solidification. These large primary Cr particles are an order of magnitude too large to be effective in precipitation strengthening. In contrast, the Cu-2 at.% Cr alloy did not form any primary Cr particles during solidification. It would be expected that yet higher cooling rates would produce a significant improvement

in tensile strength in the Cu-5 at.% Cr alloy and only a marginal improvement in the Cu-2 at.% Cr alloy.

2.9 Precipitation in Copper-Chromium Alloys

The precipitates formed by artificial ageing of solution-treated Cu-rich alloy are nearly pure Cr. The crystal structure of the precipitates and their orientation relationship to the fcc Cu matrix has been a subject of much controversy in the literature. Since the recrystallization temperature, grain size, and room and elevated temperature strength of these alloys are dependent upon the Cr precipitates, it is important to understand the sequence of precipitation in order to optimize the microstructure.

In an early X-ray diffraction study of precipitation in binary Cu alloys with up to 1.33 wt.% Cr, Williams [77] found diffuse rods in $< 111 >$ matrix directions around each reciprocal lattice point. He speculated that the Cr precipitated as coherent plates on the (111) fcc Cu matrix plane, and the crystal structure of the precipitate was either fcc, bcc, or hcp; the coherent planes in the precipitate being (111), (110), or (001), respectively. Elastic strain energies were calculated for each type of precipitate, and it was shown that the strain from an fcc precipitate was smaller than that from a bcc or hcp structure by at least an order of magnitude. Williams [77] also observed a homogeneous distribution of small precipitates in his alloys. Calculations were made in order to determine the supersaturation ratio necessary for homogeneous nucleation. Because of the large strain energy of bcc Cr in Cu relative to fcc Cr, he showed that homogeneous nucleation requires much larger supersaturation for the bcc precipitate than for the fcc precipitate. The weight of the evidence favored the formation of fcc precipitates, but the uncertainties of the thermodynamic calculations prevented Williams from drawing a definitive conclusion.

Suzuki *etal.* [78] investigated precipitation in this system by use of the TEM. A Cu-0.26 wt.% Cr alloy was solution treated at 950°C, water quenched, and aged for one hour in a temperature range of 400°C to 700°C. Artificial ageing at 400°C did not result in any visible precipitates. After ageing at 500°C, a homogeneous, high-density distribution of fine (10 nm diameter) precipitates was produced. 600°C ageing produced spherical precipitates similar in appearance to Co precipitates in Cu. It was reported however, that three directions of no contrast could be observed and from this [78] concluded that the precipitates were not spherical. Appreciable coherency strains were found, but did not produce streaking or other effects on selected area diffraction; GP zone formation was discounted by [78] for those reasons. After ageing at 700°C, coarser, but still coherent, rod-shaped precipitates were observed; the rods were parallel to {111} matrix planes.

In another TEM investigation, Rezek [79] studied precipitation in a Cu-0.35 wt.% Cr alloy solutionized at 1000°C, water quenched, and aged in a temperature range of 500°C to 700°C. The spherical and rod precipitate morphologies were observed as in the work of [78]. Selected area diffraction patterns showed no visible diffraction from the spherical precipitates; only the fcc matrix pattern was present. From this result, [79] concluded that the spherical Cr precipitates are fcc, and the rod-shaped precipitates are bcc, although they did not report the presence of a bcc diffraction pattern. Similar results were found by Knights and Wilkes [80] for a Cu-0.15 wt.% Cr alloy solutionized at 1000°C, water quenched, and aged in a temperature range of 300°C to 600°C. The first precipitation was shown by the appearance of a homogeneous distribution of coherent, spherically symmetric precipitates ranging in size from 5 nm to 10 nm. Aeging at 600°C for 4 hours produced precipitates with the rod morphology aligned in $< 110 >$ matrix directions. Selected area diffraction showed only the fcc matrix pattern

even with the presence of both spherical and rod precipitates. From this result, [80] concluded that the crystal structure of the two morphologies was fcc Cr with a very low interfacial surface energy in the Cu matrix. In a later study, Komen and Rezek [81] found the rod-shaped precipitates, produced by ageing for 3 hours at 600°C, to be bcc Cr; only the rod morphology could be observed in dark-field TEM images produced from bcc reflections. In addition, the aspect ratio of the rods was found to vary. From this, [81] concluded that the rod morphology may actually correspond to a plate morphology with the $\{110\}_{\text{bcc}}$ Cr parallel to $\{111\}_{\text{fcc}}$ Cu.

Seven precipitate morphologies were found in a TEM study [82] of a Cu-0.33 wt.% Cr alloy aged in a high temperature range of 700°C to 900°C for up to 120 hours. The overaged precipitates were described as bcc Cr laths, 10 μm in length, with a 20:1 aspect ratio; at these long times and high temperatures no fcc Cr was found. The precipitates were in a range of orientations intermediate between the Nishiyama–Wasserman and Kurdjumow–Sachs relationship: $\{110\}_{\text{bcc Cr}} \parallel \{111\}_{\text{fcc Cu}}$, $< 110 >_{\text{bcc Cr}} \| < 111 >_{\text{fcc Cu}}$, with the angle θ between $[001]_{\text{bcc}}$ and $[1\bar{1}0]_{\text{fcc}}$ in the range of 0° to 5.26°. The conjugate habit planes of the planar facets were often irrational and led Hall *etal.* [82] to propose a stepped interface model with the broad faces of the precipitates parallel to $\{111\}_{\text{fcc}}$. In another study of overaged Cr precipitates, Weatherly *etal.* [83] found only the Kurdjumow–Sachs orientation relationship with the long axis of the laths in $< 651 >$ or $< 761 >$ fcc matrix directions. In this study, only the needle-shaped precipitates with double lobe strain field contrast were examined, and this may explain why the other orientations reported by [82] were not observed. Computer modelling of strain contrast effects led [83] to conclude that bcc Cr laths could be accomadated coherently in the fcc Cu matrix.

Clarke and Stobbs [84] reported the appearance of yet two other orientation relationships found in a near-eutectic, directionally solidified 1.45 wt.% Cr alloy. The two variants of $\{111\}_{fcc} \parallel \{110\}_{bcc}$ were a modified Kurdjumow–Sachs orientation rotated by 6×10^{-2} radians about the $[0\bar{1}1]_{fcc}$ or $[111]_{bcc}$ fiber axis, and an inverted Nishiyama–Wasserman orientation rotated by 9×10^{-2} radians about the same direction. Hall *etal.* [85] compared the habit plane poles for the precipitates in a Cu-0.33 wt.% Cr alloy, aged for 120 hours at 700°C, to those of Fe-C alloys. The fcc/bcc lattice parameter ratio in the Cu-Cr system is nearly the same as that for the proeutectoid ferrite reaction; this ratio plays a role in determining the crystallography of martensitic transformations. The similarities between the locations of bainite, Widmanstätten ferrite, and Cr poles on a stereographic triangle led [85] to conclude that the Cr precipitates form by a diffusional nucleation and growth mechanism rather than by a martensitic shear transformation.

As an alternative technique to X-ray and TEM studies, many researchers used electrical resistivity measurements to detect subtle microstructural changes during the initial stages of precipitation in Cu-Cr alloys. Nishikawa *etal.* [86] studied a Cu-0.30 wt.% Cr alloy solution treated at 950°C, water quenched, and heat-treated (T_a) to three schedules; 300°C for 50 hours, 350°C for 5 hours, or 400°C for 3/4 hour. A uniform decrease in electrical resistivity was produced during the pre-ageing treatments at the different temperatures and times. The specimens were then reversion aged (T_r) in a temperature range of 400°C to 500°C. For T_a of 300°C or 350°C, the reversion treatment resulted in an initial increase in resistivity followed by a steady decline. The incremental, positive change in resistivity, $\Delta\rho$, increased with the magnitude of $(T_r - T_a)$. It was also shown that higher values of T_r resulted in larger values of $\Delta\rho$ and greater reversion rates, i.e. shorter time was required to reach $\Delta\rho$. The dependence of $\Delta\rho$

on the reversion temperature, T_r, led [86] to discount the presence of a metastable GP solvus; reversion at any temperature above the solvus should yield a constant value for $\Delta\rho$. The initial increase in resistivity was attributed to an increase in the size of the critical radius of the precipitate at higher temperatures. Small precipitates, produced during the ageing treatment and less than the size of the critical radius for the reversion temperature, were thought to dissolve during the reversion treatment and increase the solute concentration. Similar results were presented by Suzuki *etal.* [87] for a Cu-0.26 wt.% Cr alloy quenched from a solution temperature of 950°C, and aged in a temperature range of 300°C to 500°C. The specimens were reversion treated in a temperature range of 350°C to 600°C. An increase in resistivity was reported in all cases where $T_r > T_a$. As with the results of [86], [87] also found the reversion increment and the reversion rate to be temperature dependent. In addition, [87] performed split ageing experiments on the same alloy. One set of specimens was split aged at 300°C for 20 hours followed by 15 hours at 350°C. The reversion increment, $\Delta\rho$, was compared with a set of specimens that had undergone normal ageing at 350°C for 15 hours prior to reversion treatment in a temperature range of 450°C to 550°C. Split ageing produced slightly larger values of $\Delta\rho$ than normal ageing. These experimental results led [87] to support the temperature dependent critical radius theory of reversion.

In a later study, Suzuki and Kanno [88] measured the change in resisitivity of these alloys during the initial stages of normal precipitation ageing. Copper alloys with up to 1.0 wt% Cr were solutionized in a temperature range of 950°C to 1050°C, water quenched, and artificially aged in a temperature range of 300°C to 500°C. After ageing for short times, the specimens were quenched and the resisitivity was measured at room temperature. A small initial increase in resistivity was found for specimens aged at 450°C and 500°C, while an abrupt drop

in resistivity was measured for the lower aeging temperatures. The specimens aged at the higher temperatures showed a steady decline in resistivity following the transient increase. The rate of decrease in resistivity for all ageing temperatures was greater with higher solution temperatures and Cr concentration. From these results, [88] concluded that bcc Cr clusters were forming during the lower temperature ageing; the depletion of the Cr solute concentration causing the rapid decline in resistivity. The initial increase in resistivity for the alloys aged at the higher temperatures was thought to be the result of dissolution of Cr clusters formed during the quench from solution treatment. The formation of clusters and vacancy-cluster interaction in these alloys greatly complicate the precipitation ageing behavior [88].

All of the experimental work using the technique of electrical resistivity measurement during ageing and reversion led [73,86,87,88] to conclude that a metastable GP Cr phase is not formed in these alloys. It would be expected that precipitation of a coherent fcc GP zone would cause a large electron scattering when the interzone spacing is on the order of the electron mean free path, $\approx$30 nm. Very large increases in resistivity are observed during GP zone formation in Cu-Be [89,90], Al-Cu, and Al-Zn [91] alloys. The absence of this effect in the Cu-Cr system caused [73,86–88] to discount the formation of a metastable fcc Cr precipitate. These results are inconsistent with the evidence for a coherent fcc Cr phase that was shown in TEM and X-ray diffraction studies.

In an effort to settle the dispute, two studies [92,93] were performed using precipitate extraction and X-ray phase analysis on Cu-Cr alloys aged at $\approx$600°C for 7 hours. In the earlier study [92], only bcc Cr precipitates were reported. This result was thought to be inconclusive; a transformation from fcc to bcc Cr could occur upon removal of the constraint of the matrix. In the other study [93], the presence of fcc Cr precipitates with a spherical morphology was reported. The

different results reported in these two studies did not help to clarify the matter. It is not understood why [92] failed to isolate the same fcc Cr phase as [93]. In a later section of this work, possible explanations for all of the inconsistencies concerning precipitate structure in the Cu-Cr alloys that have been presented in the literature will be discussed.

2.10 Mechanical and Physical Properties of Zirconium-Copper

The Cu-Zr alloys, like the Cu-Cr alloys, exhibit good strength at high temperature while maintaining very high electrical conductivity. The most widely used of the high-conductivity high-strength alloys is Cu-0.15 wt.% Zr, produced by conventional ingot metallurgy techniques. These alloys are strengthened by cold work and to a lesser extent precipitation hardening. The decreasing solubility of Zr in Cu with decreasing temperature results in an essentially solute-free high-conductivity Cu matrix with very limited strengthening provided by Zr precipitates. This behavior is in contrast with that of the Cu-Cr alloys which exhibit strong precipitation hardening. The volume fraction of precipitates is limited by the maximum equilibrium solid solubility of the alloying element in Cu, and is much lower for Zr than Cr, as has been discussed previously. Rapid solidification processing of Cu-Zr can be used to extend the maximum solid solubility and increase the volume fraction of precipitates. In order to compare the benefits of RSP Cu-Zr to conventionally processed alloys, a brief review of the mechanical and physical properties of commercial Cu-Zr alloys is presented.

Due to the high reactivity of Zr, these alloys require some care during melting and processing. Inert or reducing atmospheres are used to prevent oxidation of the Zr at elevated temperatures. For the same reason, OFHC Cu should be used for alloying as Zr will react with any Cu_2O present to form Zr oxides.

which results in lower strengths at room and elevated temperature, and a loss in ductility.

The commercial alloys are usually hot worked in a temperature range of 900°C to 950°C following casting [94]. Protective atmospheres should also be used during this processing to avoid the formation of a Zr depletion zone near the surface of the workpiece. Hot working of these alloys results in higher strength than is possible by a simple solution and ageing treatment [44]. This effect is due to the fine grain size and strain hardening; the final hot working is done at a temperature near 750°C, resulting in precipitation and further grain refinement.

These alloys are solutionized in a temperature range of 900°C to 925°C; higher temperatures increase the solubility of Zr in Cu but result in excessive grain growth [75]. The maximum solubility at these temperatures is less than 0.15 wt.% Zr, so little benefit results from higher Zr concentration. Solution treated alloys are usually aged in a temperature range of 500°C to 550°C for 1 to 4 hours, in order to increase the electrical conductivity; 64 % IACS for the solutionized alloy, and 83 % IACS for the alloy aged at 500°C are typical values [44]. Very little precipitation strengthening occurs during the aeging treatment. The room temperature tensile strength of the solution treated alloy is ≈29 ksi, and will only increase to a value of ≈30 ksi after ageing. The ductility also remains approximately constant at about 50 % elongation. The room temperature yield strength of these alloys, however, increases from a value of 6 ksi to 13 ksi after ageing.

The Cu-Zr alloys are rarely used in the solution treated and aged condition. Cold-working is usually employed after solution treatment to work-harden the alloy, and to provide nuclei for precipitation during subsequent ageing [44,78]. Homogeneous nucleation does not occur in these low Zr concentration alloys, and

cold-work prior to ageing is necessary for increased precipitate density [78,95]. After cold-working, these alloys are usually aged in a temperature range of 375°C to 450°C to restore ductility, to increase the electrical conductivity, and to stabilize the microstructure for elevated temperature applications. The tensile strength and hardness do not diminish during the ageing process, and usually show an increase, if recrystallization is avoided. The room temperature tensile strength can approach 70 ksi for a Cu-0.15 wt.%Zr alloy, cold-reduced 85 % and aged at 400°C. The room temperature yield strength for the alloy in the same condition is ≈62 ksi, with a tensile elongation of 24 %. The optimum ageing temperatures are dependent upon the amount of prior cold-work; lower temperatures are required as the amount of cold work increases because of the greater driving force for recrystallization and increased kinetics of precipitation [78].

The high-temperature properties of Cu-Zr alloys are also very good, as most of the strength and ductility are retained at temperatures up to 450°C. It can be seen in Figure 2.18, that the tensile strength of the Cu-Zr alloy is superior to that of Cu-Cr for all temperatures up to 600°C; both alloys were cold-worked 84 % prior to ageing to peak hardness [75]. While the difference in tensile strength for the two alloys is small, the improvement in ductility at elevated temperatures for the Zr alloy is much more dramatic, Figure 2.19 [75]. The ductility of the Cu-Zr alloy remains above 72 % RA when tested in a temperature range of 23°C to 600°C, while the Cu-Cr alloy has a ductility minimum of 17 % RA at 500°C. The electrical conductivity of the Zr alloys is also better than the Cr alloys when measured in the same range of temperatures, Figure 2.21 [75]; the values for conductivity for all of these alloys are highly dependent upon the thermomechanical history of the specimens, so the data from this figure should not be universally applied to other conditions. The thermal conductivity as a function of temperature may be compared for Cu-Zr, Cu-Cr, and OFHC Cu in Figure 2.2

[12]. Both alloys exhibit very good thermal conductivity at all temperatures up to 500°C.

2.11 Precipitation in Zirconium-Copper

The commercial Cu-Zr alloys do not precipitation harden to any great extent. The primary benefit of precipitation in this alloy is to refine the grain size and to stabilize the cold-worked structure at elevated temperatures. The composition of the precipitate in the Cu-rich alloys has been a matter of some controversy, as has been discussed in section **2.6**. This phase was identified by [49,41-45] as Cu_3Zr. Other researchers have identified this phase as Cu_4Zr [46], Cu_9Zr_2 [50], or Cu_5Zr [51,52,48]. Lou and Grant [40] used electrolytic extractions to isolate the Cu-Zr precipitates in a Cu-0.18 wt.% Zr alloy. The diffraction analysis was in agreement with the calculated and observed pattern for Cu_5Zr from the results of [53], and in agreement with [54]. The Cu_5Zr composition has become the accepted stoichiometry for the precipitate in the Cu-rich alloys.

Very little information has been published on the precipitate morphology. A Widmanstätten structure of the precipitate has been reported for a Cu-0.10 wt.% Zr alloy, solution treated and aged at 500°C [44], using optical microscopy. When aged at 800°C, the same alloy showed needle shaped precipitates. TEM studies have shown that incoherent platelets form parallel to {111} matrix planes during ageing at 400°C [78,96]. The precipitates form at free dislocations, dislocation cell walls, and stacking faults [97,96,78]. The size of the precipitates is in the range of 10 nm to 30 nm, depending upon the aeging treatment. Higher precipitate densities and smaller precipitate sizes were observed in alloys cold-worked prior to ageing, as homogeneous precipitation does not occur. In the absence of cold work, precipitation is limited, resulting in a very small age hardening effect. Heavily cold worked alloys form precipitates in the dislocation

cell walls, which stabilize the deformation substructure and delay the onset of recrystallization and softening at elevated temperature [97,96,78]. Ageing at too high a temperature following cold-work results in considerable precipitate coarsening; 40 nm to 500 nm diameter precipitates are produced during recrystallization at 750°C.

Rapid solidification processing of the Cu-Zr alloys would not be expected to result in large improvements in mechanical properties over the commercial alloys if precipitation were heterogeneous. Excess solute in commercial alloys has little effect on the softening temperature [98]. The large supersaturation that is possible with RSP may, however, result in homogeneous nucleation and a better distribution of fine precipitates. These changes would dramatically alter the mechanical properties of the alloys.

2.12 Mechanical and Physical Properties of Copper-Silver Alloys

The Cu-Ag alloys exhibit good strength at moderate temperature while maintaining very high electrical conductivity. Usually only small additions of Ag are specified for the commercial binary compositions; ≈15 to 30 oz. per ton. These alloys are strengthened primarily by cold work, similar to Cu-Zr. Experimental studies on more concentrated alloys have shown that very high strengths can be developed by heavy cold work, while maintaining excellent electrical conductivity; 150 ksi tensile strength and 70 % IACS conductivity have been reported for a 5 wt.% Ag alloy [99]. Silver in solid solution depresses the electrical conductivity to a lesser extent than any other element [19,25].The decreasing solubility of Ag in Cu with decreasing temperature results in a high-conductivity Cu matrix with almost no strengthening provided by the Ag-rich precipitates [63]. This behavior is in contrast to that of the Cu-Cr alloys which exhibit strong precipitation hardening. Solution treated and aged alloys show an increase in hardness, but

the tensile strength usually decreases [100]. A primary benefit of Ag additions in Cu is the raising of the softening temperature. In this respect, Ag is inferior to Zr or Cr. The mechanical properties of the Cu-Ag alloys decrease rapidly after exposure to temperatures exceeding 300°C. The Zr and Cr alloys are relatively stable up to 500°C.

The volume fraction of precipitates in this system can be quite large because of the high solid solubility of Ag in Cu. Rapid solidification processing of Cu-Ag can be used to extend the maximum solid solubility and increase the volume fraction of precipitates. It has been shown that a continuous series of metastable solid solutions can be formed in these alloys by splat quenching [66]. In the present work, Ag was alloyed with Cu-Cr alloys in order to improve the castability during melt-spinning, and not to extend the solubility.

2.13 Properties of a Copper-Silver-Zirconium Alloy

Space Shuttle Main Engine thrust chambers are made from NARloy-Z, a Cu-3 wt.% Ag-0.5 wt.% Zr alloy developed by Rocketdyne. Very little information is available concerning the processing of this alloy during chamber fabrication. Vacuum induction melting followed by vacuum consumable electrode remelting is beneficial for reducing the amount of zirconia inclusions [1]. The cast alloy is hot worked and spun to shape in a temperature range of 680°C to 790°C, solution treated at 925°C, and aged for 4 hours at 480°C [101].

The elevated temperature tensile and yield strengths of NARloy-Z are given in Figure 2.22 [101]. It can be seen that the mechanical properties decrease gradually up to 425°C, and more rapidly at higher tempratures for the solution treated and aged alloy. The strengths at elevated temperature are intermediate between those of Cu-Zr and Cu-Cr alloys. The ductility of NARloy-Z is at least 50 % RA for temperatures up to 600°C. The thermal conductivity of this alloy is highly

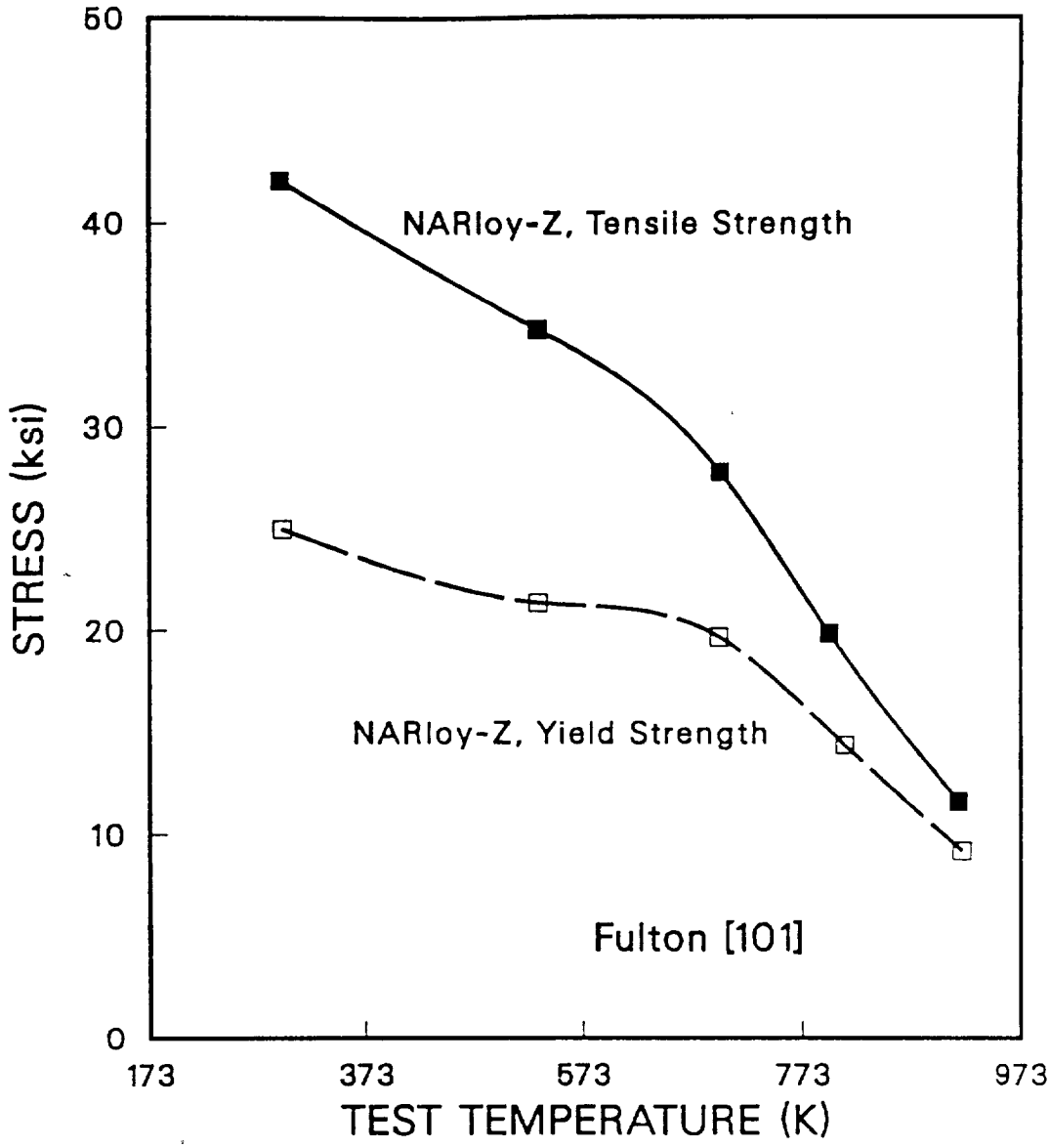

Figure 2.22. Elevated Temperature Tensile and Yield Strengths of Solution Treated and Aged NARloy–Z [101]. From the Review of [74]

dependent upon the processing conditions; aged alloys giving the highest conductivity. In Figure 2.2, it can be seen that the thermal conductivity of NARloy-Z is at least 10 % lower than Cu-Cr in the range of temperatures measured [12].

2.14 Rapid Solidification Processing

To a metallurgist, the term "quenching" means the process of rapid cooling of a solid at elevated temperature by contact with a colder media, usually a liquid or gas. The purpose of the quench is to cool the alloy at a rate high enough to retain elevated temperature phases or to cause the transformation to non-equilibrium phases. The concentration and microstructure of the desired phases can be controlled during subsequent processing at elevated or room temperatures in order to produce the optimum physical properties for the conditions of service. While alloys are most often quenched from the solid state, there are some microstructures and properties that can only be achieved by quenching from the liquid or gaseous state.

During solid state quenching, the phase boundaries should be crossed rapidly enough to suppress the formation of the equilibrium phases; the kinetics of the equilibrium reactions are usually limited by solid state diffussion, which is highly dependent upon time and temperature. The purpose of quenching from the liquid state is the same as for the solid state, except that the critical phase boundaries are the liquidus and solidus. Because of the greater atomic mobility in the liquid state, the cooling rates need to be much higher for effective liquid quenching in order to suppress the formation of the equilibrium solidification phases and structure. The most important condition to satisfy is a very rapid cooling rate during the time of the liquid to solid transformation.

The rapid quenching of liquid metals can result in many significant benefits. One of the most important of these is increased chemical and microstructural

homogeneity. Solidification processes are usually responsible for chemical segregation and phase separation; these problems are worse in large ingots where the solidification rate is slower. The long time at high temperature also results in rapid grain growth and second phase coarsening. Rapid solidification processing, however, minimizes segregation and results in much finer structures. These features improve the corrosion resistance, hot and cold plasticity, and mechanical strength of RSP alloys.

In addition to the benefits described above which are common to all RSP alloy systems, certain unique results may be obtained by application of RSP to select alloys. In systems where a very deep eutectic is present, a very rapid quench can produce an amorphous alloy, with novel physical properties. An amorphous alloy allows for the ultimate in control over the resulting microstructure during subsequent crystallization and thermomechanical processing. The absence of grains and grain boundaries in the as-cast alloys results in excellent corrossion resistance if the amorphous state is retained during processing and service. In addition, some amorphous alloys have magnetic properties which make them highly desirable and cost effective for electronic applications. Other uses for amorphous metals will become evident as the number of alloy systems increases in the future.

In crystalline alloys, RSP may also result in the attainment of higher degrees of supersaturation by extension of the solid solubility far beyond equilibrium values. Alloys that fit the rules of Hume-Rothery, respond most favorably to the techniques of RSP, and can produce a complete series of metastable solid solutions for all compositions. The systems of Cu-Ag and Ag-Pt are two such examples developed by some of the pioneers in this field [66,102]. In other systems, rapid liquid quenching can cause the formation of previously unknown metastable phases. This can only occur when the nucleation and growth kinetics of the metastable phase are faster than other competing phases, and the free energy of

the metastable phase is lower than the liquid. The metastable phases can be expected to have different physical properties than those of the equilibrium phases, and these differences may be exploited by engineering development.

In this work, RSP is used to extend the terminal solid solubility of Zr and Cr in Cu. The solute trapping during solidification can result in a high degree of supersaturation and fine scale dispersion of any precipitated phases. Relatively stable phases with minimal solid solubility in the matrix can be precipitated from the solid state by elevated temperature ageing. These precipitates tend to be uniformly distributed, and finely dispersed because of the large driving force for homogeneous nucleation in the supersaturated solid solution. The low solubility and uniform distribution results in a resistance to precipitate coarsening at high temperatures; thus the precipitates can effectively pin grain boundaries and dislocations so that the RSP alloy resists grain growth and maintains good strength. As an example, this approach has been used for high temperature Al alloys strengthened by thermally stable intermetallic phases.

There have been many methods employed to produce rapidly solidified alloys, starting from both the liquid and vapor state. The splat techniques include gun quenching and piston and anvil quenching. These two methods yield very high cooling rates, but can only produce milligrams of RSP alloy at a time. At the other extreme are the various gas atomization methods that can be continuously operated, the cooling rates, however, are also in the slow range of RSP. One notable exception is the centrifugal helium gas atomization process, with a cooling rate that is at least an order of magnitude faster than the other atomization methods. The powders produced during gas atomization can be consolidated into useful products by a number of elevated temperature/pressure processes that will not be discussed here. Plasma spraying can also be used as an alternative to more conventional gas atomization techniques to produce RSP powder for

consolidation. Large pieces and unusual geometries can be formed from RSP alloys by plasma spraying directly onto a mandrel. The self quenching techniques include laser and electron beam glazing, which are limited to small volumes of metal near the surface of the workpiece. These methods are not used to produce bulk RSP alloys, but can be very effective in modifying the surface properties of a product near the final net shape. Ribbons, wires, and flakes can be produced in a batch or continuous process by one of the variations of melt spinning. These include the single roller techniques of free jet and planar flow chill block melt spinning, melt overflow, melt extraction, and melt drag. In an effort to achieve higher cooling rates, the double roller technique of melt spinning was developed to extract heat from two sides of the solidifying ribbon; the method is not without serious technological problems. The techniques and parameters of chill block melt spinning will be discussed in greater detail in the following chapter.

CHAPTER III

EXPERIMENTAL METHODS

3.1 Introduction

When the present work was first undertaken, there was very little information available on RSP Cu alloys. There was even less information available that was specific to the production or properties of melt-spun Cu alloys. Because of the lack of available scientific and engineering data, this research was conducted in two stages. The first stage consisted of an initial screening of candidate alloys where it was determined which specific alloys could be melt spun. In addition, the alloys that could be spun successfully were then evaluated for technological promise. Only the best of these alloys were selected for the second stage of the research where a detailed scientific investigation and materials characterization was performed.

3.2 Alloy Screening

For the first stage of this work, 26 different Cu alloys were selected as candidates for melt-spinning, Table 3.1. These consisted of 7 binary alloys of Cu-Cr, 10 binary alloys of Cu-Zr, 4 ternary alloys of Cu-Cr-Zr, 4 ternary alloys of Cu-Cr-Ag, and OFHC Cu. Cr and Zr were chosen as alloying elements because of their limited solid solubility in Cu. Ag, on the other hand, has higher solubility in Cu but does not have a large deleterious effect on conductivity. This behavior for Ag is an anomaly for alloying elements in Cu. During the initial screening, alloy compositions were evaluated using three basic criteria. The primary and most important one was ribbon castability. This includes both the ease with which ribbon is produced and the reproducibility and uniformity of the product. The uniformity of shape of the product is important because the effective cooling rate

Table 3.1. Ribbon Specimen Composition

Nominal Composition (at.%)	Number of Trial Runs
OFHC Cu	2
Cu-0.8 Cr	10
Cu-1.2 Cr	3
Cu-1.8 Cr	2
Cu-2.5 Cr	1
Cu-3.0 Cr	10
Cu-5.0 Cr	43
Cu-10.0 Cr	1
Cu-1.0 Zr	3
Cu-1.3 Zr	1
Cu-2.0 Zr	1
Cu-2.5 Zr	1
Cu-3.0 Zr	2
Cu-3.5 Zr	1
Cu-4.0 Zr	1
Cu-5.0 Zr	5
Cu-9.0 Zr	1
Cu-10.0 Zr	1
Cu-1.3 Cr-1.3 Zr	1
Cu-2.0 Cr-1.0 Zr	1
Cu-2.5 Cr-2.5 Zr	1
Cu-5.0 Cr-5.0 Zr	1
Cu-5.0 Cr-1.0 Ag	1
Cu-5.0 Cr-2.0 Ag	15
Cu-5.0 Cr-3.0 Ag	3
Cu-3.0 Cr-2.8 Ag	1

during solidification is a strong function of the ribbon thickness and flatness of the wheel-side of the ribbon surface. A total of 115 melt-spin runs were made in order to produce a sufficient quantity of ribbon for this study. It was found that many of the candidate alloys could not be successfully spun into ribbon and the compositions were subsequently modified. Alloys with poor castability resulted in excessive welding to the wheel and splatter production. Initial melt-spin runs were made with dilute alloys of Cu-Cr and Cu-Zr in order to make baseline comparisons with conventional ingot cast commercial Cu alloys. Unfortunately, it was found that dilute alloys in general are not good for ribbon castability. The concentration of Cr and Zr additions was increased for later runs and the castability of the alloys improved greatly. Ag additions were made for much the same reason as they had a dramatic effect on improving the castability of the Cu-Cr alloys.

The second criteria used to evaluate candidate alloys during the initial screening was microstructural homogeneity. One of the main advantages for any type of RSP alloy production is chemical and microstructural homogeneity because this results in uniformity of mechanical properties throughout the product. In this work, it was found that there is a large variation in degree of homogeneity among the different alloy compositions despite having been melt-spun at high solidification rates. The Cu-Zr alloys were the worst in this regard, as some compositions contained four distinct microstructures over the thickness of the ribbon. This demonstrated that the microstructural evolution during solidification is so dependent upon the effective cooling rate that it could not be adequately controlled in these alloys. In contast, the Cu-Cr and Cu-Cr-Ag alloys had very uniform microstructures throughout the ribbon thickness and length. In addition, all of these alloys developed the same fine-grained columnar microstructure despite their compositional variations.

The third criteria used to evaluate candidate alloys was ductility as determined by bend tests. These tests consisted of bending the ribbon 180° until fracture occurred. The Cu-Zr showed the least ductility of any of the alloys produced. Some of them fractured after a single 180° bend test. The Cu-Cr and Cu-Cr-Ag alloys in contrast, had excellent ductility and could withstand repeated bending without fracture. Since the mode of failure in combustion chamber liners is by cracking under large plastic strains, it was desirable to select candidate alloys which could endure the large strains of these severe bend tests.

From the results of the initial screening, the 26 Cu alloys were pared down to 5. These consisted of two binary alloys, Cu-5 at.% Zr and Cu-5 at.% Cr, and three ternary alloys, Cu-3 at.% Cr-2 at.% Ag, Cu-5 at.% Cr-1 at.% Ag and Cu-5 at.% Cr-2 at.% Ag. While the Cu-Zr alloy did not fare well during the initial screening, it was included in the group for further testing for comparison with the other alloys.

3.3 Charge Preparation

Alloys were prepared for melt-spinning by vacuum induction melting the charges in high purity alumina crucibles. Alumina crucibles were chosen to avoid contamination of the melt by reaction products of the Cr or Zr. Both Cr and Zr are strong oxide formers and tend to remove oxygen from less stable oxides. The melting was carried out using direct coupled radio frequency heating to provide good stirring of the melt and to insure chemical homogeneity. Initial attempts to alloy in the melt-spin rig were not successful due to the power limitations. Only 2.5 kW of power was available for induction heating and this was inadequate to dissolve the alloying elements in Cu. It was found that Cr does not readily dissolve in Cu until the temperature of the melt is raised $\approx$200°C above the liquidus. This is most likely due to the presence of tenacious oxide films on the Cr. It is for this

reason that prealloys were prepared in a vacuum induction furnace with a 30 kW power rating.

OFHC Cu was used as the source of Cu for all compositions. It is important for these alloys to have as low an oxygen content as possible to reduce the susceptibility to hydrogen embrittlement. Hydrogen can easily diffuse through Cu and react with Cu oxides to form water. At elevated temperatures large voids are created by the expansion of internal steam pockets. The oxygen content for the alloys in this study were kept below 50 ppm for these reasons. Cr, Zr, and Ag with 99.9 % purity were used for alloying additions. The high purity of the alloying additions was important because the presence of tramp elements with high solubility in Cu would result in a large decrease in conductivity.

The prealloys were vacuum induction melted and homogenized for ≈20 minutes at 1535°C. In some cases the alloys were poured into metal molds to solidify. In others, the alloys were allowed to solidify in the alumina crucibles. After solidification, the surfaces of the round bar ingots were machined to remove any oxides present. Sections were then cut from the bars for melt-spinning. These charges for spinning were roughly 10 mm in diameter, and 25 mm in length, weighing about 25 grams.

3.4 Melt-Spinning

Rapidly solidified alloy ribbons were produced by chill block melt-spinning (CBMS). The apparatus shown in Figure 3.1, consists of an induction coil, a crucible with a narrow orifice, a pressurization cap, and a solid metal wheel mounted on a variable speed motor. The induction coil is used to melt the charge and to control the amount of superheat. The power input to the coil is manually adjusted to maintain the desired temperature. The crucible is used to contain the melt before ejection through the orifice. The pressurization cap is used to control

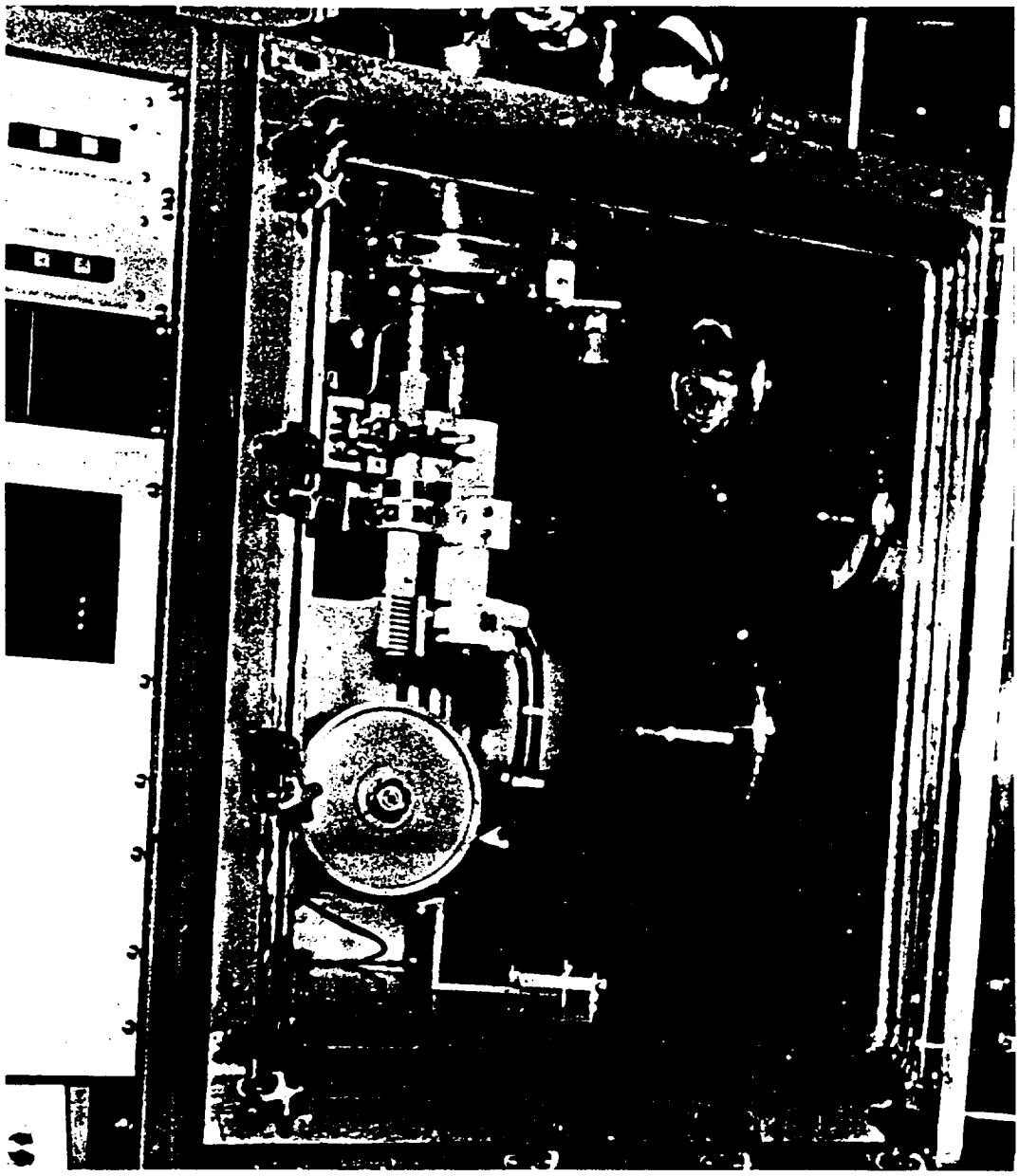

Figure 3.1. NASA Lewis Chill Block Melt-Spinning Rig Used to Produce Rapidly Solidified Ribbon

the melt delivery rate through the nozzle by applying a preset gauge pressure of inert gas to the crucible during ejection. The molten stream impinges on the rotating wheel and forms a small puddle on the surface. The heat of solidification is absorbed by the wheel and a thin ribbon is spun out from the melt puddle. The ribbon separates from the wheel at a finite distance from the melt puddle, and continues to travel at the circumferential wheel speed until slowed by collision with the chamber walls.

In this study, all of the ribbon was produced by the *freejet* mode of CBMS. This method uses an unconstrained melt stream between the crucible and wheel surface. Any perturbations in the melt stream will affect the stability of the melt puddle and can disturb the production of ribbon. Attempts were made to produce wide ribbon by use of the *planarflow* mode of CBMS. In this method, the crucible is positioned very close to the wheel so that the flat bottom of the crucible can constrain the top surface of the puddle. The puddle geometry is thus stabilized by surface tension effects, and ribbon as wide as the crucible slotted nozzle can be produced. Unfortunately, all *planarflow* runs were unsuccessful due to excessive welding of alloy to the wheel. The welded material would build up quickly on the wheel and after a few rotations destroy the crucible upon impact. After several catastrophic failures, the *planarflow* mode of CBMS was abandoned. A fixed gap of 18 mm was used for all runs of the *freejet* mode of CBMS. During heating, the crucible was positioned about 50 mm from the wheel surface to minimize heating of the wheel by inductively coupling to the coil. A mechanical traversing mechanism was used to lower the crucible to the correct gap position just prior to pressurizing and ejecting the melt.

Radio frequency induction heating was used to heat the charge via direct coupling or by use of a graphite susceptor. Direct coupling has the advantage of providing a good stirring action to insure chemical homogeneity in the melt,

while a susceptor minimizes the thermal gradients in the crucible and melt and requires less power due to more efficient coupling. The 2.5 kW of power available was barely adequate to melt the charges by direct coupling and the large thermal gradients frequently resulted in thermal stress cracking and catastrophic failure of the crucibles. These problems were minimized by improving the thermal insulation surrounding the crucible to lower the radiation losses and reduce thermal gradients.

High density alumina crucibles were selected for the majority of CBMS runs. Alumina is reasonably inert to Cu, Cr, Zr, and Ag, has good temperature resistance, low thermal conductivity, and low gas permeability. The major disadvantage is its susceptibility to thermal stress cracking. In an effort to find alternative materials for crucibles with more resistance to thermal stress cracking, some CBMS runs were made with fused silica crucibles. Fused silica has excellent thermal shock resistance due to its low coefficient of thermal expansion. In addition, it has reasonable temperature resistance for Cu alloys, low thermal conductivity, and low gas permeability. Although fused silica is not as stable an oxide as alumina, this proved to be no problem during the relatively short time the melt was in contact with the crucible. Chemical analysis of ribbons indicated that neither type of crucible was forming reaction products with the melt.

The crucible nozzles were ultrasonically drilled to provide a circular, sharp edged hole, 1.0 mm in diameter. Imperfections in the nozzle can upset the stability of the molten stream, so it is important to have a precisely drilled, uniform hole. The diameter of the hole has a large control over the melt delivery rate to the puddle. In addition, the hole diameter determines the minimum ribbon width. It was desired to produce wide ribbons for materials characterization, but the upper limit for nozzle diameter is determined by the balance between melt hydrostatic pressure and the surface tension of the melt in the nozzle. Larger nozzles resulted

in the melt dribbling out of the nozzle prior to pressurization of the crucible. A wide ribbon could also be produced by use of a slotted crucible. The *free jet* stream from a slotted orifice however, is unstable and results in width and thickness variations along the ribbon length.

The charge temperature was measured by use of a two-color infrared radiation pyrometer focused down the crucible bore through the pressurization cap and quartz sight glass. This instrument is insensitive to radiation absorbtion by smoke or lenses which will cause inaccurate temperature indications in single-color pyrometers. The charge temperature was slowly increased in order to minimize the thermal stresses on the crucible. The melt temperature was reached in ≈30 minutes. The ribbons were cast at a superheat of 30-50°C above the liquidus temperature of the binary alloys. The ternary alloys were cast at ≈1230°C. This temperature was determined empirically as ternary phase diagrams were not available for these alloys. It was found that the best Cu alloy ribbons were produced when the amount of superheat was minimized. Larger superheat resulted in the ribbon leaving the wheel surface while only partly solidified. These ribbons would then weld to each other upon collision, producing irregular multiple layers. These ribbon pile-ups also were deleterious to the rapidly solidified microstructure because of the annealing effect of one layer of hot ribbon on the next. For these reasons, only single layer ribbons were selected for materials characterization in this study.

Melt-spun ribbons were cast under vacuum or in an inert gas atmosphere to prevent oxidation of the alloys. The vacuum system was designed to prevent any backstreaming of oil into the melt-spin chamber. This was accomplished by the use of a turbo pump, a cryogenic pump, and a mechanical roughing pump controlled by a logic sequence programmed into a computer. An oil free environment promotes good melt wetting of the wheel surface and contributes to the

success of CBMS. The chamber was pumped down to less than 5×10^{-5} torr prior to charge heating for the vacuum runs or backfilling with helium (He) or argon (Ar) for inert gas runs. It was found that the chamber atmosphere has a large influence over the cooling rate and the surface geometry of the ribbons. Alloys cast in vacuum had very regular, smooth edges, with flat wheel side ribbon surfaces which replicate the minute surface details of the wheel. In contrast, alloys cast in an inert gas atmosphere had rough, saw-tooth edges and irregular, large pits in the wheel side ribbon surfaces. These effects are probably due to the entrapment of gas between the ribbon and wheel surface. Because of this effect, ribbons cast in inert gas have poorer wheel contact than those cast in vacuum, and as a result undergo a slower solidification rate. Once the ribbon leaves the wheel surface, however, the situation is reversed. In vacuum, the solid state cooling rate of the ribbon is limited by the rate at which heat can be removed by radiation. In the presence of a gas atmosphere, the solid state cooling rate is much larger because of the additional heat removed by conduction and convection. In this regard, He is a much more effective quench gas than Ar, and both gases are more effective than a vacuum. The amount of heat removed from the ribbons after leaving the wheel surface is not insignificant. Ribbons cast in vacuum could be observed emitting visible radiation for a few seconds after leaving the wheel. Since it was not possible to have both high solidification rates and high solid state cooling rates in the same ribbon, it was decided that high solidification rates were more desirable. Thus, all ribbon for this study was cast in vacuum.

AISI 4340 steel was selected as the most practical material for the CBMS wheel. In general, there is a preferred wheel composition for each specific melt-spin alloy. High conductivity Cu wheels are frequently used for many alloy systems because of their ability to extract heat from the melt puddle. In addition, wheel compositions are selected for good melt puddle wetting. Unfortunately,

Cu wheels are incompatible with Cu melt-spin alloys when cast in vacuum. The wettability is so good that ribbon is not produced because of welding of the alloy to the wheel. When Cu wheels were used in inert gas atmospheres, product welding was no longer a problem. With this combination however, only short ribbon segments were produced. These segments were too small and irregular to be used for mechanical testing or other methods of evaluation. Since continuous, uniform ribbon was necessary for material characterization, several wheel compositions were tested to find the most compatible material for these melt-spun alloys. AISI 4340 steel was selected as the wheel material for all ribbon production in this study. It was the best material tested, despite having only a modest thermal conductivity. Wheel surfaces were prepared for melt spinning by sanding with 600 grit SiC paper and cleaned with alcohol to remove oil and residue. Several different wheel diameters were tried in an effort to produce better quality ribbon. For a fixed wheel circumferential velocity, larger diameter wheels should be able to dissipate the heat from the melt puddle more effectively than smaller wheels due to the longer melt track length. Most of the ribbon for this study was produced using a 180 mm diameter solid heat sink wheel rotating at 20 m/s circumferential velocity. Higher solidification rates were achieved by increasing the wheel velocity up to 40 m/s, but at these higher speeds the product was not uniform or continuous.

The production of melt-spun ribbons is complicated by the interaction of many of the process variables. As an example, the ribbon thickness is inversely related to the rate of solidification, and is the most important parameter to control. The ribbon thickness is a complex function of the melt delivery rate to the puddle, the wetting of the wheel by the melt, and the wheel circumferential velocity. The melt delivery rate is determined by the size of the orifice in the crucible nozzle, the ejection gas pressure, and the viscosity of the melt. The viscosity of

the melt is a function of alloy composition and temperature. The wetting of the wheel by the melt is also a function of alloy composition and temperature, and in addition is affected by wheel composition. The optimum parameters could only be determined by iterative testing.

3.5 X-ray Diffraction

A Phillips model XRD computer automated diffractometer was used to measure 2θ diffractograms of the Cu alloy melt-spun ribbons. The source of radiation was Cu-Kα. The ribbons were mounted for diffraction studies on a glass slide using double sided tape. Since the x-ray beam does not penetrate deeply into the ribbon surface, diffractograms could be made for both the wheel side and free surface of the ribbon to compare the relative solidification rates. Care was taken to insure that all ribbons on a slide were oriented correctly for the particular type of diffractogram desired. The diffractograms for each alloy were used to precisely determine the lattice parameters for the fcc Cu phase, and also to detect the presence of other phases. The precise lattice parameters were determined by using a linear regression analysis of the lattice parameters as a function of $\cos^2\theta$. The error in a_o is minimized as $\cos^2\theta \Longrightarrow 0$. By use of this technique, the lattice parameters were determined within $\pm.001$ Å. X-ray diffraction is not as sensitive as transmission electron microscopy for determining the presence of second phases within the Cu matrix. The limit of detectability is approximately 3% by volume for second phases, so the absence of second phase diffraction peaks does not prove the alloy is single phase.

3.6 Heat Treatment

Melt-Spun ribbons were heat treated in a horizontal tube furnace. The furnace was designed so that flowing Ar gas was used to prevent oxidation of

the specimens. Unfortunately, Ar gas contains enough residual oxygen that the thin ribbons become oxidized. The extent of this reaction was evaluated by the color of the annealed ribbons. Long times at high temperatures resulted in dark purple ribbons instead of bright copper. In order to avoid the possibility of through-oxidation of the thin ribbons, and the subsequent confusion of experimental results, tantalum sheet getters were wrapped tightly around the ribbons before insertion in the furnace. The tantalum scavenged the oxygen before it had a chance to react with the Cu alloys and this produced much brighter ribbon. The hot zone of this furnace was only about 75 mm in length, so this restricted the annealing of long lengths of ribbon without folding. The temperature in the hot zone was maintained within $\pm 2^{\circ}$C for each set point.

Aging treatments were initiated by loading the tantalum wrapped specimens in the tube furnace at room temperature. The quartz tube was then purged with flowing Ar gas for 1 hour before heating was started. The furnace would reach the desired set point within 1 hour, the exact time being dependent upon the actual set point. The annealing times were recorded from the amount of time the furnace temperature was at the set point. The specimens were quenched after annealing by dropping them in a bath of cold water. The inability to closely monitor the aging time because of the long heat up time of this furnace lead to the construction of a high vacuum isothermal furnace. This apparatus will be discussed in the following section.

3.7 Resistivity Measurements

Since the purpose of this research was to develop alloys with excellent thermal conductivity, a means of monitoring this property had to be developed. Thermal conductivity could not be directly measured due to the ribbon geometry, but the electrical resistance was much more readily measurable. Also, it is

known that electrical and thermal conductivity behave in parallel, so that any improvements in electrical conductivity due to alloy selection or thermomechanical processing will result in improvements in thermal conductivity. In addition to measuring electrical resistance to monitor thermal conductivity, the electrical resistance changes of ribbons were measured during elevated temperature aging in order to follow the nucleation and growth of precipitates.

An isothermal horizontal tube vacuum furnace was constructed specifically to overcome the problems of aging thin ribbons in conventional furnaces. In addition, the design incorporated the ability to make in-situ resistance measurements during annealing. The furnace itself consisted of a movable, horizontal alumina tube with a single zone resistance heater. A sodium heat pipe inside the alumina tube was able to maintain a large isothermal zone ($\pm 0.5°C$ over a 250 mm length) in order to age larger specimens. A Micristar controller was used to program the furnace temperature. The ribbon specimens were loaded into a stationary horizontal quartz tube that was pumped down to $\leq 10^{-5}$ torr. The vacuum system consisted of a mechanical roughing pump, a diffusion pump, and a liquid nitrogen cold trap. The specimens were quickly heated to the desired annealing temperature by rolling the already hot isothermal furnace over the continuously pumped high vacuum quartz tube. The specimen temperatures were monitored with a fast response thermocouple inside the quartz tube adjacent to the ribbon. It took approximately 6 minutes for the specimens to reach 95 % of the desired annealing temperature. Conex fittings were used to seal the thermocouple wire and resistance probe wires for the high vacuum feed throughs.

Resistance measurements were made by using the 4-point probe method to eliminate the effect of lead resistance. Measurements were averaged using normal and reversed polarity to eliminate errors due to thermally generated EMF. The Ag plated Cu lead wires were spot welded to the ribbon specimens for good

contact at elevated temperatures. The outer two current carrying lead wires were 7.0 cm apart, while the inner leads were centered 5.0 cm apart between the outer leads. Ribbon specimens were selected for aging based on their as-cast resistance. Thirty-three specimens were prepared from a single melt-spin run of Cu-5.0 at.% Cr and their resistance was measured at room temperature. The resistance of the specimens ranged from 0.0111 Ω to 0.0491 Ω. Eight specimens that had resistance greater than 0.0440 Ω were selected for the aging experiments. The ribbons with the largest values of resistance were indicative of a good quench during rapid solidification and the largest degree of supersaturation. Ribbons with smaller values of resistance had already begun to precipitate solute during the solid state cooling following solidification. The resistance of the specimens was measured by use of a Fluke Digital Multimeter. A fast action polarity switch was installed to measure the resistance quickly in both directions. The resistance of the specimens was measured during isothermal aging at 426°C, 450°C, 475°C, 504°C, and 522°C. In order to compare the data measured at these different temperatures, the resistance values were normalized to room temperature by subtraction of the thermal contribution to resistance for each aging temperature. The thermal contribution to resistance was measured during cooling from the aging temperature to room temperature. A linear extrapolation of the thermal contribution was used also to determine the normalized room temperature resistance of the specimens during the 6 minutes of heating from room temperature to the isothermal aging temperature.

3.8 Tensile Testing

The mechanical properties of the Cu alloy ribbons were evaluated by uniaxial tensile tests of both as-cast and heat treated specimens. Initially, microhardness tests were used to measure the effective strengthening due to precipitation in

the various alloys, but these tests were unreliable because of the light loads necessary for the small specimen geometry. It was also difficult to correlate microhardness measurements with bulk mechanical properties of conventional engineering materials.

Flat sheet tensile specimens were prepared from ribbon by use of a block template. The ribbons were clamped in the template and sanded along one edge using 400 grit SiC paper. The procedure was repeated for the other edge of the ribbon. The reduced section of each flat tensile specimen was 2 cm long and nominally 0.200 cm wide. The actual dimensions for each specimen were measured prior to testing by use of a point micrometer. The specimen thickness was determined by taking the average of 10 measurements per ribbon in order to minimize large random errors. The use of the average thickness in stress calculations results in a reported tensile strength that should always err on the low side of the actual tensile strength.

An Instron floor model tensile testing machine was modified for elevated temperature ribbon tests by installation of an atmosphere chamber with temperature controlled resistance heating. The chamber was pumped down to $\leq 10^{-5}$ torr during the test by use of a mechanical roughing pump and diffusion pump. The specimens were heated for elevated temperature testing by radiation from a cylinder of tungsten mesh. The specimen temperature was monitored by a thermocouple adjacent to the ribbon, and controlled by adjusting the current to the tungsten resistance heaters. Tensile tests were performed at 23°C, 100°C, 200°C, 300°C, 400°C, 500°C, and 600°C, and these temperatureres were maintained to ±2°C. Inconel flat tensile grips were used for all tests because of their mechanical stability at these elevated temperatures. A 20 pound load cell was used for increased sensitivity of measurement of the small loads. The nominal strain rate ranged from 1×10^{-4}/s to 2×10^{-4}/s.

3.9 Electron Microscopy

Thin discs were punched directly from as-cast and aged ribbons in preparation for use in the transmission electron microscope (TEM). The 3 mm discs were thinned down electrolytically using a dual jet Struers Tenupol-2 electropolisher. Many different electrolytes were tried in an effort to obtain the optimum polishing conditions without etching effects. A solution of 33% nitric acid and methanol maintained at a bath temperature of $\approx$ -40°C was found to be an effective electrolyte. Another good electrolyte is a solution of 25% nitric acid, 25% butyl cellosolve, and 50% methanol maintained at $\approx$ 5°C. The voltage during electropolishing for both electrolytes was 9.5 Volts, while the current was about 75 mA. The perforated thin foils were rinsed in methanol and dried on absorbent paper.

The foils were examined in a Phillips 400 transmission electron microscope operating at an accelerating voltage of 120 kV. The microstructures were observed using both bright and dark field imaging. Electron diffraction was used to determine the presence of bcc Cr in the fcc Cu matrix.

3.10 Optical Microscopy

Ribbons were prepared for metallography using many of the standard techniques. Ribbons were folded back on themselves and held in a spring clip for mounting in lucite. The multiple layers help to prevent edge rounding during polishing. Fine grinding was carried out using SiC paper progressing from 320 grit, 400 grit, 600 grit, 10 μm, to 5 μm. Finally the specimens were vibration polished using 0.5 μm chrome oxide in a water base. The avoidance of orbital type polishing with diamond or alumina media results in better edge retention for these very thin specimens.

Most of the polished RSP and ingot-cast Cu alloys were etched in a solution of 2 grams of $K_2Cr_2O_7$, 100 ml of H_2O, 8 ml of H_2SO_4, and 4 drops of HCl prior to microscopic examination. The ternary Cu-Cr-Ag alloys were etched in a solution of 10 ml of 30% H_2O_2, 20 ml of H_2O, and 20 ml of NH_4OH prior to microscopic examination.

CHAPTER IV

RESULTS AND DISCUSSION

4.1 Conventional Solidification Structures

In order to provide a baseline for comparison with RSP, ingot cast alloys of NASA-Z and Cu-Cr were sectioned and prepared for metallographic examination. The microstructure of a forged billet of NASA-Z can be observed in Figure 4.1. This particular alloy has the identical composition to NARloy-Z, Cu-3 wt.% Ag-0.5 wt.% Zr, but was produced for NASA by an outside vendor other than Rocketdyne; the heat treatments were designed to duplicate those of NARloy-Z during the fabrication of Space Shuttle Main Engine thrust chambers. The mechanical and physical properties, and microstructures of the two alloys would be expected to be similar. The processing conditions were discussed in some detail in section **2.13**. In Figure 4.1, it can be seen that the microstructure consists of equiaxed grains with an average diameter of $\approx$70 μm. An extremely coarse dispersion of a dark second phase can be observed within the grains of the Cu-rich matrix. The distribution of precipitate size is bimodal with particle diameters of $\approx$0.2 μm and $\approx$4 μm. Since the maximum solid solubility of Zr in Cu is less than 0.24 wt.% [40–47] at the eutectic temperature of 980°C, it would be expected that Cu_5Zr particles would form during the relatively slow eutectic solidification of ingot casting. These particles will spherodize and coarsen when the alloy is solution treated at 925°C. The ageing treatment at 480°C produces the smaller $\approx$0.2 μm precipitates from the Zr remaining in solution after the quench from 925°C.

The size and distribution of the precipitates that are produced during the solidification and heat treatment of this alloy are much too coarse to be effective in improving the mechanical properties of the low-strength Cu matrix;

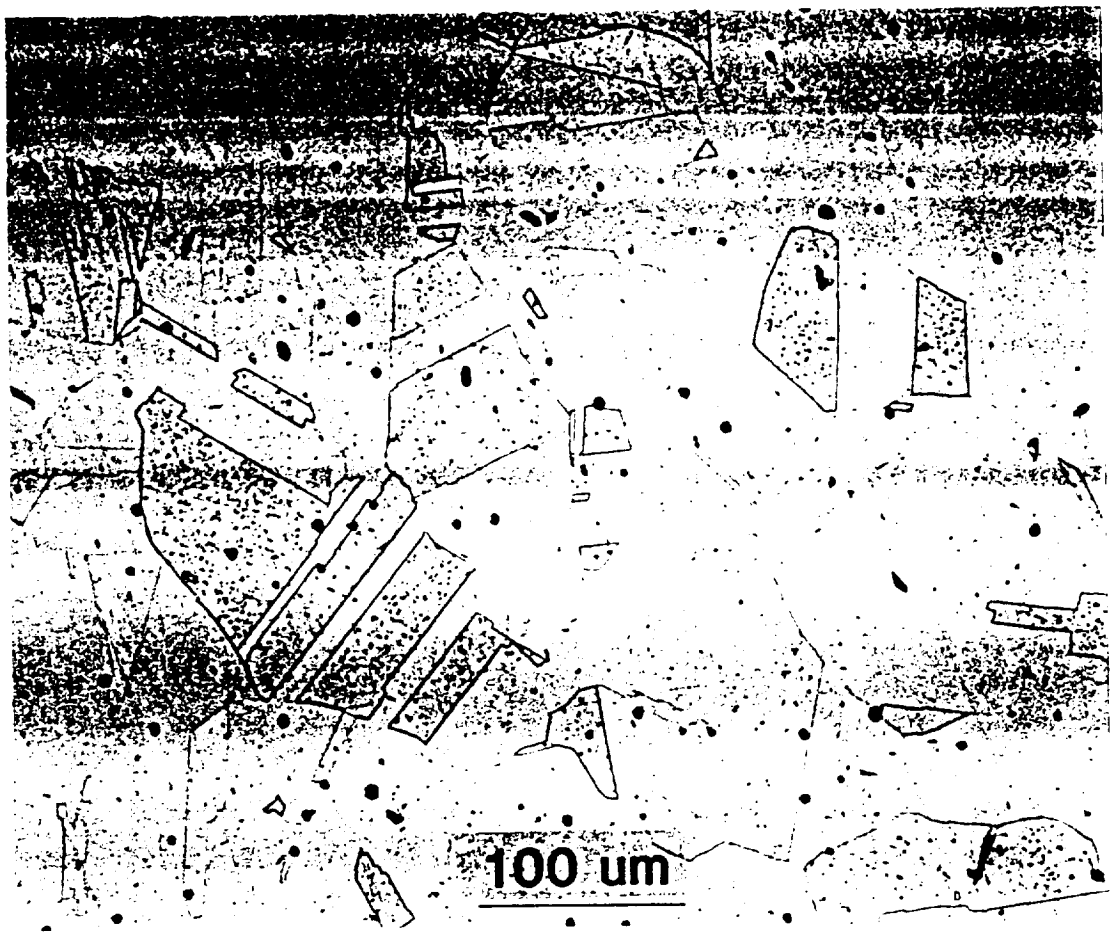

Figure 4.1. Optical Micrograph of a Forged Billet of NASA-Z, a Cu-3 wt.% Ag-0.5 wt.% Zr Alloy Produced by Conventional Ingot-Casting

the room temperature yield strength and ultimate tensile strength of NARloy-Z are approximately 25 ksi and 42 ksi, respectively [101]. The only beneficial effect that the large Cu_5Zr particles might have, is to pin grain boundaries and inhibit excessive grain growth during solution treatment. The resulting grain refinement would yield a small improvement in the strength of the alloy. From the microstructure of Figure 4.1, it can be concluded that further Zr additions will not be beneficial in improving the mechanical properties of this ingot cast alloy; in fact the converse may be true. Lowering the Zr concentration to $\approx$0.2 wt.% will reduce the number of large and incoherent Cu_5Zr particles, and should increase the ductility of the alloy by elimination of potential crack initiation sites at these hard intermetallic inclusions.

The concentration of 3 wt.% Ag in NARloy-Z is much less than the maximum solid solubility of 8 wt.% Ag in Cu at the eutectic temperature of 779°C in the binary Cu-Ag system [55]. Because of the nonavailability of a ternary Cu-Ag-Zr phase diagram, the solubility of Ag in NARloy-Z can only be approximated from the binary Cu-Ag phase diagram. The Ag is most likely completely solutionized at 925°C, and retained in solid solution following the quench. During the ageing treatment at 480°C, approximately half of the Ag will precipitate and half will remain in solution in the Cu-rich phase. The Ag precipitates in this system do not significantly increase the mechanical strength of the alloy [63], thus higher concentrations of Ag are probably not beneficial. In addition to the precipitates already described, it is quite possible that quenched and aged NARloy-Z contains a variety of Zr-Ag and Cu-Zr-Ag intermetallics. Little information is available in the literature on precipitation in this alloy, and no attempt was made in this study to analyze the compositions of the phases present.

As is true for NARloy-Z, commercial Cu-Cr alloys also suffer from the relatively slow eutectic solidification of conventional ingot casting. The microstructure of a wrought, solutionized and aged Cu-1 wt.% Cr alloy can be observed in Figure 4.2. It can be seen that the ≈80 μm grain size is similar to that of the wrought NARloy-Z. The commercial Cu-Cr alloys contain Cr in the range of 0.5 to 1.4 at.%, and the Cr in excess of the maximum equilibrium solid solubility of 0.89 at.% will solidify during the eutectic reaction. Stringers of these coarse Cr particles can be observed in Figure 4.2, aligned in the direction of rolling. These large particles are ineffective for precipitation strengthening, but as in the case for Cu-Ag-Zr, may inhibit excessive grain growth during solution treatment of the alloy. The Cr precipitates that form during ageing of the alloy to peak strength are much too small to be observed using optical microscopy. The coherent, ≈5 nm precipitates can only be observed using TEM.

Increasing the concentration of Cr in the ingot cast alloys will not yield a greater volume fraction of the small, coherent precipitates that are responsible for the strong precipitation hardening effect. The excess Cr will solidify during the pro-eutectic and/or eutectic reaction, and in either case will result in a very coarse microstructure. In Figure 4.3, the microstructure of a vacuum induction melted and ingot cast Cu-5 at.% Cr alloy can be observed. During the slow solidification of the hypereutectic alloy, the pro-eutectic Cr solidifies as dendrites, and as the temperature of the melt decreases, the remaining Cr solidifies as a pinched-rod eutectic. Because of the long time at high temperature during the slow solidification of ingot casting, the primary and eutectic Cr particles become very coarse.

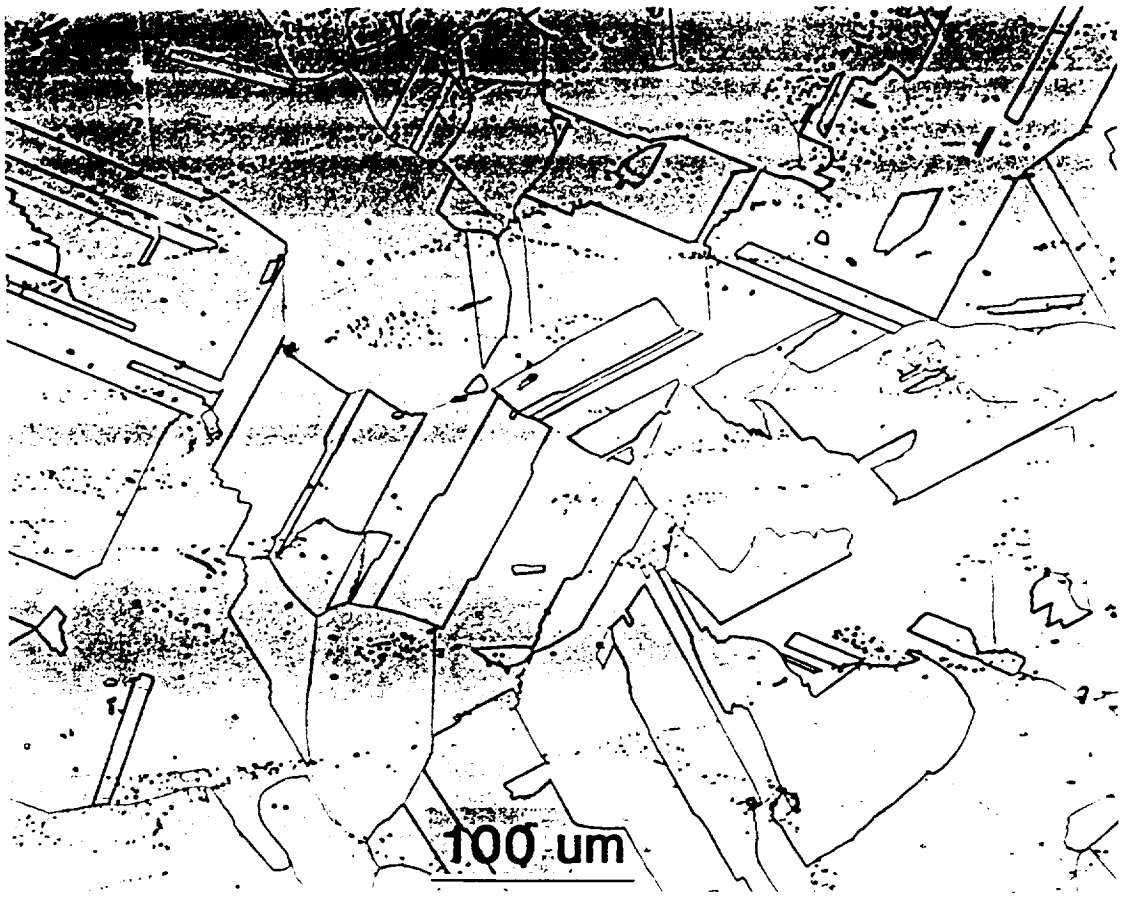

Figure 4.2. Optical Micrograph of Commercial Cu-1 wt.% Cr Alloy, Solution Treated, Quenched and Aged at 773 K for Two Hours

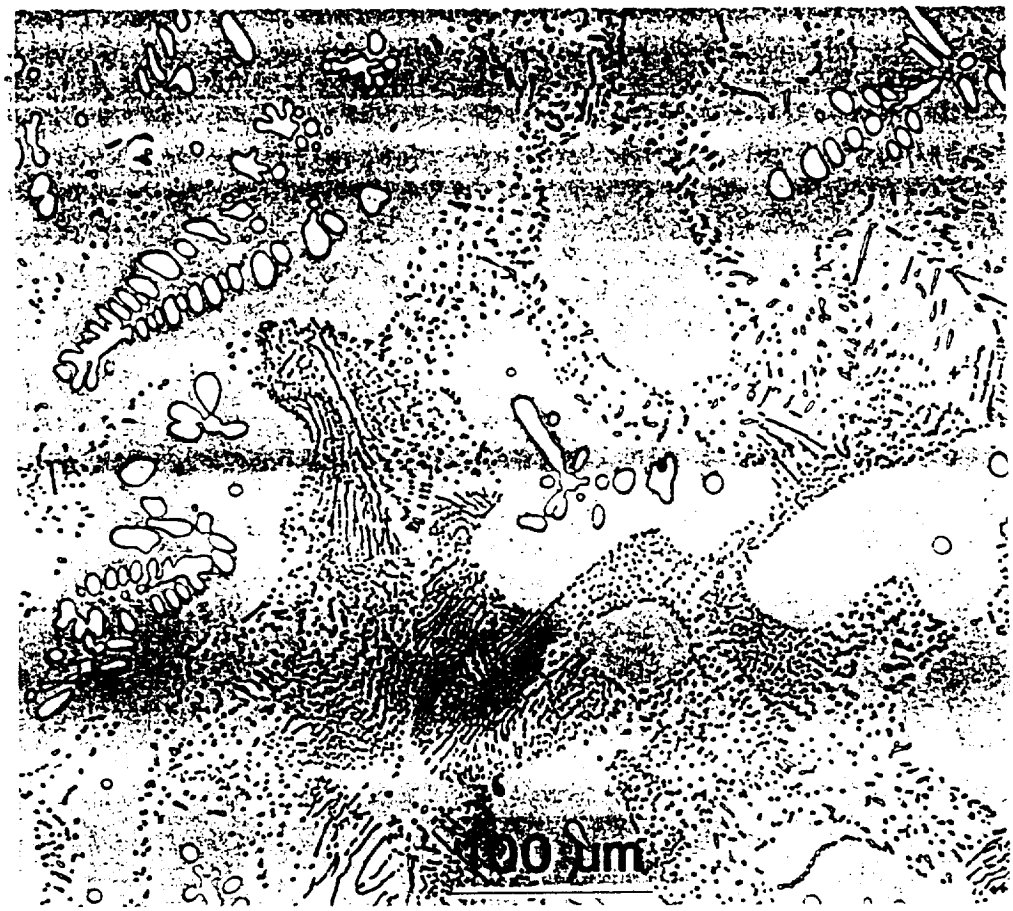

Figure 4.3. Optical Micrograph of Ingot-Cast Cu-5 at.% Cr Alloy Showing Coarse Pro-Eutectic Cr Dendrites in a Eutectic Matrix

4.2 Rapid Solidification Structures

The microstructures of the high-strength, high-conductivity Cu alloys can be greatly improved by RSP. Melt spinning yields cooling rates in the range of 10^6 °C/s during solidification, and non-equilibrium phases may be produced when their kinetics of formation are faster than those of the stable equilibrium phases. Partitionless solidification can occur at very rapid rates since solute diffusion is not required for the transformation, and this results in solute trapping in the crystalline Cu matrix during RSP. The approach taken in this work was to utilize RSP to produce a metastable Cu phase with extended solid solubility of Cr or Zr. During subsequent ageing, a large volume fraction of very fine precipitates could be produced from the highly supersaturated alloys.

The typical microstructure of a melt-spun Cu-5 at.% Cr alloy can be observed in Figure 4.4; the photomicrograph was taken using DIC for enhanced resolution. The longitudinal section of the as-spun ribbon is oriented with the chill surface of the folded ribbon toward center. It is evident that the nucleation of solid only occurred at the wheel surface of the ribbon where the thermal gradient and undercooling in the melt are greatest. The fine columnar grains solidified with a dominant $< 100 >$ growth direction approximately normal to the wheel surface. In addition, the morphology of the solidification structure is uniform throughout the ribbon thickness. The average grain size is 2 μm, measured parallel to the wheel direction at the ribbon midsection. When the CBMS alloy, Figure 4.4, is compared with the ingot cast alloy, Figure 4.3, it can be observed that the most striking differences are the complete absence of second phase particles and the amount of grain refinement in the RSP alloy. The grain size of the RSP alloy is similar in magnitude to the smallest visible Cr eutectic rods in the ingot cast alloy. It is evident from Figure 4.4 that eutectic solidification of this

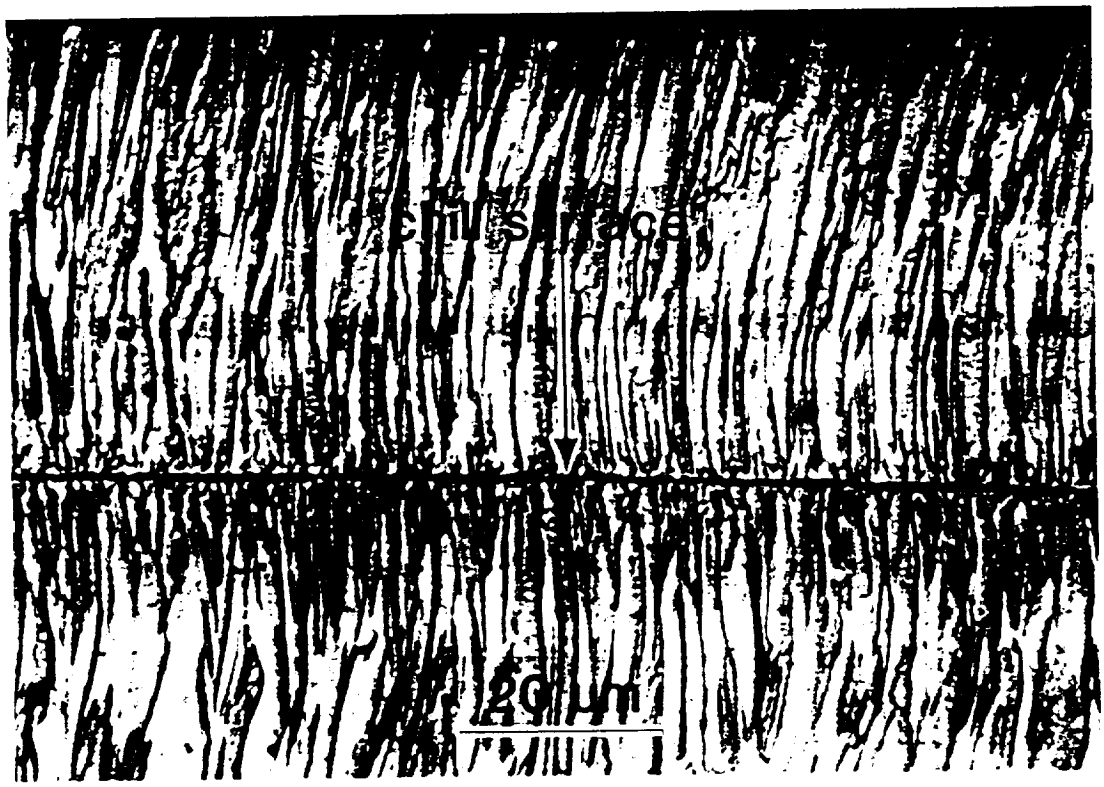

Figure 4.4. Optical Micrograph of a Longitudinal Section of As-Spun RSP Cu-5 at.% Cr Alloy Showing Uniform Columnar Grain Structure. Photograph of a Single Ribbon Folded Back Along Chill Surface

hypereutectic alloy was completely suppressed by rapid solidification. As a result, the gross segregation that is observed in Figure 4.3 for the ingot cast alloy was largely eliminated. While the absence of visible Cr precipitates in this optical micrograph for the RSP alloy is encouraging, it does not demonstrate that the solid solubility of Cr in Cu was extended; the Cr could exist as precipitates too small to be observed and yet larger than ≈5 nm, the effective size for strengthening. Evidence for extended solid solubility will be presented in later sections.

All binary Cu-Cr RSP alloys produced in this study had identical microstructures to those of Figure 4.4; these include alloys with Cr contents in the range of 1 to 5 at.%. The lower Cr concentration alloys could not, however, be reliably melt-spun as was discussed earlier. It was found that the addition of Ag greatly improved the castability of all Cu-Cr alloys. The ternary Cu-Cr-Ag ribbon had very uniform width and thickness for a given melt-spin run.

There are several possible explanations for the strong positive influence of Ag on the melt-spinning characteristics of these alloys. It would be expected that Ag additions change the wetting behavior of the melt puddle on the wheel surface. Silver might also act to increase the fluidity of the melt, which in turn may effect the puddle geometry. The themodynamics of the alloy system would also change with Ag additions, and this might alter the range of temperatures over which solidification occurs. In this work, it was found that in all of the alloy systems, increasing the concentration of alloying elements greatly improves the castability of the ribbon; this effect is true for Cr, Zr, and Ag additions in Cu. For a constant wheel speed and rate of heat transfer from the ribbon to the wheel, a large solidification temperature range corresponds to a long ribbon/wheel contact time and distance; this assumes that the ribbon does not release from the wheel until solidification is completed. One might expect higher tensile stresses in the longer lengths of ribbon in contact with the wheel surface during solidification;

these stresses may play an important role in breaking the ribbon/wheel bond and producing continuous and uniform geometry ribbon. None of the above explanations are supported by any experimental evidence in this work, and a detailed scientific investigation of this phenomenon is probably warranted for future research in this field.

The microstructures of the ternary Cu-Cr-Ag melt-spun ribbons are very similar to those of the binary Cu-Cr RSP alloys. These structures can be observed in Figure 4.5 for Cu-5 at.% Cr-2 at.% Ag, Cu-3 at.% Cr-2 at.% Ag, and Cu-5 at.% Cr-1 at.% Ag. The fine columnar grains are consistent with those of the binary Cu-Cr and have a similar grain size. The only visible difference in the optical photomicrographs is the appearance of some very fine dark precipitates in the as-cast ternary alloy ribbons. These precipitates are distributed uniformly throughout the ribbon thickness, so it is unlikely that they formed during solidification; the cooling rate during solidification is largest near the wheel surface and one would expect to see a change in the size or morphology of the precipitates with the gradient of solidification cooling rates. It is most likely that the precipitates were formed during the solid state cooling of the ribbon in the vacuum chamber after ribbon/wheel separation; thermal gradients in the ribbon are much smaller during the cooling by radiation and this would result in a more homogeneous size distribution of precipitates throughout the ribbon thickness.

The optical microstructures of the ternary Cu-Cr-Ag ribbons were independant of alloy concentration for the range of compositions studied. All of these alloys developed the same fine columnar grain structure throughout the ribbon thickness. Since the solidification cooling rate is a function of distance from the wheel surface, this implies that the ternary Cu-Cr-Ag alloys and the binary Cu-Cr alloys are rather insensitive to the solidification rate; that is, any solidification

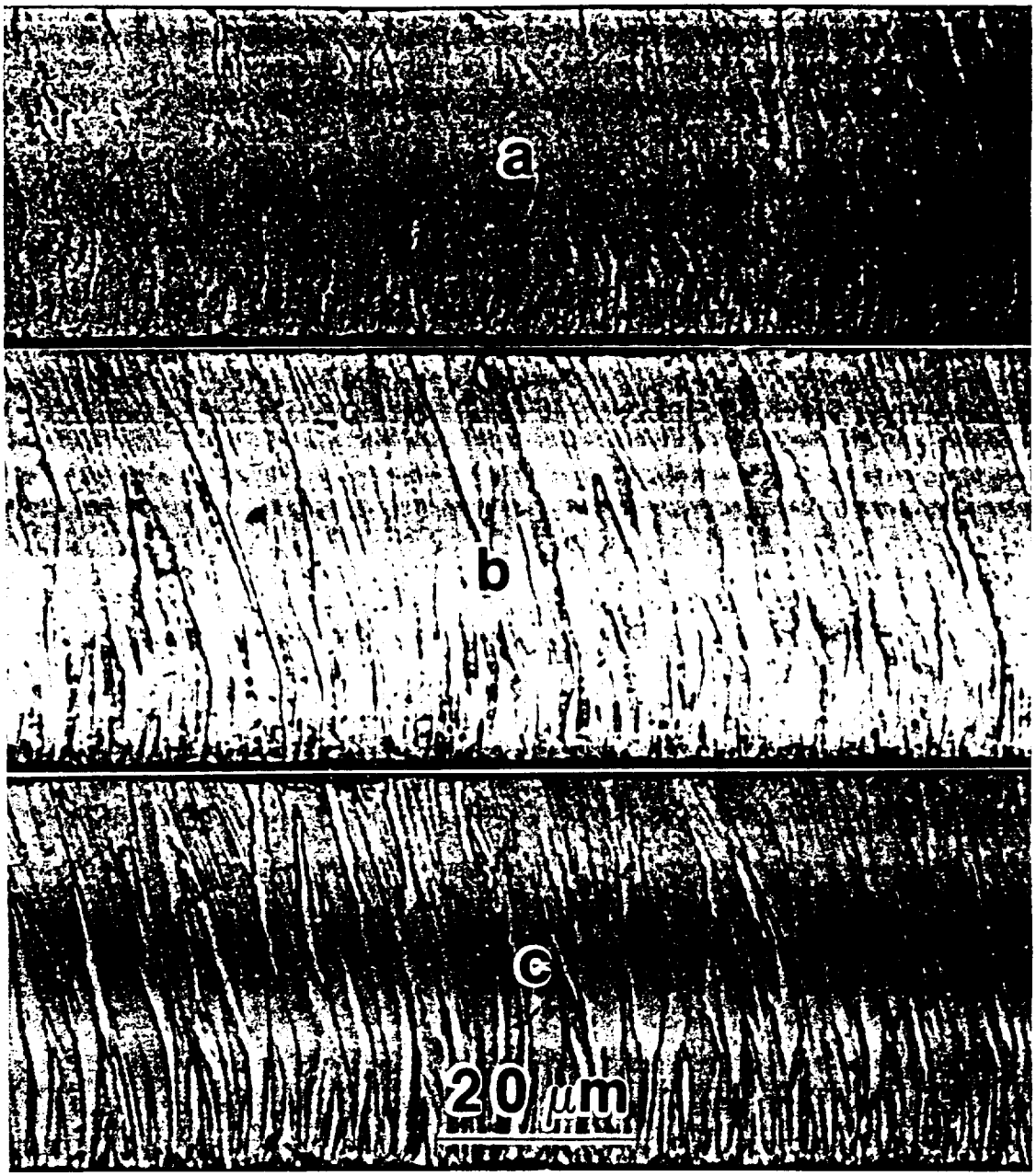

Figure 4.5. Optical Micrographs of Longitudinal Sections of As-Spun RSP a) Cu-5 at.% Cr-2 at.% Ag, b) Cu-3 at.% Cr-2 at.% Ag and c) Cu-5 at.% Cr-1 at.% Ag Alloys

cooling rate which is at least as rapid as the free-side cooling rate will produce the uniform fine columnar grain structure.

In contrast to this behavior, the microstructures of the binary Cu-Zr alloys are extremely sensitive to the solidification cooling rate, and this effect is enhanced by increasing the Zr concentration. The microstructure of an as-cast Cu-1.0 at.% Zr alloy ribbon can be observed in Figure 4.6; the orientation is chill surface down as in the other figures. It can be seen that at least three different microstructural regions are evident in the photomicrograph. Near the chill surface, there is a very fine columnar grain zone; the width of this zone is approximately 1/10 of the ribbon thickness. A little further distance towards the free-side of the ribbon, the grain size is much larger, and the grains are more equiaxed; the width of this zone extends to about 1/4 of the ribbon thickness. The remaining 3/4 of the ribbon thickness has a fairly uniform microstructure that consists of very fine equiaxed grains. In addition to the effect that Zr has on the microstructure, it should be noted that the thickness of the Cu-1.0 at.% Zr ribbon is much larger than any of the binary Cu-Cr or ternary Cu-Cr-Ag ribbons.

A small increase in the Zr concentration of the melt-spun ribbon has a dramatic effect on the microstructure, as can be seen in Figure 4.7 for a Cu-1.3 at.% Zr alloy. The fine columnar grains adjacent to the chill surface appear similar to those of the 1.0 at.% Zr alloy, but the remainder of the ribbon contains very unusual features. A sharply slanted fine grain zone can be observed next to the columnar zone. Most of the midsection of the ribbon contains a large grain size columnar zone which is very irregular. Finally, near the free-side of the ribbon the microstructure consists of fine equiaxed grains similar to the Cu-1.0 at.% Zr alloy. The additional Zr concentration also reduced the thickness of the ribbon.

Increasing the Zr concentration to 3.0 at.% produced the microstructures that are observed in Figure 4.8. This particular composition was melt-spun using

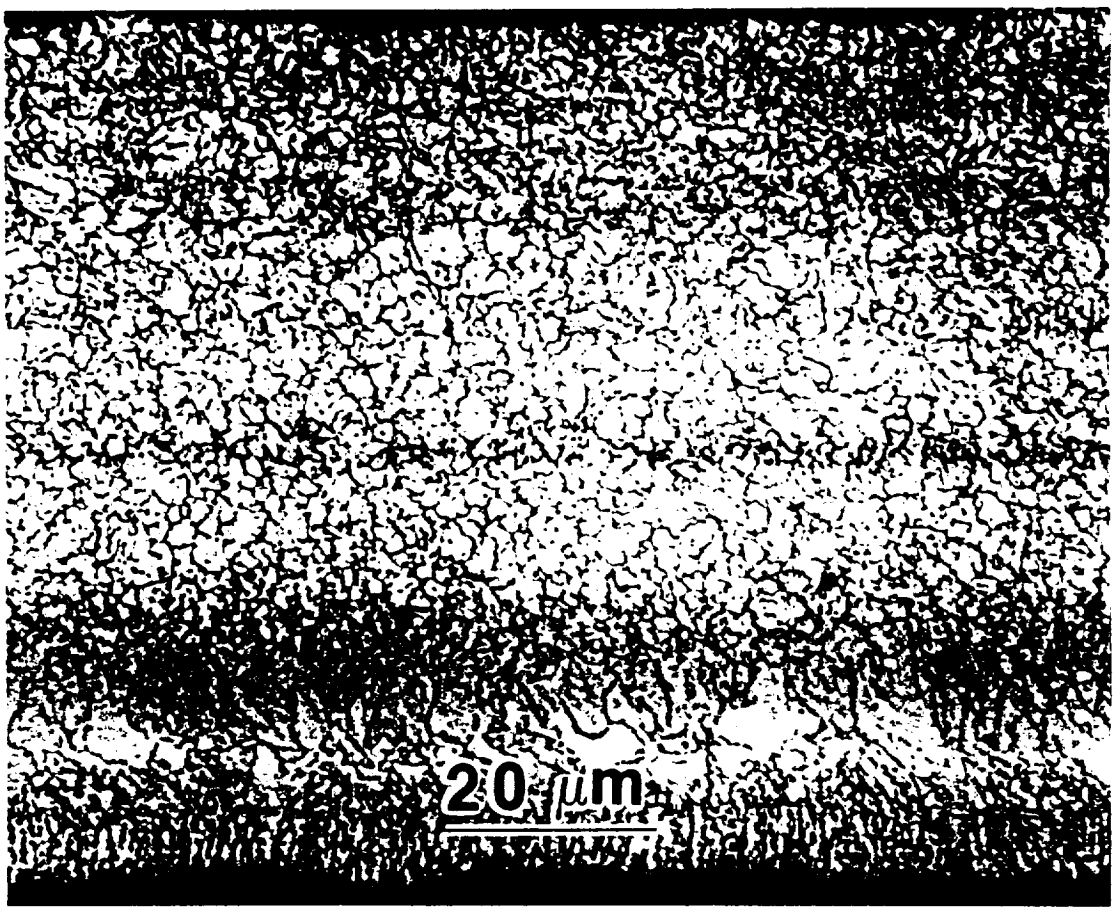

Figure 4.6. Optical Micrograph of a Longitudinal Section of As-Spun RSP Cu-1.0 at.% Zr Alloy Showing Different Microstructural Regions As a Function of Distance from the Chill Surface

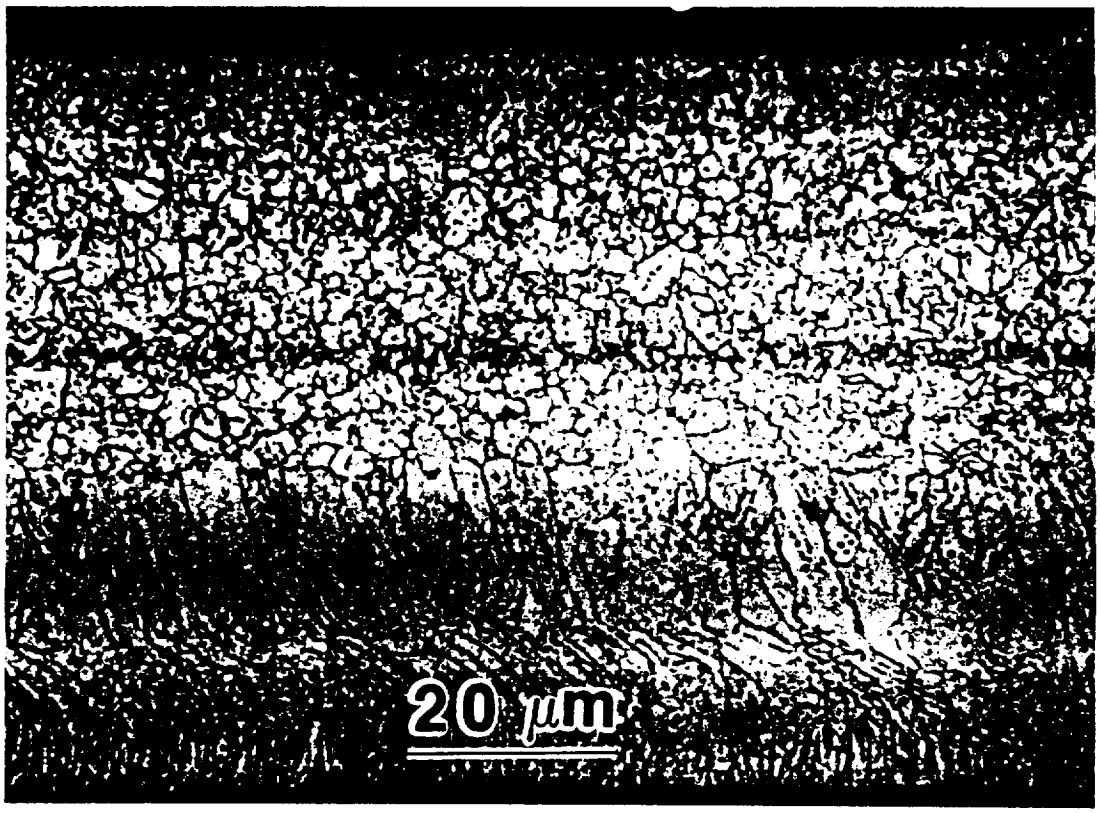

Figure 4.7. Optical Micrograph of a Longitudinal Section of As-Spun RSP Cu-1.3 at.% Zr Alloy Showing the Change in Microstructural Features Through the Ribbon Thickness

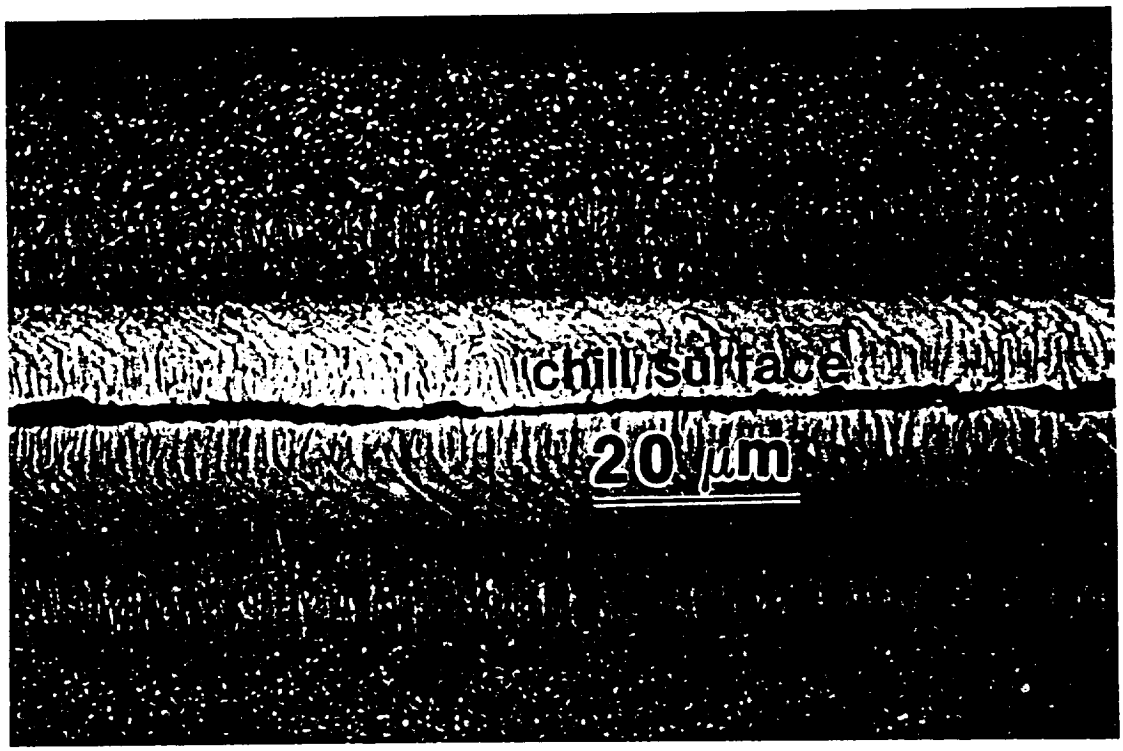

Figure 4.8. Optical Micrograph of a Longitudinal Section of As-Spun RSP Cu-3.0 at.% Zr Alloy Cast at 40 m/s

a wheel surface velocity of 40 m/s in an effort to increase the solidification cooling rate; most of the alloys were spun at 20 m/s in this study as higher wheel velocities were usually incompatible with good ribbon casting. Once more, the fine columnar grains are evident near the chill surface; these grains first grow normal to the wheel surface, and then slant sharply. In the ribbon midsection the direction of grain growth is again normal to the wheel surface and the grains are very fine and columnar. Near the free-side of the ribbon the grains are very fine and equiaxed. As was the case for the Cu-1.0 at.% Zr alloy, the ribbon thickness was reduced further by Zr additions; this is largely due to the higher wheel velocity, but an increase in the fluidity of the melt or greater melt puddle/wheel wetting may also contribute to this effect. The effect of increasing the Zr concentration to 5.0 at.% can be observed in Figure 4.9. In this alloy, only two particular microstructures are evident. The region nearest the wheel surface consists of a featureless chill zone that extends to 1/4 of the ribbon thickness. The uniformity in thickness of this layer is quite remarkable. The remaining portion of the ribbon has a microstructure consistent with the free-side microstructure observed in the other Cu-Zr alloys, that is a very fine equiaxed grain structure. The thickness of the Cu-5.0 at.% Zr alloy ribbon is roughly similar to that of the Cu-3.0 at.% Zr alloy, so the additional Zr concentration had little effect in this range.

A microhardness traverse was taken on the as-cast Cu-3.0 at.% Zr ribbon in order to determine if the gross microstructural changes had an effect on the mechanical strength of the alloy, Figure 4.10. It can be observed that the microhardness of the ribbon varies greatly with the microstructure. The regions near the wheel surface and the free surface of the ribbon are similar in the magnitude of hardness, and represent the softest regions of the specimen. The hardest zone of the ribbon is in the fine columnar grains normal to the wheel surface near the ribbon midsection. In contrast to this behavior, microhardness traverses that

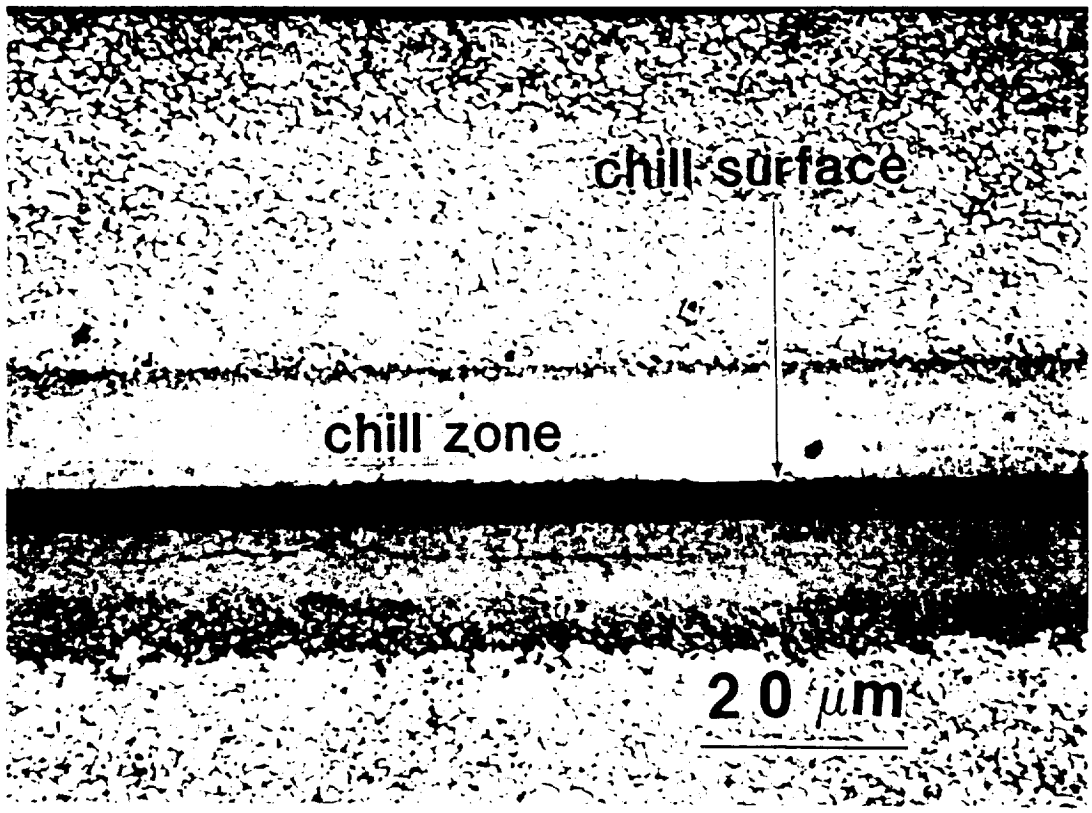

Figure 4.9. Optical Micrograph of a Longitudinal Section of As-Spun RSP Cu-5.0 at.% Zr Alloy Showing Featureless Chill Zone and Sharp Boundary with Equiaxed Grain Structure

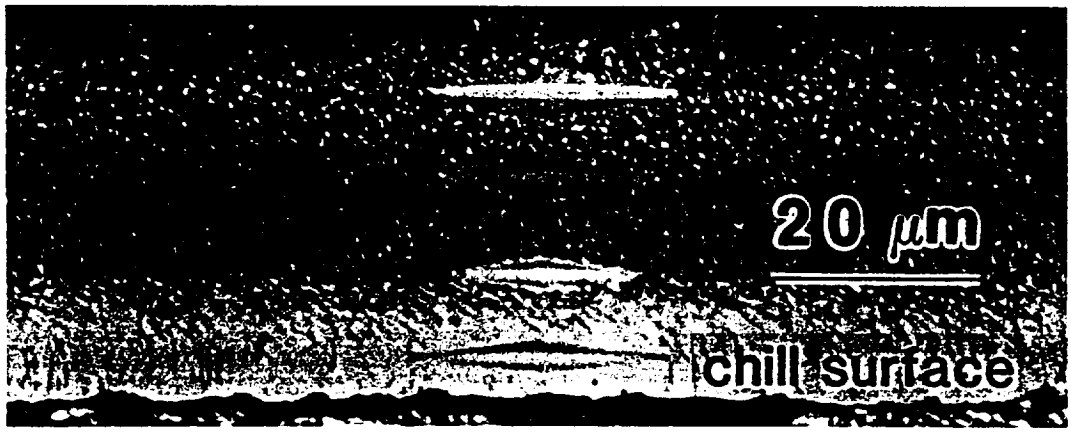

Figure 4.10. Microhardness Traverse of a Section of As-Spun RSP Cu-3.0 at.% Zr Ribbon Showing Hardness Variation as a Function of Distance from Chill Surface

were performed on Cu-Cr and Cu-Cr-Ag ribbons gave consistent measurements throughout the ribbon thickness.

The large variations in hardness that are observed in the Cu-Zr ribbon are undesirable for several reasons. One of the main advantages of RSP is the ability to produce a uniform microstructure with very little chemical segregation; this results in consolidated products with uniform physical and mechanical properties. Since the Cu-Zr ribbons do not have consistent microstructures or mechanical properties, it would be very difficult to control the processing during consolidation so as to produce the optimum microstructure and properties. For these reasons, as well as the relative lack of ductility in bend testing, the Cu-Zr RSP alloys are not nearly as promising as the Cu-Cr and Cu-Cr-Ag alloys; therefore most of the research in this work concentrated on the binary and ternary Cu-Cr-Ag alloys.

4.3 X-ray Diffraction Analysis

X-ray diffraction studies were performed on the wheel side and free surface of the as-cast ribbons for all of the compositions. The main purpose of this work was to precisely determine the lattice parameters for the fcc Cu phase in order to demonstrate the extended solid solubility due to RSP. In addition, the presence of other phases could also be detected when their volume fraction exceeded approximately 3%.

Very little data is available from the literature on extended solubilities of Cr in Cu. Falkenhagen and Hofmann [103] were able to increase the solid solubility of Cr in Cu by the use of splat cooling techniques. They reported fcc lattice parameters of 3.6178 Å and 3.6198 Å for alloy compositions of 0.97 at.% Cr and 1.63 at.% Cr, respectively. These lattice parameter values were converted from kX to Å, using a multiplier of 1.002063. It is apparent that the Cu lattice is expanded only slightly by Cr in solution; the accepted lattice parameter for

pure Cu is 3.6149 Å, thus the largest lattice expansion that has been reported is only 0.14 %. The 1.63 at.% Cr alloy of [103] is very close to the accepted eutectic composition of Cu-1.56 at.% Cr [26]. Duwez [104] reported a correlation between the location of the eutectic or peritectic in the phase diagram of an alloy system and the extent of the metastable solid solution that can be produced by rapid quenching from the melt. He demonstrated that the extended solubility limit never exceeded the eutectic or peritectic composition for alloys of Ni-Si, Ni-Ge, Ni-Sn, Co-Si, Co-Ge, Co-Sn, Co-Al, and Co-Ga. When the present work was initially undertaken, it was not known if the solubility limit of Cu-Cr could be extended further than the eutectic composition. The limit of extended solid solubility is very important since it determines the volume fraction of precipitates after subsequent ageing, and thus the strength of the alloy.

It was found from the 2θ diffractograms that the solidification and cooling rates during melt-spinning were not constant from run to run, or even within a given run. In the case of Cu-5 at.% Cr, the lattice parameter varied in the range of 3.615 Å to 3.628 Å. Ribbons with large lattice parameters could be selected by their macroscopic appearance; the best ribbons had a very flat and uniform geometry and exhibited no discoloration or warpage from slow solid state cooling in the vacuum chamber. It was also observed that the wheel-side of ribbons always had lattice parameters that were greater than or equal to the parameters that were measured on the free-side. This result is not unexpected since heat transfer occurs mainly by conduction to the wheel surface, and to a smaller degree by radiation in the vacuum chamber.

Figure 4.11 shows a plot of wheel-side latice parameters as a function of Cr concentration; the data of [103] has also been plotted for comparison. This figure clearly shows that the solid solubility of Cr in Cu was extended beyond the eutectic composition by melt-spinning. The data yields a reasonable linear fit

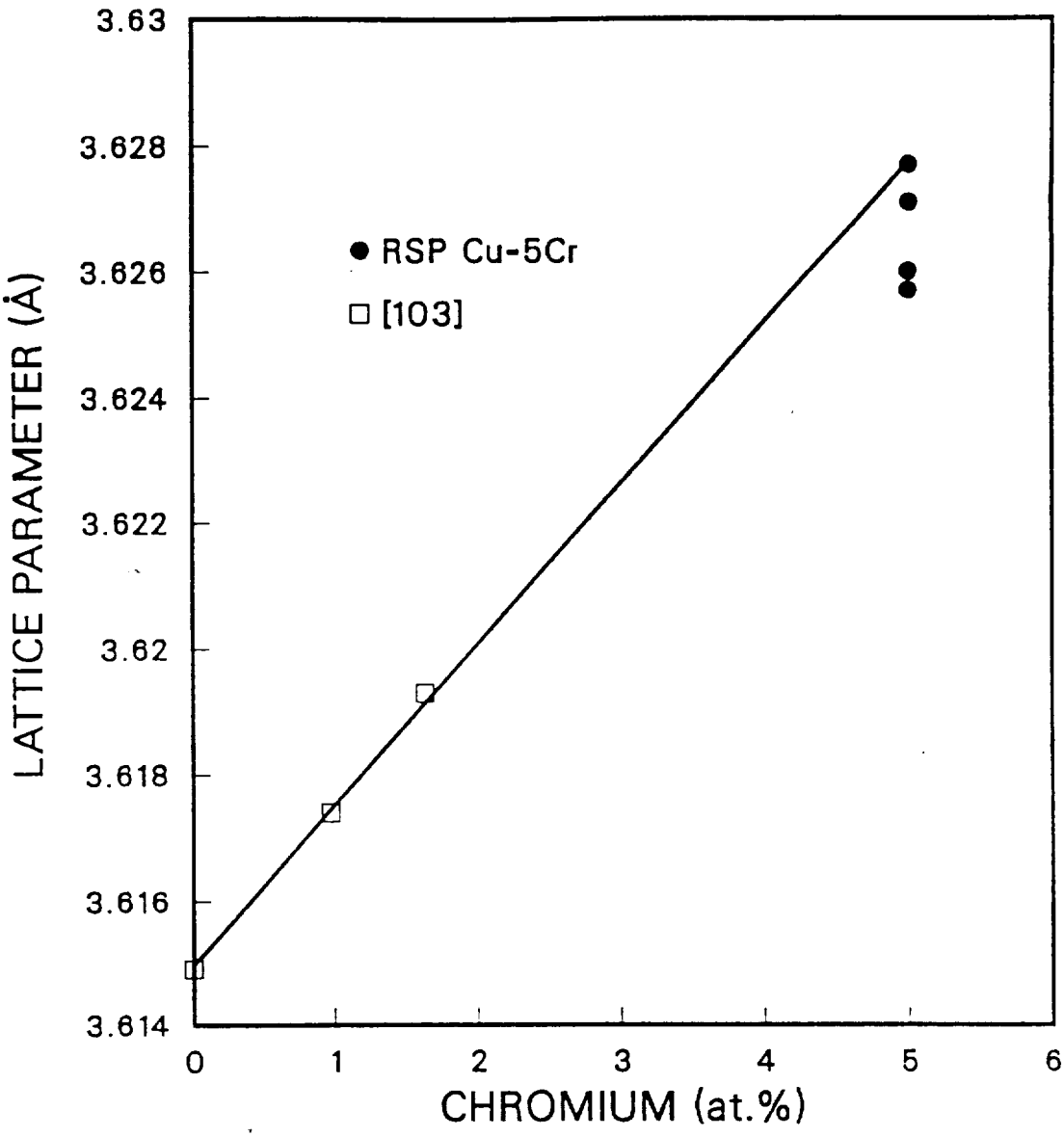

Figure 4.11. Lattice Parameter of Copper as a Function of Chromium in Solution. Dilute Alloys produced by Splat Quenching [103], Concentrated Alloys by Chill Block Melt-Spinning

with the data of [103], and from this it can be concluded that the solid solubility was extended to approximately 5 at.% Cr for these runs. The free-side parameters for the data of Figure 4.11 were approximately 0.003 Å smaller than the plotted values, thus even the slowest cooled portion of the ribbon has extended solid solubility in the range of 4 at.% Cr; the Cr concentration in solution being determined from linear interpolation of this figure.

The amount of Cr in solution cannot be determined with a large degree of certainty because of the method used to measure lattice parameters in this work, and because of the small number of data points at low Cr concentrations [103]. It should also be noted that the lattice parameter for pure Cu reported by [103] is 3.6153 Å, which differs from the accepted value of 3.6149 Å. The data of [103] has been adjusted in Figure 4.11 to account for the error in the measured parameter of pure Cu; a value of 0.0004 Å was subtracted from each of the three reported lattice parameters. In a similar manner, the data for the Cu-5 at.% Cr RSP alloy was adjusted by subtracting a value of 0.0023 Å from the measured lattice parameters since the lattice parameter of OFHC Cu was measured as 3.6172 Å in this work using the diffractometer. Precise lattice parameter measurements are typically made using the Debye–Scherrer or back–reflection focusing camera methods, which in this study were not suitable because of the difficulty in making powder specimens from the RSP ribbon. Metals and alloys are usually converted to powder by grinding or filing. The fine powder is then annealed to remove the strains introduced during comminution. This is not practical in the RSP alloy because the Cr in solution will precipitate during the annealing treatment. In addition, it is not a trivial matter to produce −325-mesh powder from the ductile Cu alloy. It is for these reasons that the diffractometer method was chosen for lattice parameter determinations despite the relative inaccuracy of this technique.

The texture of the as-cast Cu-Cr ribbon was determined by making a {111} pole figure by the diffractometer method. The {111} poles were located on a circle 54.7° from the sheet normal. From this it was concluded that the columnar grains have a dominant growth direction of < 100 > normal to the ribbon surface.

The crystal structure determined from the diffractometer studies for the RSP Cu-Cr alloys was typically fcc. In some ribbons, weak intensity diffraction peaks were observed for bcc Cr, but in no cases were any metastable phases found. All of the diffraction peaks were sharp, which is indicative of the crystalline nature of the alloy; no evidence of amorphous structure was observed. Although, one of the common applications of RSP is in the production of amorphous alloys, in this study, the extension of solid solubility does not require that solidification be so rapid as to avoid the nucleation of crystalline solid. The alloy compositions were selected on the basis of their expected mechanical properties and not because they were likely candidates for glass-forming. One of the great advantages of rapid solidification has largely been ignored until this time; that is the ability to increase the solid solubility beyond that of the equilibrium composition. The greatly extended solid solubility of Cr in Cu was necessary to obtain the large volume fraction of precipitates required for high strength, and thus was a very important achievement of this work.

For the case of the Cu-Zr alloys, there is no data available in the literature on extended solid solubility; there is however, much information available concerning the glass-forming compositions near 40 at.% Zr, which are of little practical interest in this work. It was found that the lattice expansion of Cu was much larger with Zr additions than the equivalent amount of Cr in solution. The largest wheel-side fcc lattice parameter for a Cu-3 at.% Zr ribbon was calculated as 3.642 Å; as in the parameters reported for the Cu-Cr RSP alloys, a value of 0.0023 Å was subtracted from the measured diffractometer data to normalize the

results. It should be noted that most of the Cu-Zr RSP alloys had lattice parameters significantly smaller than this value. For example, a Cu-10 at.% Zr ribbon was found to have an fcc lattice parameter of only 3.625 Å, and a Cu-9 at.% Zr ribbon had a parameter of 3.631 Å.

The Cu-Zr RSP alloys appear to be very sensitive to the effective solidification rate; the 3 at.% Zr alloy was melt-spun using a wheel surface velocity of 40 m/s, while the others were produced using a velocity of 20 m/s. This higher wheel velocity was usually impractical for ribbon production as has been discussed earlier. The 40 m/s wheel velocity results in a thinner and narrower ribbon with faster solidification cooling rates. Despite the fast solidification rate of the Cu-3 at.% Zr alloy, it was found that the free-side lattice parameter was only 3.618 Å; this implies that the amount of Zr in solution varies greatly throughout the ribbon thickness. The gradient of Zr in solution will yield nonuniform mechanical and physical properties after consolidation of the RSP product; this result is consistent with those of the microstructural observations made in section 4.2, Figures 4.8 and 4.10. It can be concluded that the metastable solid solubility of the Cu-Zr alloys were greatly extended by RSP; while this result is promising for the development of high-conductivity, precipitation hardening alloys, the inability to produce a consistent Zr supersaturation or microstructure seriously limits the utility of these alloys without further technological development in RSP.

X-ray diffraction analysis of RSP Cu-Cr-Ag alloys was performed in a manner similar to the other alloys. The wheel-side lattice parameters for Cu-3 at.% Cr-2.75 at.% Ag and Cu-5 at.% Cr-2 at.% Ag ribbons were measured as 3.636 Å and 3.631 Å, respectively. This data may be compared with the lattice parameter measurements of [61] for the binary Cu-Ag system; in that study, supersaturated alloys were prepared by quenching from the single phase region at 770°C. The lattice parameters for Cu-2.75 at.% Ag and Cu-2.1 at.% Ag were

given as 3.6337 Å and 3.6297 Å, respectively [61]. It is apparent that the ternary RSP alloys have lattice parameters only slightly larger than the binary alloys of equivalent Ag concentration. For the compositions selected, the lattice expansions are fairly independant of the Cr concentration; since the Cr appears to have only a marginal effect, it cannot be concluded that the Cr remains in solution. The converse is also difficult to prove; the absence of bcc Cr diffraction peaks on the 2θ scan would not be unexpected with the small concentration of Cr in these alloys and the relative insensitivity of x-ray diffraction. As was the case for the binary Cu-Cr alloys, these ternary alloys were found to have slightly smaller lattice parameters on the free-side of the ribbons due to the slower solidification rates. This gradient in lattice parameter was not nearly as large as in the alloys containing Zr.

All of the results on x-ray diffraction discussed up to this point have been restricted to the as-cast ribbons in order to demonstrate the ability of RSP to extend the metastable solid solubility of the Cu-rich phase. No evidence of novel metastable phases or amorphous structure was found for any of the three alloy systems studied. X-ray diffraction analysis was also performed on some of the RSP ribbons following precipitation heat treatment at temperatures greater than 500°C. As would be expected, the lattice parameters measured for the fcc phase were typically 3.615 Å after adjustment, in good agreement with the accepted parameter for pure Cu. In some cases, diffraction peaks from bcc Cr precipitates could be detected, while in others, only the fcc phase of Cu was observed.

4.4 Transmission Electron Microscopy

TEM specimens were prepared from Cu-Cr and Cu-Cr-Ag ribbons in both the as-cast and heat-treated condition. Specimens were not prepared for the RSP alloys containing Zr because of the variation in microstructural features, through

the ribbon thickness, that was observed in Figures 4.6–4.10. It was felt that the electropolishing technique could not be controlled well enough to produce thinned specimens containing the desired microstructural region. For example, ribbon specimens were typically thinned and perforated after only one to two minutes of electropolishing, and it would be difficult to adjust the depth of thinning by altering the electropolishing time.

The bright field TEM micrograph of a Cu-5 at.% Cr, RSP ribbon can be observed in Figure 4.12; the as-cast microstructure is representative of the ribbon midsection, as all of the specimens in this work were thinned from both sides. This particular specimen was produced from a ribbon that was melt-spun early on in this research, run number MS 573. The microstructure consists of $\approx$2 μm diameter, equiaxed grains containing $\approx$0.5 μm diameter cells. The regular polyhedral cells are delineated by precipitates of Cr at their boundaries. Within the cells, a very fine and dense distribution of smaller Cr precipitates can be observed. The light-colored grain boundary regions consist of a solute depleted zone with a few large Cr precipitates. In Figure 4.13, the same specimen can be observed at higher magnification; the individual spherical precipitates within the cells and at the cell boundaries are more evident.

It can be concluded from these two figures that the cooling rate during RSP was not fast enough to completely suppress the formation of Cr precipitates. No evidence of Cr precipitation was observable in the optical micrographs of this alloy because of the very fine size of the precipitates; the largest precipitates at the grain boundaries are only 540 Å in diameter, while the average precipitate diameter is in the range of 50 Å. It is also apparent that the precipitation of Cr only occurred during the solid state cooling of the ribbon once it left the wheel. There is no evidence of pro-eutectic Cr precipitation during solidification. The Cr particles, if present in the undercooled melt, would act as potent sites for

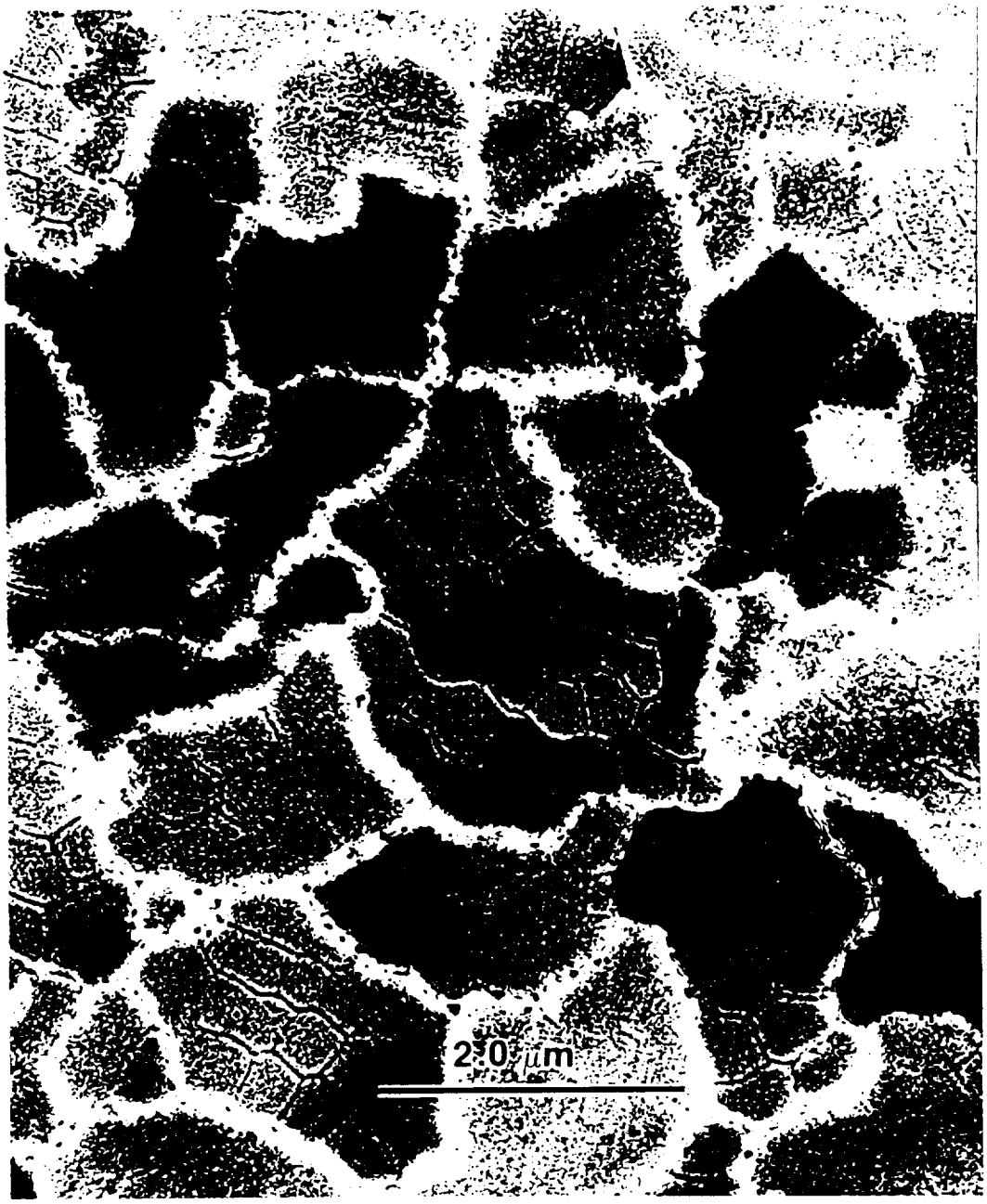

Figure 4.12. TEM Brightfield Photomicrograph of As-Spun RSP Cu-5 at.% Cr Alloy Showing Cell Structure and Cr Precipitates within Grains

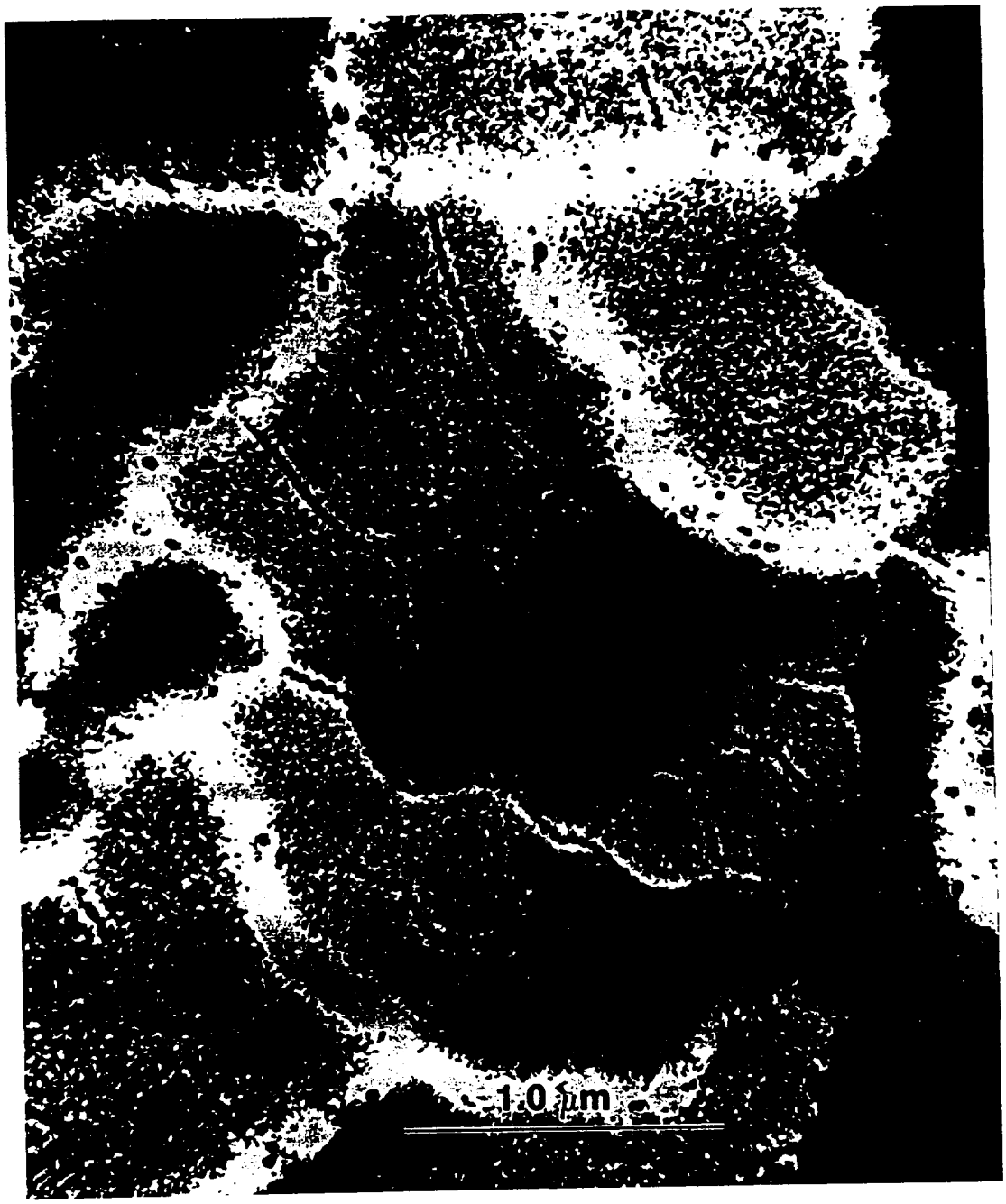

Figure 4.13. TEM Brightfield Photomicrograph of As-Spun RSP Cu-5 at.% Cr Alloy Showing Spherical Precipitates within Cells and at Boundaries

nucleation of solid and would result in a bulls-eye microstructure, which was never observed in any specimens in this work. In addition, the pinched-rod, eutectic solidification structure that is typical of ingot-cast alloys of this composition, was never observed in the RSP product.

Despite the precipitation of Cr during solid state cooling, the microstructure of the RSP alloy is very promising for mechanical properties. The high density of fine precipitates should yield very high strength, provided the average precipitate diameter is not much larger than ≈50 Å; the particle diameters are difficult to measure because of overlap, but they appear to be of the optimum size range. It would have been even better for control of the resulting microstructure and mechanical properties if the alloy would have remained supersaturated with Cr after cooling to room temperature. Precipitate coarsening studies could not be undertaken with any reliability since the as-cast particle size would not necessarily be constant. Unfortunately, it was not possible to achieve both rapid solidification and high solid state cooling in a reproducible manner for these alloys. In any event, rapid solidification is the minimum requirement for the production of a desirable microstructure in these hyper-eutectic alloys.

The very fine distribution of Cr particles is a result of homogeneous precipitation. Many alloy systems must be cold-worked prior to precipitation ageing in order to provide a high dislocation density for nucleation of precipitates. Heterogenous nucleation does not result in as good a distribution of precipitates as with homogeneous nucleation, and the strength of the alloy will suffer. As the driving force for precipitation is increased, homogeneous nucleation is more likely to occur. The large supersaturation of Cr in these RSP alloys favors homogeneous precipitation within the cells; these results are not surprising, since even in conventional ingot metallurgy Cu-Cr alloys, homogeneous nucleation is observed

at smaller concentrations of Cr [77,80]. Heterogeneous nucleation may also occur however, at nucleating sites like grain and cell boundaries.

The distribution of Cr precipitates at the grain boundaries is much too coarse to provide good strength in these regions. It was not expected that the precipitates would coarsen so rapidly during the solid state cooling from elevated temperatures. It is apparent that the grain boundaries provided a high diffusivity path for Cr, and resulted in the rather wide precipitate free zone observed in Figure 4.13. The width of this PFZ in the as-cast ribbons was found to vary in different melt-spin runs of the same composition of alloy. Even within the small area shown in Figure 4.13, the PFZ width is not constant, as it ranges from 80 nm to 180 nm.

Most of the Cu-5 at.% Cr ribbons that were produced in this study had microstructural features very similar to those of Figures 4.12 and 4.13. Despite the similarities, there were enough differences in the size of the precipitates and PFZ to make each melt-spun ribbon unique. In addition, it was found that even within the same ribbon, the solid state cooling rate was not constant. Because of this, quantitative scientific studies of precipitate coarsening during ageing were not practical. For each melt-spun run, only a few feet of good ribbon of very high cooling rate was produced. In addition, it was evident that no direct comparisons should be made using ribbons from different runs of the identical composition. For example, in Figure 4.14, the TEM bright field image of another Cu-5 at.% Cr ribbon, MS 7058, is presented; this ribbon was one of the last of the more than 100 melt-spin runs made in this work. The appearance of this specimen is quite different from the ribbon presented earlier in Figures 4.12 and 4.13. The most obvious change is the complete absence of a PFZ near the grain boundaries. This is indicative of a faster solid state cooling rate for this particular ribbon. At higher magnifications, Figures 4.15–4.18, it can be observed that very few precipitates of

Figure 4.14. TEM Brightfield Photomicrograph of As-Spun RSP Cu-5 at.% Cr Alloy Showing Absence of PFZ. Ribbon Cast from a Different Melt-Spin Run than Specimen from Figure 4.13

Figure 4.15. TEM Brightfield Photomicrograph of As-Spun RSP Cu-5 at.% Cr Alloy. Same Specimen as Figure 4.14 at Higher Magnification, Showing Absence of Precipitates within Cells

Figure 4.16. TEM Brightfield Photomicrograph of As-Spun RSP Cu-5 at.% Cr Alloy. Same Specimen as Figure 4.15 at Higher Magnification

Figure 4.17. TEM Brightfield Photomicrograph of As-Spun RSP Cu-5 at.% Cr Alloy. Same Specimen as Figure 4.16 at Higher Magnification

Figure 4.18. TEM Brightfield Photomicrograph of As-Spun RSP Cu-5 at.% Cr Alloy. Same Specimen as Figure 4.17. Fine Cr Precipitates Visible at Dislocation Cell Boundaries

Cr are present in the as-cast ribbon. Homogeneous precipitation did not occur, as precipitates are only visible at grain and cell boundaries. The precipitates in these regions are much smaller than those shown in Figure 4.13; the largest of the precipitates in Figure 4.18 are in the range of 10–12 nm, which may be compared with the ≈60 nm diameter of the precipitates within the denuded boundaries of Figure 4.13.

Because of the absence of precipitation in the specimen presented in Figures 4.14–4.18, it can be clearly observed that the cell boundaries consist of very regular shaped dislocation networks. These dislocations act as sites for heterogeneous nucleation of Cr precipitates during the solid state cooling of the as-cast ribbon; the fine, spherical precipitates are most apparent in Figures 4.15 and 4.18, in close proximity to the cell boundaries. In addition to the dislocation network at the cell boundaries, some dislocations may be observed within the cells; in some cases, these free dislocations also were nucleation sites for Cr precipitation, Figure 4.17. It is quite remarkable that the dislocation cell networks were formed with such regular geometries; most of the very straight and long cells observed in Figure 4.14 have a uniform boundary spacing of 0.5 μm. The formation of the dislocation cells most likely relieves the thermal stresses that occur during RSP; the solidifying ribbon is constrained by the adhesion to the melt-spinning wheel, thus generating residual stresses in the relatively soft Cu alloy at elevated temperatures.

Selected area diffraction was used to determine the orientation of the grains and cells. It was found that most of the grains were oriented with $< 100 >$ parallel to the microscope beam direction, in good agreement with the results of the pole figure analysis. Within a grain, the misorientation across cell boundaries is not detectable with the TEM, therefore the tilt of these boundaries is less than 1/2 degree. It would be expected that high angle grain boundaries are a better path for

the diffusion of Cr at elevated temperatures than the low energy cell boundaries. Thus, coarsening of Cr precipitates in a denuded and solute depleted zone are only observed at the grain boundaries, Figure 4.13.

For the specimen presented in Figures 4.14–4.18, a $< 100 >$ zone SAD pattern is given in Figure 4.19. Only diffraction spots from the fcc Cu matrix are visible despite the presence of Cr precipitates in the bright field images at the cell boundaries. Because of the small cell size relative to the selector aperture, the SAD pattern is from several cells within a grain. Since the precipitates at the cell boundaries do not give rise to a seperate diffraction pattern, it is concluded that the precipitates are fully coherent with the matrix, which is consistent with the results of [77,79,80].

In the case of the specimen presented in Figures 4.12 and 4.13, which shows significant precipitation of Cr at grain and cell boundaries and also within the cells, the $< 110 >$ matrix zone SAD pattern contains diffraction spots from bcc Cr, Figures 4.20 and 4.21. The bcc Cr diffraction pattern could not be indexed, but the ratio of distances from the transmitted spot to the diffraction spots was consistent with that of bcc Cr and fcc Cu. It can be observed in Figure 4.21 that there is an orientation relationship between the bcc and fcc diffraction pattern. Despite evidence of a bcc ring pattern, the most intense Cr spots are located near fcc diffraction spots. The presence of a Nishiyama–Wasserman or Kurdjumow–Sachs orientation relationship between the fcc and bcc phases in this system has been reported numerous times in the literature, [78,80–85]. In both the K–S and N–W orientation relationships, the close-packed planes of the precipitates and matrix are parallel, that is $\{110\}_{bcc} \parallel \{111\}_{fcc}$. In the N–W relationship, the $[001]_{bcc}$ and $[1\bar{1}0]_{fcc}$ directions are parallel, while in the K–S orientation, these directions are skewed by an angle of 5.26°, by rotation of the $\{110\}_{bcc}$ or $\{111\}_{fcc}$ planes about their respective plane normals.

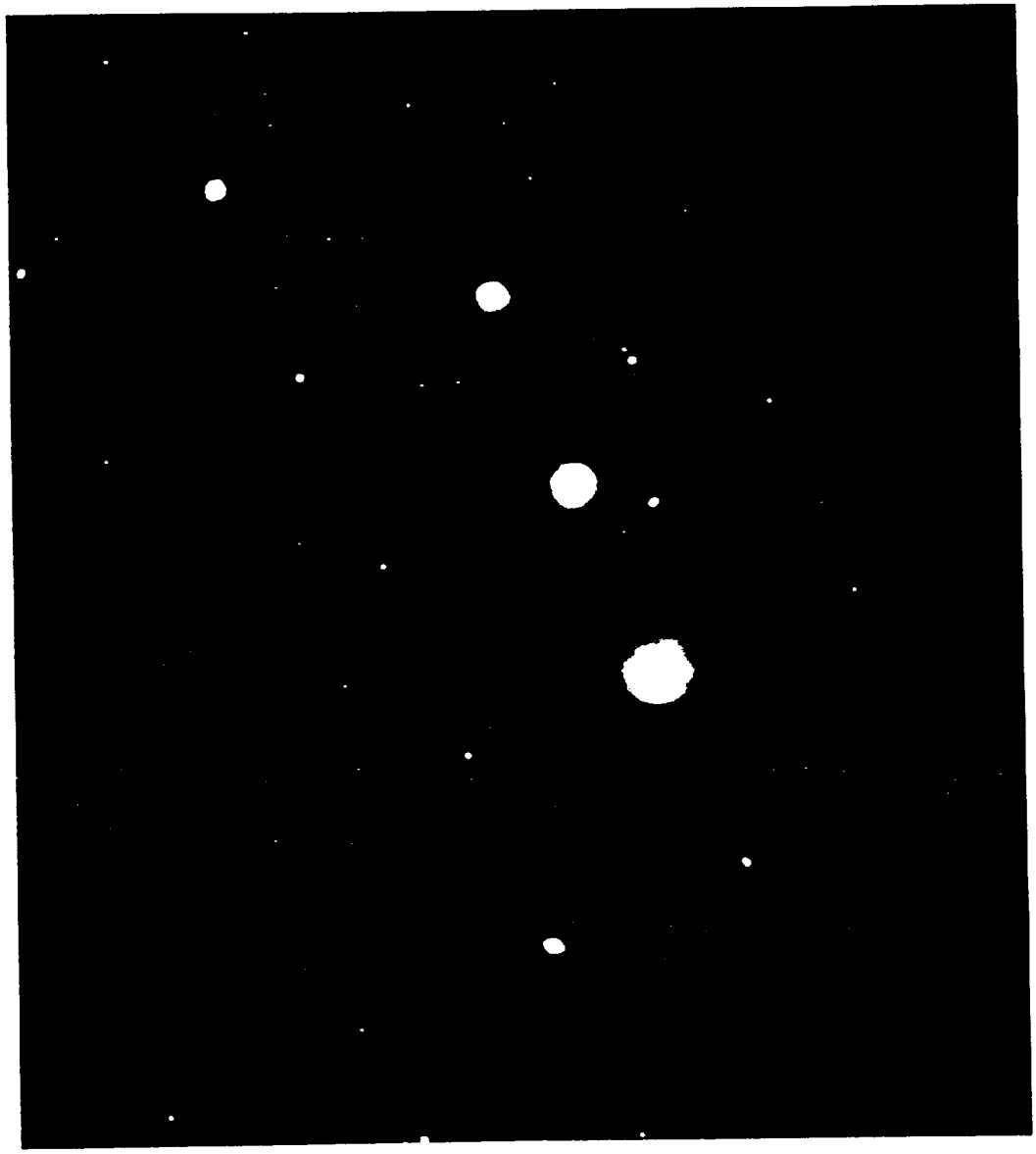

Figure 4.19. TEM Selected Area Diffraction Pattern of As-Spun RSP Cu-5 at.% Cr Alloy. Same Specimen as Figure 4.18 Showing < 100 > Cu Zone Pattern and Absence of Diffraction from BCC Cr

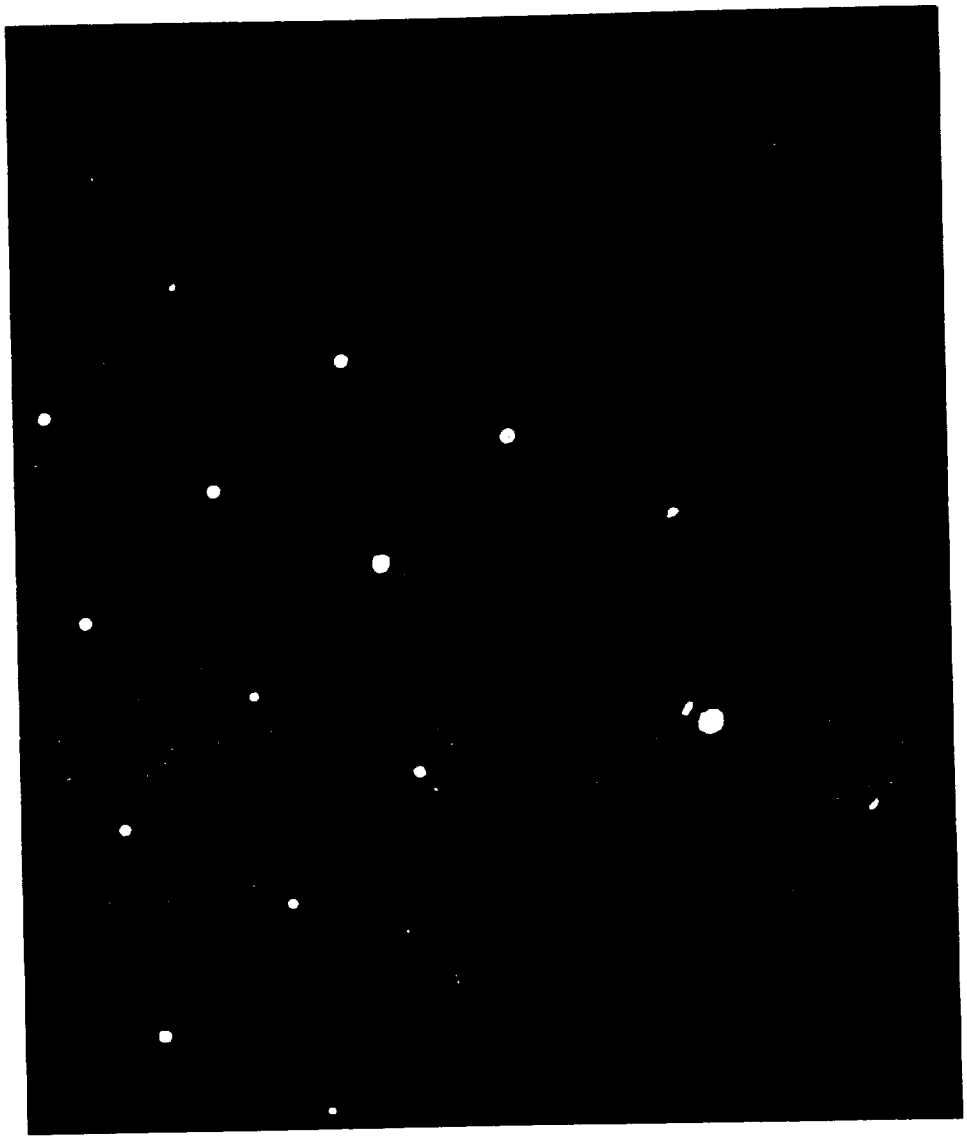

Figure 4.20. TEM Selected Area Diffraction < 110 > Matrix Zone Pattern of As-Spun RSP Cu-5 at.% Cr Alloy. Same Specimen as Figures 4.12 and 4.13. BCC Cr Diffraction Pattern Also Visible

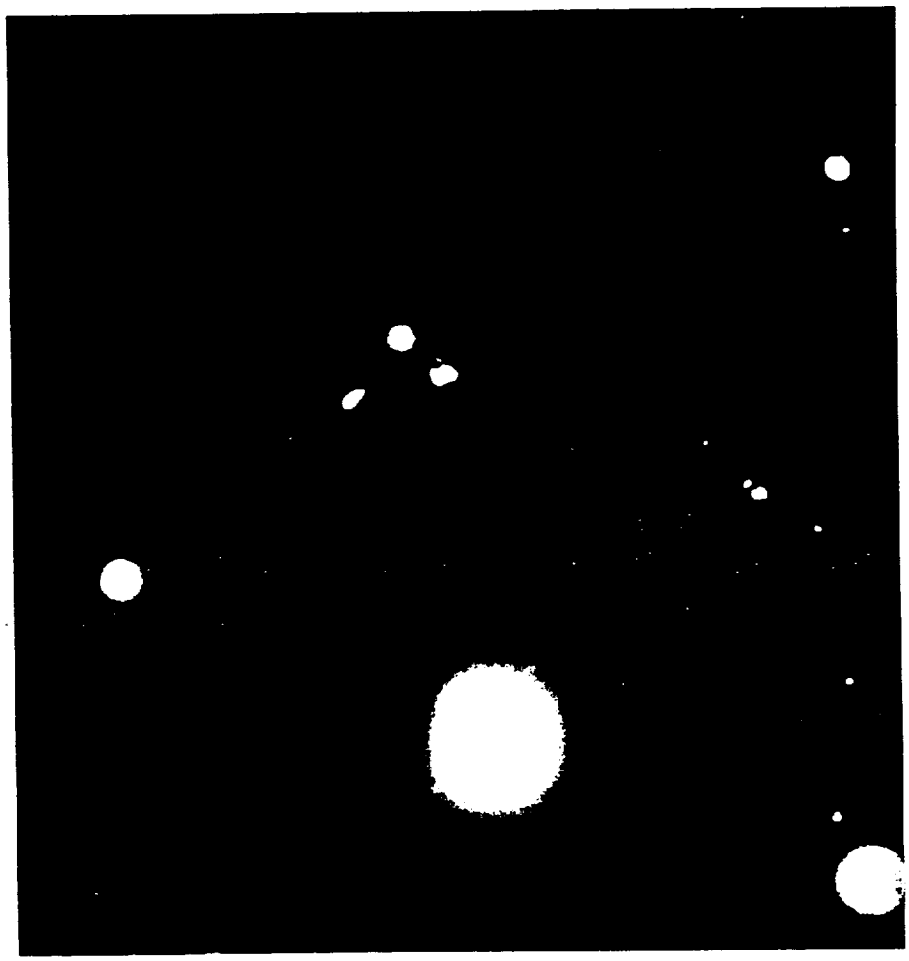

Figure 4.21. TEM Selected Area Diffraction < 110 > Matrix Zone Pattern of As-Spun RSP Cu-5 at.% Cr Alloy. Same Specimen as Figure 4.20. Orientation Relationship between FCC and BCC Diffraction Patterns Evident

The K–S and N–W orientation relationships are best observed by tilting the foil to a $< 111 >_{fcc}$ zone axis, which proved to be difficult using the standard double tilt specimen holder of the Phillips 400 TEM. Because the $< 100 >_{fcc}$ poles were usually normal to the surface of the foil, the specimen would have to be tilted 54.7° to image a $< 111 >_{fcc}$ zone axis, beyond the range of tilt of the specimen holder. Mr. Bruno Buzek was able to provide a $< 111 >_{fcc}$ zone SAD pattern for this work by use of a different TEM and specimen holder, Figure 4.22. The Cu-5 at.% Cr ribbon, MS 549, was aged at 500°C for 4 hours in a helium atmosphere prior to TEM analysis. The specimen has been indexed in Figure 4.23, and clearly shows an orientation relationship very close to K–S; the measured angle between $< 200 >_{bcc}$ and $< 220 >_{fcc}$ is 5°. Most of the diffraction spots can be accounted for by the 3 variants of the K–S relationship, while others are probably a result of non-oriented precipitates at cell boundaries. The SAD analysis of Figures 4.22 and 4.23 is in excellent agreement with the results of [82], although in their SAD pattern only one variant of K–S is shown; this is as expected since their selected area only included a single precipitate to contribute to the diffracted image.

Ageing experiments were carried out on another Cu-5 at.% Cr ribbon, MS 710, in order to observe the microstructural changes during precipitate coarsening. The bright field TEM image of the as-cast specimen is presented in Figure 4.24. The microstructural features are very similar to those of the as-cast MS 573, Figures 4.12 and 4.13. The PFZ for MS 710 however, is narrower than that of MS 573; Figure 4.24 shows a denuded region in the range of 50 to 80 nm width. This is indicative of a more rapid solid state cooling rate for MS 710. The size of the precipitates in the denuded grain boundary region of Figure 4.24 is comparable to that of MS 573; both specimens have precipitates of approximately 60 nm diameter, despite the apparent difference in the cooling rates of the two ribbons.

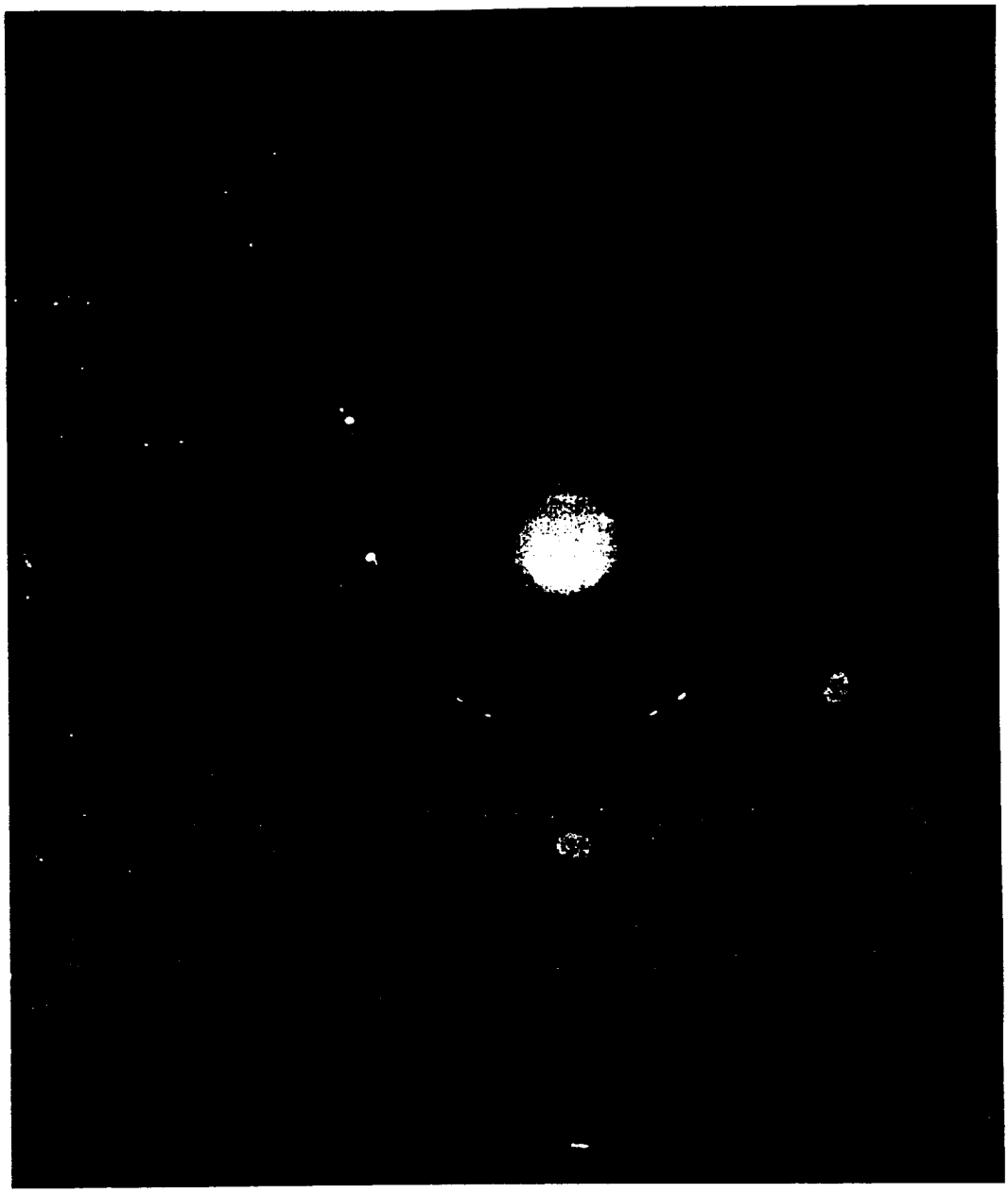

Figure 4.22. TEM Selected Area Diffraction < 111 > Matrix Zone Pattern of RSP Cu-5 at.% Cr Alloy Aged at 773 K for Four Hours

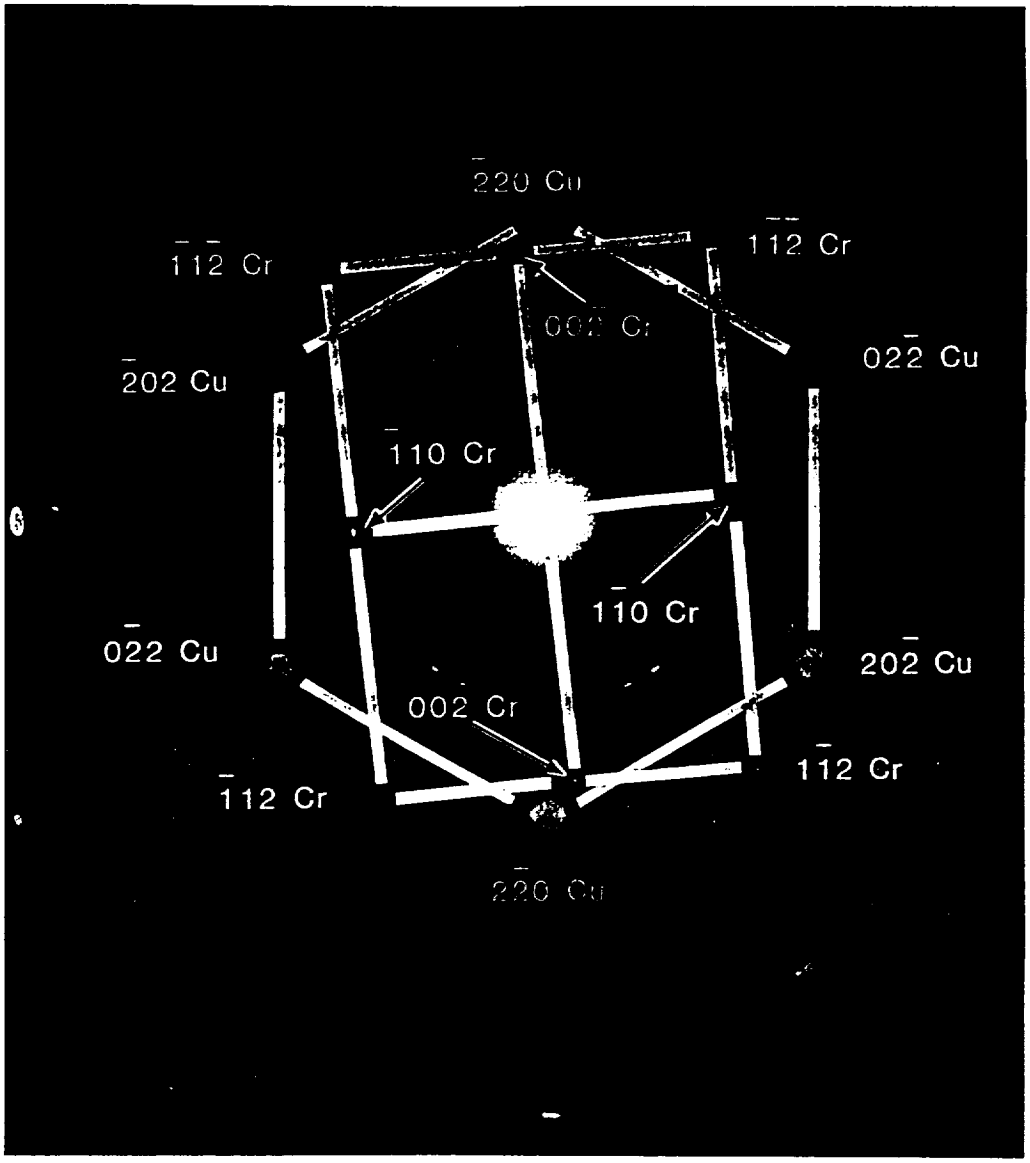

Figure 4.23. Indexed TEM SAD Pattern of Aged RSP Cu-5 at.% Cr Alloy of Figure 4.22 Showing Variants of K–S Orientation Relationship

Figure 4.24. TEM Brightfield Photomicrograph of As-Spun RSP Cu-5 at.% Cr Alloy, MS 710

In Figure 4.24, the cell structure, observed in most of the RSP specimens, is not very well defined. Other TEM specimens prepared from MS 710, however, did contain a regular shaped cell structure. The size of the homogeneously nucleated precipitates within the grains of this specimen cannot be easily determined from the bright field photomicrograph because of the high particle density and overlap of the images.

A section of ribbon from MS 710 was aged at 611°C for 15 minutes in vacuum and then water quenched. The bright field TEM image of this specimen is given in Figure 4.25. It can be observed that grain growth did not occur during the heat treatment despite the high temperature, $T_H = 0.66$. This is a result of the pinning of the grain boundaries by large Cr particles; most of the particles in the PFZ are about 57 nm in diameter, although a few rod shaped particles as large as 113 nm in length are also present. The width of the denuded grain boundary region is in the range of 28 to 70 nm. In the center of the photomicrograph, a very large solute depleted region, 280 nm in width, can be observed. The diffusion of Cr in Cu, near the grain boundary, must be very rapid at this temperature in order to dissolve most of the precipitates during Ostwald ripening. This will likely result in low strength grain boundaries because of the depletion of fine Cr precipitates. For this reason, service temperatures greater than ≈611°C are unreasonable for this particular alloy system.

In Figure 4.26, a different region of the same heat treated ribbon is presented at higher magnification. It can be observed that the cell structure is very pronounced and quite regular shaped. It is apparent that the structure did not recrystallize during the elevated temperature ageing. A high recrystallization temperature in these alloys is desirable for stability of the microstructure and mechanical properties at elevated service temperatures.

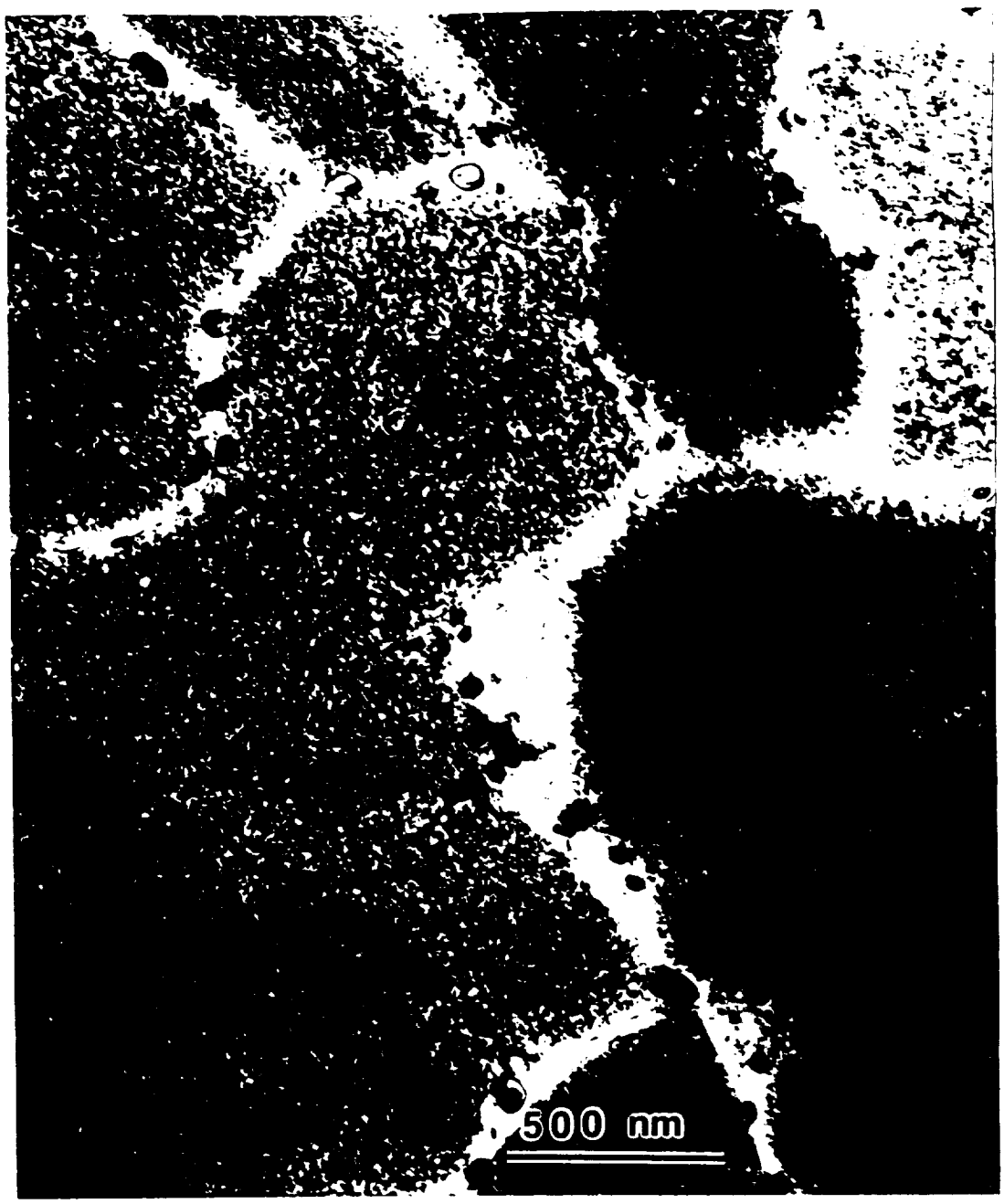

Figure 4.25. TEM Brightfield Photomicrograph of RSP Cu-5 at.% Cr Alloy, MS 710, Aged at 884 K for 15 Minutes

Figure 4.26. TEM Brightfield Photomicrograph of RSP Cu-5 at.% Cr Alloy, MS 710, Aged at 884 K for 15 Minutes, Showing Regular Polyhedral Cell Structure and Pinned Boundaries

Another section of ribbon from MS 710 was aged at 611°C for 60 minutes in vacuum and then water quenched. The bright field TEM image of this specimen is given in Figures 4.27 and 4.28. It can be observed that the grains still have not recrystallized even after a one hour exposure at the elevated temperature. The width of the denuded grain boundary region is in the range of 50 to 85 nm. In the lower right corner of the photomicrograph, a very large solute depleted region, 500 nm in width, can be observed. It is apparent that the width of the PFZ grows fairly rapidly at this temperature by dissolution of the small Cr precipitates near the grain boundaries. In Figure 4.27, it can also be observed that the large Cr particles within the PFZ have coarsened to an average diameter of ≈85 nm. The Cr particles within the cells, Figure 4.28, are much smaller than those in the PFZ; the length of these precipitates is in the range of 7 to 20 nm. The precipitates are of spherical and rod morphologies. For the specimen presented in Figures 4.27 and 4.28, a $< 100 >_{fcc}$ zone SAD pattern is given in Figure 4.29; the objective aperture covers two intense diffracted beams from the bcc ring pattern in this double exposure. In Figure 4.30, the CDF image produced from these two diffraction spots is presented. It can be observed that many of the small Cr precipitates are bright, and thus contribute to the two intense diffraction spots. This effect shows that there is an orientation relationship between the matrix and many of the Cr precipitates. In addition, the ratio of the ring diameter to the distance of the fcc matrix diffraction spots from the transmitted spot, is consistent with the lattice spacings of a pure bcc Cr phase and a solute free Cu matrix. Thus, the composition and crystal structure of the precipitates in these aged, high Cr concentration, RSP alloys are the same as in ingot-cast, commercial Cu-Cr alloys, as would be expected from the equilibrium phase diagram.

It was not possible in this work to resolve the controversy that exists in the literature concerning the crystal structure of the Cr precipitates. The TEM

Figure 4.27. TEM Brightfield Photomicrograph of RSP Cu-5 at.% Cr Alloy, MS 710, Aged at 884 K for One Hour

Figure 4.28. TEM Brightfield Photomicrograph of RSP Cu-5 at.% Cr Alloy, MS 710, Aged at 884 K for One Hour. Cell Structure Still Evident after Longer Ageing Time

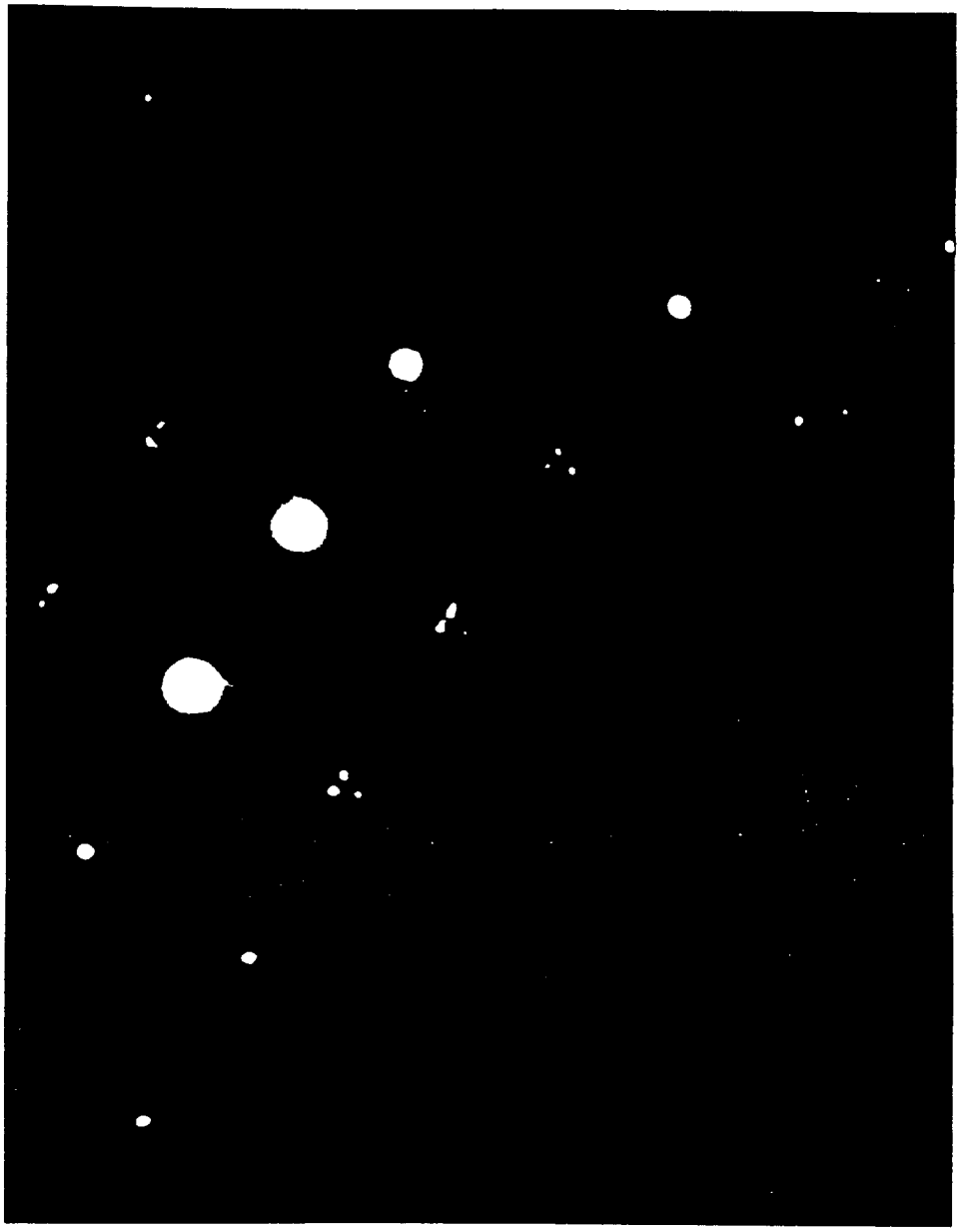

Figure 4.29. TEM Selected Area Diffraction < 100 > Matrix Zone Pattern of RSP Cu-5 at.% Cr Alloy, MS 710, Aged at 884 K for One Hour. Objective Aperture Covers Two BCC Diffraction Spots

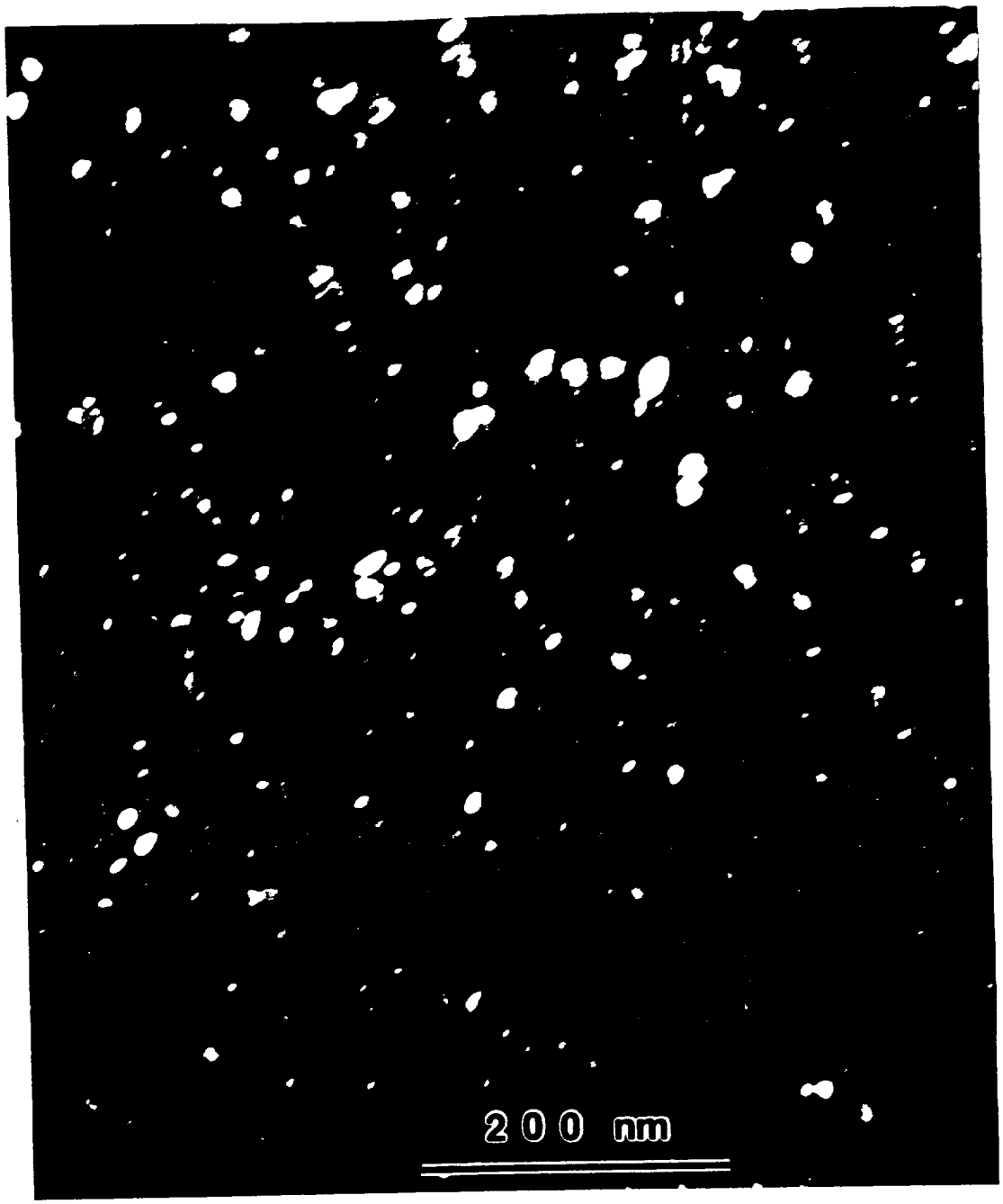

Figure 4.30. TEM Centered Dark Field Photomicrograph of RSP Cu-5 at.% Cr Alloy, MS 710, Aged at 884 K for One Hour. Bright Cr Precipitates Contributed to Diffraction Spots within Aperture of Figure 4.29

results are in reasonable agreement with the work of [77–84]. Because of the high Cr concentration in the RSP alloys, the driving force for precipitation was also very high, and this typically resulted in Cr precipitates in the as-cast ribbon. In all of the as-cast ribbon TEM specimens, except MS 7058 Figures 4.14–4.19, the precipitates produced extra diffraction spots that were indexed to a bcc Cr crystal structure. This result would be expected in an aged alloy, but is not unreasonable for the vacuum-cast RSP alloys which cooled relatively slowly in the range of ≈1000°C to room temperature following solidification. During the few seconds of solid state cooling from high temperature, the homogeneous nucleation and precipitation of bcc Cr occurred. This does not however, rule out the existence of a metastable fcc Cr precipitate. It is possible that the transformation from fcc to bcc has also taken place during the solid state cooling. The absence of a bcc diffraction pattern in the as-cast MS 7058 specimen is supportive of the existence of an fcc Cr phase. This result is not conclusive because of the small volume fraction of precipitates which are able to contribute to the diffraction pattern of Figure 4.19; it could be argued that weak bcc spots might be undetected because of their low intensity relative to the matrix spot pattern. The controversy concerning the determination of precipitate crystal structure in this alloy system has not been settled with the results of this work, and most likely will not be further clarified by TEM experiments. Other techniques, such as precipitate extraction or perhaps field ion microscopy are better suited for resolving this problem.

The microstructural features of the RSP Cu-Cr-Ag alloys are very similar to those of the binary Cu-Cr alloys. TEM specimens were prepared from a Cu-3 at.% Cr-2.8 at.% Ag, MS 705, to observe the changes in the microstructure after ageing. The bright field TEM micrograph of the as-cast specimen is presented in Figure 4.31. It can be observed that the microstructure consists of polygonal cells within grains, as in the binary Cu-Cr RSP alloys. In addition, fine precipitates

Figure 4.31. TEM Brightfield Photomicrograph of As-Spun RSP Cu-3 at.% Cr-2.8 at.% Ag Alloy, MS 705. Polygonal Cell Structure Evident in the Ternary Alloy

are present within the cells and at grain and cell boundaries. The grain and cell size is comparable to the binary alloys presented earlier. At higher magnification, the dense distribution of fine precipitates within the cells of the as-cast ribbon are easily observed, Figure 4.32. Most of the fine precipitates within the cells have a spherical shape. At the cell boundaries, however, large irregular shaped precipitates are present along with the fine precipitates. The large particles are approximately 70 nm in length, whereas the fine precipitates are about 10 nm in diameter. At higher magnification, a line of zero contrast can be observed in some of the fine spherical precipitates within the cells, Figure 4.33. The "coffee-bean" appearance is typical of precipitates that are fully coherent with the matrix, such as Co-rich precipitates in Cu. The same feature has also been observed in the low Cr concentration binary alloys of Cu that have been processed by conventional ingot solidification and precipitation treatments [79,81], although it was not seen in the RSP Cu-Cr alloys of this work. A possible explanation for the absence of this feature may be the distortion of the precipitate strain field due to a neighboring precipitate in the high Cr concentration RSP alloy. The overlap of precipitates is more frequent in the binary Cu-Cr RSP alloys than in the ternary Cu-Cr-Ag alloy of Figures 4.31–4.33, because of the greater Cr concentration in the binary alloy.

A segment of ribbon from MS 705 was aged at 500°C for one hour in an atmosphere of argon followed by a water quench. The bright field TEM image of this specimen can be observed in Figures 4.34 and 4.35. It can be seen that the area near the cell boundaries has become largely denuded of precipitates. Only a few large precipitates remain in this region. This behavior differs from that of the Cu-Cr RSP alloys during elevated temperature ageing, where only the grain boundaries became denuded and the cell boundaries remained rich in precipitates. The grains and cells have not grown or recrystallized during the annealing

Figure 4.32. TEM Brightfield Photomicrograph of As-Spun RSP Cu-3 at.% Cr-2.8 at.% Ag Alloy, MS 705, Showing Fine Spherical Precipitates within Cells and Coarse Particles at Cell Boundaries

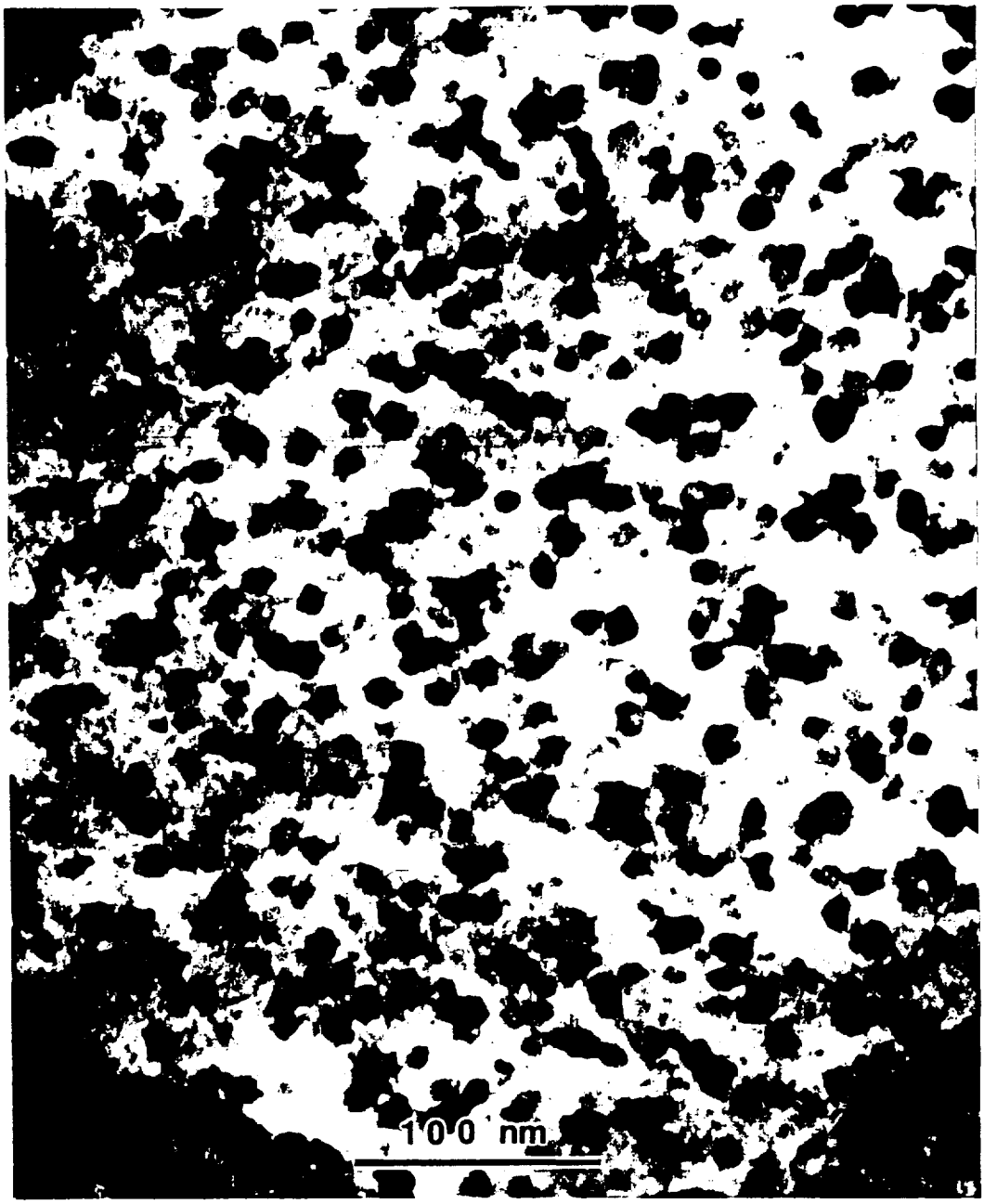

Figure 4.33. TEM Brightfield Photomicrograph of As-Spun RSP Cu-3 at.% Cr-2.8 at.% Ag Alloy, MS 705, Showing Coherent Precipitates within a Cell

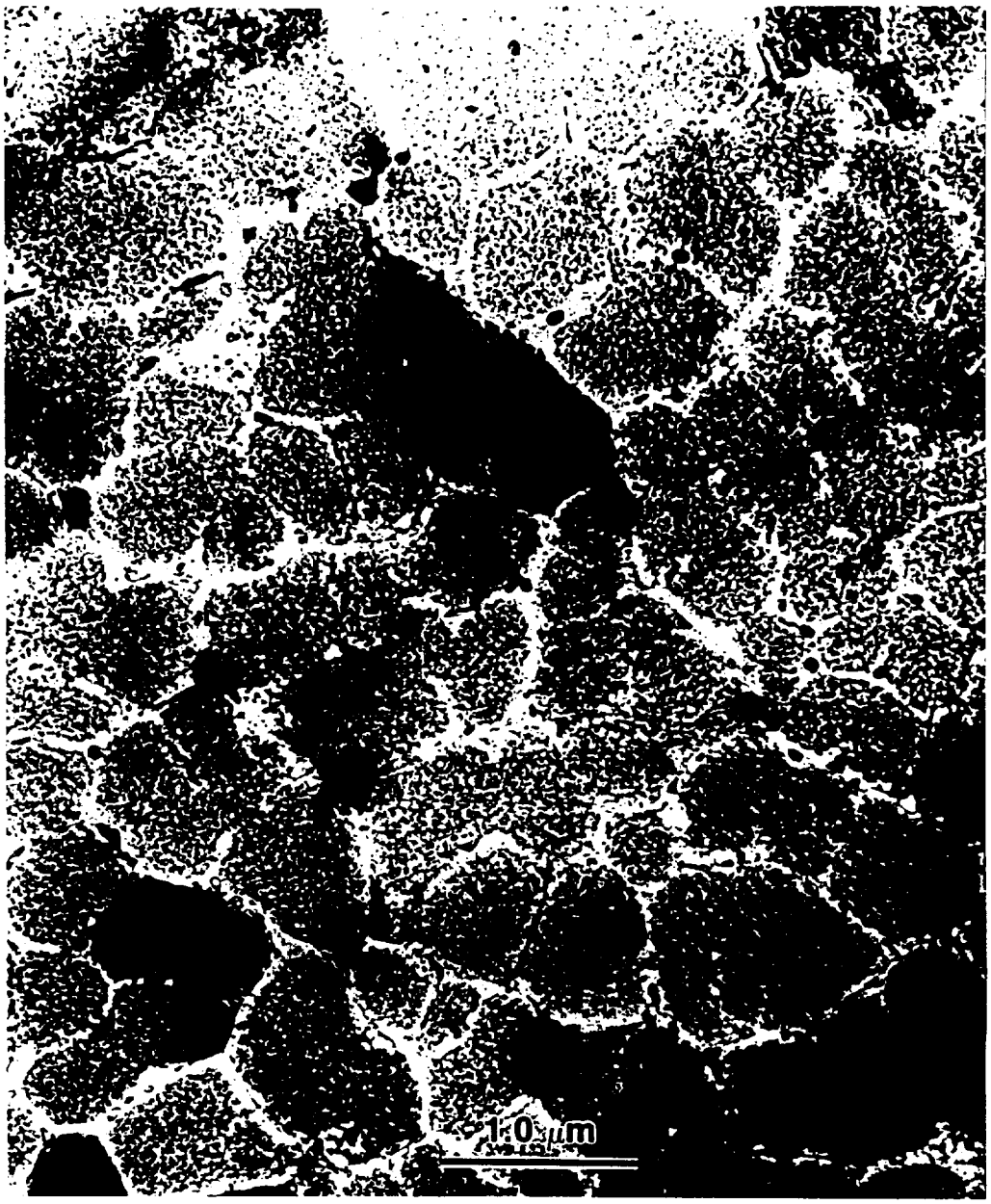

Figure 4.34. TEM Brightfield Photomicrograph of RSP Cu-3 at.% Cr-2.8 at.% Ag Alloy, MS 705, Aged at 773 K for One Hour. Precipitate Free Zone Visible at Cell Boundaries

Figure 4.35. TEM Brightfield Photomicrograph of RSP Cu-3 at.% Cr-2.8 at.% Ag Alloy, MS 705, Aged at 773 K for One Hour. Large Precipitates Visible at Cell Boundaries

treatment due to the large volume of precipitates available to pin the boundaries; grain and cell sizes of the ternary and binary RSP alloys are comparable.

Another segment of ribbon from MS 705 was aged at 600°C for one hour in an atmosphere of argon followed by a water quench. The bright field TEM image of this specimen can be observed in Figures 4.36 and 4.37. After ageing at the higher temperature, it can be seen that the microstructure still has not recrystallized, and that grain and cell growth has not occurred. Severe coarsening of some of the very dark particles can be observed near the cell boundaries; Figure 4.37 shows one of these particles at higher magnification. The composition of this dark particle was identified as silver-rich by the use of EDX. This technique could not be used to analyze the composition of other precipitates because of the relatively large spot size in comparison with the size of the precipitates. The very dark Ag-rich particles were approximately .25–.75 μm in diameter, which is comparable with the cell diameter in this alloy. It appears that in the ternary alloy, the Ag phase coarsens much more rapidly at elevated temperatures than the Cr-rich precipitates. It is very likely that the large, dark precipitates seen at the cell boundaries of Figure 4.32 of the as-cast ribbon are the same Ag-rich phase as in the aged specimen of Figure 4.37. The coarsening of the Ag precipitates at the cell boundaries occurs by dissolution of the small precipitates in these boundaries and by Ostwald ripening of the few remaining large precipitates. This results in a solute and precipitate free cell boundary which is undesirable for mechanical properties as it provides a network of low strength Cu within a higher strength precipitation hardened matrix.

4.5 Tensile Test Data

The results of room temperature tensile tests of five different compositions of RSP ribbons are presented in Figure 4.38. The data for each composition is the

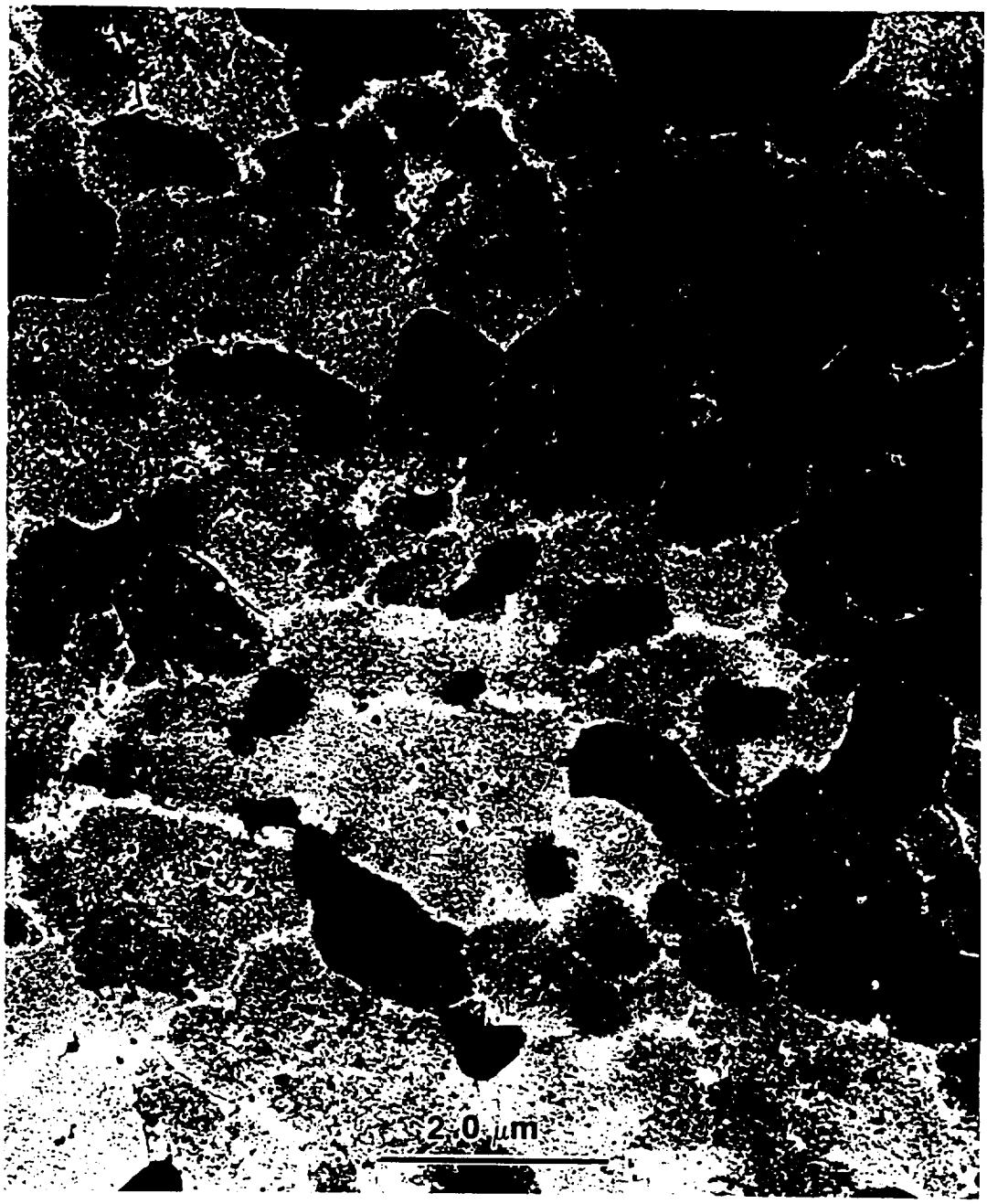

Figure 4.36. TEM Brightfield Photomicrograph of RSP Cu-3 at.% Cr-2.8 at.% Ag Alloy, MS 705, Aged at 883 K for One Hour. Severe Coarsening of Dark Particles Evident

Figure 4.37. TEM Brightfield Photomicrograph of RSP Cu-3 at.% Cr-2.8 at.% Ag Alloy, MS 705, Aged at 883 K for One Hour. Large Dark Particle at Cell Boundary is Silver-Rich

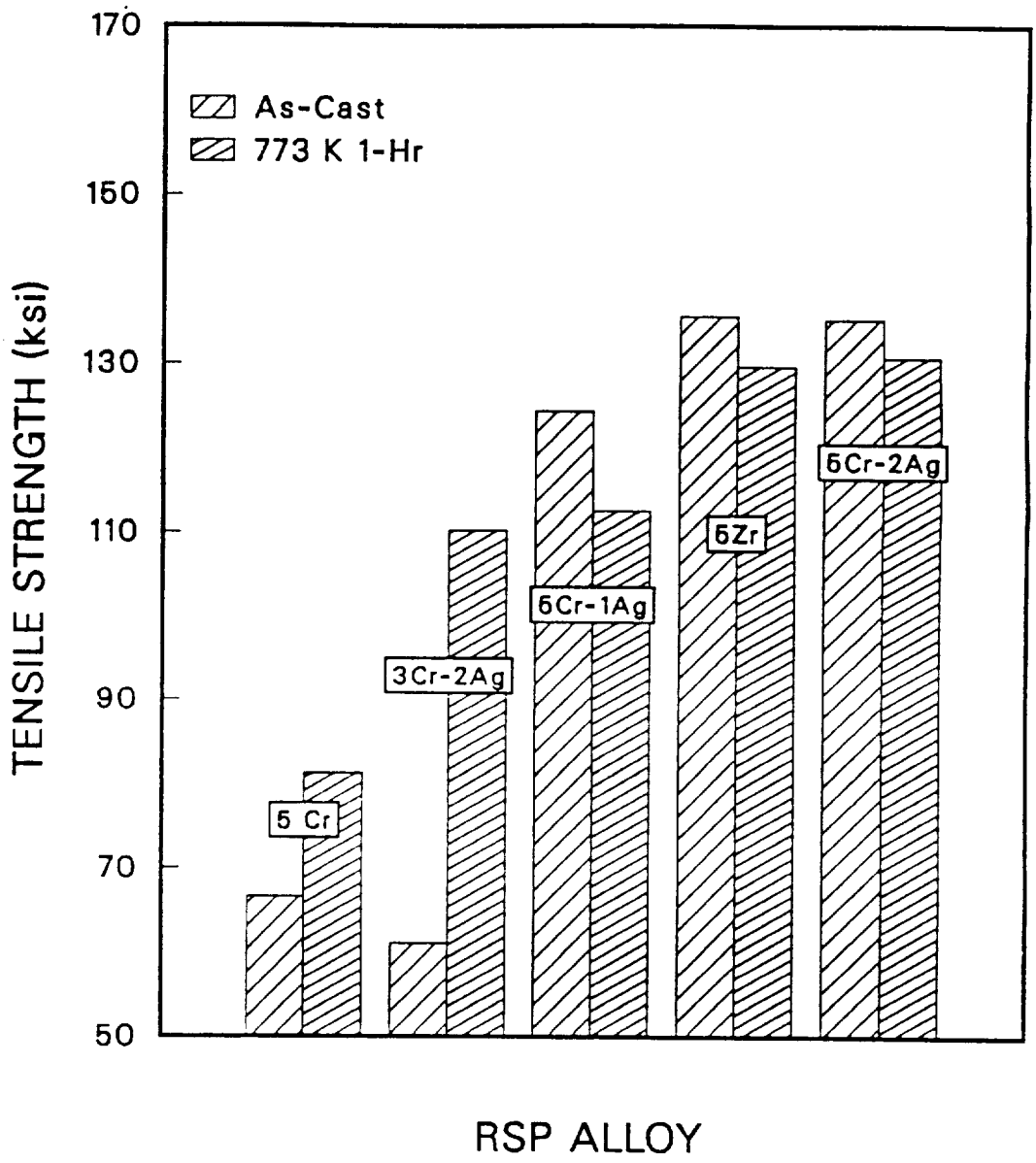

Figure 4.38. Room Temperature Tensile Strength for Five RSP Cu Alloys in As-Cast Condition and after Ageing at 773 K for One Hour

average value of four tests. The tensile properties were measured in the as-cast condition as well as after annealing for 1 hour at 773 K in Ar, followed by a water quench. A temperature of 773 K was chosen for ageing as it represents a typical temperature for precipitation hardening of commercial Cu-Cr and Cu-Zr alloys. At this temperature, the maximum precipitation hardening effect occurs after 1 hour of ageing [67], in ingot-cast Cu-Cr alloys, and overageing is not very rapid.

It can be observed that the RSP Cu-5 at.% Cr alloy has a tensile strength of 66.7 ksi in the as-cast condition and 81.3 ksi after ageing. These results may be compared with commercial Cu-1 at.% Cr alloy where the room temperature UTS is in the range of 51 to 72 ksi in the fully precipitation hardened condition [71]. It is apparent that the large volume fraction of Cr precipitates in the RSP alloy did not have a very significant effect on the tensile strength. One would expect a much larger increase in the strength of the RSP alloy following ageing, considering that the Cr concentration should yield 5 times the volume fraction of precipitates as in the commercial Cu-Cr alloy. It can only be concluded that most of the Cr precipitated and coarsened during solid state cooling of the ribbon in the melt-spinning vacuum chamber. This is consistent with the TEM results already presented, where the typical as-cast microstructure showed dense precipitation of Cr. The 66.7 ksi tensile strength of the as-cast ribbon is also indicative of a precipitation hardened microstructure, as the strength is in the range of fully hardened, commercial Cu-1 at.% Cr alloy. The RSP alloy yields only a moderate incremental increase in tensile strength of 14.6 ksi after ageing for 1 hour at 773 K. In comparison, a 22 ksi increase in tensile strength is typical for fully solutionized commercial alloys, aged to peak strength. The smaller response to ageing of the RSP alloy implies that some precipitation and coarsening has already occurred in the as-cast ribbon. It is difficult to determine the extent of precipitation in the as-cast ribbon and thus the location of ageing time origin is uncertain. The positive

increase in tensile strength, following ageing of the RSP alloy, is consistent with an alloy where at least some of the precipitates start out smaller than the ideal size for pinning mobile dislocations. The relatively small magnitude of that increase, however, would imply that only a small fraction of the precipitate population in the as-cast condition is less than the effective size for strengthening and most of the precipitates are larger than or equal to this critical size.

The tensile strength of RSP Cu-5 at.% Cr ribbon in this study may also be directly compared with the results of [76]. In that work, melt-spun ribbons of the same nominal composition were aged at 723 K for 1 hour; a tensile strength of 110 ksi was reported. This magnitude of strength is very large, considering that the microstructure is indicative of a slow solidification rate. In addition, extensive precipitation was evident in the as-cast microstructure of the optical photomicrographs. The ribbons of [76] were prepared by melt-spinning in a helium atmosphere onto the surface of a copper-beryllium wheel with a 36 m/s surface velocity. These parameters are quite different from those used in the present work; ribbons were cast at 20 m/s in vacuum onto an AISI 4340 steel wheel. The helium atmosphere for melt-spinning produces relatively large cooling rates for the solidified ribbon that has seperated from the wheel. In contrast, casting in vacuum results in slower solid state cooling due to limited convective and conductive heat transfer. The higher casting velocity of [76] should result in a higher rate of solidification and a thinner ribbon. Since the ribbon thickness is similar in the two studies, the melt delivery rate from the crucible to the puddle must have been greater for [76] and this is most likely a result of their larger ejection gas pressures.

One would expect that the experimental methods of [76] will produce a bimodal distribution of precipitate size. Large precipitates of pro-eutectic Cr will form during slow solidification, and small precipitates can nucleate from the

supersaturated matrix during elevated temperature ageing. A high degree of supersaturation is possible because of the fast solid state cooling provided by the helium atmosphere. It is felt that the high strength of these alloys is a result of the small precipitates formed during ageing and not the primary Cr particles of solidification. This is consistent with the increase in tensile strength from 59.8 ksi in the as-cast condition to 99.6 ksi after ageing for 1 hour at 773 K [76].

Despite the higher strength of the RSP alloy produced in a helium atmosphere, it should not be concluded that melt-spinning in vacuum is always an inferior technique. In the present work, some sections of ribbon were produced with only a small amount of precipitation occurring during the solid state cooling of the melt-spin process. If these ribbons had been annealed and tensile tested, it is felt that the mechanical properties would have been superior to those of [76]. It should also be noted that the tensile test results of Figure 4.38 are averaged from individual tests; for example, one of the as-cast Cu-5 at.% Cr specimens had a tensile strength of 90.3 ksi, thus the variability of the results is largely due to the selection of well-quenched ribbons. Unfortunately, during the mechanical properties testing portion of the present work, a reliable method to select ribbon specimens with high solute supersaturation had not been developed. Resistivity testing of individual segments of ribbon can provide quantitative information to determine the degree of Cr supersaturation in the as-cast alloy prior to ageing and mechanical testing. It is recommended that this method be incorporated into the experimental procedures of future researchers in the field of RSP.

In Figure 4.38, it can be observed that the average tensile strength of the Cu-3 at.% Cr-2 at.% Ag alloy, MS 720, is 61.1 ksi in the as-cast condition and increases to 110.2 ksi after ageing for 1 hour at 773 K. The individual test results of the as-cast ribbon were in the range of 49.0 ksi to 71.8 ksi and this represents a much narrower spread in the data than for the Cu-5 at.% Cr alloy.

After ageing at 773 K for 1 hour, the range in the tensile data of the ternary alloy becomes smaller: 105.7 ksi to 118.3 ksi. The large increase in strength after ageing indicates that the solid state cooling rate of the ribbon was fast enough to prevent significant coarsening of precipitates during ribbon casting. This allows for the controlled growth of precipitates during elevated temperature ageing to produce a higher strength microstructure. As was observed earlier, the microstructure of the ternary RSP alloy contains two distinct types of precipitates. If it is assumed that the precipitates exist as pure elemental bcc Cr and fcc Ag, it can be shown that the volume fraction of precipitates is 0.0299 for Cr and 0.0174 for Ag in MS 720. The volume of any precipitate, V_x, is given by

$$V_x = \frac{i_x a_x}{\rho_x} \tag{4.1}$$

where i_x is the insoluble atom fraction, a_x is the atomic weight of element x, and ρ_x is the atomic density. The volume fraction of Cr precipitates, Vf_{Cr} is given by

$$Vf_{Cr} = \frac{V_{Cr}}{V_m + V_{Cr} + V_{Ag}} \tag{4.2}$$

where V_m is the volume of Cu matrix. Therefore, after proper substitutions are made

$$Vf_{Cr} = \frac{(3-.06)\frac{52}{7.20}}{(95)\frac{63.54}{8.92} + (3-.06)\frac{52}{7.20} + (2-.8)\frac{107.87}{10.5}} = .0299 \tag{4.3}$$

This treatment also assumes that the solubilities of Cr and Ag are identical with the equilibrium solubilities of binary Cu-Cr and Cu-Ag at 773 K. Since a ternary phase diagram is not available, it cannot be determined if this last assumption is reasonable.

It is clear that the increase in tensile strength of the RSP alloys with the addition of Ag is dramatic. The alloy, MS 720, contains a smaller volume fraction of precipitates than the Cu-5 at.% Cr alloy, MS 560, yet the tensile strength is 28.9 ksi larger for the aged ternary alloy. If MS 720 is compared with the RSP

Cu-5 at.% Cr alloy of [76], the addition of Ag results in an increase of 10.6 ksi after ageing at 773 K. The beneficial nature of Ag to the mechanical properties was not expected as Ag precipitates have very little effect on the strength or hardness of conventionally cast Cu alloys [63]. In the RSP alloys, it was observed that Ag-rich precipitates form at dislocation cell boundaries; the large boundary area results in a finer distribution of precipitates than in ingot-cast alloys because of the greater number of sites for nucleation. The better precipitate distribution may result in a positive contribution to the strength of these alloys. Silver might also modify the structure or properties of the Cr-rich precipitates in a manner that would inhibit the movement of dislocations and increase the strength of the alloy, but this is just speculation as no observations were made that would support this theory. One would not expect the increase in strength due to Ag additions to be a result of solution hardening, as the solute concentration is relatively small and could not have such a large effect on the mechanical behavior.

The beneficial effect of Ag on the tensile strength is even more pronounced in the Cu-5 at.% Cr-1 at.% Ag and Cu-5 at.% Cr-2 at.% Ag alloys, MS 715 and MS 711, respectively. Both of these alloys exhibited very high tensile strength in the as-cast condition and after heat treatment. It can be observed that the strength of MS 715 decreased from 124.4 ksi to 112.6 ksi following ageing, and that MS 711 showed a smaller drop from 135.3 ksi to 130.8 ksi. The very high initial strength and the drop in strength following ageing is indicative of a precipitation hardened, as-cast microstructure. It is apparent that the microstructures of these alloys have good elevated temperature stability, as evidenced by the high retained strength following ageing at 773 K for 1 hour.

The Cu-5 at.% Cr-2 at.% Ag and Cu-5 at.% Zr compositions produced the highest strength RSP ribbons in this work. Both alloys exhibited remarkably similar strengths both as-cast and after elevated temperature ageing. The Cu-Zr

alloy however, was much less ductile in bend testing and as was observed earlier, produced distinct zones of segregated microstructural features in the RSP ribbon. It was assumed that a low ductility alloy was undesirable for good service life in a combustion nozzle liner. The Cu-5 at.% Cr-2 at.% Ag alloy was selected as the best candidate material for further development because of its high strength with ductility. The amount of strain to fracture during tensile testing of ribbons was very low because of the effect of the large ratio of specimen width to thickness, typically greater than 65. The strain to fracture was in the range of 2.4 to 8.8 % for the alloys of Figure 4.38, however, there was little correlation between the ductility as measured in tensile testing and during bend testing. All of the compositions, except for the Cu-Zr alloys, withstood repeated 180 degree bend testing without fracture. The tensile strain to fracture for the Cu-Zr alloy fell within the range of values measured for the other compositions. Because of this, the ductility of these RSP Cu alloys should not be evaluated using the tensile strain to fracture.

Elevated temperature tensile tests were performed on the Cu-5 at.% Cr-2 at.% Ag ribbons. These specimens were not heat treated prior to loading in the tensile test vacuum chamber. The total time for heat-up and testing was approximately 1/2 hour. Since the room temperature strength of this alloy is not greatly affected by ageing at 773 K for 1 hour, it would also be expected that the elevated temperature tensile properties would be insensitive to the heating time of the specimen. The tensile test results are given in Figure 4.39. It can be observed that the strength decreases with increasing test temperature, as would be expected. There is a rapid fall in strength as the test temperature exceeds 473 K. The elevated temperature strength of this RSP alloy is superior to conventionally cast NARloy-Z at temperatures up to 673 K, beyond this temperature the situation is reversed.

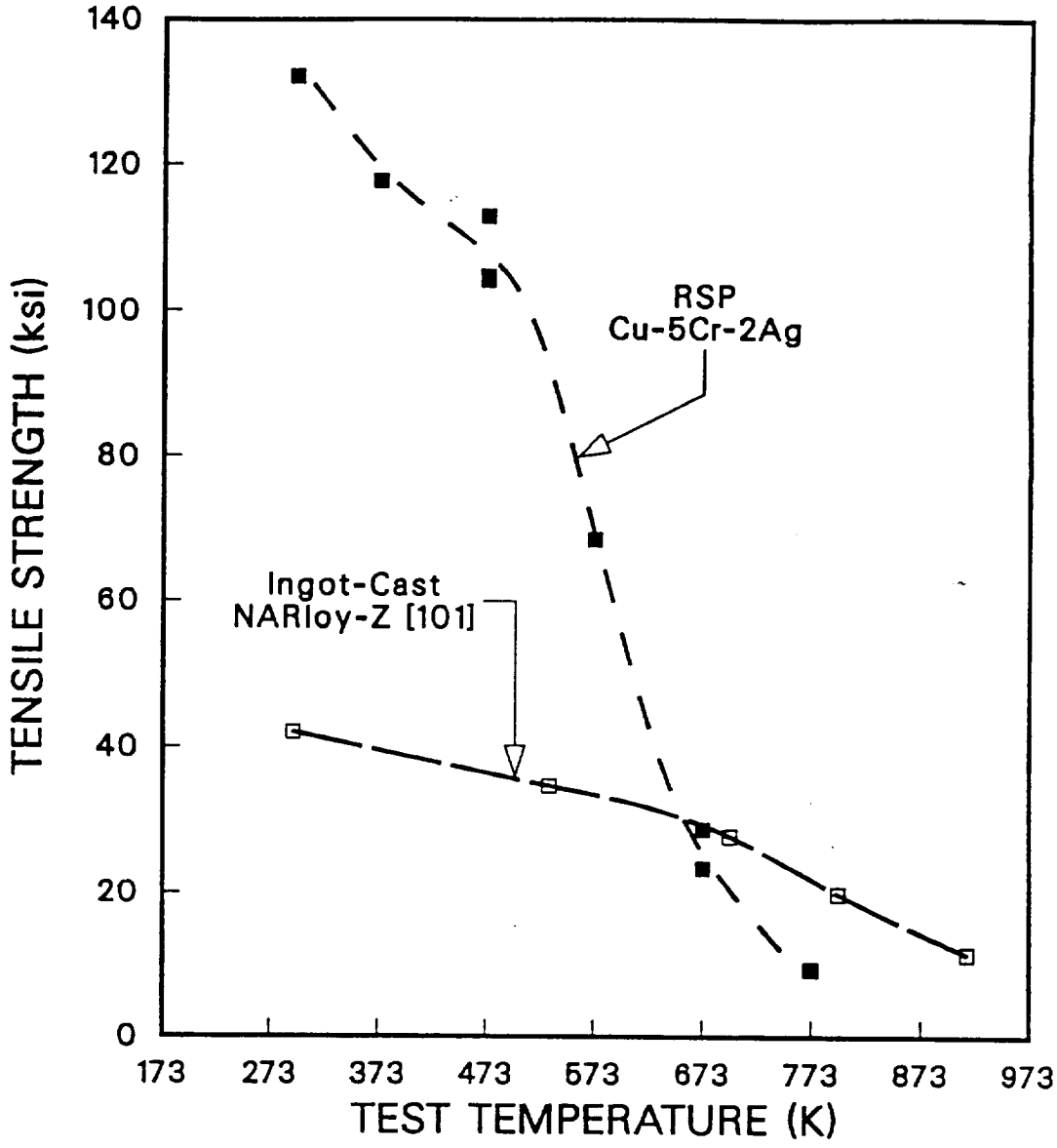

Figure 4.39. Elevated Temperature Tensile Strength of RSP Cu-5 at.% Cr-2 at.% Ag Alloy. Tensile Data for Ingot-Cast NARloy-Z Included for Comparison [101]

The poor strength of the RSP alloy at the very high temperatures was not expected, especially considering the good mechanical properties at low temperatures and the stability of the microstructure after exposure to elevated temperatures. During tensile testing, it was observed that the strain to fracture at 773 K was 15.3 %, which was much larger than any other lower temperature test. Because of the low strength and large apparent ductility at high test temperatures, an SEM investigation of the fracture surfaces was undertaken to determine if the micromechanisms for fracture were changing over the test temperature range.

It can be observed in Figure 4.40 that the SEM fractograph of the Cu-5 at.% Cr-2 at.% Ag ribbon, tested at room temperature, shows evidence of a ductile fibrous fracture with microvoid coalescence. Tensile fracture at 773 K, however, results in a very different fractograph, Figure 4.41. In this case, the fracture surface has a very smooth rippled appearance with no evidence of ductile tearing or microvoid cusps. It is clear that the fracture path is along the cast columnar grain boundaries and very little energy was absorbed during the intergranular fracture process. The smooth rippled appearance indicates that the fracture occurred by grain boundary sliding at the elevated temperature. The large apparent ductility at high test temperatures was an artifact produced by the growth of numerous intergranular cracks and voids which add to the total tensile elongation. The very fine grain size of the RSP microstructure also contributes to the severity of elevated temperature creep in these alloys. The combination of very strong precipitation hardened grains and relatively weak denuded grain boundaries is obviously not compatible with service at elevated temperatures. In order to utilize the significant benefits of a dense precipitate distribution, the grain boundaries must be strengthened to a comparable level. This might be achieved with other alloy additions that would form surface active precipitates that would segregate to and strengthen grain boundaries; the solubility of these

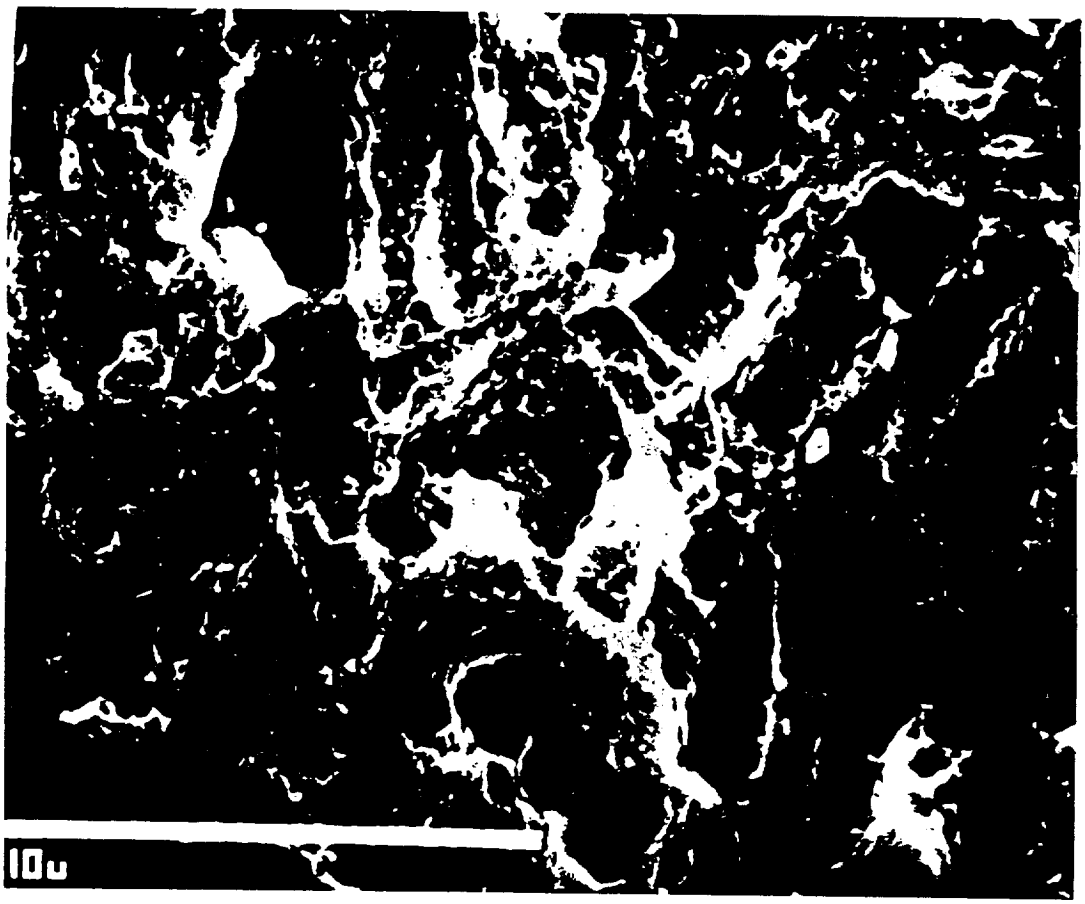

Figure 4.40. SEM Fractograph of RSP Cu-5 at.% Cr-2 at.% Ag Alloy, Aged at 773 K for One Hour and Tensile Tested at Room Temperature

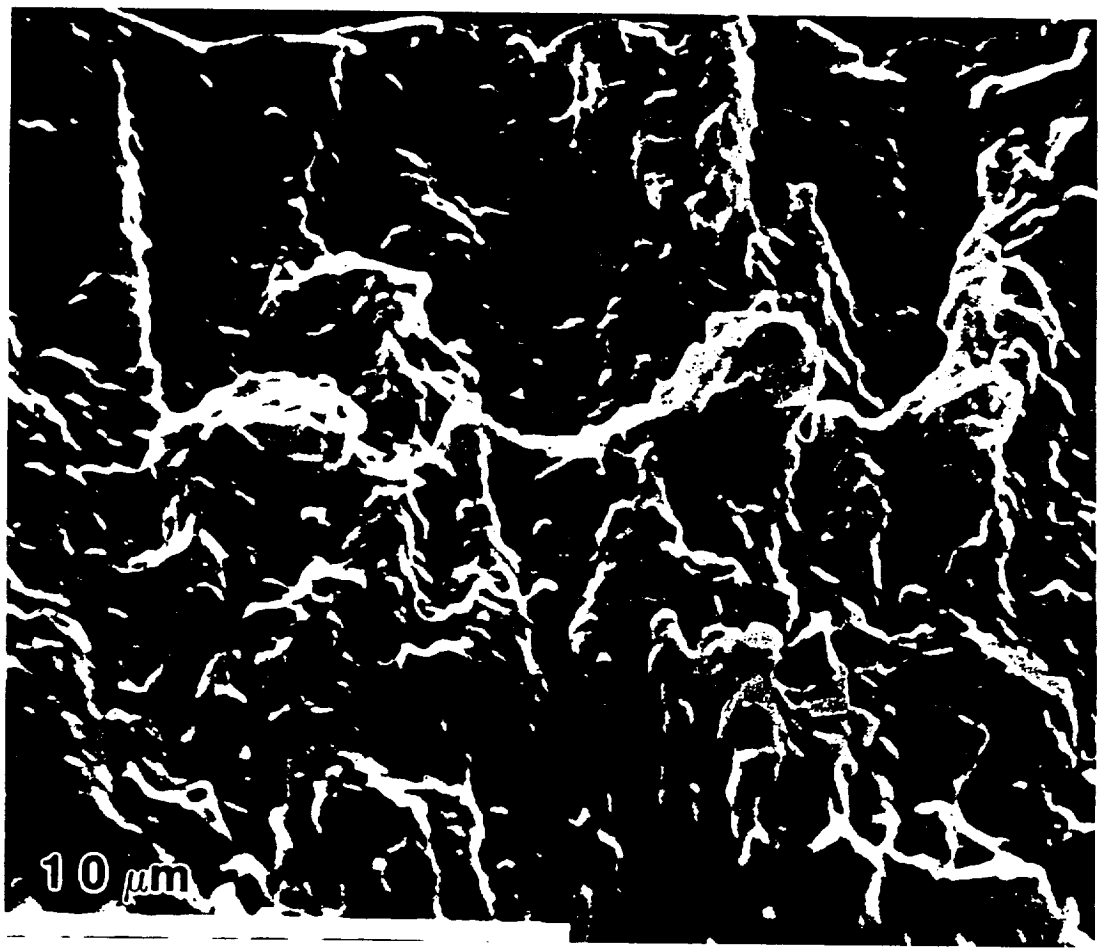

Figure 4.41. SEM Fractograph of RSP Cu-5 at.% Cr-2 at.% Ag Alloy, Tensile Tested at 773 K. Smooth Rippled Appearance Shows Evidence of Grain Boundary Sliding

elements should also be vanishingly small in order to retain the high thermal and electrical conductivity of these alloys. Boron and cerium are two possible alloying additions that might produce the desired effect, although no experimental results are available to support this speculation.

4.6 Resistivity Data

The electrical resistance of RSP Cu-5 at.% Cr ribbons was measured during isothermal ageing in order to study the kinetics of precipitation and coarsening in this system. Commercial Cu-Cr alloys have been investigated extensively with this technique, but the results have often been confusing and contradictory [69,73,80,86,87,88,103]. It was felt that the higher Cr concentration of the RSP alloys in this study would yield a larger effect on the change in resistivity during ageing than the dilute alloys studied previously and thus increase the sensitivity of the measurement technique to the reactions involving Cr.

Resistance measurements are extremely sensitive to minute changes in microstructure that occur during the initial stages of the precipitation process, which makes this technique well suited for the study of GP zone formation. It would be expected that the depletion of solute from the matrix during precipitation would cause a rapid decrease in the resistivity during the initial stage of the process. In the case of coherent GP zone formation, however, large increases in resistivity have been measured in other alloy systems; 4 % in Cu-Be alloys [90] and up to 15 % in Al-Zn alloys [91]. This effect has been attributed to electron scattering when the interzone spacing is on the order of the electron mean free path. As GP zones grow in size during ageing, the electron scattering is attenuated with an increase in the interzone spacing and the resistivity of the alloy will decrease in the usual manner by solute depletion from the matrix. Modest increases in

resistivity, up to 3 %, have been reported for dilute Cu-Cr alloys during the initial stages of elevated temperature ageing [73,86,87,88], but in those studies the effect was largest in alloys air-cooled from the solution temperature. In addition, an increase in resistivity was produced by ageing the alloys at a low temperature prior to a secondary ageing treatment at a higher temperature. The reasonable explanation for this behavior is that the effect is a result of the dissolution, at high temperature, of Cr clusters formed during quenching or during the low temperature heat treatment and not due to the formation of GP zones [73,86,87,88]. Reversion of precipitates will occur when their dimensions are smaller than the critical radius characteristic of the ageing temperature. Since the critical radius for precipitation increases with an increase in temperature, reversion of precipitates is likely to occur during a split ageing treatment whenever the secondary ageing temperature is greater than the primary ageing temperature.

The resistance ratio of RSP Cu-5 at.% Cr, during isothermal annealing for 5 temperatures, is presented in Figure 4.42. The resistance ratio is defined as the change in resistance over the initial resistance of the rapidly solidified ribbon; the resistance values at the various ageing temperatures were normalized to room temperature values by subtraction of the thermal contribution to resistance. It can be observed that the resistance ratio decreases most rapidly during the initial ten minutes of ageing in the temperature range of 699 K to 795 K. The change in resistance then becomes more gradual with increasing ageing times. It can also be observed that the decrease in resistance ratio is more rapid with increasing temperature up to 777 K; this effect becomes smaller on further increasing the ageing temperature to 795 K. At long ageing times, the curves for the two highest temperatures appear to overlap. It would be expected that for very long ageing times, the resistivity will approach the value characteristic of the equilibrium Cr

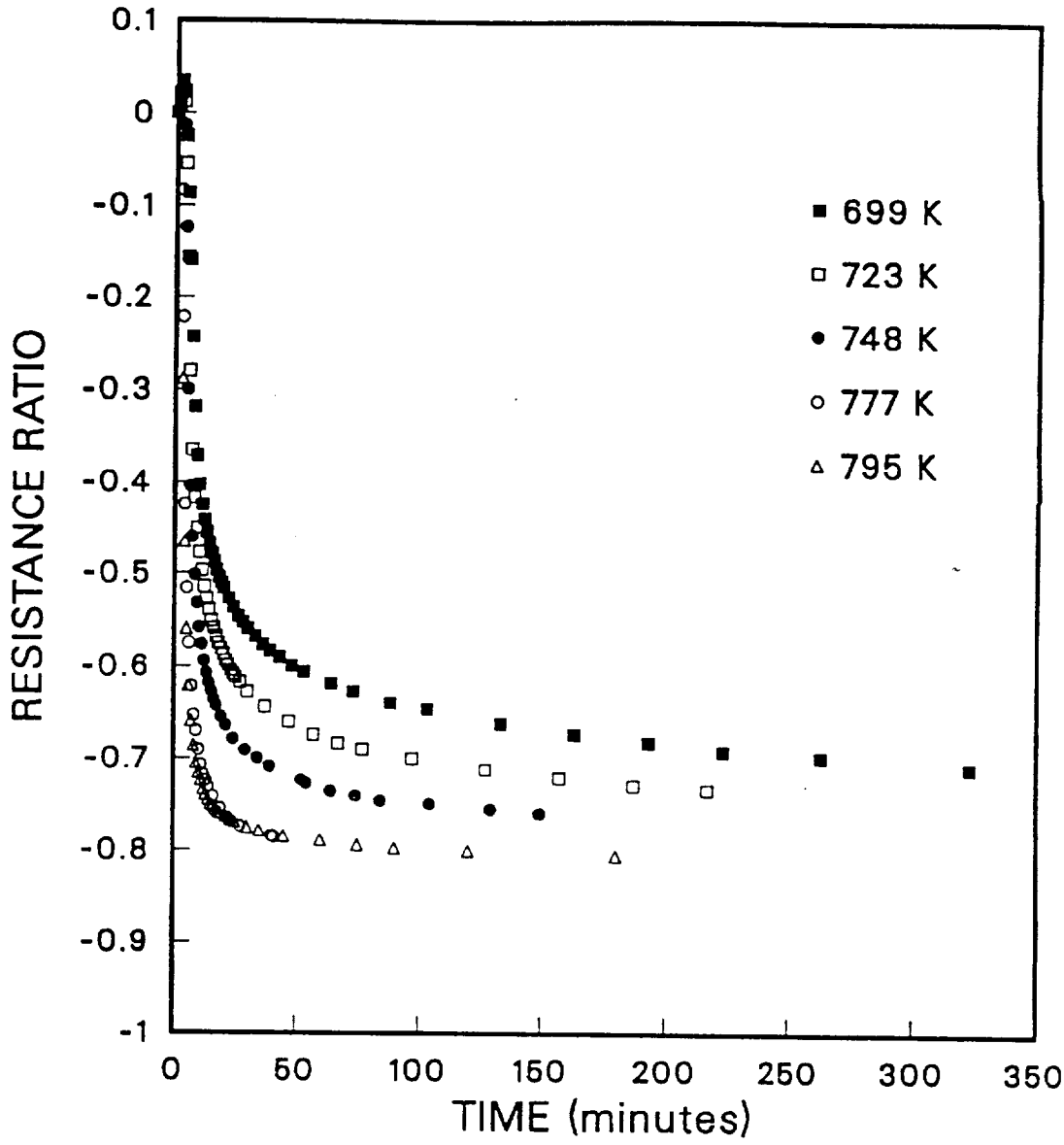

Figure 4.42. Effects of Ageing Temperature and Time on the Electrical Resistance of RSP Cu-5 at.% Cr Alloy During Isothermal Annealing

solubility for the ageing temperature; since Cr solubility increases with temperature, the equilibrium resistivity value also increases with temperature. Thus, the resistivity curves will cross at long ageing times. The magnitude of the resistance ratio drop during the initial stage of ageing for the RSP alloy is much larger than in the dilute, ingot-cast Cu-Cr alloy studied by [73]. The largest change reported was 43 % in a 1.1 at.% Cr alloy which can be compared with the ≈75 % change in resistance measured in the RSP alloy.

There are two factors that can produce this large decrease in the resistivity of the RSP alloy during ageing. Solute depletion from the highly supersaturated matrix would be expected to result in a strong decrease in the resistivity of the alloy during the initial stages of Cr precipitation. The resistivity of the RSP alloy, prior to ageing, is large because of the high Cr concentration in the matrix. After ageing, the resistivity of the Cu-Cr alloys should be only slightly dependent on the composition, since the volume fraction of precipitates does not influence the resistivity as strongly as the Cr in solution. This results in a larger decrease in resistivity for the more concentrated alloys; the same effect was observed by [73] for conventional alloys in the range of .1 to 1.1 at.% Cr. In addition to the effect of high Cr concentration, the resistivity of the alloy will be increased by the high concentration of quenched-in vacancies produced by RSP. Vacancies in solution increase the resistivity in a manner similar to Cr in solution. During ageing, the vacancies diffuse to the surface and also condense out of solution and this produces a decrease in resistivity.

It is probably incorrect to assume that the effect of solute and vacancies on the resistivity are purely additive. The vacancies act as sites for nucleation of Cr precipitates and also enhance the rate of diffusion of solute to the precipitates. Chromium clusters, formed during quenching, are sinks for vacancies. Because of

these interactions, it is difficult to characterize the complex behavior of the early stages of precipitation in terms of the change in resistivity.

The data are replotted in Figures 4.43 and 4.44 in order to more clearly show the change in the resistance ratio during the initial stages of ageing. It can be seen that the resistivity increases by $\approx$3 %, for the three lowest ageing temperatures. This resistivity peak occurs within the first two minutes of ageing. It should be noted that the ribbon specimens had not reached thermal equilibrium with the furnace at the time of the resistivity peak; for example, the actual specimen temperature at two minutes of ageing was only 397 K for the nominal ageing temperature of 699 K.

The positive increase in the resistivity is consistent with the results of [73,86–88] for dilute Cu-Cr alloys and this implies that Cr clusters, formed during the quench, are being dissolved in the matrix. It is difficult to imagine how Cr clusters could dissolve at such a low temperature as 397 K; the high temperature stability of this alloy is inconsistent with rapid solid state diffusion of Cr away from clusters and into the matrix. It is possible that the diffusion of Cr is unusually rapid at low temperatures because of the large vacancy concentration produced by RSP. This high rate of diffusion should decrease rapidly during the first several minutes of ageing as vacancies are annealed out and the vacancy concentration approaches equilibrium.

The positive increase in the resistivity might also be a result of the method used to normalize the data to room temperature values; the thermal contribution to the resistance was subtracted from the measured resistance value during temperature ramping and isothermal ageing. If the thermal response of the thermocouple was slower than that of the ribbon specimen, then the true value of the thermal contribution to the resistance would be underestimated. Thus, the normalized value of the room temperature resistivity would err on the high side and

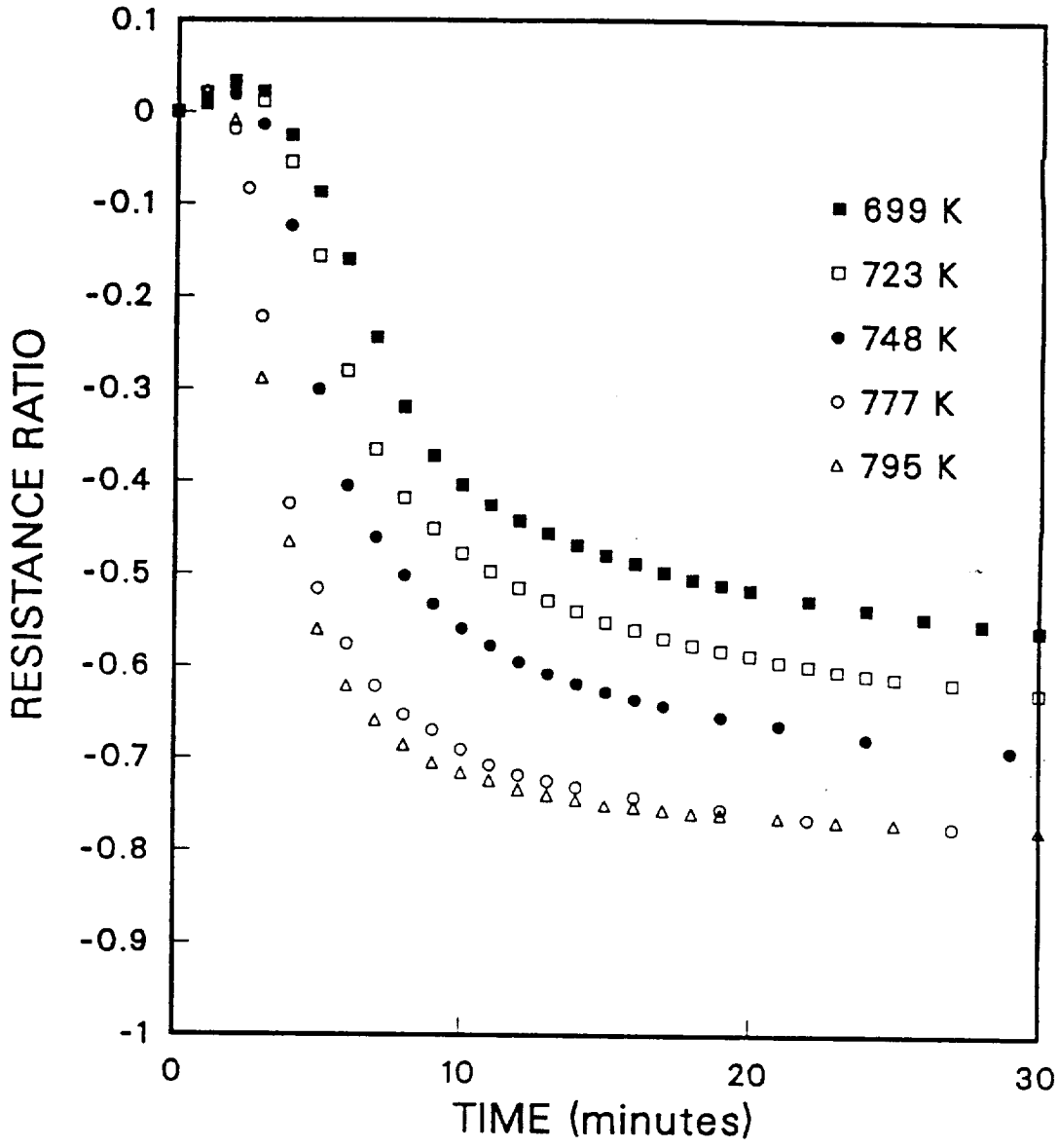

Figure 4.43. Effects of Ageing Temperature and Time on the Electrical Resistance of RSP Cu-5 at.% Cr Alloy During Isothermal Annealing

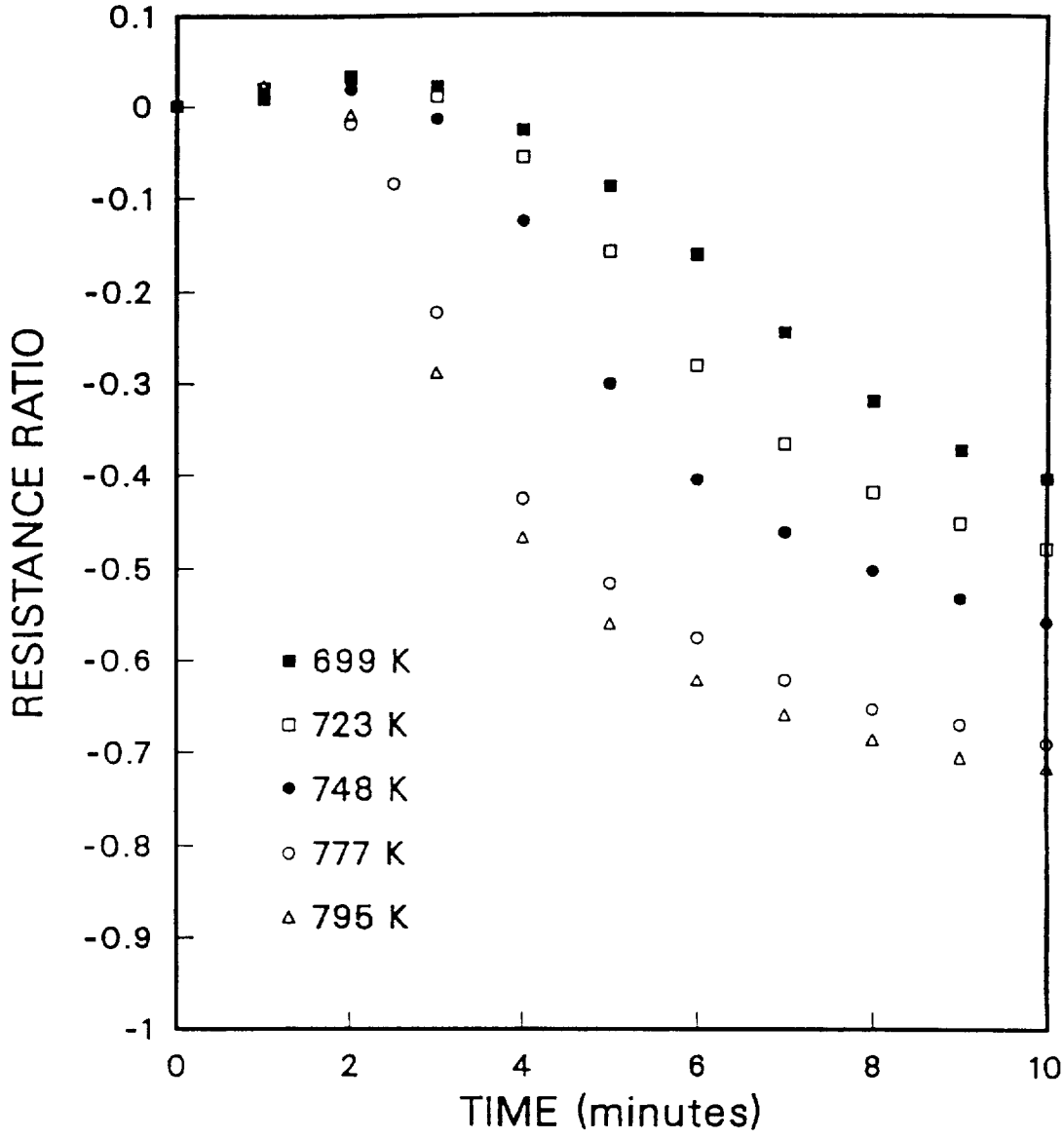

Figure 4.44. Effects of Ageing Temperature and Time on the Electrical Resistance of RSP Cu-5 at.% Cr Alloy During The Initial Ten Minutes of Annealing

could produce a false positive increase in resistivity. For example, a difference of 33 K between the specimen and thermocouple results in a 2 % error in the calculated value of the normalized resistivity ratio. It is quite possible that this magnitude of temperature difference existed during thermal ramping of the specimen, despite the close proximity of the thermocouple and specimen. It would be expected that this type of error is minimized at longer ageing times as thermal equilibrium of the system is achieved.

In any event, the magnitude of the initial positive increase in resistivity was small, despite the large Cr concentration of the RSP alloy. The results are comparable to the more dilute alloys [73,86–88]. Therefore, it can be concluded that during the initial stages of ageing, GP zone formation, if it occurs, does not produce a large increase in resistivity. The higher Cr concentration of the RSP alloy should produce a larger concentration of electron scattering sites than in the commercial alloys; this should give a much larger increase in resistivity with the increasing concentration. The absence of a large positive increase in the resistivity, however, does not preclude the formation of GP zones. It is proposed that a coherent fcc Cr precipitate nucleates from the supersaturated solid solution and transforms to bcc Cr during elevated temperature ageing. This conclusion is consistent with the TEM results of [77,79–82] and the precipitate extraction work of [93].

The absence of a significant increase in resistivity during the early stages of precipitation of GP zones may be rationalized by an analysis of the lattice misfit strain. It is proposed that the resistivity of the alloy is not greatly increased because the misfit strain of the coherent precipitates is too small to disturb the periodicity of the Cu lattice. Even though the GP interzone spacing is assumed to be of the same order of magnitude as the mean free path of the conduction electrons, in the absence of lattice strain, very little electron scattering should

occur. The lattice misfit strain of coherent fcc Cr precipitates in Cu is in the range of .64 to 1.48 %, depending on the exact method of calculation [77,93]. One such method is given as follows: The bcc lattice parameter a_{bcc} for Cr is 2.8847 Å, at 293 K. In the bcc unit cell, the distance of closest approach or the atomic diameter D_{bcc} is given by

$$D_{bcc} = \frac{\sqrt{3}}{2} a_b cc = 2.4982 \text{ Å}. \tag{4.4}$$

In the fcc unit cell, the atomic diameter D_{fcc} is increased by 3 % due to the change in coordination number from 8 to 12. The fcc atomic diameter is also known as the Goldschmidt diameter for coordination number equal to 12, and is given by

$$D_{fcc} = D_{bcc} \times 1.03 = 2.5732 \text{ Å}. \tag{4.5}$$

The fcc lattice parameter a_{fcc} for Cr is given by

$$a_{fcc} = D_{fcc} \frac{2}{\sqrt{2}} = 3.6390 \text{ Å}. \tag{4.6}$$

For fully coherent precipitates of fcc Cr in Cu, the lattice misfit δ is defined as

$$\delta = \frac{2(a_{Cr} - a_{Cu})}{a_{Cr} + a_{Cu}}. \tag{4.7}$$

After substitution of the values for the lattice parameters, the lattice misfit is calculated as

$$\delta = \frac{2(3.6390 - 3.6148)}{3.639 + 3.6148} = +.0067. \tag{4.8}$$

This small amount of lattice misfit in the Cu-Cr alloys can be compared with Al-Ag alloys, in which the misfit is also less than 1 %. The Al-Ag alloys form GP zones during low temperature ageing without producing a significant increase increase in resistivity; the maximum change in resistivity is only about 1.5 % for dilute alloys quenched from low homogenization temperatures [91]. Thus, it is not unreasonable to assume that Cr can form metastable fcc clusters in Cu during the

initial stages of elevated temperature ageing without producing a large increase in resistivity.

In the classical theory of homogeneous nucleation of precipitates in solids, there are three contributions to the total change in free energy

$$\Delta G = -V\Delta G_V + A\gamma + V\Delta G_S \tag{4.9}$$

where the nucleation of a volume V of precipitate will lower the volume free energy of the system by $V\Delta G_V$, the creation of an interface of area A will increase the surface energy of the system by $A\gamma$, and finaly, the volume V of precipitate creates an elastic strain energy due to the lattice misfit that raises the free energy by $V\Delta G_S$. If a spherical precipitate of radius r nucleates, the total free energy can be written as

$$\Delta G = -\frac{4}{3}\pi r^3(\Delta G_V - \Delta G_S) + 4\pi r^2\gamma. \tag{4.10}$$

Differentiation of this equation with respect to r yields

$$\frac{\partial \Delta G}{\partial r} = -4\pi r^2(\Delta G_V - \Delta G_S) + 4\pi r^2\gamma. \tag{4.11}$$

The critical radius of nucleation r^* is determined by setting the left side of this equation equal to zero, and by rearrangement

$$r^* = \frac{2\gamma}{(\Delta G_V - \Delta G_S)}. \tag{4.12}$$

The activation energy barrier for the formation of a homogeneous nucleus ΔG^* is the total free energy from equation (4.10) after substitution for the critical radius r^*:

$$\Delta G^* = \frac{16\pi\gamma^3}{3(\Delta G_V - \Delta G_S)^2}. \tag{4.13}$$

After examination, it can be determined that homogeneous nucleation is not likely to occur when the interfacial energy of the precipitate is large; in fact, incoherent nuclei have such a high value of γ that incoherent homogeneous nucleation

may not be possible. The formation of a coherent interface increases the lattice misfit energy and thus decreases the driving force for homogeneous nucleation. The increase in free energy from a small amount of lattice misfit can easily be compensated for by the large decrease in the interfacial energy for a fully coherent boundary. The Cu-Cr system fits these criteria quite well.

The low misfit strain of fcc Cr results in a very small strain energy contribution, $\approx$ 100 cal/mole of precipitate [77]. Thus, the homogeneous nucleation of a coherent fcc Cr precipitate is energetically favorable. The microstructural evidence for homogeneous nucleation in ingot-cast and RSP alloys is quite convincing. The precipitate distribution is very uniform and a high density of particles are nucleated even in the absence of a high dislocation density from prior cold work. The large solute concentration of the RSP alloys results in a greater supersaturation of the matrix with Cr and increases the driving force for precipitation, making homogeneous nucleation more energetically favorable in these alloys than in ingot-cast alloys.

The reaction rate for the growth of Cr precipitates may be expressed in the form of an Arrhenius equation

$$A = k \exp \frac{-Q}{RT} \tag{4.14}$$

where Q represents the activation energy for the process, T is the temperature on an absolute scale, R is the gas constant and k is a rate constant. The reaction rate A can be determined by measuring the reciprocal of time at temperature necessary to reach an arbitrary value of the fractional change in resistivity. In many studies, reaction rates were determined by the reciprocal of time for a fractional change in resistivity of 0.5 [69,73,80,103]. The fractional change in resistivity ΔR_f is defined as

$$\Delta R_f = \frac{R_s - R_t}{R_s - R_{t-\infty}} \tag{4.15}$$

where R_s is the resistivity of the fully solutionized specimen, R_t is the resistivity after ageing for time t, and $R_{t\to\infty}$ is the resistivity at very long ageing times when the transformation is complete. The Arrhenius equation is valid for any method used to measure a process controlled by a single activation energy. The fractional change in resistivity is just one such method; a more direct approach is to measure the change in precipitate diameter during coarsening [79], which was not practical for the high density of precipitates of the RSP alloys in this work.

The activation energy may be determined from a plot of the natural logarithm of the reciprocal of time against the reciprocal of the absolute temperature. The negative product of the slope of the curve and R is equal to the activation energy for the process.

In Figure 4.45, the resistivity data are plotted according to the Arrhenius method for three values of the resistivity ratio; -.3, -.6, and -.7. At very long ageing times, the resistivity ratio approached a value of -.82, which was taken as the value for complete transformation. Thus the resistivity ratios of -.3, -.6, and -.7 are equivalent to .37, .73, and .85 fractional transformation, respectively. It is apparent that there is not a unique slope despite the relatively good linear fit of the data for each of the three resistance ratios, Figure 4.45. For the two lower curves, the highest ageing temperature data points were ignored in the determination of the slopes. The actual specimen temperature was much less than the nominal value of 795 K during a significant fraction of the annealing cycle because of the very short duration of the total ageing time at high temperature; this results in erroneously longer times for the highest temperature data.

It would be expected that a single thermally activated process will yield parallel curves of a unique slope when the data are plotted in this manner. It can be concluded that the change in resistance ratio during ageing in the RSP Cu-Cr alloy cannot be described by a single thermally activated process, such as the

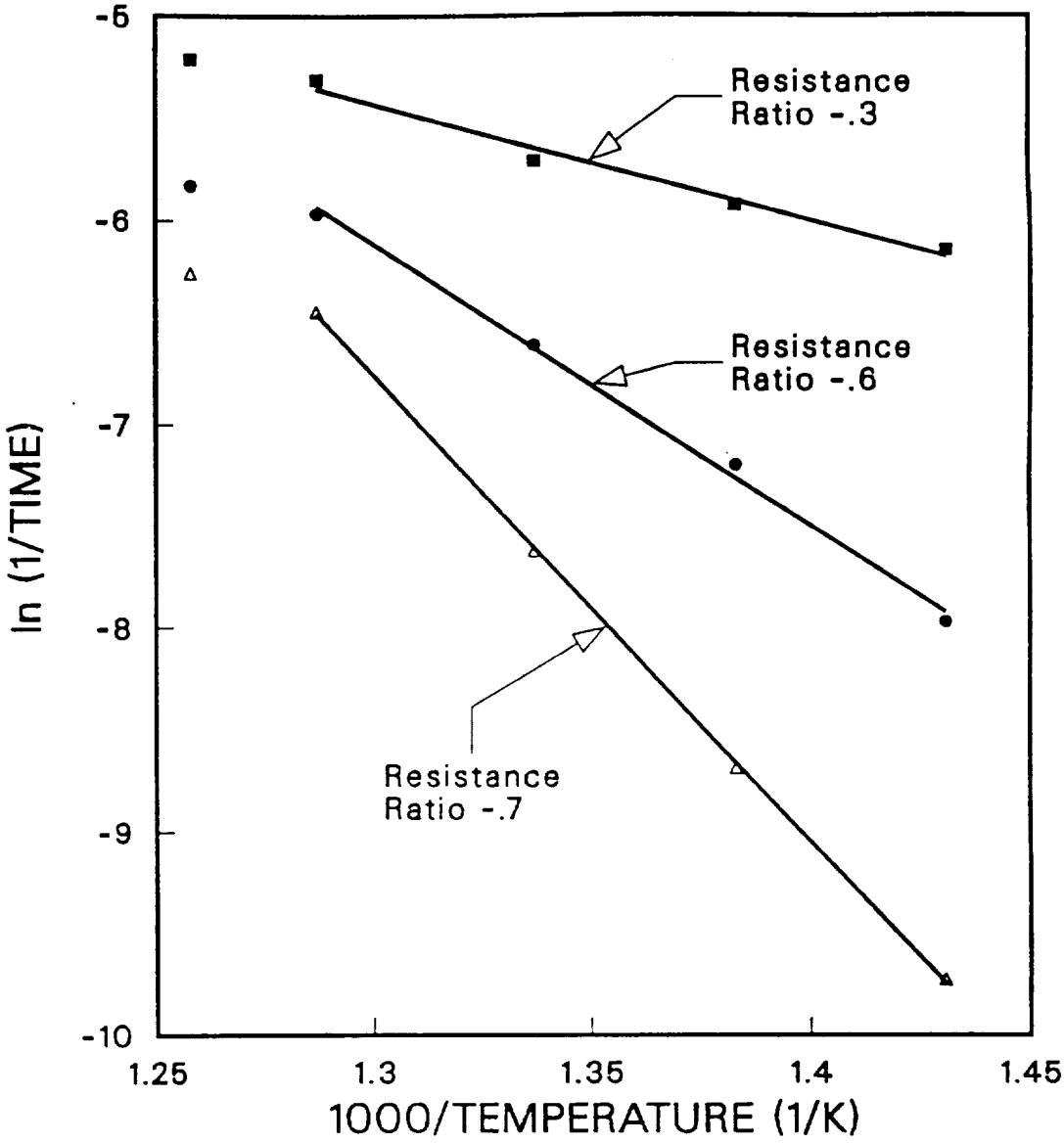

Figure 4.45. Arrhenius Plot of the Electrical Resistance Data for RSP Cu-5 at.% Cr Alloy During Isothermal Annealing

diffusion of Cr to precipitates. The activation energy determined at $\Delta R_f = .37$ is 0.49 eV (11.3 kcal/mole). This small value is not reasonable for the diffusion of a substitutional solute in Cu, and is similar in magnitude to theoretical calculations of the vacancy migration energy [73]. In Figures 4.42–4.44, it can be observed that the resistance ratio of -.3 corresponds to very short ageing times, where the change in resistivity with time is greatest. It would be expected that during the initial stage of ageing, the rapid decrease in resistivity is mainly a result of the annealing out of vacancies; thus, the measured activation energy of 0.49 eV most likely corresponds to the process of vacancy diffusion.

At longer ageing times, beyond about ten minutes, the change in resistivity with time becomes more gradual, Figures 4.42–4.44. It can be observed that for a resistance ratio of -0.7, the slopes of the isothermal ageing curves approach a value of zero. It is felt that the horizontal portion of the curves represents a steady state change in resistivity caused by coarsening of precipitates. The activation energy, determined at $\Delta R_f = .85$ is 1.97 eV (45.3 kcal/mole), Figure 4.45. This value is similar to the activation energy of 2.08 eV determined in a 0.6 wt.% Cr alloy at $\Delta R_f = 0.5$ [69]. A similar value of 2.09 eV was determined in a 0.35 wt.% Cr alloy by the more direct method of TEM measurement of the precipitate growth rate [79]. This last method is often used to determine the activation energy of diffusion in systems where the growth rate of the precipitates is controlled by the diffusion of solute. While the close agreement of these values for Q is encouraging, it should be noted that others have reported a wide range of values using the fractional resistivity transformation of 0.5: [73] reported values of 1.50 eV (34.6 kcal/mole), 1.15 eV (26.5 kcal/mole), and 1.12 eV (25.8 kcal/mole) in .30, .49, and .91 wt.% Cr alloys, respectively. In addition, [105] reported a value for Q of 1.70 eV (39.2 kcal/mole) in a 0.90 wt.% Cr alloy, and [80] reported a value of 1.35 eV (31.1 kcal/mole) in a 0.15 wt.% Cr alloy. It is likely that

the variation in reported values of activation energy is a result of the overlap of thermally activated processes; vacancy diffusion, precipitate nucleation, and precipitate growth. This condition is most likely to occur at intermediate ageing times when the slope of the change in resistivity with ageing time is changing rapidly; in the RSP alloy this change in slope occurs after about ten minutes of ageing in the temperature range studied, Figures 4.42–4.44. The resistance ratio of -.6 in the present study corresponds to this region of the curves for the higher ageing temperatures; Q is equal to 1.19 eV (27.4 kcal/mole) for $\Delta R_f = .73$, which is comparable to the values determined by [73,80].

These results show that the change in resistance during ageing for the Cu-Cr alloys is best explained by a two stage process; vacancy diffusion and annihilation during the initial ten minutes at temperature, and diffusion controlled coarsening of Cr precipitates during longer ageing times. The homogeneous nucleation of Cr precipitates should be controlled by the volume diffusion of Cr, with assistance from the excess vacancies from the rapid quench. Therefore, the activation energy of nucleation should be the same as that of diffusion, approximately 2 eV. It is probable that nucleation has begun within the first ten minutes of ageing, although the apparent activation energy for short ageing times (.49 eV for $\Delta R_f = .37$) is not greatly affected. The overall transformation rate at short ageing times may be considered as the sum of the individual reaction rates for vacancy and solute diffusion; this assumes that nucleation is not affected by the vacancy concentration, which is not strictly true. The Arrhenius plots of Figure 4.45 show that the reaction rate for vacancy diffusion is larger than the reaction rate for solute diffusion for ageing temperatures as high as 795 K, and the magnitude of this difference increases with decreasing temperature. This is illustrated by the divergence of the curves for .37 and .85 fractional transformation. As a result, the overall reaction rate is dominated by the rate for vacancy diffusion,

especially at low ageing temperatures; thus the overall activation energy does not indicate the simultaneous occurrence of nucleation. When the vacancy concentration approaches equilibrium for the ageing temperature, after several minutes of ageing, the overall reaction rate is largely determined by the diffusion of Cr.

The resistivity data may also be analyzed according to the formal theory of precipitation kinetics [106], by use of the Johnson-Mehl or Avrami equation

$$x = 1 - \exp[-(\frac{t}{\tau})^n] \tag{4.16}$$

where $x = \Delta R_f$ the fractional transformation of the process at time t, τ is a time constant, and n is the growth exponent. By rearrangement, this equation may also be written as

$$\log\log(\frac{1}{1-x}) = n\log t - n\log\tau + \log 2.3. \tag{4.17}$$

Thus a plot of $\log\log(\frac{1}{1-x})$ as a function of $\log t$ should yield a linear curve of slope equal to n, and τ is equal to the time at $x = .63$.

The resistivity data have been plotted in this manner for 5 ageing temperatures in the range of 699 K to 795 K, Figure 4.46. It can be observed that none of the curves exhibit a unique slope over the entire ageing time. The curves can best be described as having two linear portions with a transition at approximately ten minutes of ageing. The initial slope of the curves at short ageing times is in the range of 5 to 6, while at long times the value for n is in the range of .17 to .20.

At one time, it had been assumed that the value for n, determined by a kinetic investigation, provided sufficient information to deduce the growth habit of the precipitates. It is now known that this assumption is incorrect [107]. For the case of diffusion controlled growth of Cr precipitates in Cu, a value of $n \geq 2.5$ is consistent with any shape of precipitate growing from small dimensions and

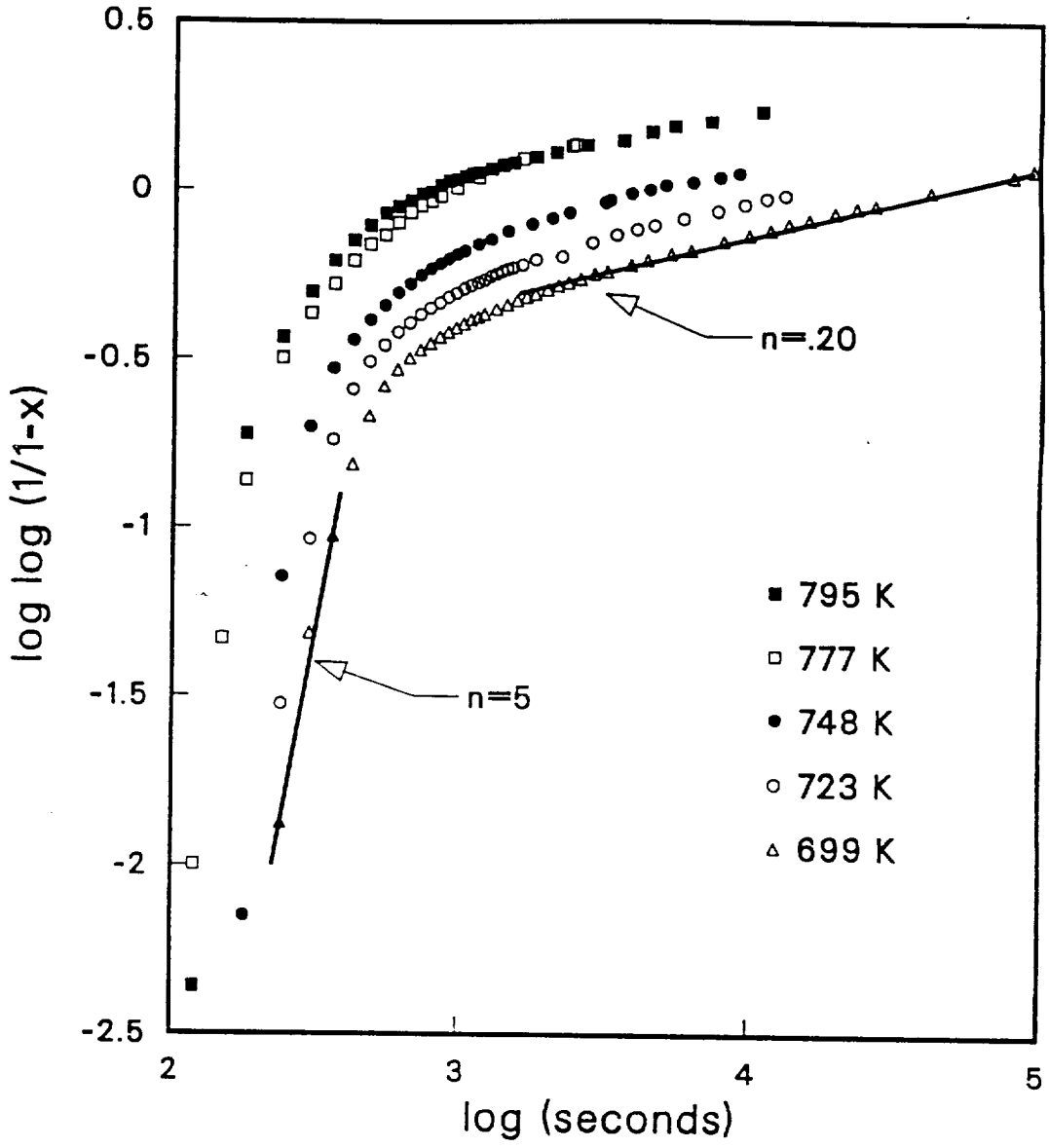

Figure 4.46. Electrical Resistance Data for RSP Cu-5 at.% Cr Alloy During Isothermal Annealing, Plotted According to the Avrami Method

with an increasing nucleation rate. The analysis is further complicated by the effects of vacancy diffusion and annihilation during the initial stages of ageing, which would be expected to the increase the value of n. The very small value of n at longer ageing times indicates that site saturation for nucleation has occurred during the first ten minutes of ageing. The annihilation of vacancies may also be thought of as a site saturation process as after a short period of ageing the equilibrium vacancy concentration will be reached; thus, the change in resistivity due to this effect will approach zero. It is not possible to deduce the shape of the precipitates at long ageing times from the value of $n \approx .2$. Other factors besides precipitate shape can strongly influence the value for n. For example, the effects of an external surface may reduce the value of n by up to 1 for a thin foil and up to 2 for a wire [107]. Despite the limitations of the Avrami exponential growth law analysis, it can reasonably be concluded that precipitation in the RSP Cu-Cr alloy is a two stage process.

The exponential growth law has been used previously to determine the kinetics of precipitation of more dilute Cu-Cr alloys [73,80,105]. Unfortunately, the results have been inconsistent. The data of [80,105] are presented in Figure 4.47 along with the RSP alloy data for comparison. It can be observed that the curves for the RSP Cu-5 at.% Cr alloy and the 1.1 at.% Cr alloy [105] fall nearly on top of each other, especially at short ageing times. In addition, the slopes of the curves are similar for most ageing times other than the transition period around ten minutes. In contrast to this behavior, the curve for the 0.18 at.% Cr alloy [80] is offset in the direction of longer ageing times, and does not clearly show the break in slope of the other curves. The RSP alloy data and the data of [105] were produced by making in-situ resistivity measurements during ageing, while the results of [73] and [80] were produced by measuring the resistivity at 303 K and liquid nitrogen temperatures, respectively. It is quite likely that the repeated

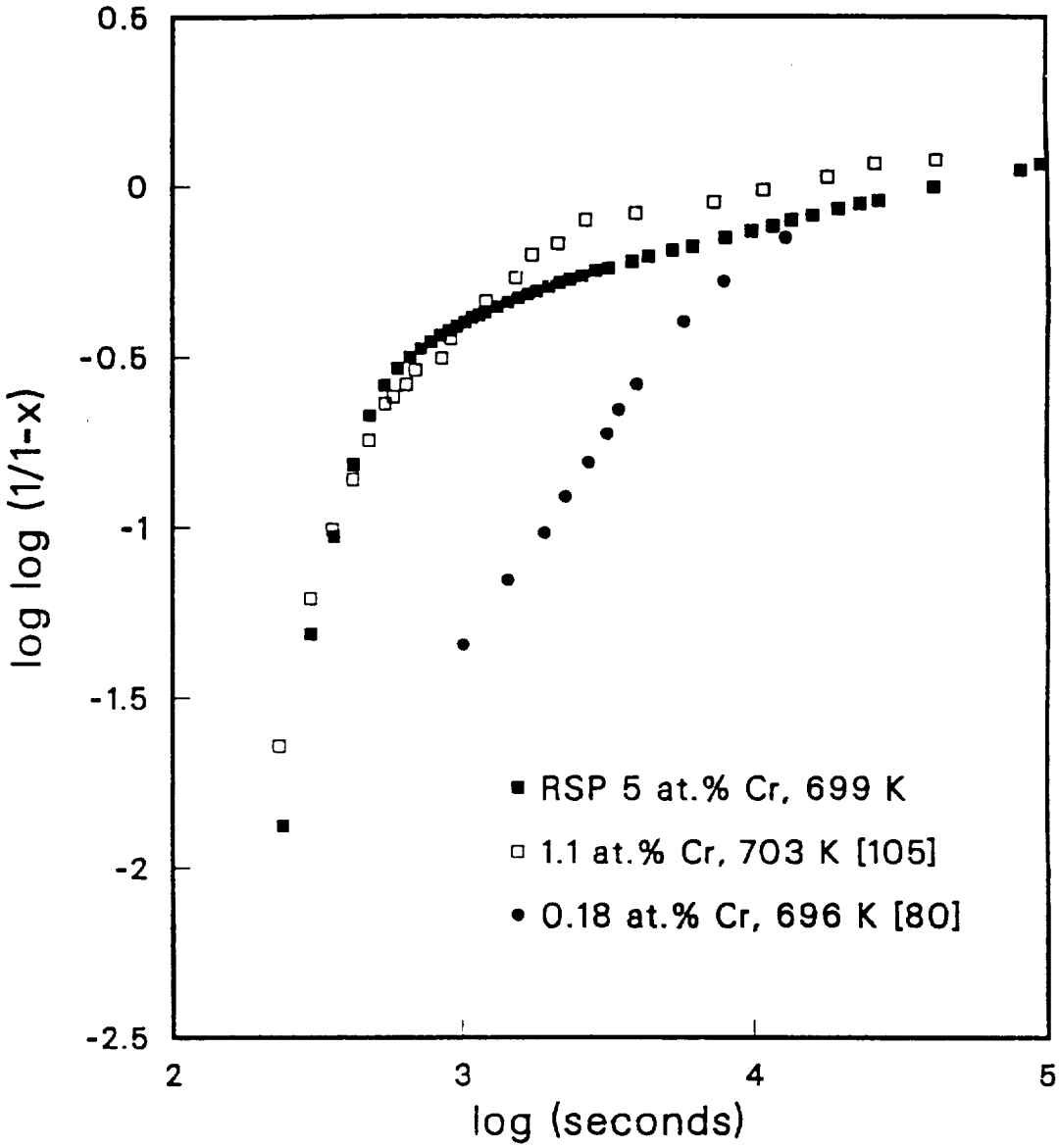

Figure 4.47. Electrical Resistance Data for Three Cu-Cr Alloys Aged at ≈700 K, Plotted According to the Avrami Method

ageing and quenching of the latter technique would introduce errors into the kinetic analysis. For example, quenched in vacancies would change the measured value of resistivity, and the thermal lag during each temperature ramping cycle would tend to offset the curve to longer ageing times. It is for these reasons that the in-situ resistivity data is felt to be more reliable.

In Figure 4.48, the data of [73,80] are presented with the RSP alloy data for an ageing temperature of $\approx$ 777 K. It can be observed that all of the data points are in reasonable agreement even though the results of [73,80] were produced by the technique of repeated ageing and quenching. Similar comparisons, made for an ageing temperature of 723 K, are not nearly as successful, Figure 4.49.

From these results, Figures 4.46–4.49, it is apparent that the precipitation kinetics are not strongly affected by the concentration of Cr in Cu. The shape of the curves and the results of the Avrami analysis are however, greatly influenced by the experimental techniques used to measure the change in resistivity during ageing.

In addition to the resistivity experiments performed on the RSP Cu-5 at.% Cr alloy, the electrical resistivity of the RSP Cu-5 at.% Cr-2 at.% Ag alloy was measured in order to evaluate the potential of these alloys for applications requiring high electrical or thermal conductivity. Since the ternary alloy contains the highest concentration of Cr and Ag of any composition in the present work, it would be expected that the electrical conductivity of any of the RSP alloys will be at least as good as the Cu-5 at.% Cr-2 at.% Ag alloy.

An absolute value of the electrical resistivity of this alloy was determined by measuring the electrical resistance of a piece of ribbon 74.2 cm in length. The density of the ternary alloy d_t was calculated by assuming that the alloying

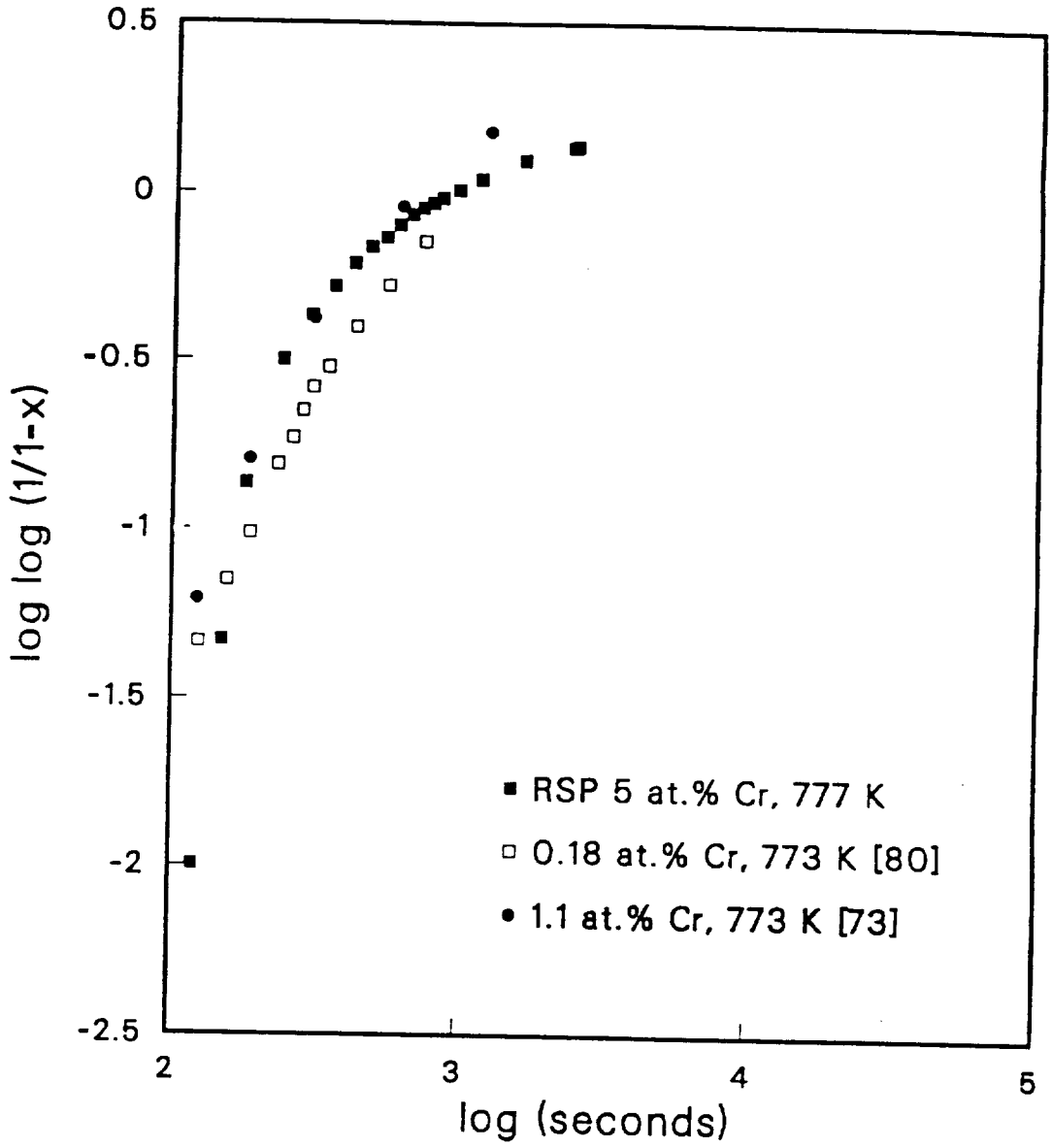

Figure 4.48. Electrical Resistance Data for Three Cu-Cr Alloys Aged at ≈773 K, Plotted According to the Avrami Method

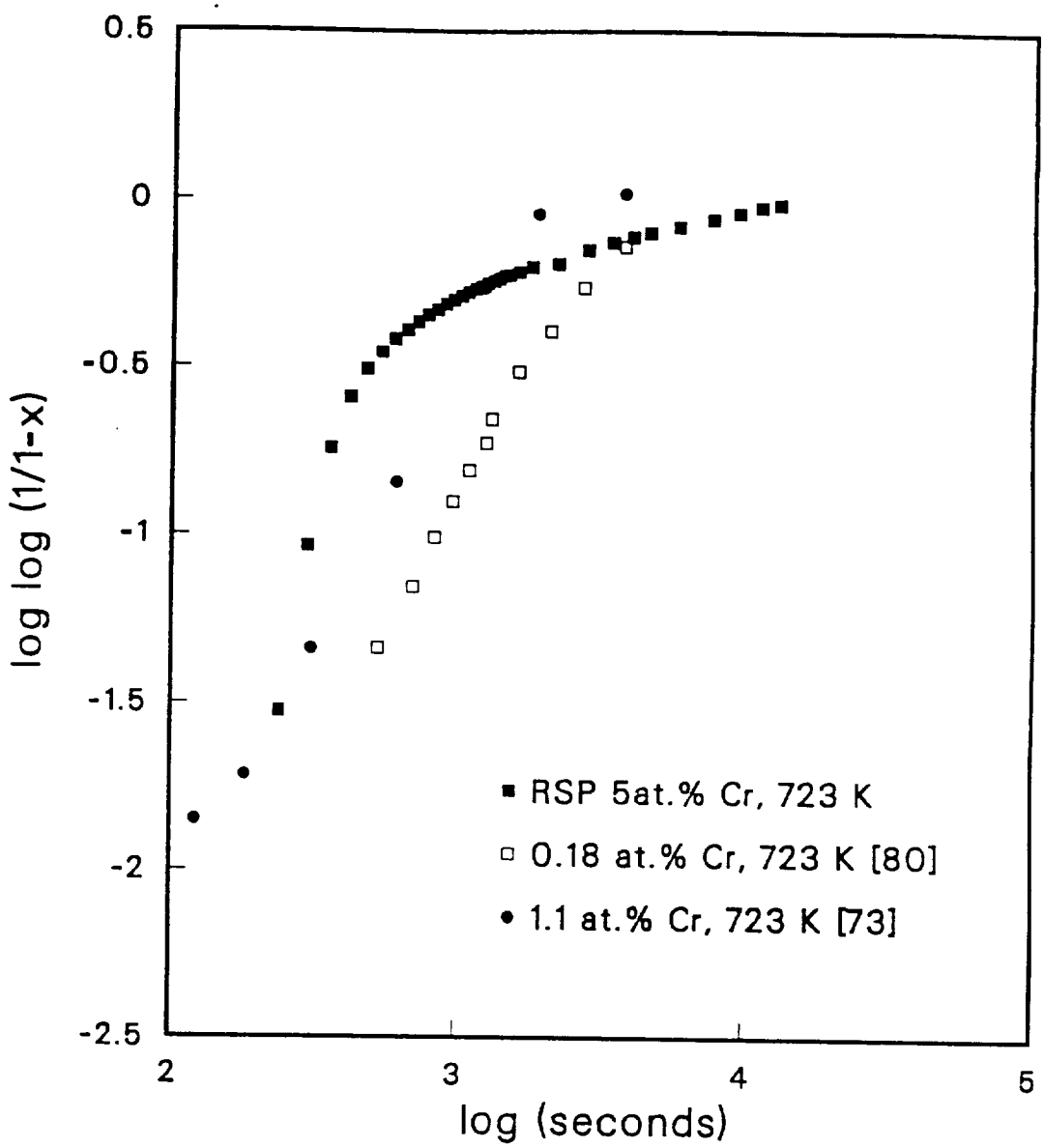

Figure 4.49. Electrical Resistance Data for Three Cu-Cr Alloys Aged at ≈723 K, Plotted According to the Avrami Method

additions are completely precipitated from solid solution as bcc Cr and fcc Ag.

$$d_t = \frac{(93 \times 63.54) + (5 \times 52) + (2 \times 107.87)}{(93)\frac{63.54}{8.92} + (5)\frac{52}{7.20} + (2)\frac{107.87}{10.5}} \tag{4.18}$$

The calculated density of 8.879 g/cm^3 is only slightly less than that of pure Cu. The resistivity is equal to the measured resistance multiplied by the cross-sectional area and divided by the length of the specimen. The cross-sectional area is equal to the mass divided by the density and length of the specimen. This assumes that the ribbon cross-section is constant, which is not strictly true. In this case, the calculated resistivity will err on the large side of the actual resistivity of the alloy. The resistance of the annealed ribbon was measured as 0.1525 ohms at 296 K, using the four-point probe method. The mass of the ribbon was measured as 0.6855 grams. After proper substitutions, the resistivity ρ is calculated as follows:

$$\rho = \frac{0.1525 \times 0.6855}{8.879 \times (74.2)^2} \tag{4.19}$$

The calculated value of 2.1385 microhms-cm is equivalent to 80.6 % IACS, and is atypical of high strength alloys produced by conventional ingot metallurgy. For example, a Cu-Be alloy of similar tensile strength, has only about one-fourth of the electrical conductivity of the RSP alloy. Conventional alloys like NARloy-Z, Cu-Cr and Cu-Zr, of similar conductivity to the RSP alloy, have less than one-half the tensile strength. Thus, rapid solidification processing of Cu-5 at.% Cr-2 at.% Ag alloy results in a very desirable combination of high mechanical strength and high conductivity. The other RSP alloys in this study would also be expected to have high electrical conductivity, although the mechanical properties are not as good as those of the Cu-5 at.% Cr-2 at.% Ag alloy.

4.7 Summary

Rapid solidification processing of Cu-Cr, Cu-Cr-Ag, and Cu-Zr alloys produced structures and properties in these materials that are unobtainable by ingot

metallurgy. In conventional Cu alloys, high conductivity is in general incompatible with high strength. Solution strengthened alloys have poor electrical and themal conductivity due to the scattering of conduction electrons from lattice distortion. Precipitation hardened alloys which have the potential for good conductivity, have limited solid solubility at elevated temperature; this restricts the volume fraction of strengthening precipitates and the mechanical properties when conventional metallurgical techniques are employed.

Rapid solidification processing provides for an alternate approach. Copper alloying additions were chosen with complete solubility in the liquid state and minimum solubility in the solid state; Ag was an exception, as it was used to greatly improve the castability of the melt-spun ribbons. Conventionally cast Cu-Cr alloys contain less than 1 at.% of finely dispersed Cr precipitates. Higher Cr concentration alloys result in eutectic solidification and coarse Cr particles with very little benefit in strength. By using RSP however, Cr concentration up to 5 at.% was accomodated in a metastable extended solid solution. Eutectic solidification was avoided and the full strengthening benefits of the large volume fraction of finely dispersed Cr precipitates was realized by subsequent elevated temperature ageing. The ageing treatment also decreased the amount of Cr in solution to increase the conductivity.

The microstructures of the Cu-Cr and Cu-Cr-Ag alloys were greatly refined by CBMS. Fine columnar grains with a dominant $< 100 >$ growth direction approximately normal to the wheel surface were produced in the as-cast melt-spun ribbons. The average grain size of 2 μm is similar in magnitude to the smallest visible Cr eutectic rods in an ingot-cast alloy. Dislocation cell boundaries of 0.5 micron diameter further refined the microstructure of the RSP alloys. The gross segregation of the ingot-cast alloy was eliminated through rapid solidification processing. During rapid solidification, Cr was trapped almost completely in

the metastable extended solid solution and this produced an expansion of the Cu lattice parameter from 0.3615 nm to 0.3628 nm for the binary Cu-5 at.% Cr alloy. Precipitation of Cr often occurred during solid state cooling of the ribbons following rapid solidification and separation of the ribbon from the melt-spinning wheel. This resulted in dislocation cell boundaries and grain boundaries decorated with fine Cr precipitates. Most of the as-cast ribbons contained a very fine and dense distribution of Cr precipitates within the cells; the typical precipitate diameter is 50 Å. The cooling rate during rapid solidification was always fast enough to avoid the eutectic reaction, however, the solid state cooling rate following solidification was usually not fast enough to fully suppress the formation of Cr precipitates. No evidence was found for the existence of novel metastable phases or amorphous structures in any of the RSP alloys of this study.

Precipitation of Cr from solid solution in the Cu-5 at.% Cr alloy occurred in a manner similar to more dilute conventional Cu-Cr alloys. The precipitation process is initiated in both cases by homogeneous nucleation. After elevated temperature ageing, the bcc Cr precipitates have a Nishiyama-Wasserman or Kurdjumow-Sachs orientation relationship with the fcc Cu matrix.

The precipitation kinetics, as measured by the change in resistivity of the binary Cu-5 at.% Cr alloy during isothermal ageing, are also similar to dilute ingot-cast Cu-Cr alloys. The change in resistance during precipitation of Cr is best explained by a two stage process; vacancy diffusion and annihilation during the initial ten minutes of ageing, and diffusion controlled coarsening of Cr precipitates during longer ageing times. The activation energy measured at short ageing times is 0.49 eV (11.3 kcal/mole), which is consistent with a calculated value for the vacancy migration energy [73]. The activation energy measured at long ageing times is 1.97 eV (45.3 kcal/mole) and represents the activation energy for the diffusion of Cr in the Cu lattice; similar values have been determined in

conventional dilute alloys by the direct measurement of the precipitate growth rate [79] and by resistance measurements [69].

The change in resistance of the Cu-Cr alloy during the early stages of ageing does not indicate the presence of a GP forming phase; only a small increase in the resistivity was measured during the first several minutes of ageing. The absence of a large positive increase in the resistivity however, does not preclude the existence of an fcc Cr phase. It is felt that Cr does in fact precipitate as a fcc phase, but the lattice misfit strain ($\approx$1.0 %) of the coherent precipitates is too small to disturb the periodicity of the Cu lattice. Even though the GP interzone spacing is assumed to be of the same order of magnitude as the mean free path of the conduction electrons, in the absence of lattice strain, very little electron scattering should occur and the resistivity of the alloy will not exhibit a large positive increase. This conclusion is consistent with the absence of bcc reflections in TEM selected area diffraction patterns, during the early stages of ageing.

The room temperature tensile properties indicate that the RSP alloys greatly benefited from the large fraction of precipitates. The Cu-5 at.% Cr-2 at.% Ag and Cu-5 at.% Zr alloys produced as-cast tensile strengths of 135.3 ksi. In addition, these alloys exhibited very good elevated temperature stability as the tensile strengths only dropped by about 5 ksi after ageing at 773 K for one hour. The elevated temperature tensile strength of the Cu-5 at.% Cr-2 at.% Ag alloy is superior to conventionally cast NARloy-Z at all temperatures up to 673 K. As the test temperature is increased, the fracture mode of the RSP alloy changes from ductile microvoid coalescence to grain boundary sliding. The very fine grain size of the RSP alloys contribute to elevated temperature creep. The combination of strong precipitation hardened grains and relatively weak denuded grain boundaries is not compatible with service at elevated temperatures. In order to utilize the significant benefits of a dense precipitate distribution, the grain boundaries

must be strengthened to a comparable level. This requires future work by other researchers in the field of RSP if these alloys are to be in service at high temperatures. At room temperature, the Cu-5 at.% Cr-2 at.% Ag alloy exhibits the remarkable combination of very high strength (130 ksi) and excellent electrical conductivity (80.6% IACS). It would be expected that the thermal conductivity of this alloy would also be excellent. This combination of mechanical and physical properties is presently unobtainable in any alloy processed by more conventional methods.

CHAPTER V

CONCLUSIONS

The results of this work lead to the following conclusions:

1. Rapid solidification processing of carefully selected Cu alloys resulted in the production of ribbons with a high volume fraction of fine precipitates in an inclusion free, high-conductivity Cu matrix.
2. The solid solubility of Cr in Cu was extended beyond the eutectic composition by RSP. Approximately 5 at.% Cr could be trapped in the metastable (Cu) phase with an expanded lattice parameter of 0.3628 nm. The solubility of Zr in Cu was extended in a similar manner.
3. The microstructures of the Cu alloys were greatly refined by CBMS. The crystalline microstructures typically consist of 2 μm diameter grains containing 0.5 μm diameter dislocation cells.
4. The cooling rate during RSP was always fast enough to avoid the eutectic solidification reaction in the binary and ternary alloys containing Cr. The solid state cooling rate following solidification was usually not fast enough to suppress the precipitation of Cr in the as-spun ribbon.
5. The room temperature tensile properties of the RSP alloys greatly benefitted from the large volume fraction of precipitates. Tensile strengths of $\approx$130 ksi were measured for Cu-Cr-Ag and Cu-Zr alloys. The elevated temperature tensile strength of RSP Cu-5 at.% Cr-2 at.% Ag is superior to conventionally cast NARloy-Z at all temperatures up to 673 K. At high temperatures, the RSP alloy fails by grain boundary sliding.
6. The electrical conductivity of RSP Cu-5 at.% Cr-2 at.% Ag (80.6 % IACS) indicates that the precipitates did not have a large deleterious effect on the conductivity of the matrix.

7. Precipitation of Cr in the RSP alloys is initiated by homogeneous nucleation. The activation energy for the coarsening of precipitates was found to be equal to 1.97 eV (45.3 kcal/mole) for ageing times beyond 20 minutes. The change in resistance during ageing of RSP Cu-5 at.% Cr is a result of vacancy annihilation and precipitate nucleation at short ageing times, and diffusion controlled coarsening of Cr precipitates at long ageing times.

BIBLIOGRAPHY

[1] Fulton, D. *Investigation of Thermal Fatigue in Non-Tubular Regeneratively Cooled Thrust Chambers,* Rockwell International Corporation, May 1973, AFRPL-TR-73-10-Vol. 2.

[2] Hannum, N.P. "Experimental and Theoretical Investigation of Fatigue Life in Reusable Rocket Thrust Chambers." *AIAA,* Paper 76-685, AIAA Conference, Palo Alto, CA, July 1976.

[3] Quentmeyer, R.J. "Experimental Fatigue Life Investigations of Cylindrical Thrust Chambers." *AIAA,* Paper 77-893, AIAA Conference, Orlando, FL, July 1977.

[4] Bever, M.B. *Encyclopedia of Materials Science and Engineering,* Vol. 2, 1986, Pergamon Press, Oxford.

[5] N.G. *OFHC Brand Copper,* 1957, The American Metal Company, Limited, New York, New York.

[6] Klemens, P.G., Williams, R.K. "Thermal Conductivity of Metals and Alloys." *International Metals Reviews,* Vol. 31, No. 5, 1986, pp 197–215.

[7] Laubitz, M.J., Matsumura, T. "High-Temperature Transport Properties of Palladium." *Can. J. Phys.,* Vol. 50, 1972, pp 196–205.

[8] Laubitz, M.J., Matsumura, T., Kelly, P.J. "Transport Properties of the Ferromagnetic Metals. II. Nickel." *Can. J. Phys.,* Vol. 54, 1976, pp 92–102.

[9] Powell, R.W. "Correlation of Metallic Thermal and Electrical Conductivities for Both Solid and Liquid Phases." *Intern. J. Heat Mass Transfer,* Vol. 8, 1965, pp 1033–1045.

[10] Smith, C.S., Palmer, E.W. "Thermal and Electrical Conductivities of Copper Alloys." *Trans. AIME,* Vol. 117, 1935, pp 225–245.

[11] Schofield, F.H. "The Thermal and Electrical Conductivites of Some Pure Metals." *Proc. Roy. Soc. (London),* Vol. A107, 1925, pp 206–227.

[12] Siu, M.C.I., Carroll, W.L., Watson, T.W. "Thermal Conductivity and Electrical Resistivity of Six Dilute Copper Alloys and Comparison With the Smith-Palmer Equation." *NBS Rep NBSIR 76-1003,* prepared for NASA, March, 1976.

[13] Gschneidner, K.A. Jr. *Solid State Physics,* ed. Seitz, F., Turnbull, D., Vol. 16, 1964, Academic Press, New York, New York.

[14] Ho, C.Y., Ackerman, M.W., Wu, K.Y., Oh, S.G., Havill, T.N. "Thermal Conductivity of Ten Selected Binary Alloy Systems." *J. Phys. Chem. Ref. Data,* Vol. 7, No. 3, 1978, pp 959–967.

[15] Chalmers, B., Quarrell, A.G. *The Physical Examination of Metals,* 2nd edition, 1960, Edward Arnold Limited, London.

[16] Reed-Hill, R.E. *Physical Metallurgy Principles,* 2nd edition, 1973, D. Van Nostrand, London.

[17] Matthiessen, A., Vogt, G. "The Electrical Resistivity of Alloys." *Ann. Physik. Chem. (Pogg. Folge),* Vol. 122, 1864, pp 19–31.

[18] Norbury, A.L. "The Electrical Resistivity of Dilute Metallic Solid Solution." *Trans. Faraday Soc.,* Vol. 16, 1922, pp 570–602.

[19] Linde, J.O. "Elektrische Eigenschaften verdünnter Mischkristallegierungen III. Widerstand von Kupferund Goldlegierungen, Gesetzmassigkeiten der Widerstandserhöhungen." *Ann. d. Physik* Vol. 15, 1932, pp 219–248.

[20] Mott, N.F. "The Electrical Resistance of Dilute Solid Solutions." *Proc. Camb. Phil. Soc.,* Vol. 32, 1936, pp 281–290.

[21] Hibbard, W.R. Jr. "Electrical Resistivity of Dilute Binary Terminal Solid Solutions." *Trans. AIME,* Vol. 200, 1954, pp 594–602.

[22] Sedström, E. "Peltier Effect, and Thermal and Electrical Conductivities of Some Solid Metallic Solutions." *Ann. d. Physik,* Vol. 59, 1919, pp 134–144.

[23] Svensson, B. "Magnetic Susceptibility and Electrical Resistance of the Mixed Crystal Series Pd-Ag and Pd-Cu." *Ann. d. Physik,* Vol. 14, 1932, pp 699–711.

[24] Mott, N.F. "A Discussion of the Transition Metals on the Basis of Quantum Mechanics." *Proc. Phys. Soc.,* Vol. 47, 1935, pp 571–588.

[25] Pawlek, F., Reichel, K. "Der Einfluss von Beimengungen auf die elektrische Leitfähigkeit von Kupfer." *Z. Metallkde.,* Vol. 47, 1956, pp 347–356.

[26] Chakrabarti, D.J., Laughlin, D.E. "The Cr-Cu (Chromium-Copper) System." *Bulletin of Alloy Phase Diagrams,* Vol. 5, No. 1, 1984, pp 59–68.

[27] Timberg, J.M., Toguri, J.M. "A Thermodynamic Study of (Copper + Chromium) by Mass Spectrometry." *J. Chem. Thermodyn.,* Vol. 14, 1982, pp 193–199.

[28] Kuznetsov, G.M., Fedorov, V.N., Rodnyanskaya, A.L. "Investigation of Phase Diagrams of Cu-Cr System." *Izv. Vyssh. Ucheb. Zaved., Tsvetn. Met.,* Vol. 3, 1977, pp 84–86.

[29] Hindrichs, G. "Some Cr and Mn Alloys." *Z. Anorg. Chem.,* Vol. 59, 1908, pp 414–449.

[30] Siedschlag, E. "Cr-Cu-Ni Alloys." *Z. Anorg. Chem.*, Vol. 131, 1923, pp 173–190.

[31] Corson, M.G. "Cu Alloy Systems with α-Phase Having Variable Limits and Their Use for Hardening of Cu." *Rev. Met.*, Vol. 27, 1930, pp 83–95.

[32] Alexander, W.O. "Annealing Characteristics and Solid Solubility Limits of Cu and Cu Alloys Containing Cr." *J. Inst. Met.*, Vol. 64, 1939, pp 93–109.

[33] Hibbard, W.R. Jr., Rosi, F.D., Clark, H.T. Jr., O'Herron, R.I "The Constitution and Properties of Cu-Rich Cu-Cr and Cu-Ni-Cr Alloys." *Trans. AIME,* Vol. 175, 1948, pp 283–294.

[34] Doi, T. "Studies on Cu Alloys Containing Cr (1st Report). On the Cu Side Phase Diagram." *J. Jpn. Inst. Met.*, Vol. 21, No. 5, 1957, pp 337–340.

[35] Zakharov, M.V., Osintsev, O.E. "Phase Diagram of Cu Corner of Cu-Ni-Cr System." *Izv. Vyssh. Ucheb. Zaved., Tsvetn. Met.*, Vol. 5, 1967, pp 152–155.

[36] Drits, M.E., Rokhlin, L.L., Bochyar, N.R., Lysova, E.V., Rozenberg, A.K., Nikolaev, A.K., Shparo, N.B. "Solubility of Cr and Hf in Cu Solid State." *Izv. Vyssh. Ucheb. Zaved., Tsvetn. Met.*, Vol. 2, 1967, pp 122–125.

[37] Gordon, P. *Principles of Phase Diagrams in Materials Systems*, 1968. McGraw-Hill, New York, New York.

[38] Shchirin, V.F., Rosenberg, V.M., Belousov, N.P. "Determining Concentration of Solid Solution of Cr Bronze from Magnitude of Electrical Resistance." *Izv. Vyssh. Ucheb. Zaved., Tsvetn. Met.*, Vol. 12, 1971, pp 85.

[39] Priester, P., Fargette, B., Whitwham, D., Diner, O., Herenguel, J. "Properties Imparted by the Dispersoid-Type Structure in Copper-0.8% Chromium Alloy Precipitated by Heating." *Memoires et Etudes Scientifiques de la Revue de Metallurgie*, Vol. 68, No. 10, 1971, pp 665–686.

[40] Lou, M.Y.W., Grant, N.J. "Identification of Cu_5Zr Phase in Cu-Zr Alloys." *Met. Trans. A.* Vol. 15A, 1984, pp 1491–1493.

[41] Pogodin, J.S., Shumova, J.S., Kugucheva, F.A. "Constitution and Properties of Copper-Zirconium Alloys." *Comptes Rendus (Doklady) de l'Académie des Sciences de l'URSS*, Vol. 27, 1940, pp 670–672.

[42] Allibone, T.E., Sykes, C. "The Alloys of Zirconium." *J. Inst. Metals*, Vol. 37, 1928, pp 173–187.

[43] Raub, E., Engel, M. "Alloys of Zirconium with Copper, Silver, and Gold." *Z. Metallkde.,* Vol. 39, 1948, pp 172–177.

[44] Saarivirta, M.J. "High Conductivity Copper-Rich Cu-Zr Alloys." *Trans. AIME,* Vol. 218, 1960, pp 431–437.

[45] Zwicker, U. "Untersuchungen an Kupfer-Zirkonium-Legierungen." *Metall.,* Vol. 16, 1962, pp 409–412.

[46] Showak, W. "The Solid Solubility of Zirconium in Copper." *Trans. AIME,* Vol. 224, 1962, pp 1287–1298.

[47] Donachie, M.J. Jr. "An Investigation of the Copper-Rich Portion of the Copper-Zirconium Phase Diagram by Electron-Probe Microanalysis." *Journal of the Institute of Metals,* Vol. 92, 1963–1964, p 180.

[48] Perry, A.J., Hugi, W. "A Contribution to the Copper-Rich Copper-Zirconium Phase Diagram." *Journal of the Institute of Metals,* Vol. 100, 1972, pp 378–380.

[49] Lundin, C.E., McPherson, D.J., Hansen, M. "System Zirconium-Copper." *Trans. AIME,* Vol. 197, 1953, pp 273–278.

[50] Vitek, J.M. " Electron Microprobe Investigation of the Intermediate Phases in the Cu-Zr System." *Z. Metallkde.,* Vol. 67, H. 8, 1976, pp 559–563.

[51] Hillman, G., Hofmann, W. "Diffusionmessungen im System Kupfer-Zirkonium." *Z. Metallkde.,* Vol. 56, H. 5, 1965, pp 279–285.

[52] Meny, L., Champigny, M., Beltrando, R., Salaun, P. " Diffusion à l'État Solide dans les Systèmes Zirconium-Cuivre et Zirconium-Nickel. Étude des Composés Intermétalliques Formés. " *Journal de Microscopie,* Vol. 6, 1967, pp 111–112.

[53] Forey, P., Glimois, J-L., Feron, J-L., Develey, G., Becle, C. "Cristallochimie-Préparation, Identification et Structure Cristalline de Cu_5Zr." *C.R. Acad. Sc. Paris,* t. 291, 1980, pp 177–178.

[54] Bsenko, L. "Crystallographic Data for Intermediate Phases in the Cu-Zr and Cu-Hf Systems." *Journal of the Less-Common Metals,* Vol. 40, 1975, pp 365–366.

[55] Hansen, M., Anderko, K. *Constitution of Binary Alloys,* 2nd edition, 1958, McGraw-Hill Book Company, Inc., New York, New York.

[56] Heycock, C.T., Neville, F.H. "Complete Freezing-Point Curves of Binary Alloys Containing Silver or Copper Together with Another Metal." *Phil. Trans. Roy. Soc. (London),* Vol. A189, 1897, pp 32–36, pp 57–58.

[57] Hirose, T. *On the Silver-Copper Alloys,* Rept. Imp. Mint, Osaka, No. 1, 1927,pp 1–74, also in Proc. World Eng. Congr. Tokyo, 1929, Vol. 36, 1931, pp 37–111.

[58] Stockdale, D. "The Composition of Eutectics." *J. Inst. Metals,* Vol. 43, 1930, pp 193–211.

[59] Broniewski, W., Koslaoz, S. "Alloys of Silver and Copper." *Compte. rend.,* Vol. 194, 1932, pp 973–975.

[60] Chaston, J.C. *Equilibrium Diagram of System Copper-Silver, Annotated Equilibrium Diagram Series, no. 10.,* 1953, The Institute of Metals, London.

[61] Ageew, N.W., Hansen, M., Sachs, G. "Changes in Properties During the Cooling of Supersaturated Silver-Copper Alloys." *Z. Physik,* Vol. 66, 1930, pp 350–376

[62] Stockdale, D. "The Solid Solutions of the Copper-Silver System." *J. Inst. Metals,* Vol. 45, 1931, pp 127–140.

[63] Smith, C.S., Lindlief, W.E. "The Equilibrium Diagram of the Copper-Rich Copper-Silver Alloys." *Trans. AIME,* Vol. 99, 1932, pp 101–118.

[64] Schmid, E., Siebel, G. "Mixed-Crystal Formation with Single and Polycrystalline Materials." *Z. Physik,* Vol. 85, 1933, pp 36–55.

[65] Owen, E.A., Rogers, J. "X-ray Study of the Copper-Silver Alloys." *J. Inst. Metals,* Vol. 57, 1935, pp 257–266.

[66] Duwez, P., Willens, R.H., Klement, W.Jr. "Continuous Series of Metastable Solid Solutions in Silver-Copper Alloys." *J. Appl. Phys.,* Vol. 31, 1960, pp 1136–1137.

[67] Doi, T. "Studies on Copper Alloys Containing Chromium (2nd Report)." *J. Jpn. Inst. Met.,* Vol. 21, No. 12, 1957, pp 720–724.

[68] Lyman, T. *Metals Handbook, Properties and Selection of Metals,* Vol. 1, 8th edition, 1969, ASM, Metals Park, Ohio.

[69] Köster, W., Knorr, W. "Eigenschaftsänderungen während der Aushärtung einer Kupfer-Chrom-Legierung." *Z. Metallkde.,* Vol. 45, 1954, pp 350–356.

[70] Suzuki, H., Kawakatsu, I., Kitano, H. "Some Properties of Copper-High Zirconium-High Chromium Alloys." *J. Jpn. Inst. Met.,* Vol. 31, No. 4, 1967, pp 342–346.

[71] N.G. *AMCHROM Brand Copper, Interim Publication,* 1983, AMAX Copper, Inc., New York, New York.

[72] Koda, S., Isono, E. "On Heat-Treatable Copper-Chromium Alloy (I)." *J. Jpn. Inst. Met.*, Vol. 16, 1952, pp 213–217.

[73] Nagata, K., Nishikawa, S. "Aging and Reversion Phenomena of Cu-Cr Alloy." *Report of the Institute of Industrial Science, The University of Tokyo,* Vol. 24, No. 4, (Serial No. 153), 1975, pp 115–168.

[74] N.G. *Thrust Chamber Material Exploratory Technology Program, Literature Review of Copper Base Alloys,* Report FR-18383-1, May 1984, Pratt and Whitney Aircraft, Government Products Division, West Palm Beach, Fl.

[75] Saarivirta, M.J., Taubenblat, P.P. "Some High-Temperature Properties of Copper-Zirconium and Copper-Chromium High-Conductivity Alloys." *Trans. AIME,* Vol. 218, 1960, pp 935–939.

[76] Morris, M.A., Morris, D.G. "Microstructures and Mechanical Properties of Rapidly Solidified Cu-Cr Alloys." *Acta metall.*, Vol. 35, No. 10, 1987, pp 2511–2522.

[77] Williams, R.O. "Precipitation in Copper-Chromium Alloys. " *Trans. ASM,* Vol. 52, 1960, pp 530–544.

[78] Suzuki, H., Kanno, M., Kawakatsu, I. "The Strength of Copper-Zirconium-Chromium Alloy in Relation to Its Aged Structure." *J. Jpn. Inst. Met.*, Vol. 33, No. 5, 1969, pp 628–633.

[79] Rezek, J. "Technical Note: Kinetics of Precipitate Growth in the Copper-Chromium System." *Canadian Metallurgical Quarterly,* Vol. 8, No. 2, 1969, pp 179–182.

[80] Knights, R.W., Wilkes, P. "Precipitation of Chromium in Copper and Copper-Nickel Base Alloys." *Met. Trans.*, Vol. 4, No. 10, 1973, pp 2389–2393.

[81] Komen, Y., Rezek, J. "Precipitation at Coherency Loss in Cu-0.35 Wt Pct Cr." *Met. Trans. A,* Vol. 6A, 1975, pp 549–551.

[82] Hall, M.G., Aaronson, H.I., Kinsman, K.R. "The Structure of Nearly Coherent fcc: bcc Boundaries in a Cu-Cr Alloy." *Surface Science,* Vol. 31, 1972, pp 257–274.

[83] Weatherly, G.C., Humble. P., Borland, D. "Precipitation in a Cu-0.55 wt.% Cr Alloy." *Acta metall.*, Vol. 27, 1979, pp 1815–1828.

[84] Clarke, D.R., Stobbs, W.M. "The Crystallography of Phase Interfaces in the Unidirectionally Solidified Cu-Cr Eutectic Alloy." *Metal Science,* Vol. 8, 1974, pp 242–246.

[85] Hall, M.G., Aaronson, H.I., Lorimer, G.W. "Considerations on a Martensitic Mechanism for the fcc→bcc Transformation in a Cu-0.33 wt.% Cr Alloy." *Scripta metall.*, Vol. 9, No. 5, 1975, pp 533–542.

[86] Nishikawa, S., Nagata, K., Kobayashi, S. "Reversion Phenomena of Cu-Cr." *J. Jpn. Inst. Met.*, Vol. 30, No. 8, 1966, pp 760–765.

[87] Suzuki, H., Kitano, H., Kanno M. "Reversion Phenomena in Cu-Zr-Cr Alloys." *J. Jpn. Inst. Met.*, Vol. 33, No. 3, 1969, pp 334–338.

[88] Suzuki, H., Kanno, M. "Initial Aging Phenomena in Copper-Chromium Alloys." *J. Jpn. Inst. Met.*, Vol. 37, No. 1, 1973, pp 13–18.

[89] Guy, A.G., Barrett, C.S., Mehl, R.F. "Mechanism of Precipitation in Alloys of Beryllium in Copper." *Trans. AIME,* Vol. 175, 1948, pp 216–239.

[90] Sachslehner, F., Gröger, V., Stangler, F. "Investigation of Precipitation Hardening in Cu-2Be-0.2Co by Vickers Microhardness and Electrical Resistance." *Metal Science,* Vol. 18, March 1984, pp 153–157.

[91] Turnbull, D., Rosenbaum, H.S., Treaftis, H.N. "Kinetics of Clustering in Some Aluminum Alloys." *Acta metall.*, Vol. 8, 1960, pp 277–295.

[92] Guha, A. *Precipitation and Coarsening Behavior in Two Copper-Base Alloys: Copper-Titania, Copper-Chromium,* Ph.D. Thesis, University of Pittsburgh, 1977

[93] Rdzawski, Z., Stobrawa, J. "Structure of Coherent Chromium Precipitates in Aged Copper Alloys." *Scripta metall.*, Vol. 20, 1986, pp 341–344.

[94] N.G. *AMZIRC Brand Copper, Interim Publication,* 1983, AMAX Copper, Inc., New York, New York.

[95] Fargette, B. "Interaction of Cold Work, Recovery, Recrystallization, and Precipitation in Heat-Treatable Copper Alloys." *Metals Technology,* Vol. 6, No. 5, 1979, pp 194–201.

[96] Bushnev, L.S., Payuk, V.A., Korotayev, A.D. "The Ageing of Copper-Zirconium and Copper-Aluminum-Zirconium Alloys." *Fiz. metal. metalloved.*, Vol. 37, No. 3, 1974, pp 573–579.

[97] Nagai, T., Henmi, Z., Sakamoto, T., Koda, T. "Effect of Precipitates on Recrystallization Temperature in Cu-Cr, Cu-Zr and Cu-Zr-Cr Alloys." *Trans. JIM,* Vol. 14, 1973, pp 462–469.

[98] Hodge, W. "Some Properties of Certain High-Conductivity Copper-Base Alloys." *Trans. AIME,* Vol. 9, 1957, pp 408–412.

[99] Hodge, W., Jaffee, R.I., "A High Strength-High Conductivity Copper-Silver Alloy Wire." *Trans. AIME,* Vol. 180, 1949, pp 15–31.

[100] Cox, W.F., Sykes, C. "Precipitation in the Alloys of Copper and Silver During Age-Hardening." *J. Inst. Metals,* Vol. 66, 1940, pp 381–387.

[101] Fulton, D. *Investigation of Thermal Fatigue in Non-Tubular Regeneratively Cooled Thrust Chambers,* Rockwell International Corporation, May 1973, AFRPL-TR-73-10-Vol. 1.

[102] Klement, W.Jr., Luo, H.L. "Metastable Solid Solutions in Silver-Platinum Alloys." *Trans. AIME,* Vol. 227, 1963, pp 1253–1254.

[103] Falkenhagen, G., Hofmann, W. "Die Auswirkung extrem hoher Abkühlungsgeschwindigkeit auf die Erstarrung und das Gefüge binärer Legierungen." *Z. Metallkde.,* Vol. 43, 1952, pp 69–81.

[104] Duwez, P. "Structure and Properties of Alloys Rapidly Quenched from the Liquid State." *Trans. ASM,* Vol. 60, 1967, pp 605–633.

[105] Lenhart, R.E. *Some Mechanical and Electrical Properties of Copper-Nickel-Chromium Alloys,* Report No. 55-RL-1395, Sept. 1955, General Electric Research Laboratory.

[106] Servi, I.S., Turnbull, D. "Thermodynamics and Kinetics of Precipitation in the Copper-Cobalt System." *Acta metall.,* Vol. 14, No. 2, 1966, pp 161–169.

[107] Christian, J.W. *The Theory of Transformations in Metals and Alloys Part I Equilibrium and General Kinetic Theory,* second edition, Pergamon Press, Oxford.